Constitutive Model and Solder Joint Reliability Predictions for BGA Packages Subjected to Aging

by

Munshi M. Basit

A dissertation submitted to the Graduate Faculty of
Auburn University
in partial fulfillment of the
requirements for the Degree of
Doctor of Philosophy

Auburn, Alabama
August 1, 2015

Keywords: lead-free solder, aging, silver content, solidification profile, constitutive models, mechanical properties, finite element model, and reliability

Approved by

Jeffrey C. Suhling, Chair, Quina Distinguished Professor of Mechanical Engineering
Hareesh V. Tippur, McWane Professor of Mechanical Engineering
Michael J. Bozack, Professor of Physics
James S. Davidson, Professor of Civil Engineering

Abstract

Isothermal aging causes detrimental changes in the microstructure, mechanical response, and failure behavior of lead free solder joints in electronic assemblies. Traditional finite element based predictions for solder joint reliability during thermal cycling accelerated life testing are based on solder constitutive equations (e.g. Anand viscoplastic model) and failure models (e.g. energy dissipation per cycle model) that do not evolve with material aging. This work has implemented a theoretical framework for correcting this limitation and including aging effects in the reliability modeling. The developed approach involved the use of: (1) a revised set off Anand viscoplastic stress-strain relations for solder that included material parameters that evolve with the thermal history of the solder material, and (2) a revised solder joint failure criterion that included aging effects.

To determine the effects of aging, uniaxial tensile tests were conducted on SAC305 samples that were aged for various durations (0-360 days) at a temperature of 100 ^{o}C. Mechanical tests have been performed using both water quenched (WQ) and reflowed (RF) SAC305 samples (two unique specimen microstructures). For each set of aging conditions, several sets of constant strain rate and temperature tests were conducted on the aged solder samples. Using the measured uniaxial test data, the Anand parameters were calculated for each set of aging conditions, and the effects of aging on the nine Anand model parameters were determined. From the experimental results, the

differences between the extracted Anand model parameters of water quenched and reflowed samples were high for samples with no prior aging. For both the water quenched and reflowed specimens, significant degradation of the mechanical properties was observed with aging. After long aging times, the water quenched and reflowed SAC305 materials were found to exhibit similar mechanical properties, and thus their Anand parameters converged and became nearly identical.

Moreover, an investigation on the Anand constitutive model and its application to SAC solders of various silver contents (i.e. SACN05, with N = 1, 2, 3, 4) has been performed. For each alloy, both water quenched (WQ) and reflowed (RF) solidification profiles were utilized to establish two unique specimen microstructures, and the same reflow profile was used for all four of the SAC alloys so that the results could be compared and the effects of Ag content could be studied systematically. The nine Anand parameters were determined for each unique solder alloy and microstructure from a set of stress strain tests performed at several strain rates and temperatures. As expected, the mechanical properties (modulus and strength) increase with the percentage of Ag content, and these changes strongly affect the Anand parameters. The sensitivity of the mechanical properties and Anand parameters to silver content is higher at lower silver percentages (1-2%). After deriving the Anand parameters for each alloy and microstructure, the stress-strain curves have been calculated for various conditions, and excellent agreement was found between the predicted results and experimental stress-strain curves. In addition, tensile testing was performed on reflowed SACN05 specimens subjected to 180 days of aging at 100 ^{o}C. After this severe level of aging, any further

changes in the mechanical response and properties from subsequent aging will be rather small.

The developed Anand constitutive equations for solder with aging effects were then incorporated into standard finite element codes. The applied aging-aware failure criterion was based on the Morrow-Darveaux (dissipated energy based, DeltaW) approach, with both the fatigue criterion for crack initiation and the crack growth law incorporating material constants that depend on the prior aging of the solder material. In the simulations, BGA packages were subjected to isothermal aging followed by thermal cycling accelerated life testing. The Anand model parameters were chosen based on the prior aging conditions.

The model predictions were correlated with solder joint reliability test data for the same components. The experimental test vehicle incorporated several sizes (5, 10, 15, 19 mm) of BGA daisy chain components with 0.4 and 0.8 mm solder joint pitches (SAC305). PCB test boards with 3 different surface finishes (ImAg, ENIG and ENEPIG) were utilized. Before thermal cycling began, the assembled test boards were divided up into test groups that were subjected to several sets of aging conditions (preconditioning) including 0, 180, and 360 days aging at T = 125 ^{o}C. After aging, the assemblies were subjected to thermal cycling (-40 to +125 ^{o}C) until failure occurred. The failure data for each test group were fit with the two parameter Weibull model, and the failure plots have demonstrated that the thermal cycling reliabilities of pre-aged assemblies were significantly less than those of analogous non-aged assemblies with degradations of up to 53% for one year of prior aging.

The coefficients in the aging aware crack growth model were selected to reflect the board surface finish and SAC solder combination. With this approach, good correlation was obtained between the new FEA-based reliability modeling procedure that includes aging and the entire set of measured solder joint reliability data that includes multiple component sizes, prior aging conditions, and board surface finishes.

Acknowledgments

Many people have been a part of my graduate education as teachers, friends, class mates and well-wishers. Dr. Jeffrey C. Suhling, my supervisor first and foremost, has been all of them. Frankly, this study would not have been possible without his valuable advice and immeasurable help. Although the mere expression of thanks is not appropriate, it is my great pleasure to bestow my deep sincere gratitude to him.

I owe deep sincere gratitude to my Ph.D. advisory committee members Dr. Michael J. Bozack, Dr. Hareesh V. Tippur, Dr. James Davidson, and Dr. John L. Evans for their valuable discussions and advice. I have taken several courses from them related to my research. I have gathered much knowledge from them in class and outside of class.

Special thanks to all of my friends, lab mates, co-workers including Dr. Jordan Roberts, Dr. Mohammad Motalab, Dr. Zijie Cai, Dr. Safina Hussain, Dr. Muhannad Mustafa, Dr. Nusratjahan Chhanda, John Marcell, Md Hasnine, and Michael Palmer for their help, encouragement, and friendship.

Finally, I am very much grateful to my family members specially my late father Kaiser Ahammad and my late mother Sharifa Akhter for their endless love and support of my studies. Also, I would like to thank my wife Nusrat Jahan for her understanding and love during the study period. Her support and encouragement was in the end what made this dissertation possible.

Table of Contents

List of Tables

List of Figures

CHAPTER 1

INTRODUCTION

1.1 Lead Free Solders in Electronic Packaging Industry

In the past, eutectic 63Sn-37Pb has been the most extensively used soldering alloy in the electronic industry. Eutectic Sn-Pb solders were very attractive due to their relatively low melting temperature (183 °C), excellent ductility, good reliability, and for their superior wettability and compatibility with most substrates and devices [1]. With the emergence of the modern electronic packaging technology over the last few decades, solder alloys have been the primary interconnect material used in electronic packaging. There is a general trend towards products that minimize harmful effects on the environment and human health. This trend is further reinforced by the RoHS ban on harmful substances and WEEE regulations on recycling and minimizing of electronic wastes.

In June 2000, the EU adopted two directives, the Waste of Electrical and Electronic Equipment (WEEE) and the Directive of the Restriction of the Use of Certain Hazardous Substances (RoHS) [2]. The WEEE directive requires that lead has to be removed from any end-of-life electrical or electronic components. The RoHS specifically bans lead from electrical and electronic components manufactured after July 1, 2006. As a result of the enforcement of the directives, all electrical or electronic equipment and devices produced in or imported to E.U. member states must comply with these lead-free standards except those items that are exempted from the bans. In addition to legislation enforcement there are emerging detection technologies to enforce

compliance. So due to the general push towards the eco-efficiency and green electronics, manufacturers are motivated for the adoption of lead free electronics. Therefore, the conversion to lead free solders in the global electronic market appears imminent [3].

In the United States, as soon as lead-free solder legislation was proposed, the lead-free solder project headed by the NCMS initiated research and development of lead-free solder in a program lasting 4 years [4]. The results of the project have been made available in a database and offer information on such matters as modifying equipment and processes for selecting alternative materials. The project initially selected for study 79 types of alloys considered at the time to be potential candidates for use in lead-free solder. Basic attributes considered included toxicity, resource availability, economic feasibility, and wetting characteristics. The selection process narrowed the field down to the final seven alloys, and these received secondary evaluation for reliability and ease of mounting manufacturing. Evaluation of the individual alloys did not result in the final selection of a single candidate, but three alloys, Sn–58Bi, Sn–3.5Ag–4.8Bi, and Sn–3.5Ag, were recommended as candidates.

Screening comments indicated that the Sn–58Bi eutectic alloy was not suitable for use as standard solder due to the scarcity of Bi resources. However, since this material can be used for mounting at less than 200 C, and has chalked up a 20-year plus record of use in mainframe computers, this solder was deemed suitable for special applications. These results were used to construct a database on lead-free solder that includes the information in these tables along with other items such as (1) recommended applications for lead-free solder, (2) alloy composition guidelines reflecting price and availability, (3) database of the 7 selected alloys and comparison with Sn–Pb eutectic alloy, (4) data on

the characteristics of the other 70 eliminated alloys, (5) optimal process conditions using various test PWBs, (6) strength evaluation and metallurgical reaction analysis for the selected alloys and various surface mounting process reactions, (7) predicted life (using NCMS Project proprietary life prediction software) and thermal fatigue evaluation for 4 of the selected alloys, and (8) assessment of nontoxicity and alloy composition.

In selecting suitable alternative of Sn-Pb soldering materials, it is important to take into consideration that the properties of the alternative solders are comparable or superior to Sn-Pb solders. Compatible candidates of the Sn-Pb solders must have the following behaviors [5]:

- melting temperature similar to eutectic Sn-Pb for a similar reflow profile
- sufficient wettability for good metallization process
- good electrical properties for transmitting electrical signals
- strong mechanical properties for good fatigue resistance and reliability
- inexpensive and easier manufacturability

1.2 Prevailing Lead Free Solder Choices

Among various alloy systems that are considered as lead-free solder candidates, Sn-Ag-Cu alloys have been recognized as the most promising because of their relatively low melting temperature (compared with the Sn-Ag binary eutectic lead free solder), superior mechanical properties, and good compatibility with other components [6-8]. Sn-Ag-Cu alloys are widely used as lead-free solutions for ball-grid-array (BGA) interconnection in the microelectronic packaging industry as solder balls and pastes. Although no “drop in” replacement has been identified that is suitable for all applications, Sn-Ag, Sn-Ag-Cu (SAC), and other alloys involving elements such as Sn, Ag, Cu, Bi, In,

and Zn have been identified as promising replacements for standard 63Sn-37Pb eutectic solder. Industries have proposed several SAC alloys which include 96.5Sn-3.0Ag-0.5Cu (SAC305) in Japan, 95.5Sn-3.8Ag-0.7Cu (SAC387) in the EU, and 95.5Sn-3.9Ag-0.6Cu (SAC396) in the USA. The International Printed Circuit Association has suggested that 96.5Sn-3.0Ag-0.5Cu (SAC305) and Sn-3.9Ag- 0.6Cu (two near-eutectic alloys) will be the most widely used alloys in the future [9]. This prediction is attributed to their good mechanical properties, acceptable wetting properties, and suitable melting points [10-12].

A relatively large number of lead free solder alloys have been proposed so far, including binary, ternary and even quaternary alloys. More than 70 alloys have been identified in the literature. Among them, the majority of the alloys are Sn-based alloys, that is, Sn is the preferred major constituent. In fact, Sn-rich lead free alloys have occupied more than 80% in the wave solder market share and more than 90% in the reflow solder (http://www.ameslab.gov/files/LeadFreeSolder_Foundation.pdf) market share (Figure 1.1). The main benefits of the various SAC alloy systems are their relatively low melting temperatures compared with the 96.5Sn–3.5Ag binary eutectic alloy, as well as their superior mechanical and solderability properties when compared to other lead-free solders. There are some major challenges for the current series of lead-free solders. SAC series alloys have a higher melting temperature, around 217 °C, compared to 183 °C for the eutectic Sn-Pb solders. They thus require higher reflow temperature during the manufacturing process, which can lead to reliability problems. The excessive buildup of intermetallic formed at the interface between the solder joints and the copper pad can also cause reliability problems. High costs are another issue for lead-free solders.

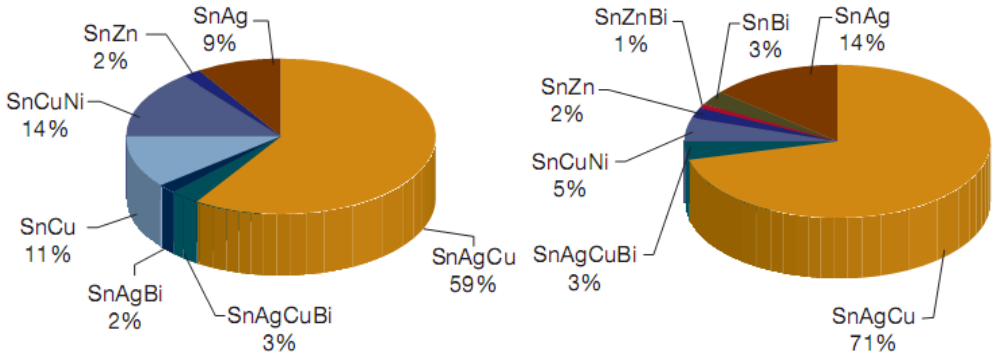

(a) Wave Solders (b) Reflow Solders

Figure 1.1 Lead Free Solder Market Share

1.3 Different Lead Free Solder Alloys

There are several Pb-free solder candidates that have been considered for replacing Sn-Pb solders. The candidates primarily originate from a group of adequate binary alloy systems, which are further developed by adding small quantity of third or fourth elements in order to (1) lower the solder melting temperature and (2) increase its wettability and reliability [13].

As illustrated in Figure 1.1, Sn-based lead free solders are widely used and have been regarded as the best option for replacing eutectic Sn-Pb solder thus far. Actually, most of these lead free candidates originate from binary alloy systems and some are further optimized by adding small amount of third chemical elements in order to lower the melting point and/or increase the wettability and reliability [14]. Figure 1.2 summarizes popular lead free choices available on the market and their current applications.

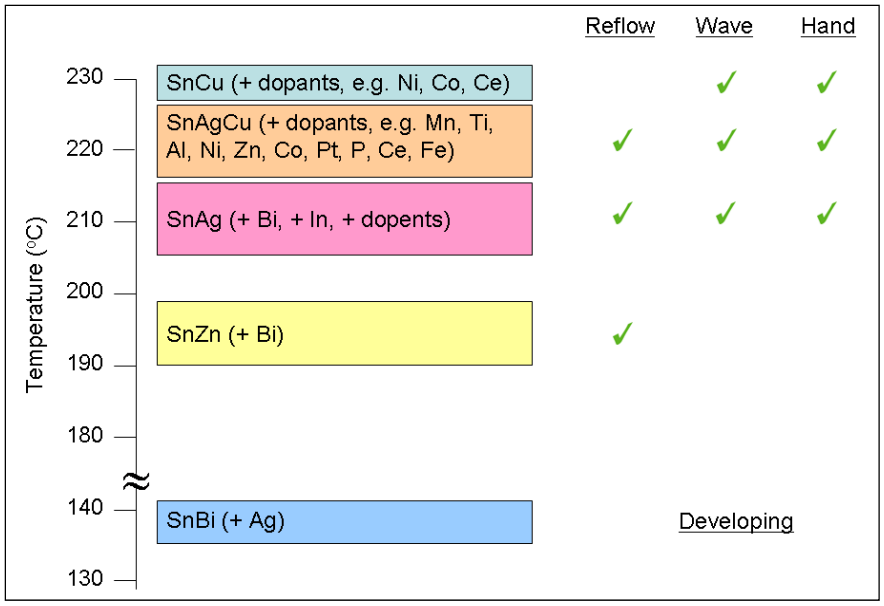

(Lee, N. C., Professional Development Course, ECTC 2011)

Figure 1.2 Prevailing Lead Free Choices and Their Applications

1.3.1 Sn-Cu System

The Sn-Cu binary system has a eutectic composition of 99.3Sn-0.7Cu and a melting temperature of 227 °C. This alloy is preferably used in wave soldering and might be suitable for high temperature applications required by the automotive industry. But it has unsatisfactory wettability and low thermal resistance. Furthermore, Sn-Cu alloys have relatively poor mechanical properties [15].

1.3.2 Sn-Ag System

The Sn-Ag binary system has a eutectic composition of 96.5Sn-3.5Ag in weight percentage and a melting temperature of 221 °C. The solidified microstructure of the eutectic alloy features β-tin phase with dendritic globules and inter-dendritic regions with a eutectic dispersion of Ag_3Sn precipitates within β-tin matrix [15]. Although this alloy does not have excellent wettability, its joint strength is very good. However, the

diffusion rate for Cu from the Cu base into the solder is accelerated by high reflow temperatures and the Sn concentration gradient between solder and base metal. For this reason, a layer of brittle Cu_6Sn_5 intermetallic is often observed near the interface between Cu pads and bulk solder balls, which is known to be detrimental to the reliability of the electronic assembly.

1.3.3 Sn-Zn System

The eutectic composition of the Sn-Zn binary system is 91Sn-9Zn with a eutectic temperature of 199 °C which is near that of eutectic Sn-Pb (183 °C). The lamellar microstructure consists of alternating Sn-rich and Zn-rich phases, which is similar to the eutectic Sn-Pb system. However, Zn-Cu phases are known to decrease the reliability of Sn-Zn/Cu assemblies. The presence of Zn in solder alloys easily leads to oxidation and corrosion due to the high oxidation potential of Zn. Zn reacts with flux to form hard paste and it also causes oxidation and corrosion problems due to the high oxidation potential of Zn.

1.3.4 Sn-Bi System

The eutectic Sn-Bi alloy has a eutectic composition of 42Sn-58Bi and a relatively low melting temperature of 139 ^{o}C. It has been recommended as a promising replacement for Sn-Pb solders. This alloy has equivalent, even better properties than 63Sn-37Pb and is suitable for low temperature applications. Additionally, eutectic Sn-Bi solder has proven to have better manufacturability than Pb-Sn. However, Bi has a tendency to precipitate from the solder matrix aggregate along grain boundaries through which cracks can occur, resulting in early failures of solder joints due to the

embrittlement of the interface between and bulk Sn-Bi solder joint and the Cu pad [16, 17].

1.3.5 Sn-In System

The eutectic point of Sn-In binary system is 50.9Sn-49.1In and the melting temperature is 117 °C. There are two phases in the eutectic microstructure: an In-rich, psudo-body-centered tetragonal phase, β, which has 44.8% Sn, and a hexagonal Sn-rich phase, γ, with 77.6% Sn. Despite its low melting temperature and limited tendency to scavenge gold compared to Sn-Pb solders, the high material cost and low availability greatly handicaps its application in the electronics packaging industry.

1.3.6 Sn-Ag-Cu System

As shown in Figure 1.1, SnAgCu (SAC) has been the most popular, widely used lead free solder in today's market. Although they are still not identified as the "drop in" replacement for all applications, a variety of SAC alloys with different chemical compositions have been the proposed by various user groups and industry experts. These include: SAC105 (98.5Sn-1.0Ag-0.5Cu), SAC205 (97.5Sn-2.0Ag-0.5Cu), SAC305 (96.5Sn-3.0Ag-0.5Cu), and SAC405 (95.5Sn-4.0Ag-0.5Cu), known as the SACN05 series; SAC387 (95.5Sn-3.8Ag-0.7Cu), SAC396 (95.5Sn-3.9Ag-0.6Cu), and SAC357 (95.2Sn-3.5Ag-0.7Cu), identified as near eutectic SAC choices; SAC3810 (95.2Sn-3.8Ag-1.0Cu), SAC3595 (95.55Sn-3.5Ag-0.95Cu), SAC0307 (9Sn-0.3Ag-0.7Cu), and SAC107 (98.3Sn-1.0Ag-0.7Cu), designed for special needs such as high temperature application, drop and shock optimization, etc. The main benefits of the various SAC alloy systems are their relatively low melting temperatures compared with the 96.5Sn-

3.5Ag binary eutectic alloy, as well as their superior mechanical and manufacturability properties when compared to other lead free solders [18].

Figure 1.3 shows a typical 3-D ternary phase diagram. The contours on the top surfaces of the figure represent the isothermal lines. Each of the 3 sectors represents the binary phase diagram of two of the three elements. The center of the diagram, where the isothermal lines reach the common, lowest point, is the eutectic point of the ternary system. Figure 1.4 is the top view (2-D) of the ternary phase diagram of Sn-Ag-Cu.

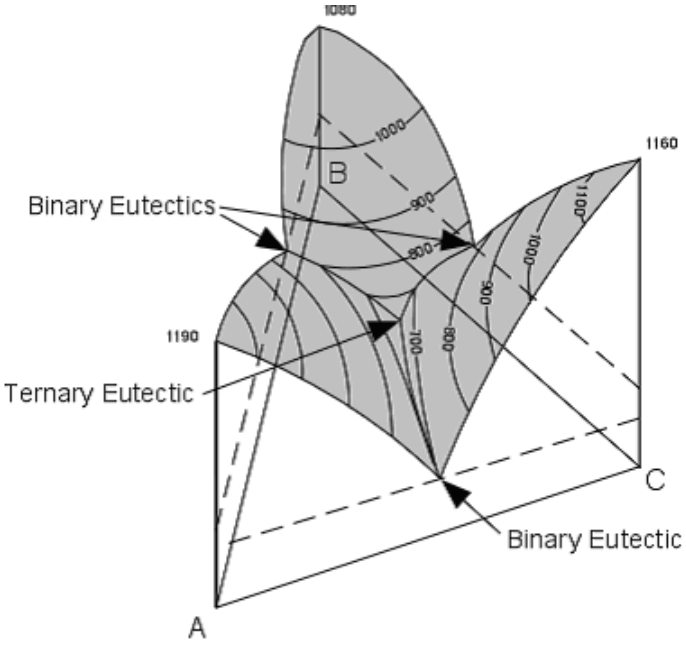

Figure 1.3 Typical 3-D Ternary Phase Diagram

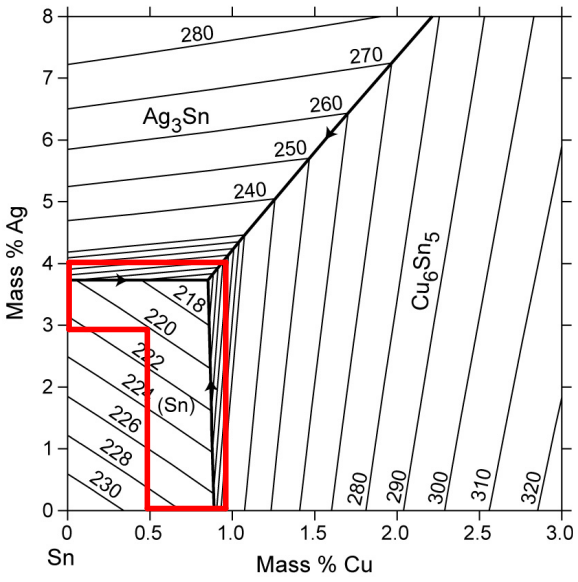

Figure 1.4 Sn-Ag-Cu Ternary Phase Diagram

The area indicated in the red box is the near eutectic region. Most of the SAC alloy compositions currently on the market are within this region. The eutectic and near eutectic melting temperature has been determined to be 217 °C, although the precise eutectic point is not known [19].

In SAC alloys, the formation of intermetallic compounds between the primary elements Sn and Ag, and Cu affect all the properties of the alloys. There are three possible intermetallic compounds that may be formed: Ag_3Sn forms due to the reaction between Sn and Ag (Figure 1.5) and Cu_6Sn_5 forms due to the Sn and Cu reaction. The compound Cu_3Sn will not form at the eutectic point unless the Cu content is high enough for the formation of Cu_3Sn at higher temperatures, so in bulk specimens Cu_3Sn is not presented. There is no reaction between Ag and Cu to form any kind of intermetallic compounds. The particles of intermetallic compounds possess much higher strength than the bulk material. Fine intermetallic particles in the Sn matrix can therefore strengthen

the alloys. The intermetallic compounds can also improve the fatigue life of the solders, as SAC alloys are reported to be 3-4 times better fatigue properties than the Sn-Pb eutectic solders. The higher fatigue resistance is believed to be contributed by the interspersed Ag_3Sn and Cu_6Sn_5 particles, which pin and block the movement of dislocations. The many patents that have been granted for SAC systems have limited their use and hindered research on several of the SAC alloys. However, many familiar alloy such as SAC305 and SAC405 are not patented to avoid excessive licensing and fees [18].

Despite the benefits mentioned above, SAC family solders sometimes are still questionable as complete substitutes for eutectic Sn-Pb because of costs, some patent issues (particularly outside Europe), aesthetic consideration (dross problem of SAC solders), and relatively high melting temperature (217 ^{o}C vs. 183 ^{o}C).

1.3.7 Sn-Ag-Cu + X System

SnAgCu alloys have shown potential to be successful substitutes for eutectic Sn-Pb, however, the industry is still looking for a "perfect" solution. According to the results of many recent studies, performance characteristics of solder alloys are able to be optimized by doping, that is, by adding a small amount of other alloying elements into the SAC solder alloys.

The proposed doping element candidates include Bi, Ni, Co, Ge, Zn, La, Mg, Mn, Ce, Ti, Fe, In, B, etc. For example, adding 0.05% (wt.) Ni can successfully stabilize the microstructure, inhibit the excessive consumption of metal base and thus increase the reliability of the solder joints [20-22]. In addition, doping rare earth (RE) elements can

significantly enhance wettability, refine microstructure and improve ductility of SAC alloys [23-26].

Even though dopants can greatly alter the mechanical, electrical and physical behavior of SAC solders, the effect on melting temperature, however, is found to be negligible. This is another advantage for doped solder alloys because manufacturers can still use the same processing conditions as conventional SAC alloys.

Meanwhile, the known issues for SAC-X solders are also apparent. For instance, the material properties and interfacial behavior of solder alloys have been demonstrated to be very sensitive to the quantity of the X-additive. As a result, it takes much more time and cost to figure out the optimal composition levels for the dopants.

1.4 Characteristics and Applications of Sn-Ag-Cu Solder Material

The advantages of SAC series over other Pb-free systems include relatively low melting temperatures, superior mechanical and solderability properties, and good tolerance for Pb contamination. These characteristics give SAC alloys good compatibility with existing electronics packaging infrastructure. In fact, there is a long history of using 95.5Sn–3.0Ag–0.5Cu (SAC305) to form solder joints for BGA packages. The high market share (≈ 70%) by SAC series alloys on a global scale provides strong evidence of its world-wide acceptance. Also, nanoscale lead-free solders ("nano-solders") have been proposed and investigated in the development of nano-soldering technique for nanoscale assembly and integration. Tin (Sn)-based and indium (In)-based lead-free nano-solders have been synthesized directly onto multisegmented nanowires using electro deposition method in nanoporous templates. Furthermore, high temperature lead free solders are being used in medical industries today where a variety of intrusive

procedures used requiring tools, instruments, sensors and components in materials that are inert with respect to reactions with the body [27]. Also, new surgical techniques have been developed to improve the quality of operations, reduce the risk to patients and reduce the pain experienced by patients. Environmental concerns and the concern about toxicity and health hazards indicate that there is a drive to develop and use lead-free solders.

1.5 Mechanical Properties of Lead Free Solders

Electronics equipment is somewhat unusual as all categories of engineering materials may exist in close proximity. For example, a printed circuit board is often a fiber-reinforced polymer (it is a composite); a chip may be located on a ceramic and the tracking and solder will be metallic materials. Solder joints are used to mount chips and components onto printed circuit boards (PCB) and thus create an electrical circuit. Therefore, an ideal solder material needs both excellent conductivity to transmit signals and adequate strength to provide mechanical support and connection. The mechanical properties of solder alloys are therefore critically important in producing reliable products. Among the all mechanical properties of solders, tensile properties and creep are of particular concern. Also most failures of solder joints in electronic assembly are caused by fatigue/fracture [28], special focus has also been given to understand and analyze this behavior.

1.5.1 Tensile Properties (Stress-Strain Behavior)

Under the action of an increasing stress, metals usually exhibit elasticity, plasticity, and a maximum in stress is followed by necking and fracture. The slope of the linear elastic portion of the stress vs. strain plot is the modulus, and the stress at termination of elastic behavior is the yield stress. The extent of deformation prior to fracture is known as ductility. Ceramics display only elastic behavior until fracture, which is associated with cracking and very limited deformation (brittleness). Polymers may exhibit both characteristics above according to the temperature. Above the glass transition temperature, T_g, extensive deformation due to mechanisms quite unlike those in metals may follow a small degree of elasticity. Below this temperature, polymers exhibit ceramic-like behavior. In all material categories, the maximum stress attained is the tensile/compressive/shear strength according to the mode of stressing employed. Composites are physical mixtures and exhibit the averaged properties of their components, taking into account the proportions of each. These characteristic features of monotonic behavior are summarized in Figure 1.5. Figure 1.5(a), (b), and (c) illustrates the overall mechanical behavior of non-ductile, ductile, and polymeric materials, respectively. The fracture strains of brittle materials and the yield strains of metals are generally less than 1% (the yield strain of most solders is approximately 0.1–0.2%). The amount of deformation prior to the attainment of maximum strength is between about 3% and 7% for common solder alloys.

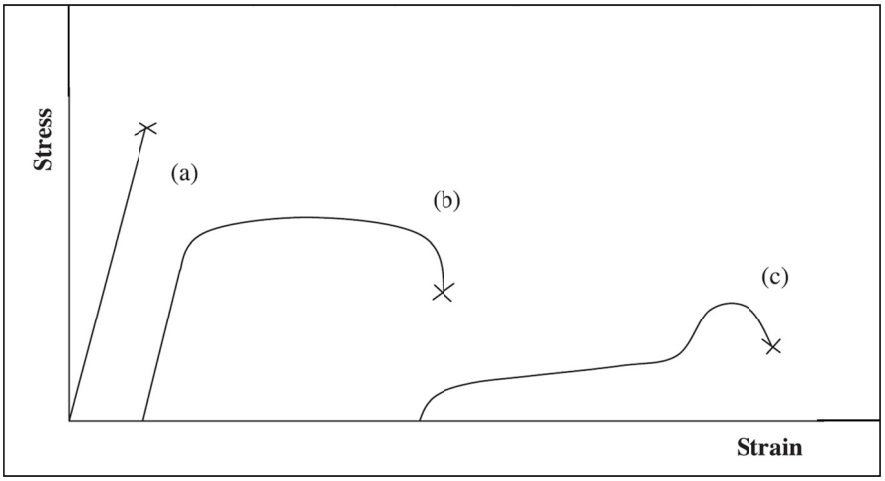

Figure 1.5 Schematic Overview of Mechanical Behavior

Tensile properties indicate how the material will react to forces being applied in tension. Although solder joints are rarely under pure tensile/compressive loading, tensile properties are still crucial indicators for design purposes. Through tensile tests, several material properties can be determined, such as effective modulus, yield strength (YS), ultimate tensile strength (UTS), elongation, etc. In most of the cases, engineering stress-strain curves are employed by neglecting the change in cross sectional area.

Figure 1.6 shows a typical engineering stress strain curve for a solder alloy. Tensile properties are generally described by stress-strain curves. A typical engineering stress-strain curve for solder alloys consists of an elastic region and a plastic region. In the elastic region, when the stress is reduced, the material will return to its original shape. In this linear region, the material obeys the relationship defined by Hooke's Law. However, since the effective modulus includes small inelastic deformations or time-dependent deformations such as creep, it is usually smaller than the dynamic modulus measured by acoustic or ultrasonic wave methods, which largely eliminates the inelastic

deformation due to rapid wave propagation [29-31]. Also, Ralls, et al. [32] showed that the elastic modulus of a metal will decrease with increasing temperature. The underlying reason for this is because the distance between adjacent atoms increases at higher temperatures, which in turns decrease the elastic modulus.

When the load is high enough to exceed the elastic limits the material will experience plastic deformation, which is permanent. At this stage the material is undergoing a rearrangement of its internal molecular or microscopic structure, in which atoms are being moved to new equilibrium positions. Specimens subject to plastic deformation will simultaneously elongate and decrease in diameter. The Yield Stress (YS) is defined as the stress level that causes the onset of plastic deformation. However, the precise YS is difficult to measure. In engineering practice, a specified small amount of plastic deformation is used, with 0.2% being the widely accepted value [28]. This is determined by a line parallel to the elastic slope that passes through a strain level of 0.% (Figure 1.6). When the load is removed at a point above the yield stress, the stress-strain curve will unload along a line approximately parallel to the initial modulus.

The ultimate tensile strength (UTS) is the maximum engineering stress level reached in a stress-strain test. In ductile materials similar to solders, the UTS levels are usually well outside of the elastic portion, and the elastic strain is very small compare to the plastic strain. When necking occurs, the engineering stress decreases and the specimen eventually fails.

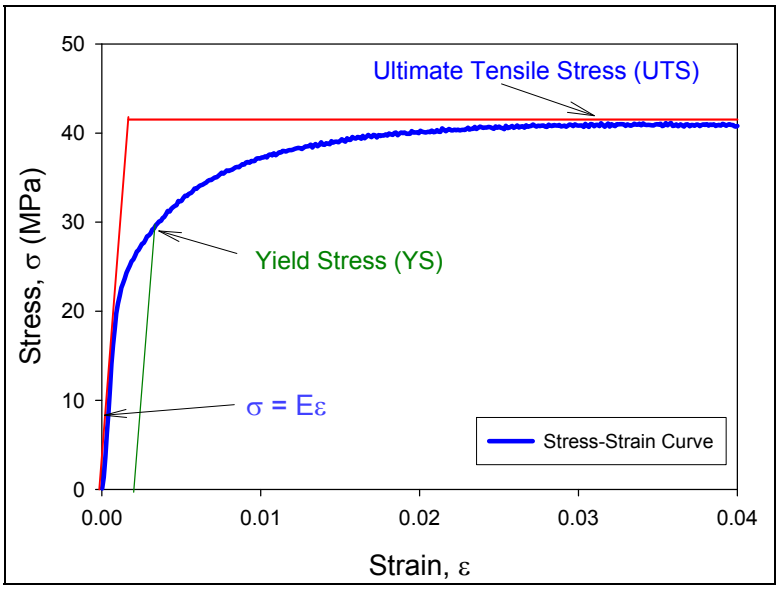

Figure 1.6 Typical Stress-Strain Curve of solder Alloy

1.5.2 Creep

Elevated temperature time-dependent deformation, or creep, is a critical behavior that affects the performance of solder interconnections. Significant creep often occurs due to the contribution is a result of the low solidus temperature of solder alloys. Even room temperature (T = 25 C) represents an elevated temperature for the Pb-free alloys, as indicated by a high homologous temperature, $T_h = T/T_m$, (T is the use/process temperature and T_m is the melting temperature of solder) for these and nearly all electronic solders. Therefore, there is a significant likelihood for creep to occur in solder interconnections, even under modest stresses.

Due to the CTE mismatches in the packaging materials, electronic assemblies are subjected to thermal-mechanical stresses. Creep deformation is one of the major failure modes of solder joints due to its high homologous temperature [33]. When T_h is greater than $0.5T_m$, the creep deformation will be the dominate deformation mode in metallic

materials [34]. For the Sn-Pb eutectic solder, T_m is 183 °C and the T_h is $0.65T_m$ at room temperature. For typical lead free solders T_h is approximately $0.61T_m$ at room temperature (T_m = 217 °C). Since both of these homologous temperatures are greater than $0.5T_m$, creep is not negligible for most solder materials even at room temperature. Consequently, solder alloys will undergo significant creep in normal use conditions. For example, if the normal operating temperature is considered as -40 °C to +125 °C in the actual assemblies, then the lead free solder T_h is between 0.48 to 0.81, which is in the range of rapid creep deformation.

1.5.3 Creep Curve

Creep is a time-dependent permanent deformation that occurs when a material supports a constant load for a very long period of time at a constant temperature. Creep deformation tends to be rapid when the homologous temperature is above $0.5T_m$. The level of load/stress and the temperature are dominant factors in creep. Figure 1.7 shows a typical creep curve, which generally consists of three stages after the initial instantaneous elastic strain when a constant load is applied [35]. In every creep tests there is an initial strain that is due to the elastic jump during application of the load. The strain rate starts with a very high magnitude and decreases rapidly with time in the first stage of creep test (primary creep). This is caused by work hardening, which restricts the deformation. The second stage is called Secondary Creep, or Steady-State Creep, where the strain rate becomes approximately constant. The steady state creep rate is due to the dynamic balance of strain hardening and recrystallization [31] and is mostly a region of plastic deformation. Creep of solders is very important because many researchers use the steady state creep rate within finite element simulations to predict the solder stress, strain, and

life. The tertiary creep region occurs when rupture is imminent, and typically features an abrupt change to a nearly constant but significantly increased creep rate.

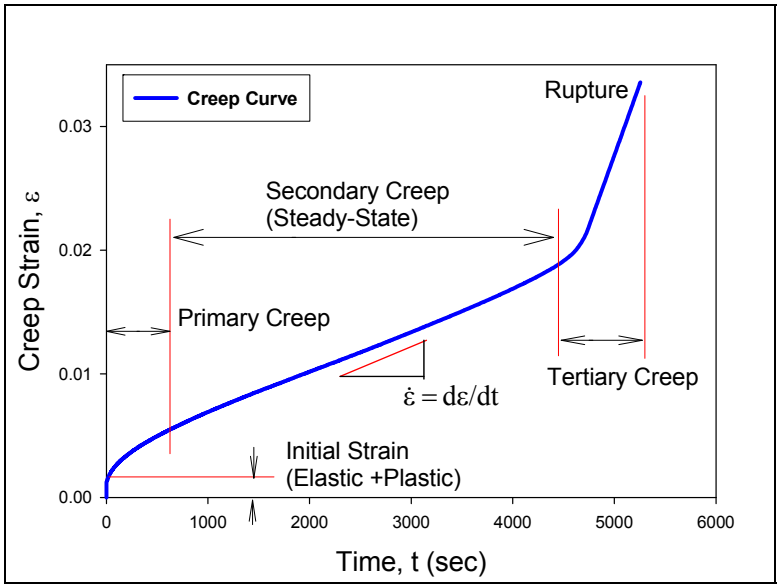

Figure 1.7 Typical Creep Curve

1.5.4 Mechanisms of Creep Deformation

Several creep mechanisms have been proposed such as dislocation glide, dislocation creep, grain boundary diffusion, and lattice diffusion, which can be summarized in a creep deformation map, as shown in Figure 1.8 [35, 36]. Such deformation diagrams were first introduced by Ashby in 1972 [36], and have been widely accepted and studied by other researchers in the area. In the deformation map shown in Figure 1.8, the abscissa is the homologous temperature and the ordinate is the normalized tensile or shear stress. The top of the map is bounded to the theoretical or ideal stress, below which is the onset of dislocation glide. Dislocation glide occurs at high stress levels over the entire homologous temperature range. In this case, the dislocation moves

along the slip planes [37]. Dislocation creep is characterized by a high-temperature deformation mechanism with homologous temperatures greater than $0.5T_m$ and requiring intermediate high stress. Such deformation results from diffusion controlled dislocation movement, with dislocations climbing away from barriers.

Coble proposed a grain boundary based diffusion mechanism, which involves atomic or ionic diffusion along the grain boundaries [38]. Such deformations occur at intermediate and low stress levels over an intermediate to low temperature range. Nabarro-Herring Creep, or lattice/bulk diffusion occurs at low stress levels and high temperatures. In this case, interstitial atoms and lattice vacancies along the gradient of a grain boundary migrate in reversed directions in the presence of tension or compression pressure. Lattice or bulk diffusion becomes the primary deformation mechanism under this circumstance [39]. If there is no pressure, interstitial atoms and lattice vacancies will migrate in proportion to the gradient of their concentrations. Under pressure, the lattice defects tend to move in directions to relieve the imbalance of pressure. Such movements will eventually cause creep deformation.

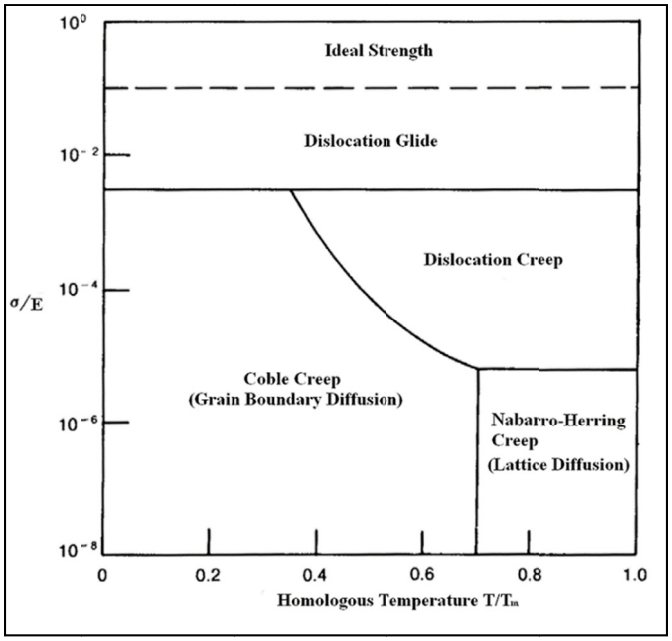

Figure 1.8 A Typical Creep Deformation Map

Grain-boundary sliding may also be involved in the creep deformation at high temperatures [31], where the displacement of grains can be induced by stress. However, this is not an independent deformation mechanism, and will accompany one or more of the above deformation mechanisms.

Due to the high homologous temperature ($> 0.5T_m$) of most solder alloys under normal operating conditions, the stress level determines the creep deformation mechanism. At low stress levels, the controlling mechanism is lattice diffusion and grain-boundary diffusion. As the stress rises to intermediate levels, dislocation creep takes over, and at high stress level, dislocation gliding becomes dominant. Additionally, the contribution of grain boundary gliding to creep deformation should be taken into account at all stress levels.

1.5.5 Shear

Solder joints in microelectronics systems are often subjected to shear loading due to the thermal cycling conditions and CTE mismatches of the materials in an assembly. A typical shear stress-strain diagram is shown in Figure 1.9. Similar to tension (Figure 1.6), when a material is subjected to shear loading, it will have a linear elastic region and a proportional limit τ_{pl}. In the elastic region, when the stress is reduced, the material will return to its original shape.

After yielding, plastic deformation and strain hardening take place, for stress levels between the proportional limit to the ultimate share stress τ_u. Then, the stress starts to decrease until failure. Hooke's Law also holds for shear stress-strain responses at small shear strains, and the slope of the initial region of the curve G is called the shear modulus or modulus of rigidity. In isotropic materials, the shear modulus can also be expressed in terms of the elastic modulus and Poisson's ratio.

Electronic assemblies often are subjected to combined shear deformation, warpage, and distortion under the action of thermal or power cycling. Combined tension and shear loading can act on solder joints in these operating conditions.

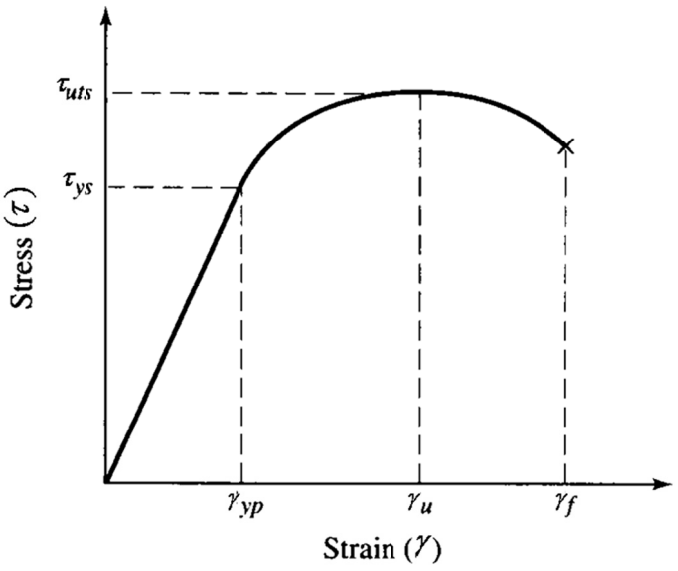

Figure 1.9 Typical Shear Stress-Strain Response for Ductile Materials

1.5.6 Fatigue

Electronic equipment rarely experiences a single constant or a continuously increasing stress. More common are stress or strain fluctuations induced by the service conditions, and these give rise to fatigue failure (failure due to a number of cycles, the magnitude of which is insufficient to cause failure in a single application). The key design parameters are the stress/strain, amplitude, and the number of cycles, N_f, necessary for failure. The fatigue process involves the initiation and gradual growth of cracks until the remaining section of the material can no longer support the applied load. It is by far the most common mode of failure in engineering applications.

When subjected to temperature changes, stresses or strains in electronic assemblies are typically developed due to the mismatches in the coefficients of thermal expansion (CTE) of the soldered components and the PCB. Cyclic temperature changes, either due to the external environment or power switching, can therefore lead to

substantial alternating stresses and strains within the solder joints. During cyclic loading, micro cracks form within the solder material followed by macro cracks which leads to damage and ultimately to fatigue failure.

A hysteresis loop is a convenient means of depicting cyclic stress–strain relationships during fatigue as shown in Figure 1.10. The width of the loop is equal to the total strain range, $\Delta\varepsilon$, which is made up of a small elastic strain range and a lager plastic strain range. The area enclosed by the loop is a measure of the plastic strain energy required to produce the observed deformation. This type of representation is very convenient when considering more complex and real cycles. During strain controlled fatigue, the stress range necessary to maintain the strain limits may increase (cycling hardening) or decrease (cycling softening). These changes may be due to the deformation process or cracking. Similarly, for stress-controlled fatigue, the strain range necessary to maintain the stress level may increase or decrease.

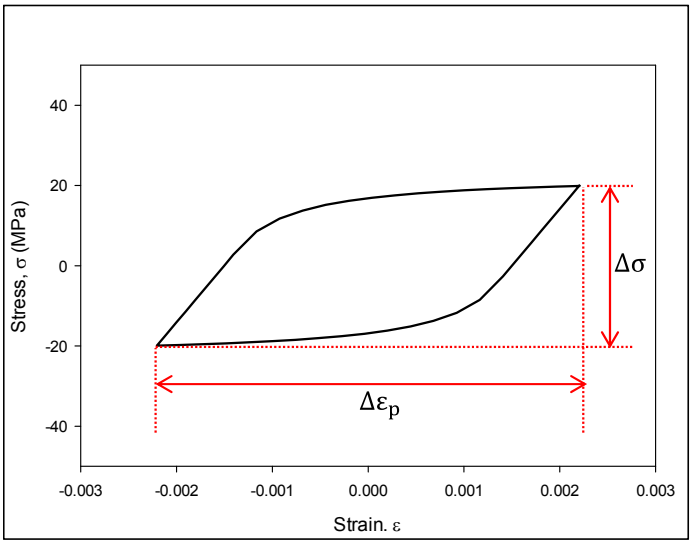

Figure 1.10 A Typical Hysteresis Loop

It has been observed that for a strain-controlled fatigue test, the peak stress drops continuously during cyclic loading due to damage accumulation. The plastic strain range also increases due to material softening. During the test, cyclic tension-compression loading causes damage accumulation eventually resulting in crack initiation. Different stages of peak stress drop during a fatigue test are shown in Figure 1.11. It is seen that the stress drops rapidly during the initial cycles due to damage accumulation and material softening. A steady state stage is then attained where grain growth progresses, re-crystallization occurs in the microstructure, and micro-voids form as shown in Figure 1.12. In the tertiary region, the stress drops rapidly when macro cracks initiate and crack growth progresses to final rupture of the material. The number of cycles until fracture is commonly defined as the fatigue life of the material. Generally the number of cycles at 50% drop of the tensile load is taken to be the fatigue life as recommended by ASTM [40, 41]. After crack initiation, the crack growth rate depends on the dissipation of plastic strain energy per cycle in the solder joint. If the fatigue data obeys a linear relationship when plotted on a log-log plot of plastic strain range vs. number of cycles, it generally obeys the Coffin-Manson law [42]. Also, if the fatigue data obeys a linear relationship when plotted on a log-log plot of dissipated strain energy density vs. number of cycles, it generally obeys a Morrow type low cycle fatigue law.

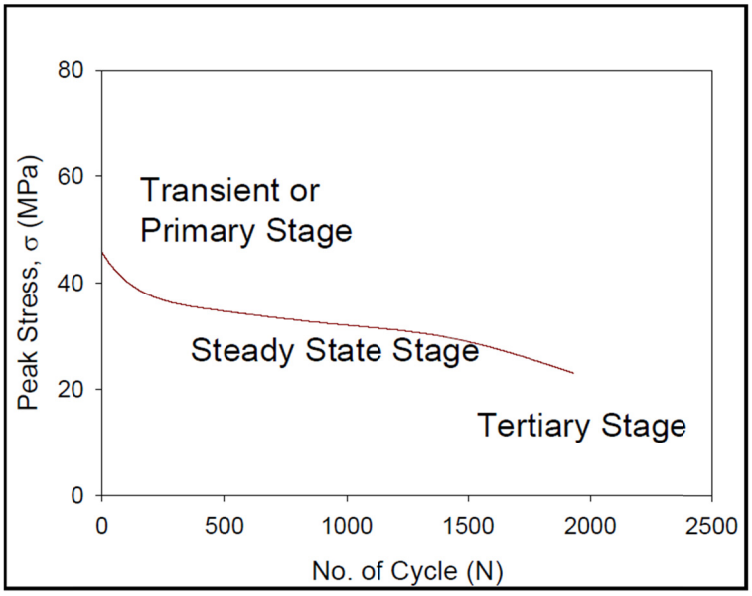

Figure 1.11 Different Stages of Stress Drop During Fatigue Test [41]

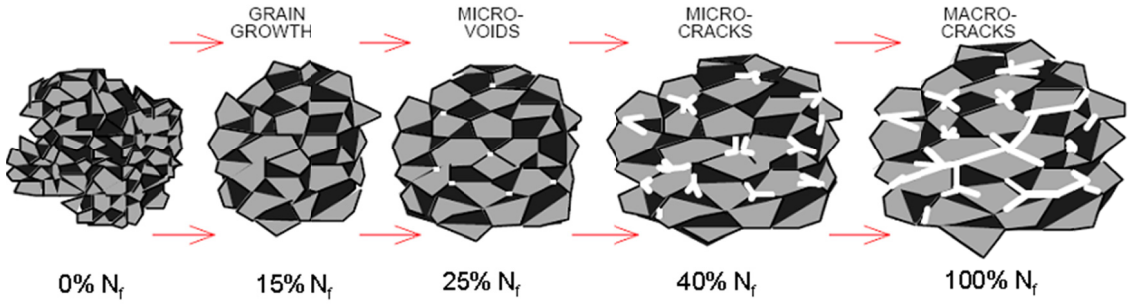

Figure 1.12 Depiction of the Effects of the Accumulating Fatigue Damage [41]

1.6 Objectives of This Research

The goals of this research are to systematically study the effects of aging on mechanical behavior of lead free solder alloys and to develop new constitutive equations and reliability models that include aging effects to predict solder joint reliability in microelectronic packaging. The following objectives will be achieved in this research:

(1) Develop specimen preparation procedures that produce uniaxial testing coupons with consistent microstructures comparable to actual lead free solder joints in commercial electronic packages;

(2) Investigate the mechanical properties of different Pb-free solder alloys (SAC105, SAC205, SAC305, SAC405) prepared using both water quenched and reflowed solidification profile at different strain rates and temperatures;

(3) Determine the evolution of the Anand parameters of SACN05 alloys with aging time;

(4) Investigate the effects of silver content on the mechanical properties and the Anand constitutive model;

(5) Explore the effects of aging on the accumulated plastic work in lead free solder joints using the Anand viscoplastic model;

(6) Predict the life of microelectronic components using finite element analysis of BGA assemblies and reliability models that include aging effects. Also, correlate the predicted life with the experimental thermal cycling reliability data.

1.7 Organization of the Dissertation

This dissertation mainly focuses on studying the procedures for reliability prediction with aging effects for lead free solder materials, and the application of aging aware constitutive models for solders. The study is presented in the following chapters:

Chapter 1: Introduction to lead free solders alloys and mechanical properties of solder materials.

Chapter 2: Literature review on isothermal aging effects, mechanical properties, constitutive models, life prediction and reliability models, and finite element analysis of electronic packages that consist of lead free solder materials.

Chapter 3: Description of experimental procedure, uniaxial tensile data processing, and constitutive modeling of lead free solders alloys, and determination of Anand parameters.

Chapter 4: Investigation of the effects of aging and solidification profile on the material properties of solder alloy and Anand constitutive model for lead free solder alloys.

Chapter 5: Exploration of the effects of silver content and severe aging on the material properties and Anand constitutive model of different lead free solder alloys.

Chapter 6: Simulation of the effects of aging and surface finish on the reliability of lead free solder joints in PBGA assemblies subjected to thermal cycling using finite element analysis.

Chapter 7: Summary and conclusions of the dissertation.

CHAPTER 2

LITERATURE REVIEW

2.1 Introduction

The ongoing transition to lead free soldering has been motivated by environmental concerns, legislative mandates, and market differentiation. Many researchers have attempted to measure the key mechanical properties of lead free solders. However, large discrepancies have been found in the published data from various groups. The observed disagreements in the test results are largely attributed to the lack of "standards" including variations in the as-cast/solidified microstructures of the test specimens, and differences in the test methods and data acquisition. All of these possibilities might make the measured data incomparable to each other. Moreover, aging effects, mostly neglected in majority of the studies, may further exacerbate these problems.

Apart from the above mentioned reasons for the discrepancies in solder material properties, another critical factor is aging effects. Aging is mostly neglected in the majority of prior studies, which will further exacerbate these problems. It has been observed from recent studies that isothermal aging leads to large reductions (up to 50%) in several key material properties for lead free solders including stiffness (modulus), yield stress, ultimate strength, and strain to failure [43]. Even more dramatic evolution has been observed in the creep response of aged lead free solders, where up to 100X increases were found in the steady state (secondary) creep strain rate (creep compliance) of SAC solders that were simply aged at room temperature [44, 45]. For elevated

temperature aging at 125 C [46], the creep strain rate was observed to change even more dramatically (up to 10,000X increase for SAC105).

In real applications, solder joints are continuously exposed to aging/thermal cycling during service. It has been well documented that the microstructure, mechanical response, and failure behavior of solder materials are constantly evolving under such circumstances [47-85]. It has also been demonstrated that aging effects are universally detrimental to reliability and cause reductions in stiffness, yield stress, ultimate strength, and strain to failure, as well as highly accelerated creep. Solder joints with highly degraded microstructure and material properties are so vulnerable that the service life of the package is often severely shortened.

The components of electronic packages undergo complex stress-strain conditions during the assembly process as well as when subjected to thermal or power cycling. This happens due to the CTE mismatch of different parts of the components so for a reliable product design, it is very important to have well-established and reliable constitutive models for lead free solder alloys to perform accurate solder joint stress-strain analysis or creep analysis. Among all the widely used constitutive models, however, none of them take aging effects into account. In addition, current finite element prediction methods for solder joint reliability do not take into account aging effects which are very critical for lead free solders. Thus, it is necessary to study constitutive models for solders that include aging effects and to also incorporate the aging included constitutive models in FEA analysis for the better predictions of solder joint reliability.

2.2 Aging Effects on Material Properties

Studies on the effects of aging on solder material properties are primarily divided into two groups, which are aging effects on bulk solders and aging effects on solder joints. These are described in subsequent sub-sections.

2.2.1 Aging Effects on Bulk Solders

Evolution of mechanical properties with aging in both Sn-Pb and lead free solders has been reported in recent years. Researchers have done numerous studies on the effects of aging on bulk solder properties as well as some studies on solder joints in actual components. Most studies show aging has significant effects on the mechanical properties of solder materials. In 1956, Medvedev [47] reported a 30% loss of tensile strength for bulk Sn-Pb solder after 450 days of room temperature (RT) aging, and a 23% loss in tensile strength for solder joints under a similar exposure. Room temperature aging effects on solder alloys has been presented by Lampe [48]. He showed that after 30 days of room temperature aging, the shear strength and the hardness of Sn-Pb and Sn-Pb-Sb solders reduced by approximately 20%. Miyazawa [74] reported reduction of hardness and microstructural coarsening for Sn-Pb solders aged at 25 and 100 ^{o}C for 1000 hours.

Xiao, et al. [63] investigated the stress-strain behavior of SAC396 solder alloy which were subjected to aging at 25 and 180 ^{o}C for various amount of time. They have shown that the strength reduces by 25% for aging at room temperature for 35 days and a 33% reduction for aging at 180 C for 9 days. Ding, et al. [62] investigated the influence of aging on fracture behavior of Sn-Ag solder in tensile tests. They have shown that the solder samples tensile strength reduce very quickly for isothermal aging at 180 ^{o}C for 120

hours. Ma, et al. [45] studied the evolution of elastic modulus, yield strength, and ultimate tensile strength of SAC305 and SAC405 solder alloys under various aging conditions. A linear-exponential model was developed to describe the material property evolution. They have shown that the material properties decreased dramatically in the first 20 days for both room temperature aging as well as elevated temperature aging. After 20 days of aging, the properties change slowly and linearly and it continues for longer aging time.

Zhang, et al. [46] also studied the aging effects on tensile properties of SACN05 (N = 1%, 2%, 3% and 4% silver) series solders for different amount of aging at temperatures 25-125 ^{o}C. They have demonstrated that the mechanical properties degraded more dramatically when the aging temperature was increased. The data also shows that the degradation becomes linear with longer aging time. Cai, et al. [59] have also shown that the aging effects are significant for lead free solders (SAC105, SAC205, SAC305 and SAC405) for room temperature aging as well as elevated temperature aging. They have also shown that the aging effects can be reduced by using certain dopants to (e.g. Bi, In, Ni, La, Mg, Mn, Ce, Co, Ti, Zn, etc.) SAC solder alloys to enhance the reliability of lead free solders. Finally, Mustafa, et al. [70] have demonstrated that the hysteresis loop area in cyclic (tension/compression) loading of various SAC solder alloys changes significantly with aging. For strain controlled tests, the hysteresis loop area deceases and for the stress controlled tests, the loop area increases with aging time.

Using ball-shear tests, Yoon, et al. [86] reported that the shear strength significantly decreased after aging for one day, and then remained constant. The fractures always occurred in the bulk solder. Kim, et, al. [87] found that in 900 hour aging

experiments, the shear strength of 3Sn-97Pb and 63Sn-37Pb decreased by 25% and 20%, respectively. The growth of Cu_6Sn_5 and Cu_3Sn intermetallics were also measured. Similarly, Kim, et al. [88] found that the shear strength of SAC305 solder decreased during isothermal aging for all the test temperatures considered. Using cyclic stress-strain tests, Dompierre, et al. [89] demonstrated that the stress amplitude dropped by 30% in aged specimens. They also highlighted the hardening/softening behavior of the studied alloy.

2.2.2 Aging Effects on Solders Joints

Isothermal aging effects have also been reported to lower the strength and to reduce reliability of solder joints. The mechanical response of solder joints to external loading can be different from the bulk solders due to fine microstructure, grain orientation (single grain and multigrain), and the presence of intermetallic compounds at joint boundaries.

Coyle, et al. [90] reported 20% shearing strength reduction in BGA solder joints after 240 hours of aging at room temperature. A 10% shearing strength reduction has been reported by Lee, et al. [91] for BGA packages just after 3 days of room temperature aging. Chilton, et al. [92] reported a 15% fatigue strength reduction for Sn-Pb solder joints that were aged for 60 days at room temperature. Li, et al. [93] studied elevated temperature aging effects on flip-chip packages with SAC solders. They have shown that the shear strength of solder bumps subjected to aging at 80 ^{o}C decreased gradually with aging. Also, for elevated aging temperatures of 150 and 175 ^{o}C, the degradations of shear strengths of the bumps were much faster. They also reported that the fracture of the solder bumps occurred in the bulk solder. Koo, et al. [94] found that 63Sn-37Pb solder

joint shear strength was significantly affected by aging at 170 °C for up to 21 days, while the analogous deteriorations for Sn-3.5Ag solder were much smaller. Darveaux [56] found at a 10% to 30% reduction in solder joint strength for 24 hours of aging at 125 ^{o}C. All of the solder joints failed within the bulk solder and exhibited high ductility. In addition, the ductility the Pb-free solder joints has been shown to decrease decreased with increased aging [63]. Oliver, et al. [95] reported that the joint strength of Sn-3.5Ag and SAC325 solders on both Ni/Au and Sn/Pb pad metallizations were unchanged after aging at room temperature as well as elevated temperature for 1000 hours. They also found reduction in the shear strength of Sn-Pb solder joints. These results are in contradictions to the findings of most studies as discussed above.

Pang, et al. [96] studied the aging effects on the mechanical properties and fatigue life of Sn-Pb solder joint specimens that were subjected to thermal cycling conditions from -40 to 125 ^{o}C. They have shown that the shear strength reduces significantly for specimens that were subjected to 1000 thermal cycles. They have also shown that the fatigue life of the specimens dropped by 6 times compared to non-cycled specimens. Zhou, et al. compared the joint strengths of SAC387 on both Cu and Ag substrates at an aging temperature of 170 °C, and concluded that aging had little effect on the SAC/Ag interface, but dramatically softened the SAC/Cu joint. The softening difference was said to be due to lower residual stresses at the SAC/Ag joint interface. Chen, et al. [72] studied the effects of aging on the solder bump shear strength for both Sn-Pb and Sn-3.5Ag solders. They reported that shear strength for both solder materials decreases after aging at 150 ^{o}C for 1500 hours, 8.9% for Sn-Pb solder bumps and 5.3% for Sn-3.5Ag.

Kim, et al. [65] also reported similar results in which they reported an average 5% decrease in joint strength in stud bump samples for aging at 150 ^{o}C for 300 hours.

The degradations of the stiffness, strength, and creep compliance with aging are expected to be universally detrimental to reliability of solder joints in lead free assemblies. This has been demonstrated explicitly in the recent investigation of Lee and coworkers [91], where aging has been shown to degrade the Thermal Cycling Reliability (TCR) of lead free Plastic Ball Grid Array (PBGA) assemblies subjected to Accelerated Life Testing (ALT). They have shown dramatic degradation in fatigue life of BGA components with SAC 305 solders, which were subjected to thermal cycling from 0 to 100 ^{o}C with prior aging at either 100 or 150 ^{o}C. The amount of life degradation was found to be dependent on the surface finish of the PCB substrates, with 44% degradation observed for ENIG surface finish and 20% degradation observed for OSP surface finish under the most severe aging conditions (1000 hours at 150 ^{o}C) prior to thermal cycling accelerated life testing.

In a similar study, Lee, et al. [97] showed that the lifetime of wafer-level chip scale packages with SAC305 solder interconnects was reduced by 29% for 500 hours of aging at 150 ^{o}C. Zhang, et al. [80] have investigated the effects of isothermal aging on the thermal-cycling reliability of PBGA components. They found that for 180 days of prior aging at 125 ^{o}C that the reliability of SAC105 components dropped by 53%. Smetana, et al. [98] have performed an extensive study on the effects of prior isothermal preconditioning (aging) on the thermal cycling lifetime for a variety of components. Similar to the investigations discussed above, it was observed that prior aging reduced the thermal cycling characteristic life of SAC BGA assemblies subjected to 0 to 100 ^{o}C

cycling. It was also found that changes occurred in the Weibull slope, suggesting other failure modes were created by aging. They also found that prior aging increased the thermal cycling reliability of certain components (e.g. 2512 chip resistors and certain QFNs). Similar results of improved reliability with aging were found for components subjected to a smaller thermal cycling range of 20 to 80 ^{o}C. This led them to conclude that aging does not universally reduce solder joint fatigue life.

The effects of aging on the degradation of the thermal cycling reliability of lead free BGA assemblies have been studied recently by Zhang, et al. [80]. In their studies, PBGA daisy chain test assemblies were subjected to up to 2 years of aging (25, 55, 85, and 125 ^{o}C), followed by thermal cycling from -40 to 125 ^{o}C or -40 to 85 ^{o}C to failure. They have shown that for all component sizes and lead free solder alloys, the solder joint thermal cycling reliabilities of the BGA components were severely reduced by prior aging. For up to 360 days prior aging for the components with Im-Ag PCB surface finish and thermal cycling from -40 to 125 ^{o}C, they have observed clear degradation in life for aged components relative to non-aged components and the amount of degradation was exacerbated with higher aging temperatures. Using the 63.2% Weibull characteristic life (η) as a failure metric, the reliability was observed to decrease by 37% (180 days aging) and 53% (360 days aging) for the 19 mm BGA components subjected to aging at 125 ^{o}C prior to thermal cycling.

Hu, et al. [99] reported that as-reflowed Sn37Pb/Cu solder joints had better shear strength than the aged solder joints, and that the shear strengths of the aged joints decreased with increasing aging time. Aging was found to cause increasing thickness of brittle IMC layers and coarsening of Pb-rich and Sn-rich phases in the solder matrix. In

addition, Wang, et al. [100] studied the effect of isothermal aging on joint strength as well as fracture behavior of solder bumps. They reported that the impact resistance degraded due to prior isothermal aging because of increases in the thickness of the IMC layers at the joint interfaces. The effects of isothermal aging and multiple-reflow process on the fracture force of the solder joints were examined and compared by Choi, et al. [101]. They reported that the strength of SAC105 solder joints decreased by 58% after aging for 200 hours.

Zhang, et al. [102] found that the tensile strength of solder joints at low strain rates decreased with increasing aging time, although the tendency was not monotonic at the early stage of aging. All of the solder joints had similar tensile curves but different fracture morphologies and fracture processes. At high strain rates, the tensile strength of the solder joints was much higher and decreased monotonously with increasing aging time, with identical fracture process and fractographies. Growth of intermetallic compounds and degradation of material properties of solder joints due to thermal aging has also been reported by the other authors [103-105].

2.3 Aging Effects on Creep Properties

It has been found in the literature that aging at room temperature as well as elevated temperatures have significant effects on creep deformation of lead free solder alloys. Darveaux, et al. [56] reported a faster creep rate for aged solder specimens than non-aged specimens. For both SAC305 and SAC405 solders and for aging at 125 ^{o}C for one day, they found 20 times increase in the creep rate for aged specimens. Xiao, et al. [63] found that SAC396 showed much lower absolute creep rates compared with eutectic Sn-Pb and ascribed this increase in creep resistance to the finely dispersed intermetallic

compound (IMC) precipitates in the Sn matrix. Wiese, et al. [57,106] investigated the creep behavior of SAC387 solder with short (one day at 125 ^{o}C) and long (49 days at 125 ^{o}C) thermal storage times. They found that the creep rate of solder increase significantly for short time aging at 125 ^{o}C but relatively smaller changes occurred for longer aging times.

Ma, et al. [44] studied the evolution of secondary creep rate with aging for SAC305 and SAC405 solders. They showed that the secondary creep rates for SAC solders increase with aging at either room temperature or elevated temperature. Also, for both SAC solders exposed to elevated temperature aging, the effects were much higher than those for room temperature aging. A more detailed investigation was conducted by Zhang, et al. [46] on aging effects on the creep behavior of lead free solders. They reported that for 180 days aging at 125 ^{o}C, the secondary or steady state creep rate of SAC105 solder increased by about 10,000 times. Also, for other aging temperatures (25 to 125 ^{o}C), they found that the both the primary and secondary creep rates increase with 180 days aging. Finally, Cai, et al. [59] demonstrated that by using certain types of dopants in SAC solders, the aging effects on steady state creep rate can be reduced. They showed that for no aging the creep rates of doped solders were higher than SAC105 and SAC205 due to lower silver contents of the doped solders compared to SAC105. However, with 180 days aging at temperatures 25 to 125 ^{o}C, the secondary creep rates of the doped solders were smaller than the creep rates of SAC105.

2.4 Constitutive Modeling for Solder Materials

In microelectronics packaging, complex stresses and strains are usually generated in the components due to the CTE mismatch of different materials. Solder interconnects are usually subjected to deformations that lead to three-dimensional stress and strain states. The solder material constitutive law plays an important role in the development of thermo-mechanical models for microelectronic assemblies. Under thermo-mechanical loading, the solder material undergoes elastic and in-elastic deformations. Elastic deformations are recoverable, while inelastic deformations consist of time-independent plastic deformations and time-dependent creep deformations, which are not recoverable. Solder constitutive behavior can be represented by a combination of elastic, plastic (isotropic or kinetic hardening), and viscoplastic/creep models.

2.4.1 Constitutive Modeling for Stress-Strain Tests

The linear elastic region in a uniaxial stress-strain curve can be modeled by Hooke's law where stress and strain are related by an elastic modulus (E). The plastic strain hardening region can be modeled by a time-independent non-linear stress-strain relationship based on either isotropic or kinematic strain hardening. Isotropic hardening assumes that the origin of the von Mises yield surface remains stationary in the stress space and the size of its yield surface expands resulting from strain hardening. In kinematic hardening, the von Mises yield surface does not change in size, but the origin of the yield surface is allowed to translate in the stress space to model strain hardening effects of increasing plastic flow stress. For solder materials, the tensile stress and strain curves are dependent

on the test temperature and strain rate. The elastic modulus (E), yield stress (YS) and the tensile strength (UTS) properties vary with temperature and strain rate.

For a typical thermal cycling temperature range from -40 to 125 ^{o}C, these mechanical properties reduce with the increase in temperature. The solder material has a homologous temperature from 0.5 to 0.8 for this temperature range. Also, the creep deformation in a solder material is highly dependent on the stress and temperature state. Thus, a time-dependent elastic-plastic-creep constitutive model, or viscoplastic constitutive model, is needed to facilitate finite element modeling for simulation of solder joint reliability during thermal cycling tests. High temperatures induce transitions in macroscopic fracture, and these transitions parallel the changes in the strength and ductility of materials [31]. Materials lose strength at higher temperatures. Hertzberg stated that the material strength increases with the testing strain rate, following a form similar to Holloman's Equation [31], where stress is related to strain rate through some strain hardening exponent.

Solder alloys possess very high homologous temperatures. The properties of solder alloys are strongly dependent on both the temperature and strain rate. Jones, et al. [107, 108] have observed an approximately linear relationship between the strength and temperature. Pang, Shi and co-workers [109] have observed similar experimental results, with a near linear relationship with temperature and a power law relation with the strain rate. Several other studies have also observed similar material behavior for both Sn-Pb eutectic and lead-free solder alloys [110-113].

The Ramberg-Osgood model describes the elastic-plastic behavior of materials, and can be used to describe to describe the stress-strain curve of solder materials [114].

In prior work, the Ramberg-Osgood model hardening exponent n and the stress coefficient σ_o were modified to be temperature and strain rate dependent. The temperature and strain-rate dependent modified Ramberg-Osgood model was also applied by Pang, et al. [114].

2.4.2 Constitutive Modeling for Creep

In general, the creep behavior of materials consists of three different stages: primary creep, secondary creep, and tertiary creep. In the primary creep regime, the material undergoes strain hardening, resulting in a decreasing strain rate with time. In the secondary stage, also known as steady-state creep regime, the creep strain rate is essentially constant, showing a very slow decrease. In tertiary stage, strain rate increases with time and ultimately results in failure of the material. Solder alloys are often subjected to steady-state creep regime under typical thermo-mechanical loading conditions. Constitutive modeling of creep deformation is needed to predict the end-of-life of electronic components by using finite element analysis. A constitutive creep model is established by conducting creep tests at different temperatures and stress levels. The materials constants are important in determining the accuracy of end-of–life predictions for solder joints using finite element analysis. Large discrepancies between the creep model and experimental data would degrade the accuracy of these predictions.

The minimum creep rate may be linked with the applied stress, σ, by a series of equations according to the dominant creep mode. There are mainly three types of creep modes, namely, power law creep, exponential creep, and combination creep. Creep is highly sensitive to both applied stress level and to test temperature. As a thermally

activated process, the creep rates increase exponentially with temperature. The effect of stress is dependent upon the controlling creep mechanism. The two widely used creep models are the Dorn power law model [115], and the Garofalo hyperbolic sine model [34]. In logarithmic coordinates, the Dorn power law model yields a linear relationship between the creep strain rate and applied stress for a specified temperature. Nonlinear experimental curves for creep, however, have been found over the entire stress range. The high stress regime exhibits the largest stress exponent n, and the low stress regime exhibits the smallest n value for any given temperature. This phenomenon is referred to as "power law break down" and indicates that the Dorn model is not suitable for fitting data obtained over large stress ranges.

The Garofalo model was established for matching creep behavior at both low and high stresses. At low and medium stresses, the creep strain rate depends on stress to the power n. At high stresses, the creep strain rate is an exponential function of stress. The model is able to predict the creep deformation over intermediate temperature regimes for the entire stress range, but it underestimates the creep deformation at both low (-40 °C) and high (125 and 150 °C) temperatures.

Ma and Suhling [43] have evaluated the creep parameters in the two models for various Pb-containing and Pb-free solder alloys and found large discrepancies in the creep data for solder alloys of the same chemical composition. There are several reasons that could explain the differences, including the specimen design, variations in testing method and test conditions used by different researchers, and storage time and temperature before the creep test. Moreover, it is important to recognize that the creep behavior of bulk solder significantly differs from solder in a joint due to the effects of

microstructure evolution, intermetallic compound formation, and constraint due to different methods of assembly. Since creep modeling is often to be incorporated in finite element analysis to predict the end-of-life of electronic package, the discrepancies in material constants will directly affect the accuracy of prediction.

A third widely used creep constitutive model was proposed by Weise, et al [106], and is often referred to as the double power law. They identified two mechanisms for steady state creep deformation for the bulk and PCB samples. They attributed them to climb controlled (low stress process) and combined gliding/climbing (high stress process) behavior and represented steady state creep behavior using two power law terms. In electronic packages, thermal mismatch induced stresses can result in extensive plastic deformation at solder joints, which is responsible for the low cycle thermal fatigue failure of solder materials. An expression for the strain was proposed by Yang, et al. [116] where total strain was divided into elastic, plastic, and creep strains.

Apart from these models, several other creep constitutive models have been proposed by researchers. Shi, et al. [117] established a unified dislocation-controlled creep constitutive model that described the creep deformation of solder alloy over a wide temperature range (-40 to 150 °C) and explained the temperature dependencies of the stress exponent n and activation energy Q. For creep strain rates at very low stress levels, they further developed a unified diffusion-controlled creep constitutive model to describe low temperature Coble creep and high temperature Nabarro-Herring creep. Clech [118] established obstacle-controlled creep models for both Pb-containing and Pb-free solder alloys. Creep deformation is impeded by discrete obstacles (phases, precipitates, grain boundaries, and other defects) distributed throughout the Sn-matrix in Sn-based solders.

By taking these impeding elements into consideration, the rate-dependent obstacle-controlled creep models are able to resolve the anomalies observed in the classical analysis of creep data including stress and/or temperature dependences of activation energies and stress exponents in the Power Law or Hyperbolic Sine models.

2.4.3 Anand Viscoplastic Constitutive Model

Since solder alloys are used at high homologous temperatures, creep deformations are significant. The Garofalo Hyperbolic Sine model and Dorn Power-Law model focus on steady-state creep data, which only involves a portion of the total creep deformation. Constitutive models for solders are principally divided into two groups. One is rate-independent plasticity (stress-strain response) and the other is rate-dependent steady state creep (creep deformation developed as a function of strain rate or time). However, it is very difficult to separate the plastic strain from the creep strain based on the mechanical tests of solder alloys. Therefore, a unified plastic/creep constitutive relation is highly desirable. The Anand model was initially proposed by Anand [119, 120], and is considered to be a unified model that does not require explicit yield conditions or loading/unloading criteria. The instantaneous response of the material is dependent on its current state. The Anand model also employs a single scalar internal variable "*s*" to represent the isotropic resistance to inelastic flow of the material. This scalar variable is believed to be related to the dynamic process of strain hardening and dynamic recovery. The Anand model is implemented in both the ANSYS and ABAQUS commercial finite element packages.

There are a total of nine parameters in the Anand model: A, Q, m, n, a, h_0, ξ , $\hat{s}$, and s_0. One method to obtain the values of these parameters for a specific material is to perform a series of stress-strain tests over a wide range of temperatures and strain rates. Using the measured UTS and the stress-strain data for each temperature and strain rate and using the non-linear least squared fit options, the values of the 9 Anand parameters can be determined. However, there are big discrepancies among the literature values of the Anand parameters for lead free solders [121]. The Anand model will be discussed in more detail in Chapter 3.

A large number of researchers have used the Anand model for electronic packaging applications. For example, Che, et al. [122] have demonstrated four different constitutive models for the Sn-3.8Ag-0.7Cu solder alloy including elastic-plastic, elastic-creep, elastic plastic with creep, and the viscoplastic Anand model. They showed that the Anand model was consistent with fatigue life predictions for lead free solders. Pei, et al. [123] performed monotonic tensile tests at a wide range of different temperatures and strain rates with two types of lead free solders (Sn3.5Ag and Sn3.8Ag0.7Cu) to get the material parameters of the Anand constitutive model. They showed that using temperature dependent values of the nine constants in the model gave better matching with the experimental results. Mysore and coworkers [125] conducted double lap shear tests on Sn3.0Ag0.5Cu solder alloy and used the results to fit the materials constants in the Anand model. They reported there were significant differences in results obtained with bulk samples and those found with solder joint specimens. A modified Anand Constitutive model was proposed by Chen, et al. [129] that involved using temperature dependent values of one of the model parameters (h_o). Amagai, et al. [130] have

established values for the Anand model constants for Sn3.5Ag0.75Cu and SAC105 (Snl.0Ag0.5Cu) lead free solders. In their work, one of the nine required constants was ignored (s_o), and only 8 were specified. Kim, et al. [131] presented values for all 9 constants for SAC105 lead free solder. A modified Anand model was presented by Bai, et al. [128] for SAC305 (Sn3.0Ag0.5Cu) and Sn3.5Ag0.7Cu lead free solders. Their approach employed temperature and strain rate dependent values of for one of the model parameters (h_o).

The Anand model has also been widely used in the finite element simulation of solder interconnection in electronic components [132-135]. There are various sets of Anand model parameters available in literature for a specific solder alloy composition. Unfortunately the predictions (stress-strain or creep) using the different sets of constants differ significantly, which is very alarming. For example, Figure 2.1 shows the predicted stress-strain curves for SAC305 solder using various sets of Anand constants from the literature. The solid black curve is the predicted stress-strain curve using the constants found in this study (see Chapter 4). The predicted UTS, elastic modulus, and yield stress from all of these sets of parameters at the same temperature and strain rate were significantly different. Thus, a reliable method of determining the best set of Anand parameters is necessary to accurately predict the mechanical behavior of the solder material using this constitutive model.

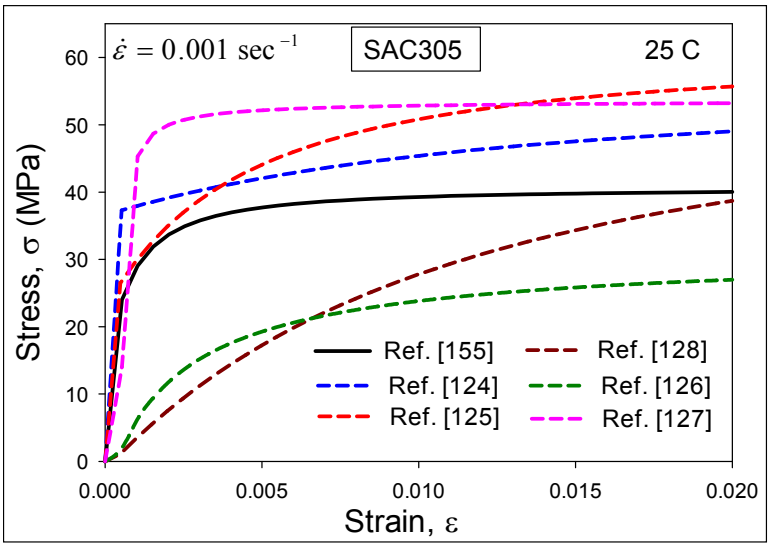

Figure 2.1 Differences in Stress-Strain Curve Predictions in Literature

2.5 Modeling of Solder Joint Reliability

In order to make faster, cheaper, and more reliable electronic products, it is very important for the packages to be evaluated at early design stages by simulation tools. Solder joint reliability models based on actual test data, accurate constitutive modeling, dominant damage mechanisms, and appropriate simulation, are needed to perform this task. Electronic packages often undergo thermal and/or power cycling conditions throughout their service life. CTE mismatch induced stresses/strains are the root cause of most solder joint failures. Solder joints fail mostly due to the fatigue caused by the thermal or power cycling operations. The procedure of reliability modeling can be divided in two major steps:

(1) Finite element modeling to predict stresses, strains, and deformations of the solder joints during thermal cycling. The required output parameters (e.g.

plastic strain or energy density per cycle) are extracted by post-processing the finite element analysis results.

(2) Application of a solder life prediction model to the output parameters of the finite element analysis to calculate the number of cycles until failure of the solder joint. The material constants in the life prediction model for the solder need to be evaluated from the experimental crack growth data for components having similar geometric form factors.

Syed [136] has used double power law and hyperbolic sine creep equations to predict the reliability of solder joints in BGA assemblies. He showed that failure criteria based on accumulated strains and dissipated energy density per cycle can provide good predictions of the measured mean life of solder joints. In addition, it was demonstrated that the energy density approach better captures low temperatures and high stress effects than the accumulated creep strain approach. Schubert, et al. [137] have presented thermo-mechanical analyses that predicted the life of solder joints in flip chip on board (FCOB) and PBGA assemblies for both SnPb and SnAgCu solders. They have also used double power law and hyperbolic sine creep constitutive equations, as well as accumulated creep strain and strain energy density methods for the fatigue life models. Both fatigue models were found to fit their experimental failure data reasonably well. Also, SAC solders were shown to perform poorer for stiffer components and higher strain levels.

An energy-partitioning approach has been used by Zhang, et al. [138] for SAC396 solder alloy. The model constants for creep and plasticity were obtained from correlating partitioned creep and plastic work to mechanical cycling testing results. In addition, lead

free SAC solders were found to have better low-stress creep resistance than SnAg solders. Zahn [139] used a volume average energy density method to predict the life of 63Sn37Pb and SAC405 solder joints. He also explored model simplifications based on symmetry, and found that one-eighth models are the smallest that can yield correct results, and that diagonal slice symmetry models yield different accumulated energy per cycle values than the true three-dimensional case.

Lee and coworkers [140] have classified solder fatigue models into five categories: stress based, plastic strain based, creep strain based, energy based, and damage based. Other methods have been classified as empirical models. They have shown a general procedure to choose an appropriate fatigue model based on the package conditions and limited finite element analysis times. They identified 14 models in the literature, which were developed based upon various assumptions, including the manner in which the physical and metallurgical aspects of fatigue are taken into account. The characteristics of the 14 identified fatigue models are presented in Table 2.1.

Ridout, et al [141] have classified the methods of calculating solder cycles to failure into three categories, analytical methods, combined constitutive law and fatigue methods, and damage mechanics methods (Figure 2.2). They have reported that the constitutive law and fatigue law class of methods (encompassing FEA and other alternatives) are very popular, providing more accurate predictions with fewer restrictions than analytical methods. However, they have with increased set up time and computational cost. The damage mechanics based methods require considerably more effort both in implementation and computational cost and their predictive capability is unproven.

Fatigue Model	Model Class	Parameters	Coverage	Applicability
Coffin-Manson	Plastic strain	Plastic strain	Low cycle fatigue	All
Total Strain	Plastic + elastic strain	Strain range	High and low cycle fatigue	All
Solomon	Plastic shear strain	Plastic shear strain	Low cycle fatigue	All
Engelmaier	Total shear strain	Total shear strain	Low cycle fatigue	Leaded & leadless, TSOP
Miner	Superposition (plastic and creep)	Plastic failure & creep failure	Plastic shear and matrix creep	PQFP, FCOB
Knecht & Fox	Matrix creep	Matrix creep shear strain	Matrix creep only	All
Syed	Accumulation of creep strain energy	gbs energy and mc energy	Implies all coverage	PBGA, SMD, NSMD
Dasgupta	Total strain energy	Energy	Joint geometry accounted for	LLCC, TSOP
Liang	Stress/strain energy density based	Energy	Constants from isothermal low cycle fatigue tests	BGA and leadless joints
Heinrich	Energy density based	Energy	Hysteresis curve	BGA
Darveaux	Energy density based	Damage + energy	Hysteresis curve	PBGA, leadless
Pan	Strain energy density	Strain energy density and plastic energy density	Hysteresis curve	LCCC
Stolkarts	Damage accumulation	Damage	Hysteresis curve & damage evolution	All
Norris & Landzberg	Temperature and frequency	Temperature frequency	Test condition vs. use conditions	All

Table 2.1 Summary of Solder Joint Fatigue Models [137]

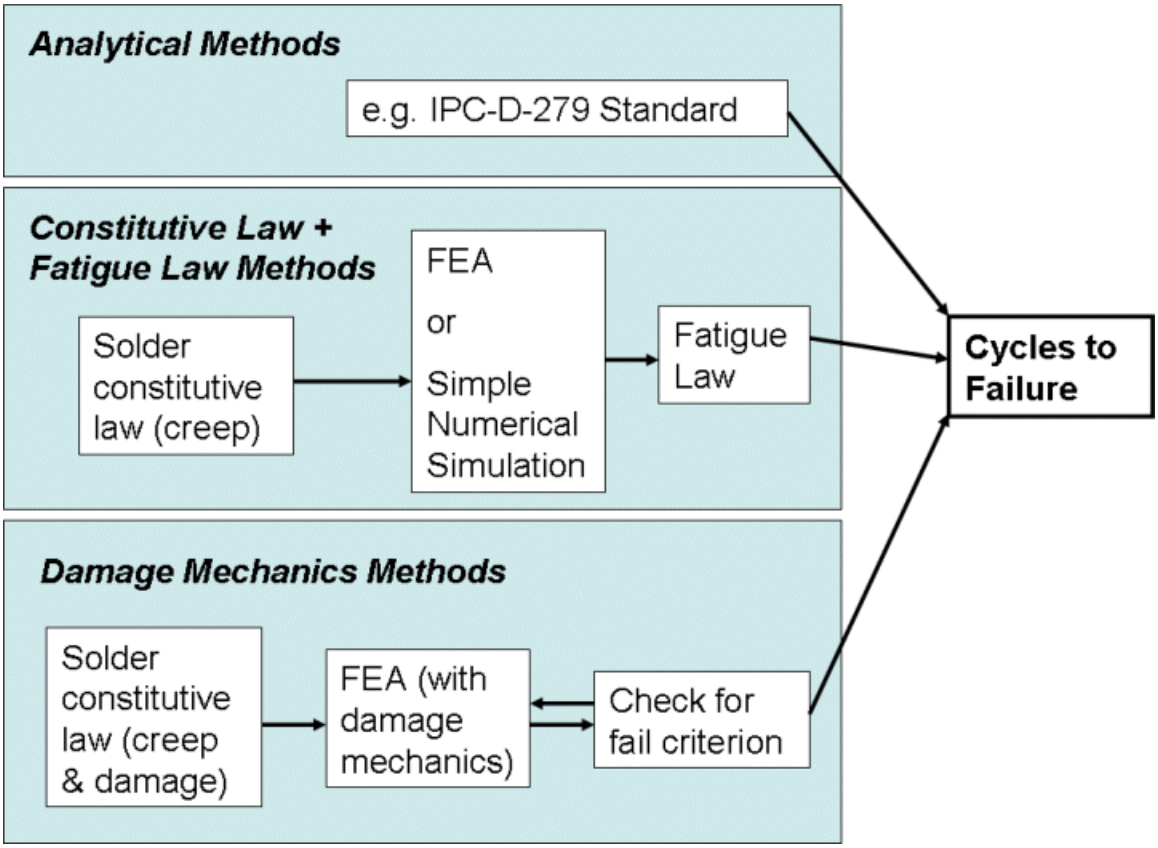

Figure 2.2 Modeling Methods to Calculate the Cycles to Failure [124]

A damage mechanics based fatigue life model has been presented by Tang and Basaran [142]. They have coupled an internal damage variable with a unified viscoplastic model to characterize the response of solder alloys. Gustafsson, et al. [143] have used the volume average energy method to predict the life of BGA solder joints and have shown that a linear global model with a nonlinear submodel drastically overestimates the life in comparison with the nonlinear global models.

Pang, et al. [144] have predicted flip chip solder joint reliability by using dwell creep (creep during dwell times) and full creep (creep during the whole analysis) methods. They have shown that the dwell creep method predicts much longer fatigue life of the solder joints than the full creep method. Shnawah, et al. [145] have studied the thermal

cycling and drop impact reliability of SAC solder joints. A significant thermal cycling performance improvement was found for assemblies made from SAC305/SAC405 solders relative to those assembled with lower silver content SAC105 solder. Liu, et al. [146] have used finite element analysis to examine pad design and found that the fatigue lifetime of BGA solder joints with dent pad OSP surface finish is 25% lower than that for flat pad Ni/Au surface finish. Thermal cycling reliability of a BGA SiP has been investigated by Yu, et al. [147]. They have found that the failure position changed relative to conventional BGA packages. Vasudevan and Fan [148] have incorporated acceleration terms into conventional fatigue models to examine the effects of thermal cycling range and frequency.

Darveaux [149] has presented energy dissipation based models for crack initiation and crack growth rate in solder joints. These types of models have been subsequently used by many researchers for life prediction of the SnPb and SAC solders. The four constants in the failure models are determined by curve fitting using the experimental failure data, where the energy dissipation per cycle is found from FEA simulations.

2.6 Summary and Discussion

Isothermal aging has been found detrimental to the mechanical properties and the reliability of lead free solder materials. The dramatic changes in the material properties, constitutive and failure behavior of bulk solder materials as well as solder joints have been reported in the literature. However, traditional finite element based predictions for solder joint reliability during thermal cycling accelerated life testing are based on solder constitutive equations (e.g. Anand viscoplastic model) and failure models (e.g. energy dissipation per cycle model) that do not evolve with material aging. Thus, there will be

significant errors in the calculations with lead free SAC alloys that illustrate dramatic aging phenomena.

Large discrepancies in measured solder mechanical properties from one study to another have been found and widely acknowledged due to the differences in the microstructures of the tested samples. This problem is exacerbated by the aging issue, as it is clear that the microstructure and material behavior of the samples change rapidly even at room temperature. For elevated temperature aging, this effect has been found to cause more dramatic change in the microstructure, material behavior and the reliability of lead free solder. Thus, the effects of aging on solder behavior must be better understood so that more accurate viscoplastic constitutive equations can be developed for SnPb and SAC solders. Without such well-defined relationship, it is doubtful that finite element reliability predictions can ever reach their full potential.

In the current study, effects of aging on the lead free solder material have been investigated by performing stress-strain tests for a wide range of temperature, strain rate and aging conditions. Also, creep tests for wide range of temperature and stress level have been performed for specimens that were aged for different duration of time. Using the tensile test or creep data for different aging condition, the Anand viscoplastic constitutive model has been modified to include the aging effects. The modified Anand model with aging effects has been implemented in the finite element software ANSYS for accurate prediction of the thermal cycling reliability of lead free solder joints.

The discussion on life prediction or reliability models for lead free solders includes the model parameters that do not evolve with material aging. The energy based Darveaux model has four parameters (K_1, K_2, K_3 and K_4) and has been used in this study

to calculate the thermal cycling reliability of solder joints. The effects of aging on these four parameters have been determined through the results of experimental investigations (fatigue tests and reliability tests). Empirical models for these parameters have been developed to include the aging effects, and by combining the finite element results with the reliability model, cycles to failure of the solder joint in a PBGA assembly have been determined for different aging conditions. Finally, good correlations have been found between the predictions of the constitutive and reliability models that include aging effects, and the experimental thermal cycling reliability data.

CHAPTER 3

EXPERIMENTAL DETAILS AND CONSTITUTIVE MODELING

3.1 Introduction

In this chapter, a novel specimen preparation technique is presented. This unique approach is able to fabricate micro-scale uniaxial tensile specimens without further modification and machining. The test specimens are formed in glass tubes with rectangular cross-section by using a vacuum suction system. The specimens are then cooled by either a water quenched cooling profile or a specifically designated reflow profile. For the current work, uniaxial samples with nominal dimensions of 80 (length) × 3 (width) × 0.5 (height) mm were utilized. Uniaxial tensile tests were then carried out by using a micro tension torsion testing system. Empirical constitutive model was adopted to represent the collected raw data and to extract the desired mechanical properties of the solder materials of interest.

The Anand viscoplastic constitutive model is the most widely used material model in the finite element analysis of solder materials. This model unifies the creep and plasticity of solder by making use of a stress equation, a flow equation, and an evolution equation. It has nine parameters which are typically determined from uniaxial stress-strain tests at several strain rates and temperatures using a multistep parameter determination procedure. The theoretical equations for the uniaxial stress-strain response (constant strain rate) has been derived from the Anand viscoplastic model. Procedures for extracting the Anand model constants from experimental stress-strain data have also been established.

3.2 Uniaxial Test Specimen Preparation Procedure

Solder uniaxial samples have been fabricated by machining of bulk solder material [53], or by melting of solder paste in a mold [54, 62-63]. Use of a bulk solder bars is undesirable, because they will have significantly different microstructures than those present in the small solder joints used in microelectronics assembly. In addition, machining can develop internal/residual stresses in the specimen, and heat generated during turning operations can cause localized microstructural changes on the exterior of the specimens. Reflow of solder paste in a mold causes challenges with flux removal, minimization of voids, microstructure control, and extraction of the sample from the mold. In addition, many of the developed specimens have shapes that significantly deviate from being long slender rods. Thus, undesired non-uniaxial stress states will be produced during loading.

Other investigators have attempted to extract constitutive properties of solders by direct shear or tensile loading [55-57], or indenting [58], of actual solder joints (e.g. flip chip solder bumps or BGA solder balls). While such approaches are attractive because the true solder microstructure is involved, the unavoidable non-uniform stress and strain states in the joint make the extraction of the correct mechanical properties and stress-strain curves from the recorded load-displacement data very challenging. Also it can be difficult to separate the various contributions to the observed behavior from the solder material and other materials in the assembly (bond pads, silicon die, PCB/substrate, etc.).

In an attempt to avoid many of the specimen preparation pitfalls identified above, a novel specimen preparation procedure was developed. Compared with other specimen fabrication approaches, this unique technique is able to make micro-scale uniaxial tensile

specimens with no requirement of further machining/cutting. The solder specimens in this study were formed in high precision rectangular cross-section glass tubes using a vacuum suction process. The tubes were then cooled by water quenching and sent through a SMT reflow to re-melt the solder in the tubes and subject them to any desired temperature profile (i.e. same as actual solder joints). The solder is first melted in a quartz crucible using a pair of circular heating elements (see Figure 3.1). A thermocouple attached on the crucible and a temperature control module is used to direct the melting process. One end of the glass tube is inserted into the molten solder, and suction is applied to the other end via a rubber tube connected to the house vacuum system. The suction forces are controlled through a regulator on the vacuum line so that only a desired amount of solder is drawn into the tube. The specimens are then cooled to room temperature using a user-selected cooling profile.

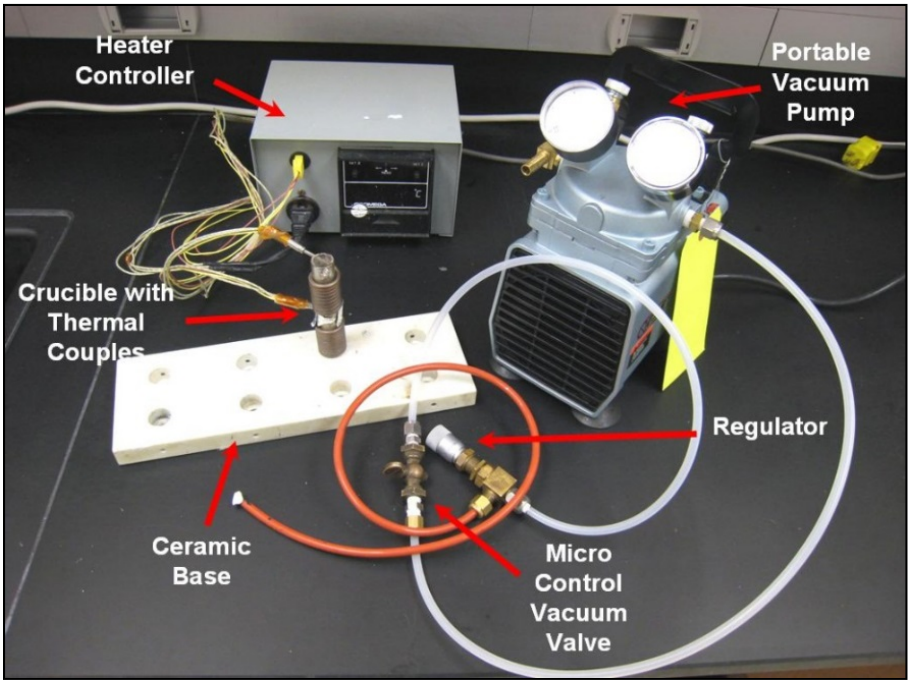

Figure 3.1 Specimen Preparation Hardware

In order to see the extreme variations possible in the mechanical behavior and microstructure, two different cooling profiles were employed in this work:

(1) Water Quenching (WQ): water quenching of the tubes (fast cooling rate),

(2) Reflowed (RF): controlled cooling using a surface mount technology solder reflow oven.

Typical temperature versus time plot for water quenching is shown in Figure 3.2(a). For the reflow oven controlled cooling, the tubes are first cooled by water quenching, and they are then sent through a reflow oven (9 zone Heller 1800EXL, see Figure 3.3) to re-melt the solder in the tube and subject it to the desired temperature profile. Thermo-couples are attached to the glass tubes and monitored continuously using a radio-frequency KIC temperature profiling system to ensure that the samples are formed using the desired temperature profile (same as actual solder joints). Figure 3.2(b) illustrates the reflow temperature profile used in this work for lead free solder specimens.

Typical glass tube assemblies filled with solder and final extracted specimens are shown in Figure 3.4. For some cooling rates and solder alloys, the final solidified solder samples can be easily pulled from the tubes due to the differential expansions that occur when cooling the low CTE glass tube and higher CTE solder alloy. Other options for more destructive sample removal involve breaking the glass or chemical etching of the glass. The final test specimen dimensions are governed by the useable length of the tube that can be filled with solder, and the cross-sectional dimensions of the hole running the length of the tube. In the current work, uniaxial samples were formed with nominal dimensions of 80 x 3 x 0.5 mm. A thickness of 0.5 mm was chosen because it matches the height of typical BGA solder balls.

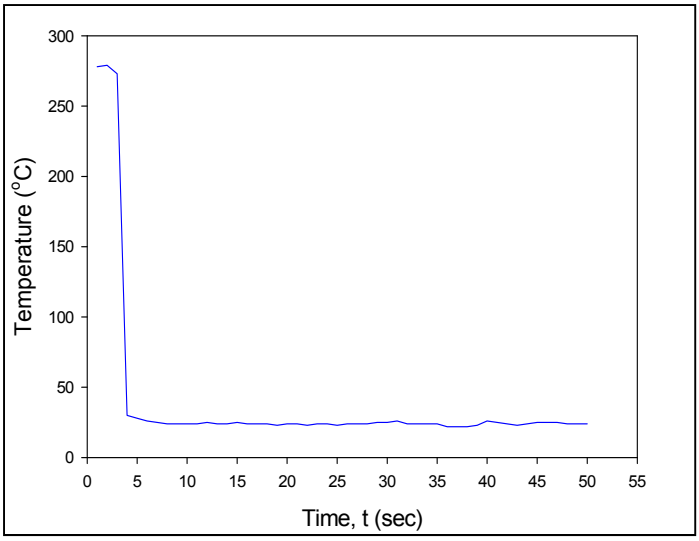

(a) Water Quenching Profile, WQ

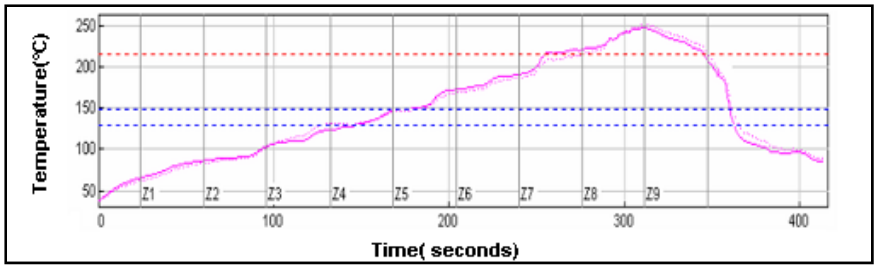

(b) Reflow Profile, RF

Figure 3.2 Specimen Cooling/Reflow Profiles

Figure 3.3 Heller 1800EXL Reflow Oven

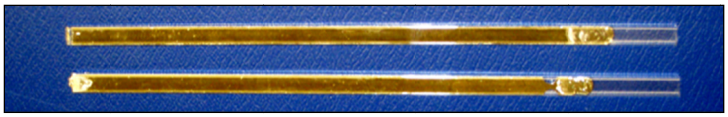

(a) Within Glass Tubes

(b) After Extraction

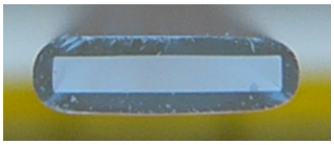

(c) Cross-Section

Figure 3.4 Solder Uniaxial Test Specimens

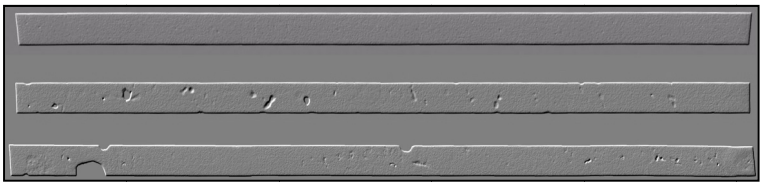

Figure 3.5 X-Ray Inspection of Solder Test Specimens (Good and Bad Samples)

The described sample preparation procedure yielded repeatable samples with controlled cooling profile (i.e. microstructure), oxide free surface, and uniform dimensions. By extensively cross-sectioned on several specimens, the microstructure of any given sample is proven to be very consistent throughout the volume of the sample. In addition, the specimen preparation method has been demonstrated to yield repeatable sample microstructures for a given solidification temperature profile. Samples were inspected using a micro-focus x-ray system to detect flaws (e.g. notches and external indentations) and/or internal voids (non-visible). Figure 3.5 illustrates results for good and poor specimens. With proper experimental techniques, samples with no flaws and voids were generated.

3.3 Mechanical Testing System

A MT-200 tension/torsion thermo-mechanical test system from Wisdom Technology, Inc., as shown in Figure 3.6, has been used to test the samples in this study. The system provides an axial displacement resolution of 0.1 micron and a rotation resolution of 0.001°. Testing can be performed in tension, shear, torsion, bending, and in combinations of these loadings, on small specimens such as thin films, solder joints, gold wire, fibers, etc. Cyclic (fatigue) testing can also be performed at frequencies up to 5 Hz. In addition, a universal 6-axis load cell was utilized to simultaneously monitor three forces and three moments/torques during sample mounting and testing. Environmental chambers added to the system allow samples to be tested over a temperature range of -185 to +300 °C.

During uniaxial testing, forces and displacements were measured. The axial stress and axial strain were calculated from the applied force and measured cross-head displacement using:

$$\sigma = \frac{F}{A} \qquad \varepsilon = \frac{\Delta L}{L} = \frac{\delta}{L} \tag{3.1}$$

where σ is the uniaxial stress, ε is the uniaxial strain, F is the measured uniaxial force, A is the original cross-sectional area, δ is the measured crosshead displacement, and L is the specimen gage length (initial length between the grips). The gage length of the specimens in this study was 60 mm, so that the specimen length to width aspect ratio was 20 to 1 (insuring true uniaxial stress states).

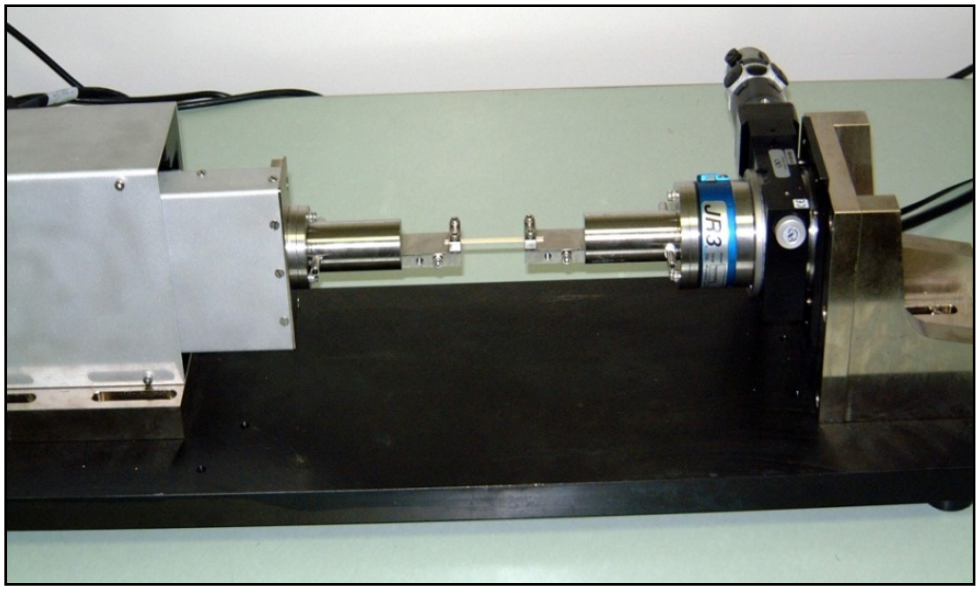

Figure 3.6 MT-200 Testing System with Solder Sample

3.4 Typical Testing Data and Data Processing

3.4.1 Typical Testing Data

A typical recorded tensile stress strain curve for solder with labeled standard material properties is shown in Figure 3.7. The notation "*E*" is taken to be the effective modulus, which is the initial slope of the stress-strain curve. Since solder is viscoplastic, this effective modulus will be rate dependent, and will approach the true elastic modulus as the testing strain rate approaches infinity. The yield stress σ_Y (YS) is taken to be the

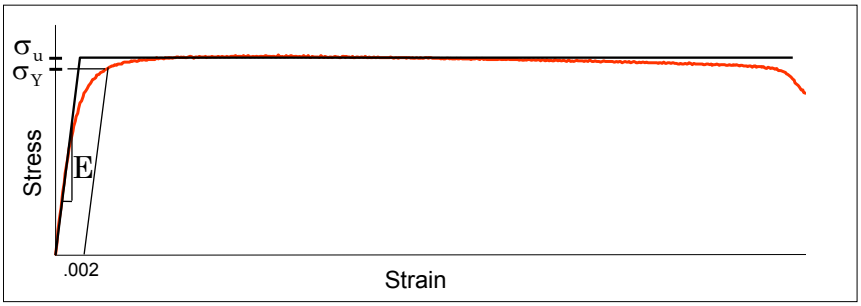

(a) Typical Solder Stress-Strain Curve (Whole Curve)

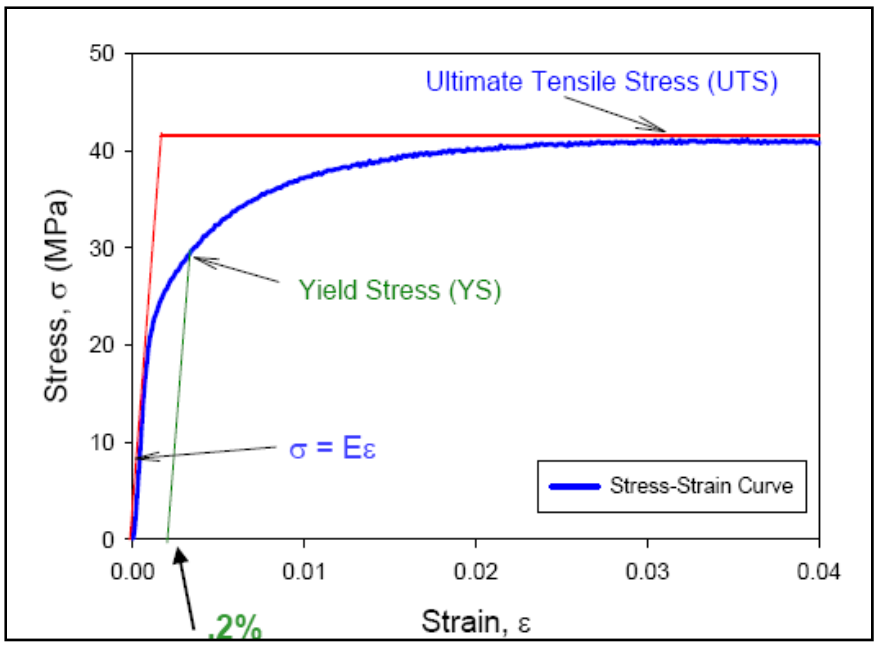

(b) Typical Solder Stress-Strain Curve (Enlarged at Small Strain Range)

Figure 3.7 Typical Solder Stress-Strain Curve and Material Properties

standard 0.2% yield stress (upon unloading, the permanent strain is equal to $\varepsilon = 0.002$). Finally, the ultimate tensile strength σ_u(UTS) is taken to be the maximum stress realized in the stress-strain data. As shown in Figure 3.7(a), the solders tested in this work illustrated nearly perfect elastic-plastic behavior (with the exception of a small transition region connecting the elastic and plastic regions). As the strain level becomes extremely high and failure is imminent, extensive localized necking takes place. These visible reductions in cross-sectional area lead to non-uniform stress-states in the specimen and drops in the applied loading near the end of the stress-strain curve.

3.4.2 Data Processing

For the uniaxial stress-strain tests, a total of 10 specimens have been tested at a specific aging/testing condition. From the recorded stress-strain data, a set of averaged material properties were extracted. In this work, a single "average" curve was generated to represent a set of 10 recorded stress-strain curves for a certain testing configuration. Although, several different mathematical models can be used to represent the observed data, an empirical four parameter dual hyperbolic tangent model has been demonstrated to be the best option for accurately capturing the variations in both elastic and visco-plastic regions:

$$\sigma = C_1 \tanh(C_2\varepsilon) + C_3 \tanh(C_4\varepsilon) \tag{3.2}$$

where C_1, C_2, C_3, C_4 are material constants to be determined.

When consider extreme small strain situation ($\varepsilon \to 0$), the effective modulus (E) can be estimated as:

$$\lim_{\varepsilon\to 0} \frac{d\sigma(\varepsilon)}{d\varepsilon} = \lim_{\varepsilon\to 0} C_1C_2\left\{\left(1-\tanh^2(C_2\varepsilon)\right)+C_3C_4\left(1-\tanh^2(C_4\varepsilon)\right)\right\} \tag{3.3}$$

When consider extreme large strain situation ($\varepsilon \to \infty$), the ultimate tensile strength (UTS) can be obtained by:

$$\lim_{\varepsilon\to 0} \sigma(\varepsilon) = C_1 + C_3 \tag{3.4}$$

Figure 3.8 illustrates a typical set of 10 solder stress strain curves measured under similar conditions, and the corresponding curve fitting of Eq. 3.2 to the data. Ten raw stress-strain curves are truncated at their UTS and then fitted by the proposed model. The

excellent representation provided by the four parameter empirical model suggests that it indeed provides a mathematical description of a suitable "average" stress-strain curve for a set of experimental curves measured under fixed preconditioning/testing conditions.

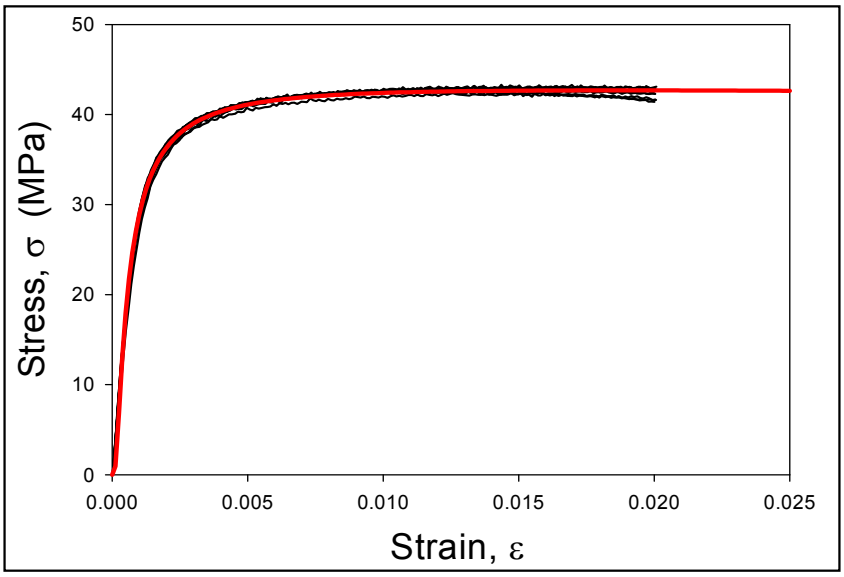

Figure 3.8 Solder Stress-Strain Curves and Empirical Model

3.5 Anand Viscoplastic Constitutive Model

Anand, et al. [105, 106] proposed a popular set of viscoplastic constitutive equations for rate-dependent deformation of metals at high temperatures (e.g. in excess of a homologous temperature of $0.5T_m$). Although it was originally aimed at hot working of high strength aluminum and other structural metals, the so-called Anand model has been adopted successfully to represent isotropic materials such as microelectronic solders (SnPb and lead free) with small elastic deformations and large viscoplastic deformations.

3.5.1 Primary Equations of Anand Viscoplastic Constitutive Model

The Anand model uses a scalar internal variable s to represent the isotropic resistance to plastic flow offered by the internal state of the material. It unifies the creep and rate-independent plastic behavior of the solder by making use of a stress equation, a flow equation, and an evolution equation. The model needs no explicit yield condition and no loading/unloading criterion.

For the one-dimensional case (uniaxial loading), the stress equation is given by

$$\sigma = cs;\ c < 1 \tag{3.5}$$

where s is the internal valuable and c is a function of strain rate and temperature expressed as

$$c = c\,(\dot{\varepsilon}_p, T) = \frac{1}{\xi}\sinh^{-1}\left\{\left[\frac{\dot{\varepsilon}_p}{A}e^{\left(\frac{Q}{RT}\right)}\right]^m\right\} \tag{3.6}$$

and where $\dot{\varepsilon}_p$ is the inelastic (plastic) strain rate, T is the absolute temperature, ξ is the multiplier of stress, A is the pre-exponential factor, Q is the activation energy, R is the universal gas constant, and m is the strain rate sensitivity. Substituting Eq. (3.6) into Eq. (3.5), the stress equation can be expressed as:

$$\sigma = \frac{s}{\xi}\sinh^{-1}\left\{\left[\frac{\dot{\varepsilon}_p}{A}e^{\left(\frac{Q}{RT}\right)}\right]^m\right\} \tag{3.7}$$

Rearranging Eq. (3.7) and solving for the strain rate yields the flow equation of the Anand model:

$$\dot{\varepsilon}_p = A e^{-\left(\frac{Q}{RT}\right)} \left[\sinh\left(\xi \frac{\sigma}{s}\right)\right]^{\frac{1}{m}} \tag{3.8}$$

The differential form of the evolution equation for the internal variable s is assumed to be of the form

$$\dot{s} = h(\sigma, s, T)\dot{\varepsilon}_p$$
$$\dot{s} = \left[h_o \left(1 - \frac{s}{s^*}\right)^a \operatorname{sign}\left(1 - \frac{s}{s^*}\right)\right] \dot{\varepsilon}_p ; \quad a > 1 \tag{3.9}$$

where, the term $h(\sigma, s, T)$ is associated with the dynamic hardening and recovery processes. Parameter h_o is the hardening constant, a is the strain rate sensitivity of the hardening process, and the term s* is expressed as

$$s^* = \hat{s} \left[\frac{\dot{\varepsilon}_p}{A} e^{\left(\frac{Q}{RT}\right)}\right]^n \tag{3.10}$$

where $\hat{s}$ is a coefficient and n is the strain rate sensitivity of the saturation value of the deformation resistance. Eq. (3.9) can be integrated to yield the final version of the evolution equation for the internal variable s:

$$s = \hat{s} \left[\frac{\dot{\varepsilon}_p}{A} e^{\left(\frac{Q}{RT}\right)}\right]^n - \left[\left(\hat{s} \left[\frac{\dot{\varepsilon}_p}{A} e^{\left(\frac{Q}{RT}\right)}\right]^n - s_o\right)^{(1-a)} + (a-1)\left\{(h_o)\left(\hat{s} \left[\frac{\dot{\varepsilon}_p}{A} e^{\left(\frac{Q}{RT}\right)}\right]^n\right)^{-a}\right\}\varepsilon_p\right]^{\frac{1}{1-a}} \tag{3.11}$$

Or,

$$s = s(\dot{\varepsilon}_p, \varepsilon_p) \tag{3.12}$$

The final equations in the Anand model (1D) are the stress equation in Eq. (3.7), the flow equation in Eq. (3.8), and the integrated evolution equation in Eq. (3.11). These

expressions include 9 material parameters (constants): A, ξ, Q/R, m in Eqs. (3.7, 3.8); and constants h_o, a, s_o, $\hat{s}$, and n in Eq. (3.11).

3.5.2 Theoretical Formulation for Uniaxial Stress-Strain Response

The post yield uniaxial stress-strain relations predicted by the Anand model are obtained by substituting the expression for internal variable 's' from Eq. (3.11) into the stress equation in Eq. (3.7). This calculation results in:

$$\sigma = \frac{1}{\xi}\sinh^{-1}\left\{\left[\frac{\dot{\varepsilon}_p}{A}e^{\left(\frac{Q}{RT}\right)}\right]^m\right\}\left(\hat{s}\left[\frac{\dot{\varepsilon}_p}{A}e^{\left(\frac{Q}{RT}\right)}\right]^n - \left[\left(\hat{s}\left[\frac{\dot{\varepsilon}_p}{A}e^{\left(\frac{Q}{RT}\right)}\right]^n - s_o\right)^{(1-a)} + (a-1)\left\{(h_o)\left(\hat{s}\left[\frac{\dot{\varepsilon}_p}{A}e^{\left(\frac{Q}{RT}\right)}\right]^n\right)^{-a}\right\}\varepsilon_p\right]^{\frac{1}{1-a}}\right) \quad (3.13)$$

For a uniaxial tensile test performed at fixed (constant) strain rate $\dot{\varepsilon}_p$ and constant temperature T, this expression represents highly nonlinear stress-strain behavior (power law type function) after yielding:

$$\sigma = \sigma(\varepsilon_p) \quad (3.14)$$

Anand model predictions for the yield stress (σ_Y) and the Ultimate Tensile Strength (UTS = maximum/saturation stress) can be obtained by considering limiting cases of Eq. (3.13). The UTS is given by the limit as ε_p goes to ∞ :

$$\mathrm{UTS} = \sigma\big|_{\varepsilon_p\to\infty} = \frac{\hat{s}}{\xi}\left[\frac{\dot{\varepsilon}_p}{A}e^{\left(\frac{Q}{RT}\right)}\right]^n \sinh^{-1}\left\{\left[\frac{\dot{\varepsilon}_p}{A}e^{\left(\frac{Q}{RT}\right)}\right]^m\right\} \equiv \sigma^* \quad (3.15)$$

The yield stress is given by the limit as ε_p goes to 0:

$$\sigma_Y = \sigma\big|_{\varepsilon_p \to 0} = c s_0 = \frac{1}{\xi} \sinh^{-1}\left\{\left[\frac{\dot{\varepsilon}_p}{A} e^{\left(\frac{Q}{RT}\right)}\right]^m\right\} \; s_0 = c s_0 \equiv \sigma_0 \tag{3.16}$$

Using the saturation stress (σ^* = UTS) relation in Eq. (3.15), the post yield stress-strain response (power law) in Eq. (3.13) can be rewritten as:

$$\sigma = \sigma^* - \left[\left(\sigma^* - c s_0\right)^{(1-a)} + (a-1)\left\{\left(c h_0\right)\left(\sigma^*\right)^{-a}\right\} \varepsilon_p\right]^{1/(1-a)} \tag{3.17}$$

3.5.3 Determination Procedure of the Model Parameters from the Stress-Strain Data

As discussed above, the nine parameters of the Anand model are A, ξ, Q/R, m, h_o, a, s_o, $\hat{s}$, and n. One method to obtain the values of these parameters for a specific material is to perform a series of stress-strain tests over a wide range of temperatures and strain rates [105, 106]. From the measured data, the value of the saturation stress (σ^* = UTS) can be obtained for several strain rates and temperatures. In addition, the stress-strain (σ, ε) data for each temperature and strain rate can be recast as stress vs. plastic strain data (σ, ε_p) by using

$$\varepsilon_p = \varepsilon - \frac{\sigma}{E} \tag{3.18}$$

where E is the initial elastic modulus of the material at the specific temperature and strain rate being considered. The Anand model parameters can be obtained by following procedure

1. Determine the values of the parameters $\hat{s}$, ξ, A, Q/R, n and m by non-linear regression (least squares) fitting of Eq. (3.15) to the saturation stress vs. strain rate and temperature data.

2. Determine the values of parameters s_o, h_o, and a by non-linear regression (least squares) fitting of Eq. (3.17) to the stress vs. plastic strain data at several strain rates and temperatures.

3.6 Summary and Discussion

A unique specimen preparation procedure was developed in this study to fabricate micro-scale uniaxial tensile specimens. All solder specimens were formed in glass tubes with rectangular cross-section by using a vacuum suction system. Two cooling profiles were adapted in this study, including water quenching and controlled reflow oven cooling. Typical uniaxial samples with nominal dimensions of $80 \times 3 \times 0.5$ mm were utilized. Uniaxial tensile tests were performed by using a multifunctional microtester. In this study, the experimental data were modeled by empirical constitutive laws so that the corresponding mechanical properties of solder materials could be extracted.

The theoretical equations for the uniaxial stress-strain response (constant strain rate) of solder has been derived from the Anand viscoplastic model. Procedures for extracting the Anand model constants from experimental stress-strain data were also established.

CHAPTER 4

EFFECTS OF AGING AND SOLIDIFICATION PROFILE ON THE ANAND VISCOPLASTIC CONSTITUTIVE MODEL FOR SAC305 SOLDER

4.1 Introduction

In this chapter, the Anand viscoplastic stress-strain relations have been adapted for Pb-free solders to include material parameters that evolve with the thermal history of the solder material. In particular, aging effects have been examined by performing uniaxial tensile tests on SAC305 samples that were aged for various durations (0-360 days) at temperature of 100 C. Using the measured uniaxial test data, the Anand parameters were calculated for each set of aging conditions, and the effects of aging on the nine Anand model parameters were determined. Mechanical tests have been performed using both water quenched (WQ) and reflowed (RF) SAC305 samples (two unique specimen microstructures). The variations of the Anand model parameters with aging time have been characterized, and empirical relationships were established to model the observed changes.

4.2 Test Matrix

The aging and stress-strain test matrices are shown in Tables 4.1 and 4.2, respectively. The effects of aging on the nine Anand model parameters have been examined by performing stress-strain tests on SAC305 (96.5Sn-3.0Ag-0.5Cu) lead free solder samples that were aged for various durations (0-360 days) at a temperature of 100 C. The aging conditions included the baseline/reference state of no aging, as well as 8 different aging times including 1, 5, 20, 60, 120, 180, 270, and 360 days at 100 C, as

shown in Table 4.1. For each set of aging conditions, stress-strain experiments were performed at five temperatures (T = 25, 50, 75, 100, and 125 C) and three strain rates ($\dot{\varepsilon}$ = .001, .0001, and .00001 sec^{-1}), for both water quenched and reflowed specimens as described in Table 4.2. Using the measured stress-strain data and calculation procedure discussed above, the nine Anand model material parameters have been determined for each of the aging times.

	Aging Time								
	0 day	1 day	5 days	20 days	60 days	120 days	180 days	270 days	360 days
RF	√	√	√	√	√	√	√	√	√
WQ	√	√	√	√	√	√	√	√	√

Table 4.1 Aging and Initial Microstructure Test Matrix

Temp. (C)	Reflow (RF)			Water Quenched (WQ)		
	10^{-3}/s	10^{-4}/s	10^{-5}/s	10^{-3}/s	10^{-4}/s	10^{-5}/s
25	√	√	√	√	√	√
50	√	√	√	√	√	√
75	√	√	√	√	√	√
100	√	√	√	√	√	√
125	√	√	√	√	√	√

Table 4.2 Stress-Strain Test Matrix for Each Aging Time

4.3 Effects of Solidification Profile on the Mechanical Properties

To study the effect of solidification profile on the mechanical properties of lead free solder, it has been prepared the tensile specimens by using water quenched (WQ) and reflowed (RF) solidification profiles. The temperature vs. time variations for the

water quenched and reflowed profile are shown in Figure 3.2(a) and 3.2(b) respectively. The water quenched solidification profile follows the quick cooling procedure that cool down the molten specimen to room temperature within few seconds (10 sec). Due to this extremely quick cooling procedure, the specimens yielded very fine microstructure. Figure 4.1(a) illustrates the microstructures for the SAC305 specimen prepared by WQ cooling procedure. In this WQ specimen, it can be seen in that β-Sn dendrites are very small in size and that the IMC particles are extremely fine and evenly distributed across the β-Sn matrix. The reflowed temperature profile was chosen to match one that is typical for BGA solder joints. It could be noted that all of the specimen were first prepared by water quenched. After that several specimens were subsequently sent through a reflow oven to re-melt the solder in the tubes. In this work, it was used a nine zone Heller 1800EXL oven, which allowed a great flexibility in tailoring the temperature profile. A radio-frequency KIC temperature profiling system was used to monitor the solder temperature and control the reflow process using thermocouples attached to the glass tubes. Due to this slower cooling procedure, the microstructure of the reflowed specimen become much coarser compared to the water quenched specimen as shown in Figure 4.1(b). Figure 4.1(b) shows the microstructure of reflowed specimen where the β-Sn dendrites are much larger, and the IMC particles become much coarser and appear in conglomerates around the dendrites.

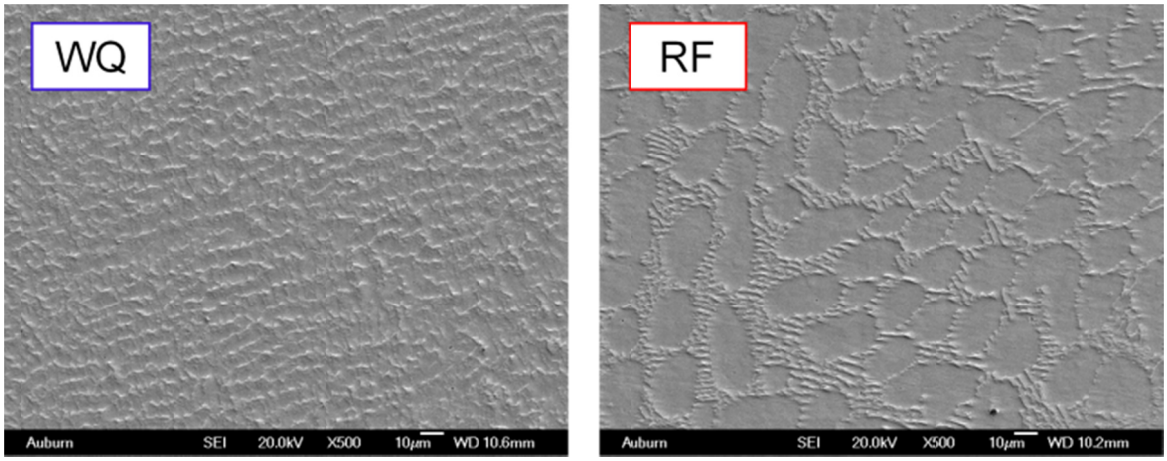

(a) (b)

Figure 4.1 Water Quenched and Reflowed Microstructure

To determine the effect of solidification profile on the mechanical properties of lead free solder, uniaxial tensile testing of the water quenched and reflowed lead free solder specimens has been performed. Stress-strain data were measured at five temperatures (T = 25, 50, 75, 100, and 125 ^{o}C), and three strain rates ($\dot{\varepsilon}$=.001, .0001, and .00001 sec^{-1}) for each SACN05 alloy microstructure (WQ and RF), as shown on the text matrix in Table 4.2. Figure 4.2 illustrates the comparison between water quenched and reflowed stress-strain curves for SAC305 with no aging (0 days aging) prior to testing (samples were tested immediately after prepared and cooling) for strain rates of $\dot{\varepsilon}$ = 0.001, 0.0001, and 0.00001 sec^{-1}. The dashed curves represent the water quenched results whereas solid lines are for the reflowed results. In each plot, the 5 colored curves are the stress-strain results for temperatures of T = 25, 50, 75, 100, and 125 ^{o}C. Each curve is the "average" stress-strain curve representing the fit to the 10 recorded raw stress-strain curves for a given set of temperature, strain rate, and aging conditions. For example, the top (black) curve in each plot is the average stress-strain curve at room temperature (25 ^{o}C), blue at 50 ^{o}C, green at 75 ^{o}C, deep red is 100 ^{o}C and the bottom

(red) curve in each plot is the average stress-strain curve at 125 ^{o}C. From the curves in Figure 4.2, it is observed that the effective elastic modulus, yield stress (YS), and ultimate tensile strength (UTS) all decrease monotonically with temperature as expected. For a particular temperature and strain rate, the water quenched and reflowed specimens exhibit dramatically different mechanical properties because their microstructures are different as shown in Figure 4.1. The water quenched samples (Dashed data) have superior mechanical properties relative to the analogous reflowed samples because they have finer microstructure. For example, the UTS values of the water quenched samples for $\dot{\varepsilon} = 0.001$ sec^{-1} are 74.1, 60.2, 52.5, 45.5, and 36.3 MPa at temperatures of 25, 50, 75, 100, and 125 ^{o}C, respectively; whereas the corresponding UTS values for the reflowed samples are 38.5, 33.1, 26.8, 20.5, and 19.1 MPa. Thus, the strength values for the water quenched samples are approximately double those of the reflowed samples at every temperature. Similar results were observed for the yield strength (YS). However, the differences in the initial effective elastic moduli of the water quenched and reflowed samples were quite small. Analogous results were obtained for the other two strain rates of $\dot{\varepsilon} = 0.0001$ sec^{-1} and $\dot{\varepsilon} = 0.00001$ sec^{-1}. The comparison between the UTS values of WQ and RF specimen are plotted in Figure 4.3.

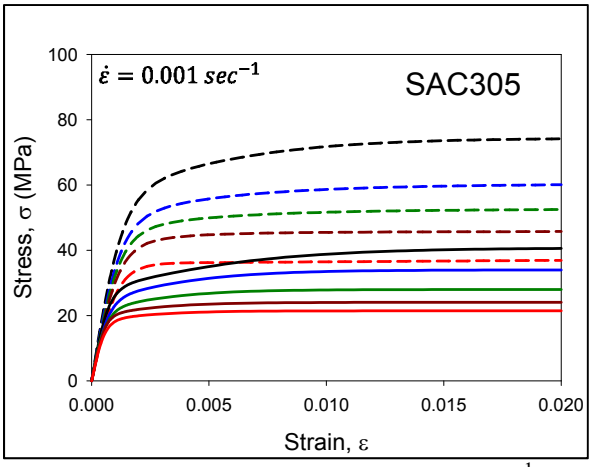

(a) Testing at Strain Rates 0.001 sec^{-1}

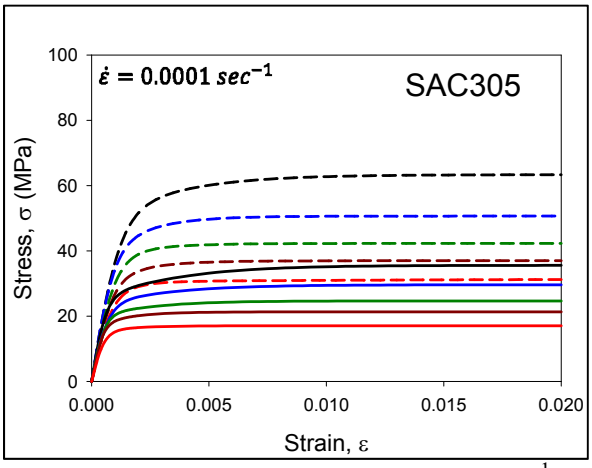

(b) Testing at Strain Rates 0.0001 sec^{-1}

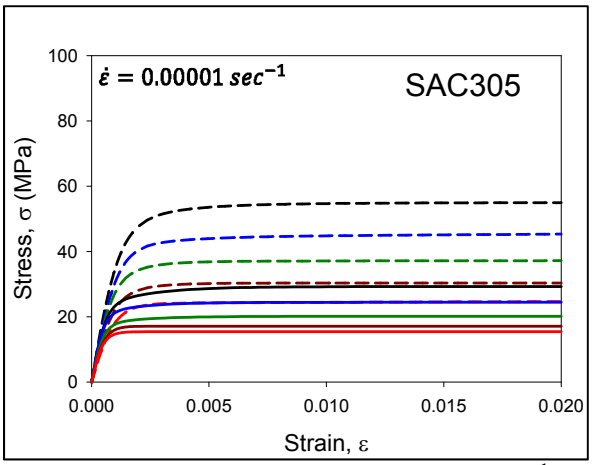

(c) Testing at Strain Rates 0.00001 sec^{-1}

Figure 4.2 Comparison between Water Quenched (WQ) and Reflowed (RF) Stress-Strain Curves

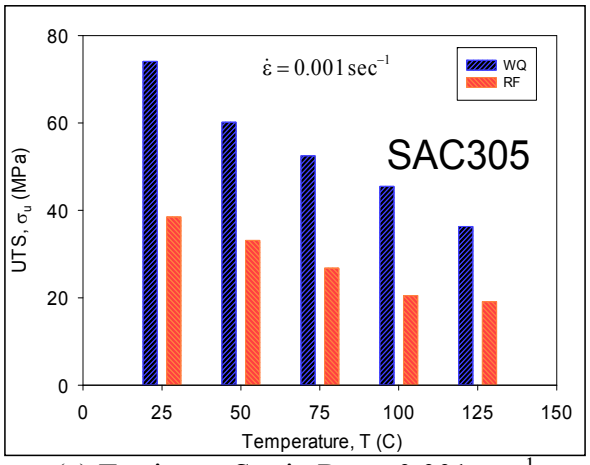

(a) Testing at Strain Rates 0.001 sec^{-1}

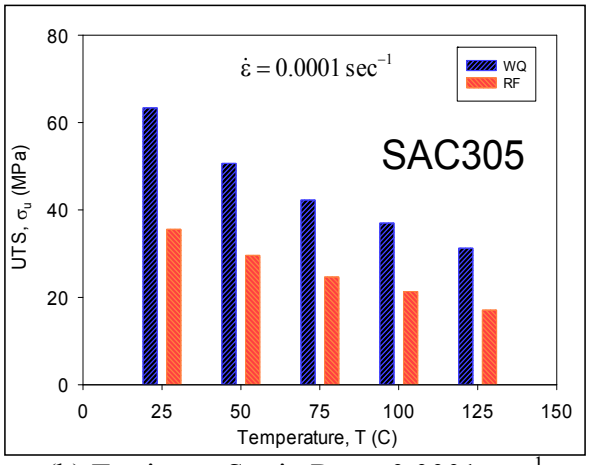

(b) Testing at Strain Rates 0.0001 sec^{-1}

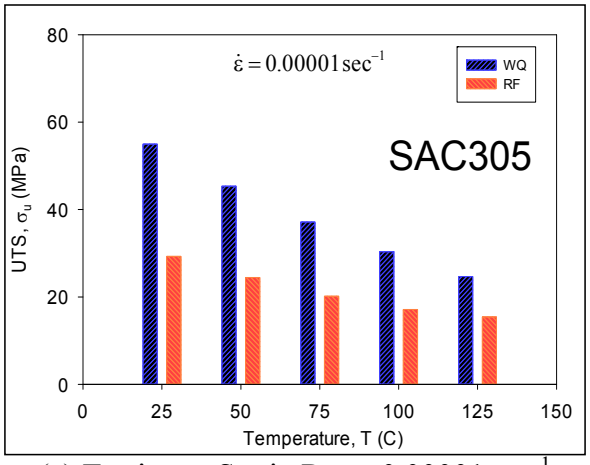

(c) Testing at Strain Rates 0.00001 sec^{-1}

Figure 4.3 Comparison between Water Quenched (WQ) and Reflowed Ultimate Strength [No Aging]

4.4 Effects of Aging on the Mechanical Properties

The effects of aging on the stress strain curves of water quenched and reflowed with $\dot{\varepsilon}$ = 0.001, 0.0001, and 0.00001 sec^{-1} are shown in Figures 4.4, 4.5, and 4.6, respectively. The various colored curves in each graph represent the data for different testing temperature. In particular, the black top curve in each graph is for 125 ^{o}C testing temperature, and the bottom red curve in each graph is for room temperature testing condition. As expected, aging also causes large degradations in the both the room temperature and elevated temperature mechanical behavior of SAC solders, with large degradations in the material properties (elastic modulus, yield stress, and UTS). The changes in UTS (maximum/saturation stress) with aging are especially evident from the plots in Figures 4.4-4.6. It can also be seen that the majority of the changes in the material properties at each temperature occur during the first 20 days of aging, with slower degradations occurring from 20 to 360 days of aging.

Results for water quenched and reflowed microstructures can be compared by examining analogous pairs of stress-strain curves in Figures 4.3-4.6. Initially (prior to aging), the differences between the mechanical properties of water quenched and reflowed alloys were large. As aging progressed, the differences became smaller as the microstructures converged to similar states. For example, from Figure 4.3 at T = 25 ^{o}C with no aging, the ultimate strength of the water quenched alloy is 50% higher than the corresponding value for the reflowed alloy. The differences between the ultimate strengths of water quenched and reflowed microstructures become much less as aging progresses. At T = 25 ^{o}C and 20 days aging, the ultimate strength of the water quenched alloy is only 15% higher than the corresponding value for the reflowed alloy.

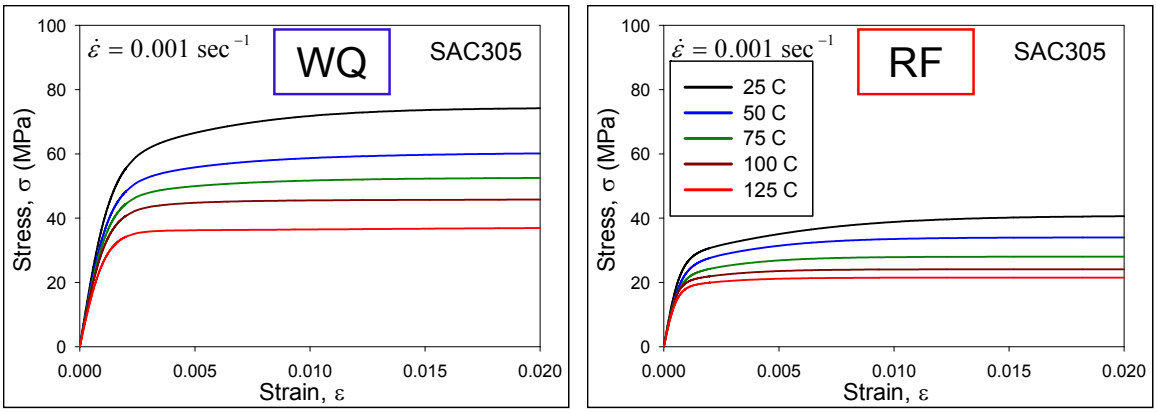

(a) No Aging

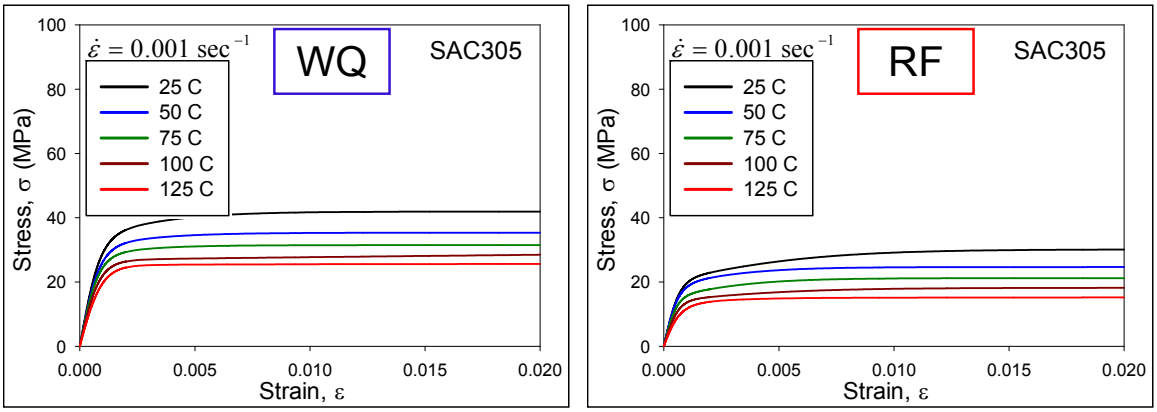

(b) 1 Day of Aging

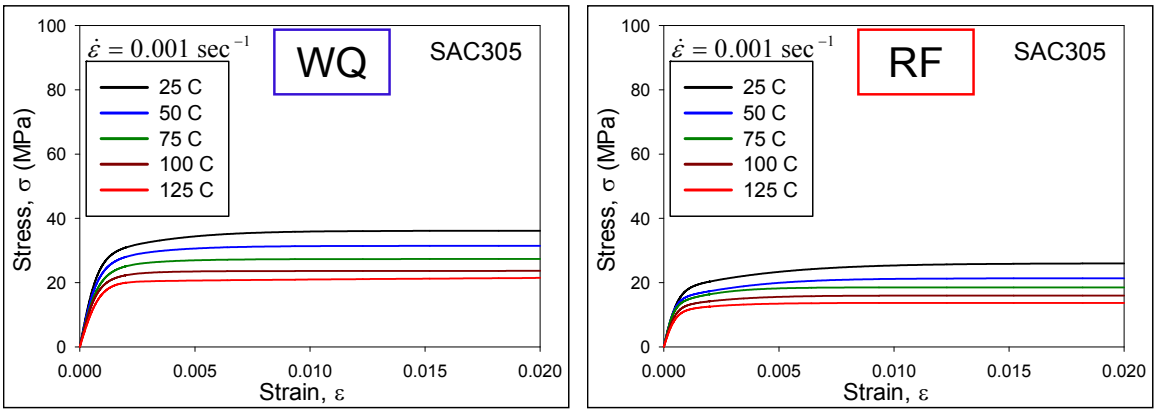

(c) 5 Days of Aging

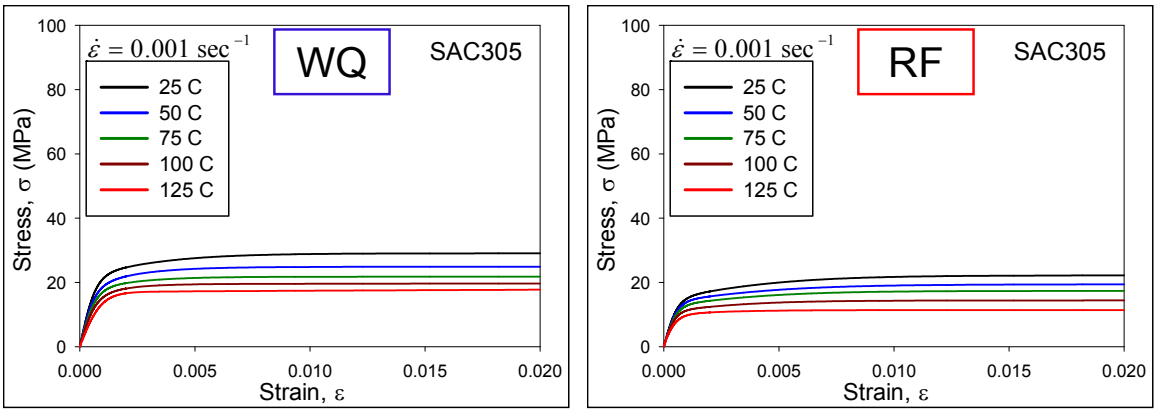

(d) 20 Days of Aging

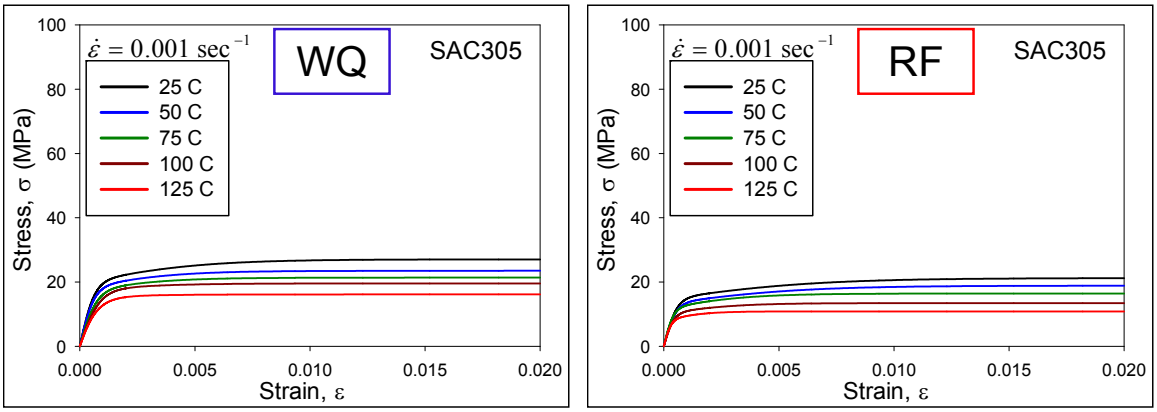

(e) 60 Days of Aging

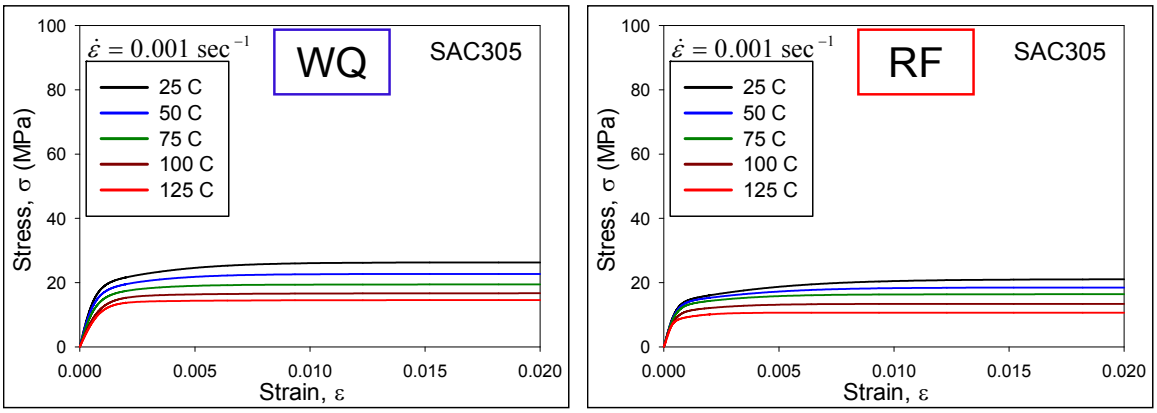

(f) 120 Days of Aging

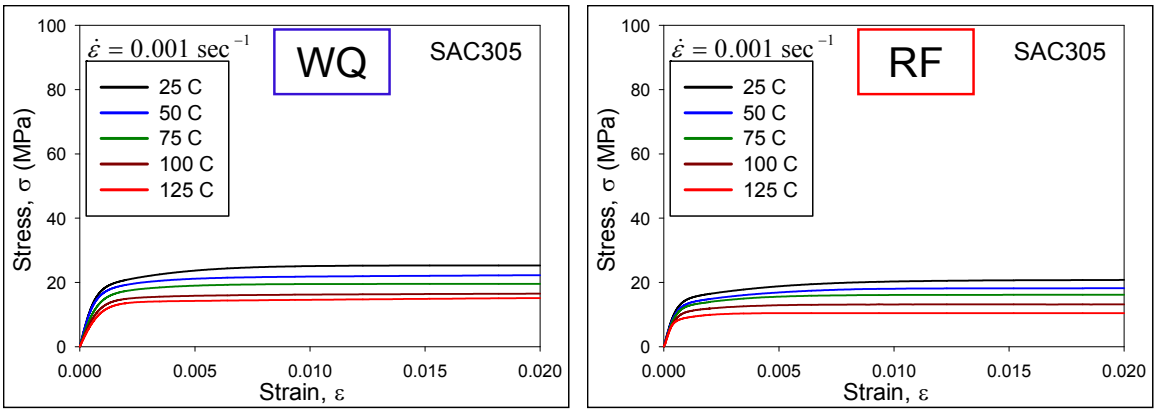

(g) 180 Days of Aging

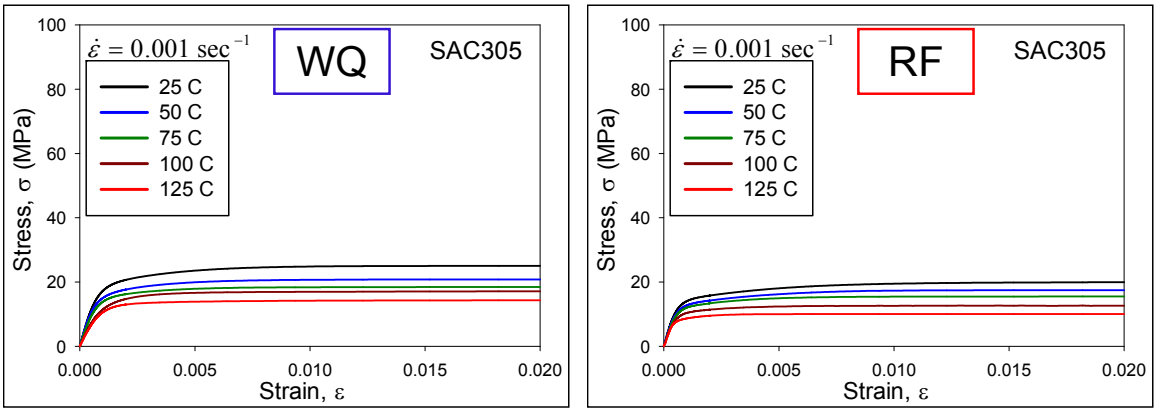

(h) 270 Days of Aging

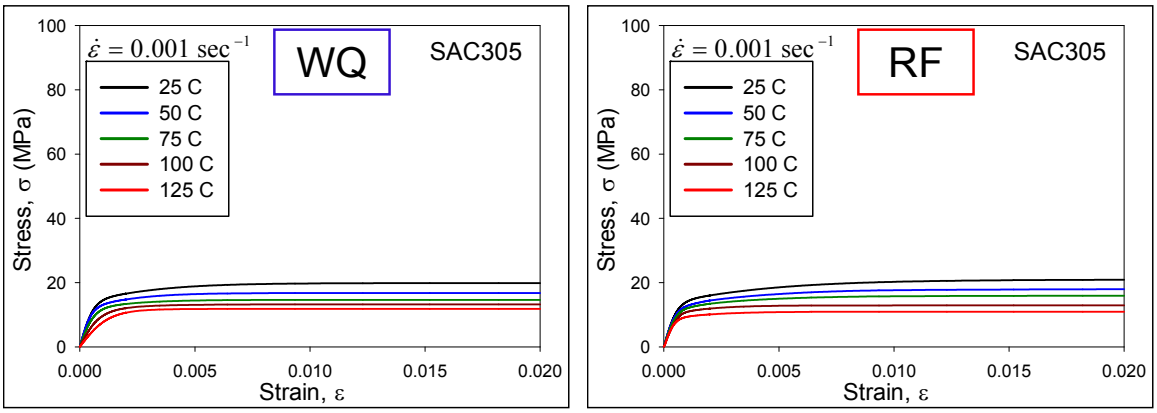

(i) 360 Days of Aging

Figure 4.4 Effects of Aging on the Stress-strain Curves Testing at Strain Rates 0.001 sec^{-1}

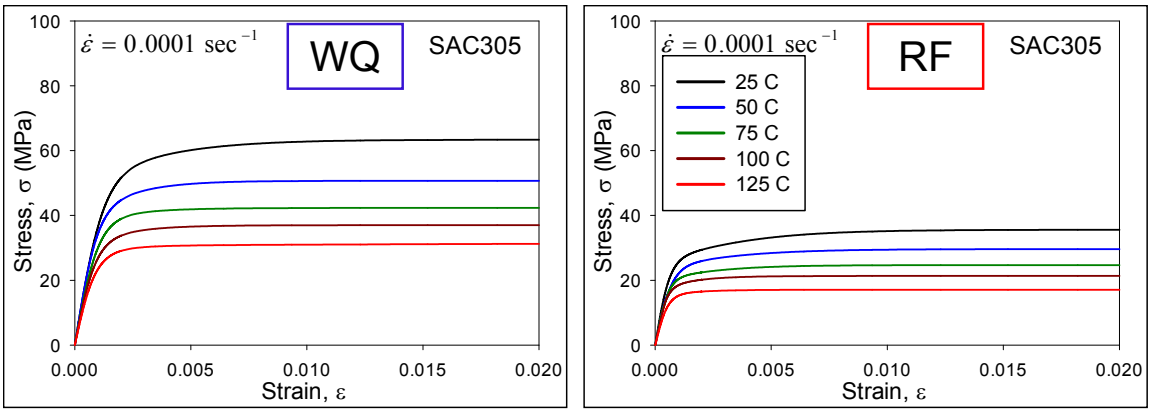

(a) No Aging

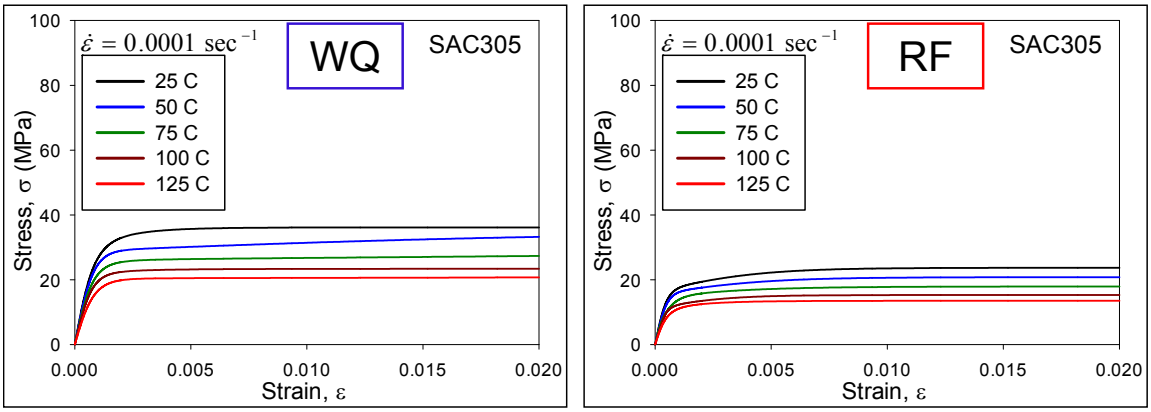

(b) 1 Day of Aging

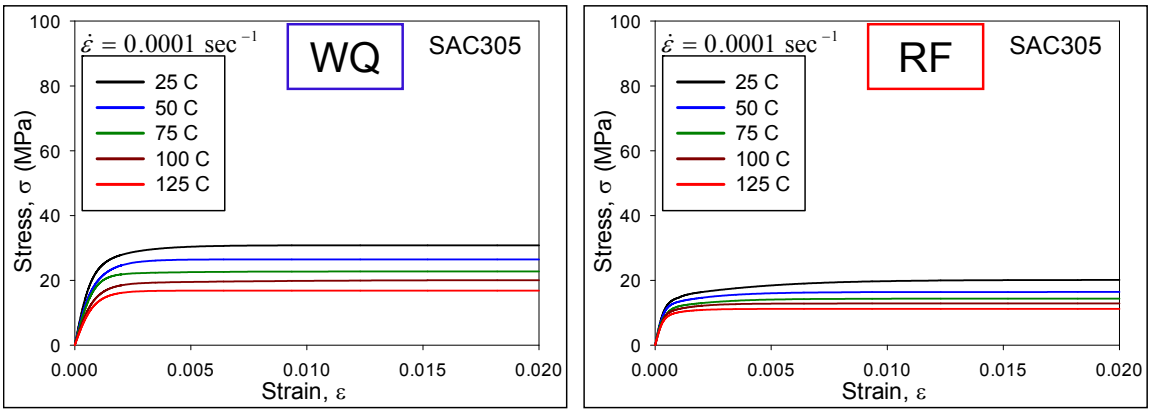

(c) 5 Days of Aging

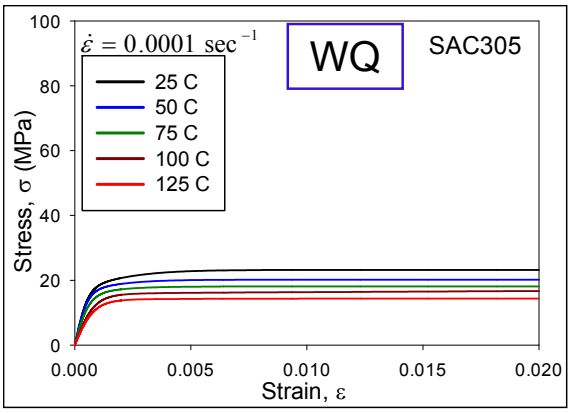

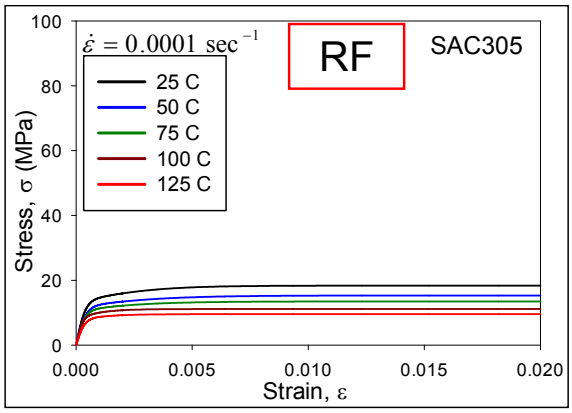

(d) 20 Days of Aging

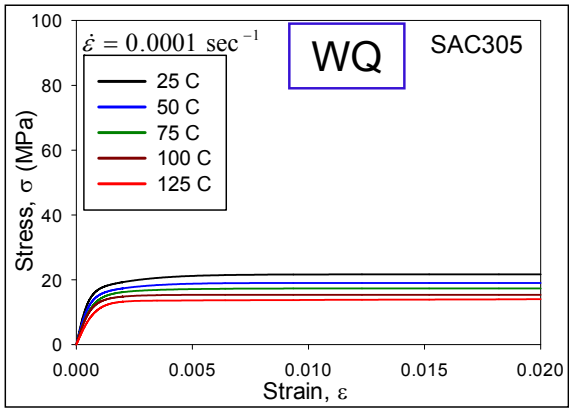

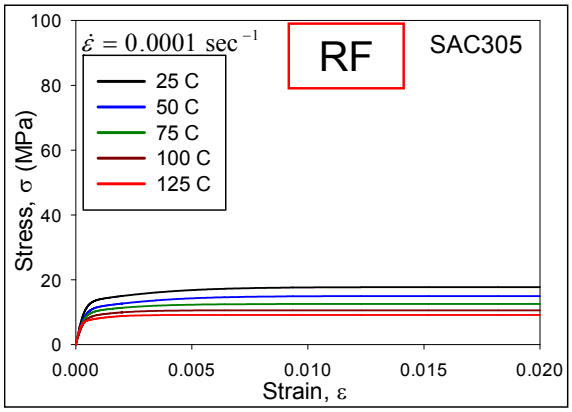

(e) 60 Days of Aging

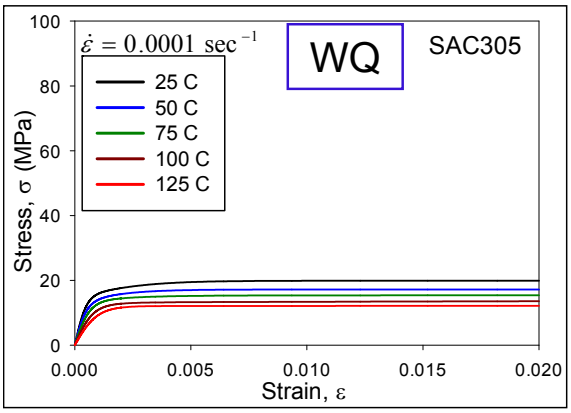

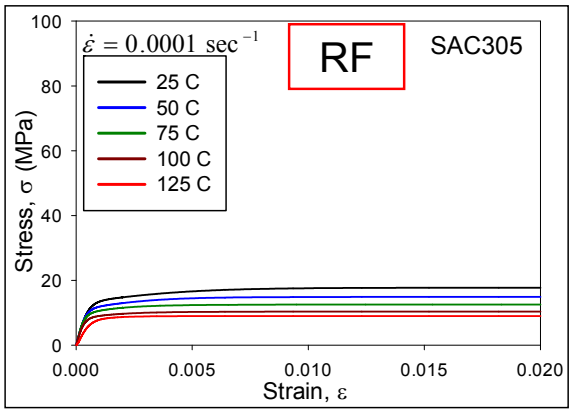

(f) 120 Days of Aging

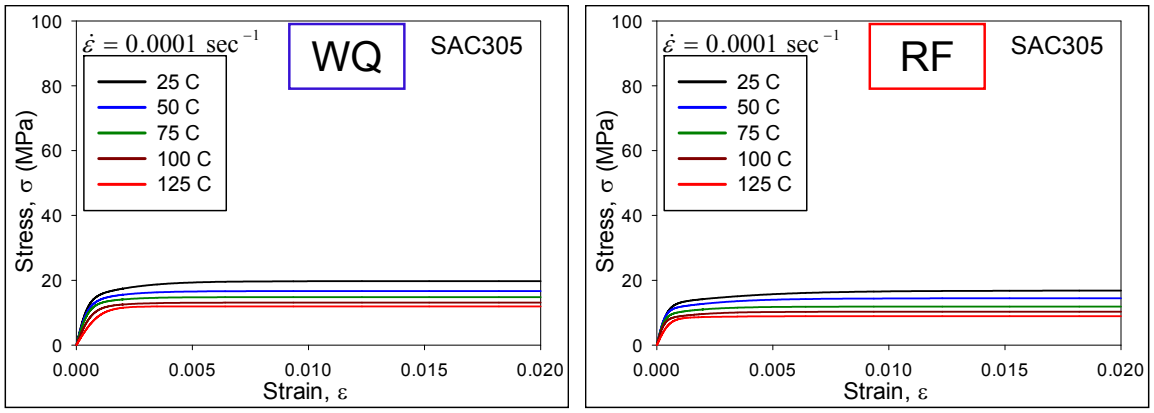

(g) 180 Days of Aging

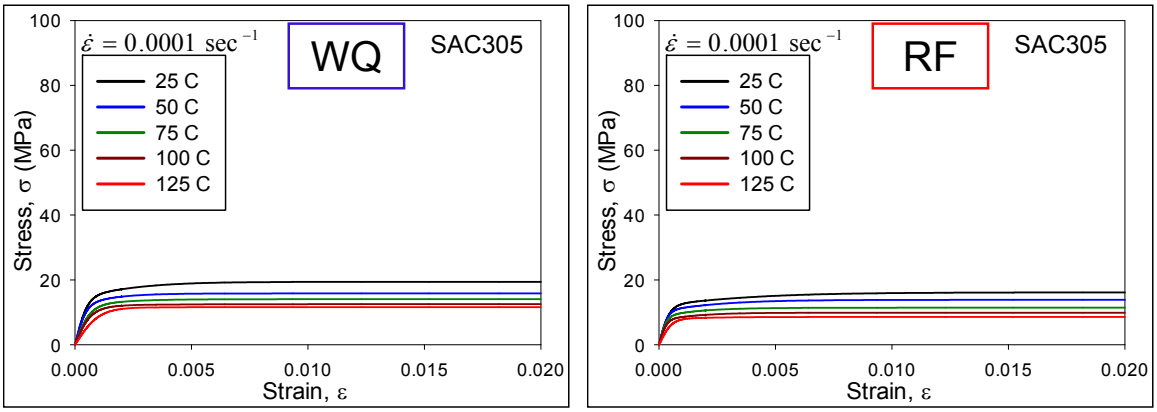

(h) 270 Days of Aging

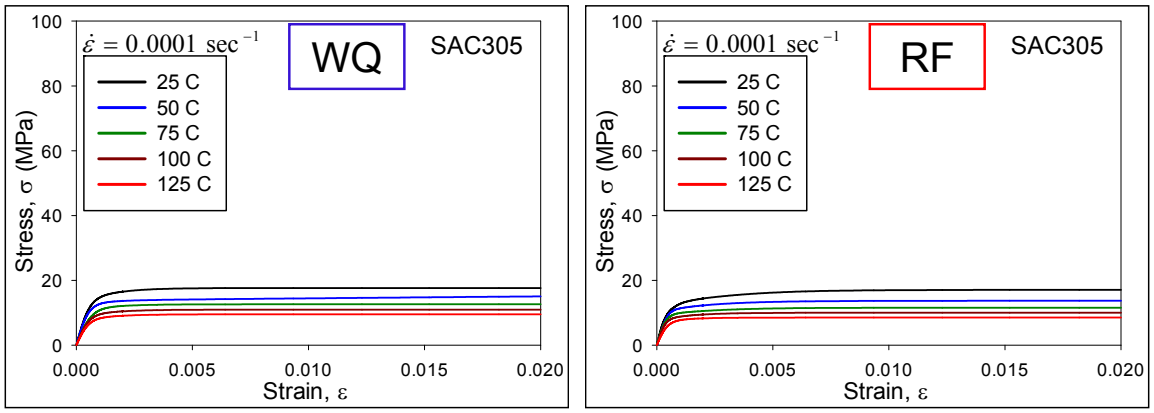

(i) 360 Days of Aging

Figure 4.5 Effects of Aging on the Stress-strain Curves Testing at Strain Rates 0.0001 sec^{-1}

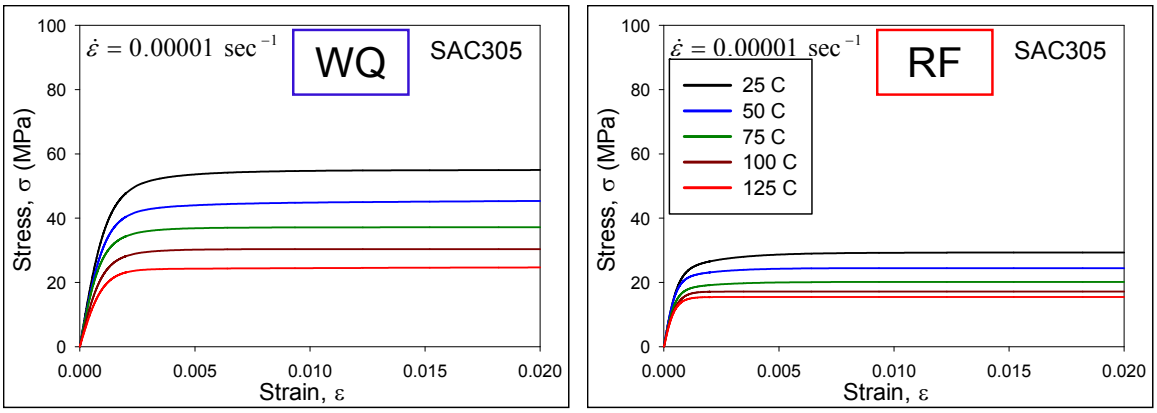

(a) No Aging

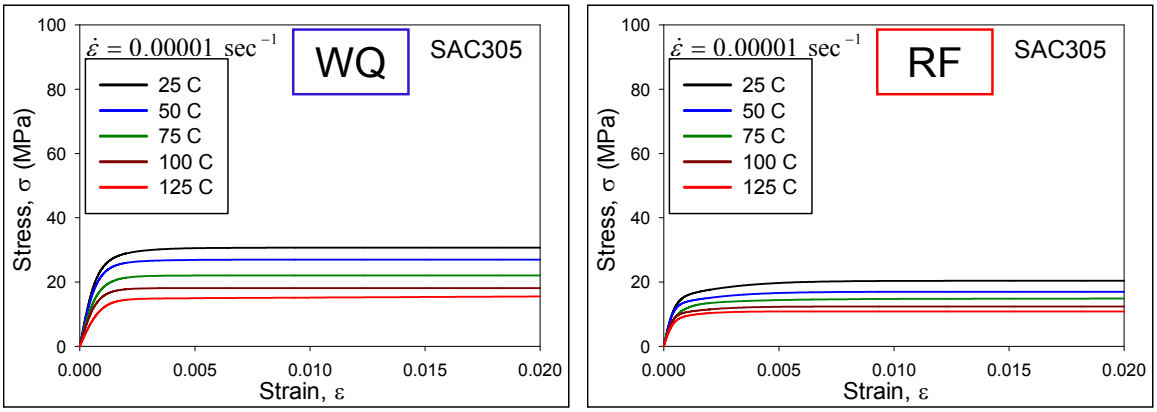

(b) 1 Day of Aging

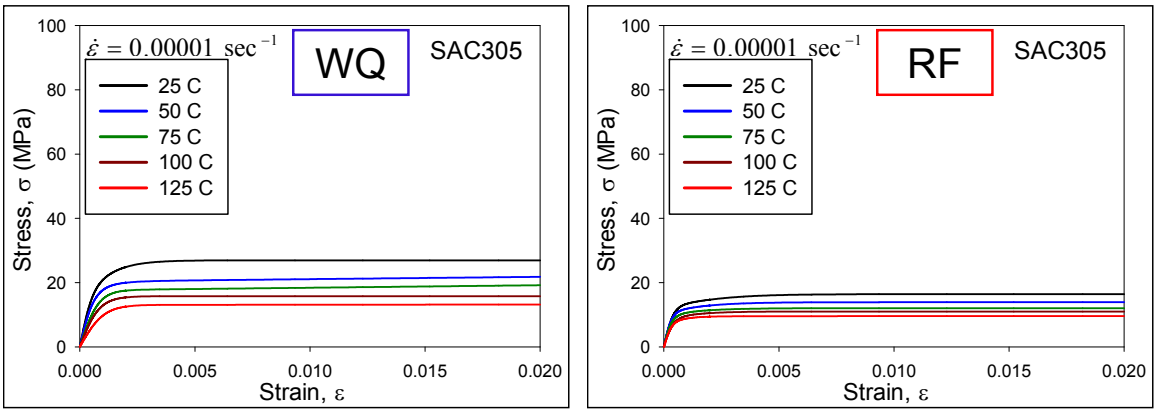

(c) 5 Days of Aging

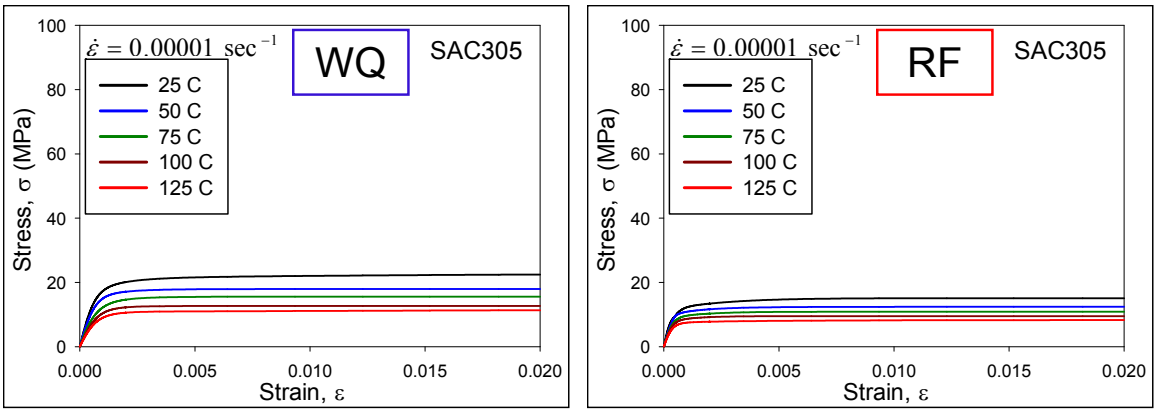

(d) 20 Days of Aging

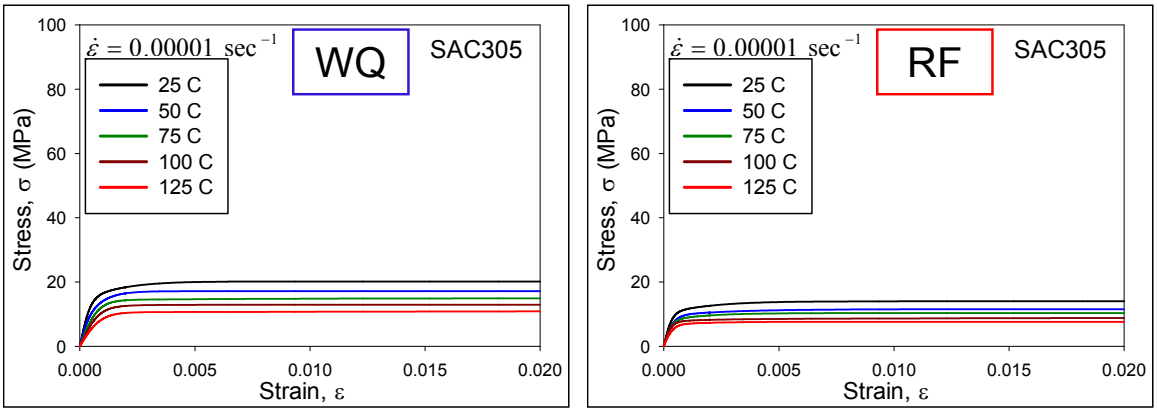

(e) 60 Days of Aging

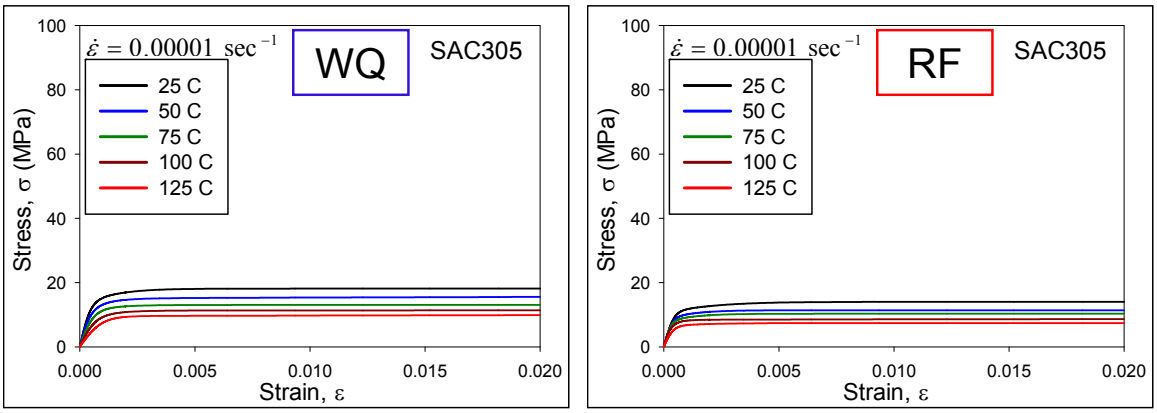

(f) 120 Days of Aging

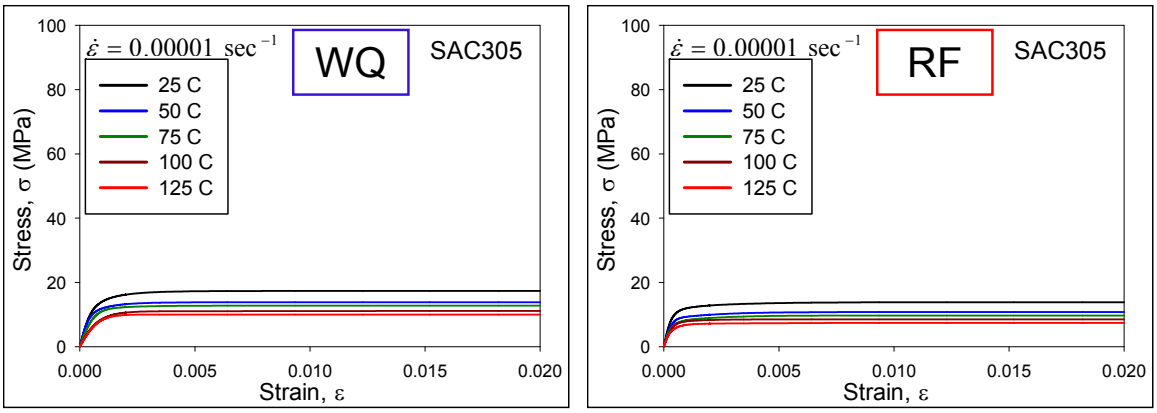

(g) 180 Days of Aging

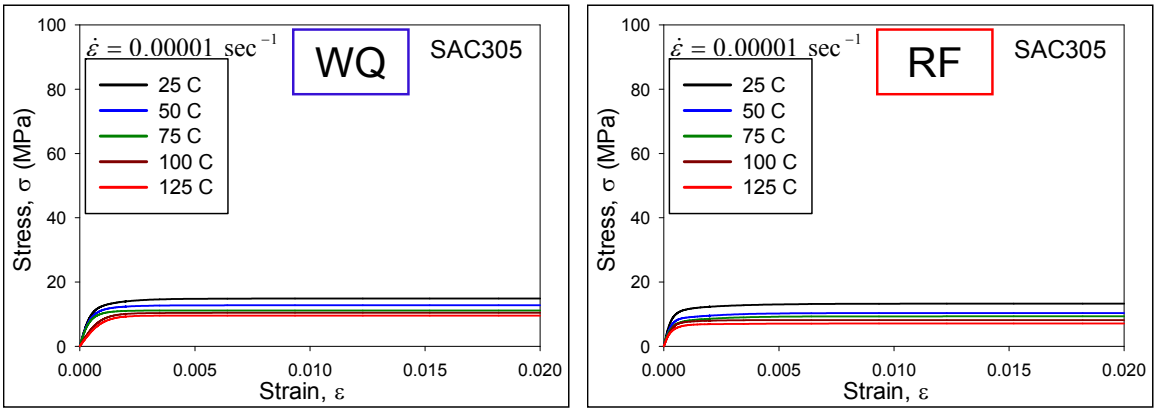

(h) 270 Days of Aging

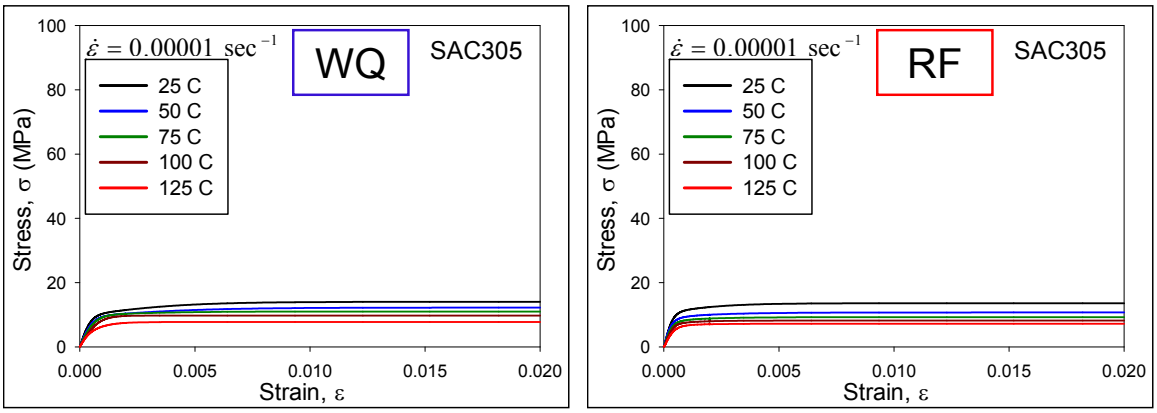

(i) 360 Days of Aging

Figure 4.6 Effects of Aging on the Stress-strain Curves Testing at Strain Rates 0.00001 sec^{-1}

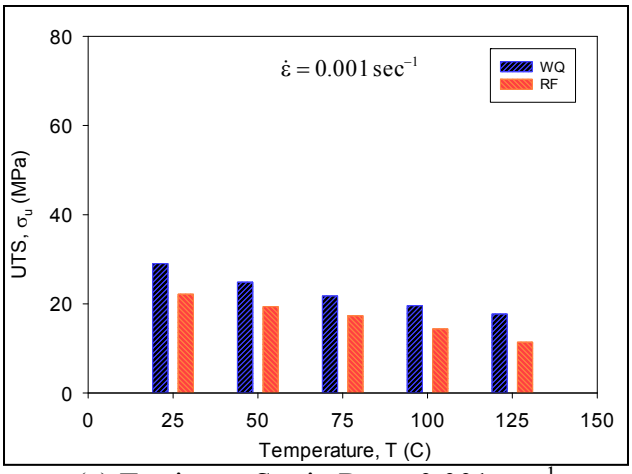

(a) Testing at Strain Rates 0.001 sec^{-1}

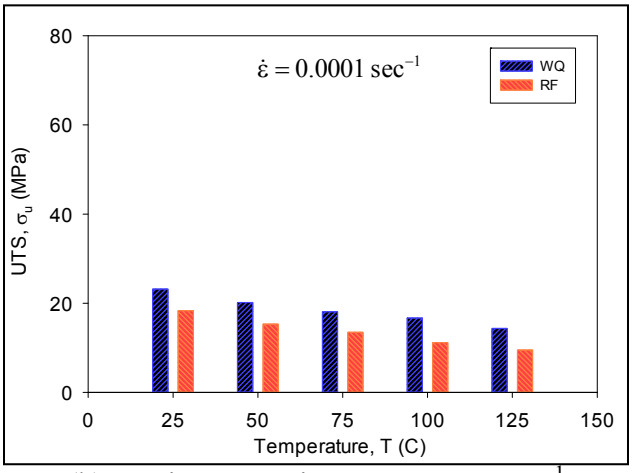

(b) Testing at Strain Rates 0.0001 sec^{-1}

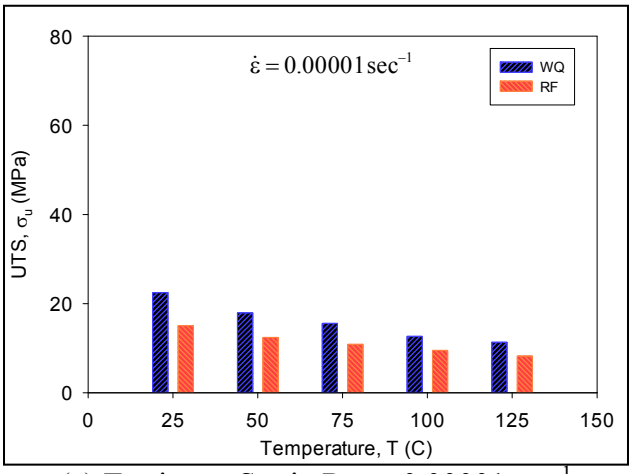

(c) Testing at Strain Rates 0.00001 sec^{-1}

Figure 4.7 Comparison between Water Quenched (WQ) and Reflowed Ultimate Strength [20 Days Aging]

4.5 Effects of Aging on the Anand Material Parameters

Using the nonlinear regression analysis procedure presented above, the Anand model parameters for SAC305 lead free solder material (water quenched and reflowed microstructures) have been determined for each aging time from the temperature and strain rate dependent stress-strain data. The calculated values are given in Tables 4.3 and 4.4 for the water quenched and reflowed microstructures, respectively.

Par. No.	Anand Par.	Units	0 Days Aging	1 Days Aging	5 Days Aging	20 Days Aging	60 Days Aging	120 Days Aging	180 Days Aging	270 Days Aging	365 Days Aging
1	s_o	MPa	32.2	24.85	18.6	12	9	7.5	7.0	6.5	5.6
2	Q/R	1/K	9320	9320	9320	9320	9320	9320	9320	9320	9320
3	A	sec^{-1}	2800	3375	3675	3850	3950	4000	4020	4095	4210
4	ξ	-	4	4	4	4	4	4	4	4	4
5	m	-	0.29	0.25	0.23	0.215	0.21	0.2	0.2	0.19	0.1788
6	h_o	MPa	186,000	160,000	140,000	110,000	90,000	81000	79500	78000	73708
7	$\hat{S}$	MPa	44.67	33.47	30	26	25	24.3	24	23	21.4
8	n	-	0.0120	0.0070	0.0040	0.0025	0.0020	0.0016	0.0015	0.0012	0.00101
9	a	-	1.72	1.86	1.96	1.99	2.01	2.03	2.04	2.04	2.05

Table 4.3 Anand Model Parameters for SAC 305 Solder for Various Aging Times at 100 ^oC [Water Quenched]

Par. No.	Anand Par.	Units	0 Days Aging	1 Days Aging	5 Days Aging	20 Days Aging	60 Days Aging	120 Days Aging	180 Days Aging	270 Days Aging	365 Days Aging
1	s_o	MPa	21.0	16.65	13.5	8.0	6.0	5.9	5.8	5.7	5.4
2	Q/R	1/K	9320	9320	9320	9320	9320	9320	9320	9320	9320
3	A	sec^{-1}	3501	3776	3960	4065	4095	4105	4110	4175	4210
4	ξ	-	4	4	4	4	4	4	4	4	4
5	m	-	0.25	0.226	0.21	0.19	0.18	0.18	0.18	0.18	0.18
6	h_o	MPa	180000	151000	135050	103218	89682	80825	77540	76130	73708
7	$\hat{S}$	MPa	30.2	27.7	26.0	22.8	22.3	22.0	21.9	21.7	21.4
8	n	-	0.0100	0.0058	0.0030	0.0015	0.0011	0.0010	0.0098	0.001	0.001
9	a	-	1.78	1.91	1.98	2.01	2.03	2.04	2.05	2.05	2.06

Table 4.4 Anand Model Parameters for SAC 305 Solder for Various Aging Times at 100 ^{o}C [Reflowed]

The effects of aging and microstructure on the Anand model parameters for SAC305 can be visualized by plotting the extracted model parameters vs. aging time. Such graphs are presented in Figure 4.8 for the nine parameters s_o, Q/R, A, ξ, m, h_o, $\hat{s}$, n, and a. Results for both the water quenched and reflowed microstructures are included on each graph in Figure 4.8. The discrete parameter values in these plots illustrate smooth variations with aging, and empirical mathematical models with linear and nonlinear terms have been able to accurately represent the variations of all of the Anand parameters with aging time.

Parameters Q/R and ξ were found to be constant, and thus independent of both aging and microstructure. This is logical since Q is the activation energy of the SAC solder, which should be constant independent of aging and solidification profile. Material constant ξ was also specified to be the same for water quenched and reflowed

samples because they have the same chemical (alloy) composition. The other 7 parameters (s_o, A, m, h_o, $\hat{s}$, n, and a) all exhibit rapid changes during the first 20 days of aging, and then slow variations for aging times between 20 and 360 days. The slow variations for longer aging times were found to be approximately linear with the aging time. The mathematical expressions for the aging time dependent empirical models used in Figure 4.8 are tabulated in Figure 4.9. In all cases, the models included constant and linear terms with aging time, along with a nonlinear functional term.

From the plots in Figure 4.8, it can be observed that for small aging times, the Anand parameters for the water quenched SAC305 alloy were found to vary more rapidly with aging time relative to the analogous variations for the reflowed SAC305 alloy. For longer aging times, the water quenched and reflowed values of each Anand parameter began to approach each other (converge), since the microstructures are becoming similar after extensive durations of aging.

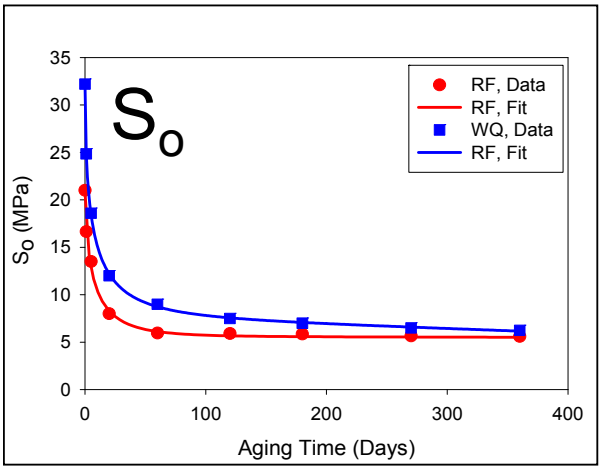

(a) Variation of s_o with Aging Time

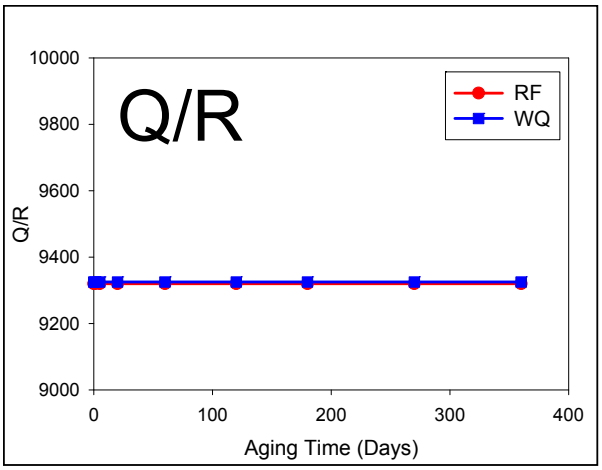

(b) Variation of Q/R with Aging Time

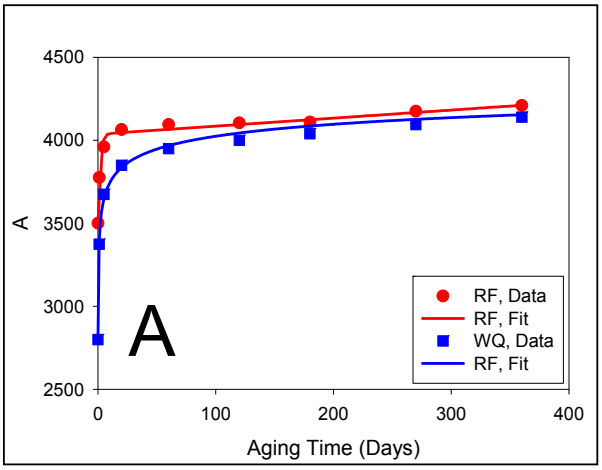

(c) Variation of A with Aging Time

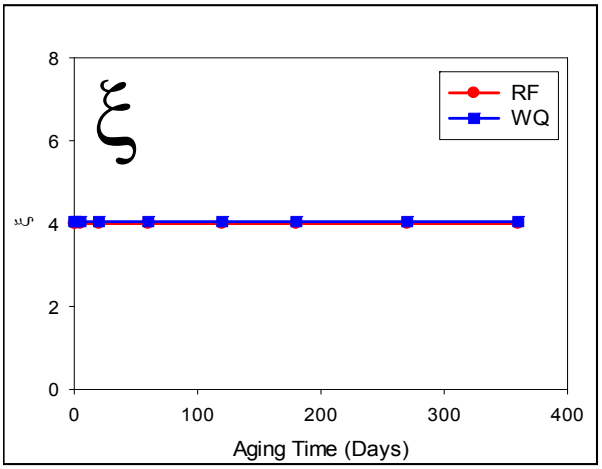

(d) Variation of ξ with Aging Time

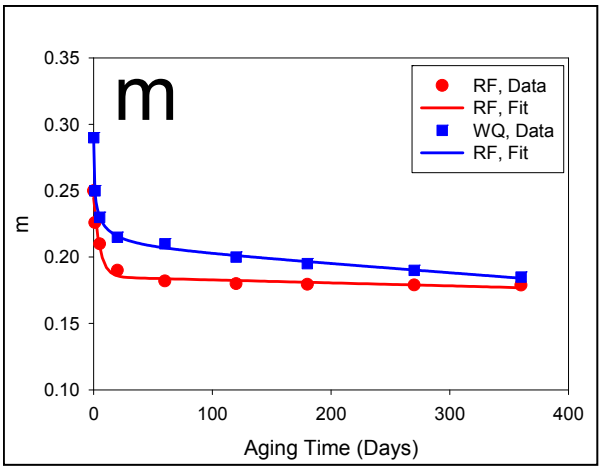

(e) Variation of m with Aging Time

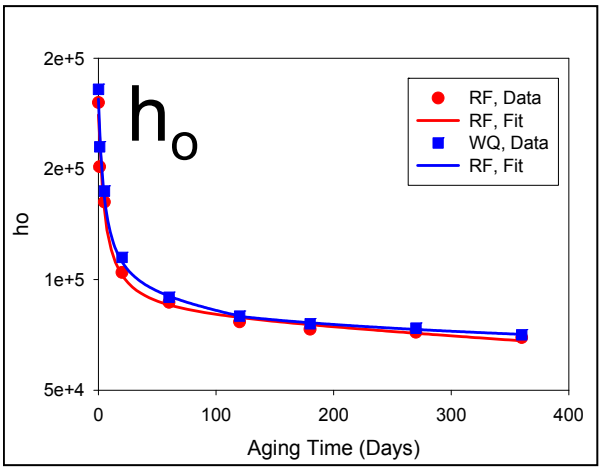

(f) Variation of h_o with Aging Time

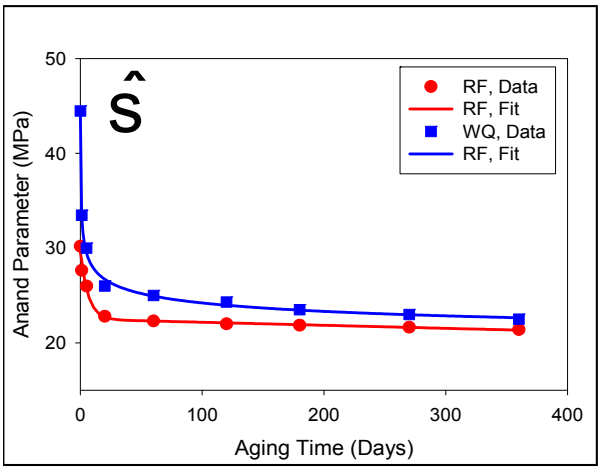

(g) Variation of $\hat{s}$ with Aging Time

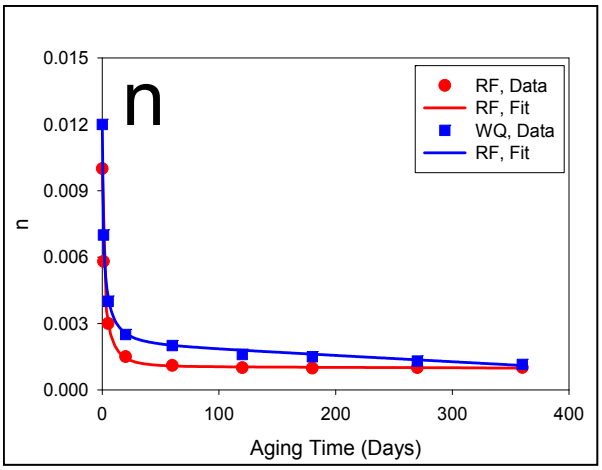

(h) Variation of n with Aging Time

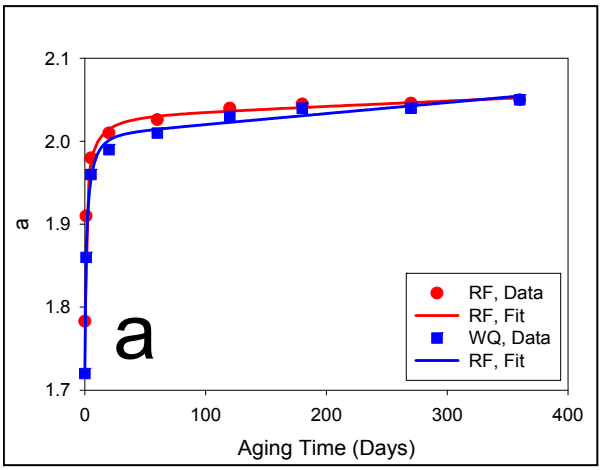

(i) Variation of a with Aging Time

Figure 4.8 Variation of the Anand Model Parameters with Aging Time [SAC305, WQ and RF]

Anand Constant	Form of Empirical Fitting Equation
S_o, m, n, a	$\text{Parameter} = C_o + C_1 t + C_2 e^{-C_3 t^{C_4}}$
A, $\hat{s}$	$\text{Parameter} = C_0 + C_1 t + C_2 (1 - e^{-C_3 t})$
h_o	$\text{Parameter} = C_0 + C_1 t + \frac{C_2}{C_3 + e^t}$
Q/R, ξ	$\text{Parameter} = C_o$

Figure 4.9 Empirical Models for Variation of the Anand Model Parameters with Aging Time

4.6 Correlation of the Predictions of the Anand Model with the Experimental Stress-Strain Data

Equation. (3.11) include 9 material parameters A, ξ, Q/R, m, n, h_o, a, s_o, and $\hat{s}$. The values of these Anand material parameters for each aging condition are given in the Table 4.3 and 4.4. Using Eq. (3.11) and the Anand model parameters in Tables 4.3 and 4.4, the stress (σ) vs. plastic strain (ε_p) curves can be predicted for each aging condition and solder microstructure at selected strain rates and temperatures. These results can then be converted to stress (σ) vs. total strain curve (ε) by adding the elastic strain to the plastic strain:

$$\varepsilon = \varepsilon_e + \varepsilon_p \qquad \varepsilon_e = \frac{\sigma}{E} \tag{4.1}$$

where E is the initial elastic modulus of the SAC alloy at the selected strain rate and temperature.

Figure 4.10 illustrates the correlations between the model predictions and the experimental stress-strain curves for the water quenched SAC305 alloy and no aging. In this case, the Anand model constants in Table 4.3 for 0 days aging were utilized. The experimental curves were those shown earlier in Figure 4.2. Good correlations are obtained, with the Anand model able to represent the stress-strain curves accurately over a wide range of temperatures and strain rates. Analogous comparisons for the water quenched alloy and 20 days aging are shown in Figure 4.11. In this case, the Anand model constants from Table 4.3 for 20 days aging were utilized, along with the experimental data. Again, good correlations were obtained for all temperatures and strain rates.

Analogous comparisons are made in Figures 4.12 and 4.13 for the reflowed SAC305 alloy with no aging and 20 days aging, respectively. In these cases, the Anand parameters from Table 4.4 were utilized. Again, excellent agreement has been found between experimental and calculated curves. Similar comparisons have been performed for all of the other aging conditions (1, 5, 60, 120, 180 and 360 days aging at 100 ^{o}C), and the water quenched and reflowed samples. In all cases, the Anand model predictions match the experimental stress-strain curves well for all strain rates and temperatures. Therefore, the updated Anand model parameters can be used to model both aging induced degradation behavior and microstructural effects on the stress-strain curves.

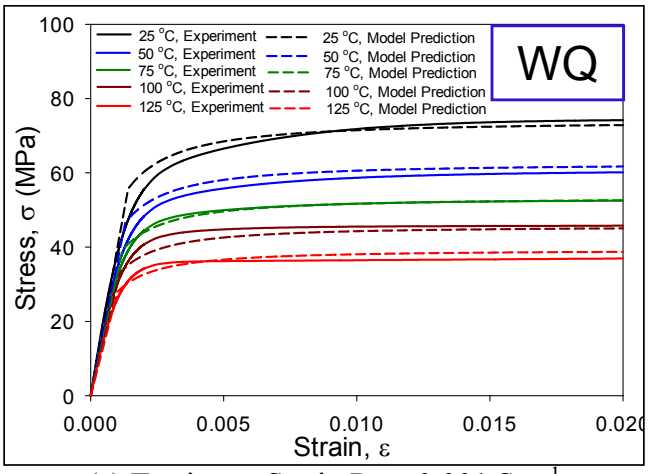

(a) Testing at Strain Rate 0.001 Sec^{-1}

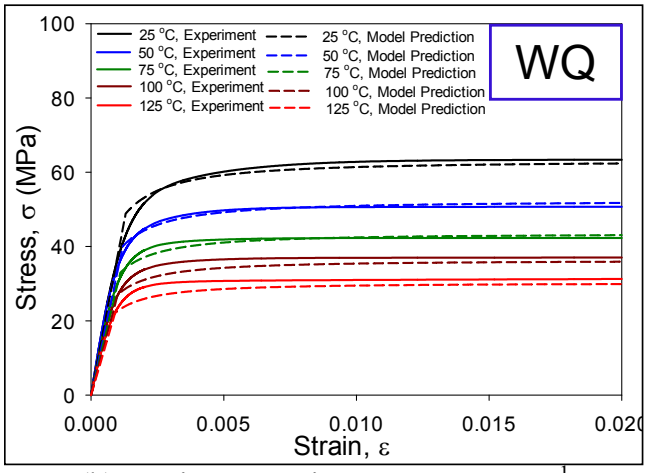

(b) Testing at Strain Rate 0.0001 Sec^{-1}

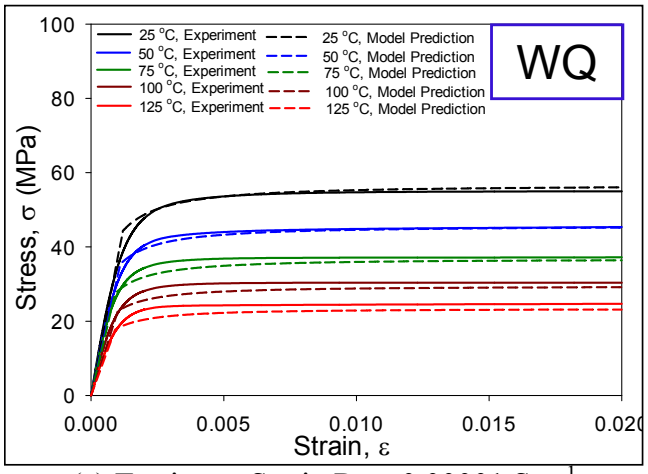

(c) Testing at Strain Rate 0.00001 Sec^{-1}

Figure 4.10 Correlation of the Anand Model Predictions with Experimental Stress-Strain Data [SAC305, Water Quenched, No Aging]

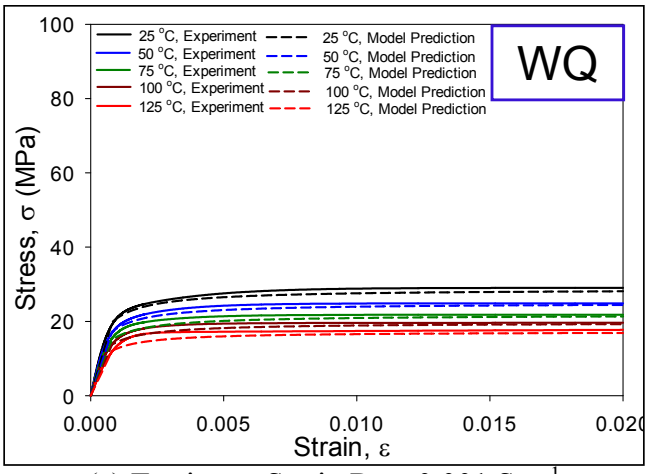

(a) Testing at Strain Rate 0.001 Sec^{-1}

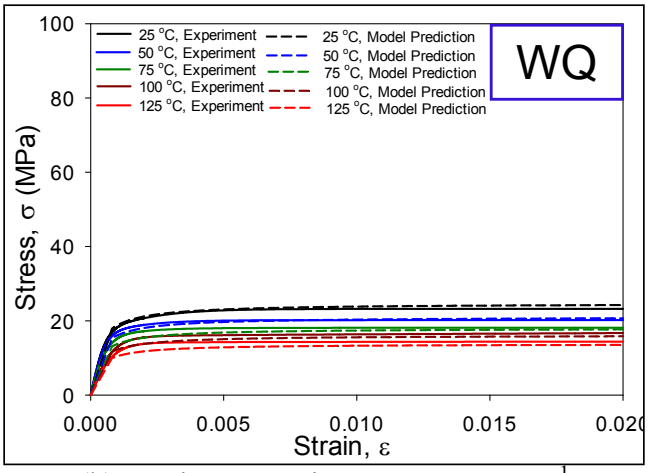

(b) Testing at Strain Rate 0.0001 Sec^{-1}

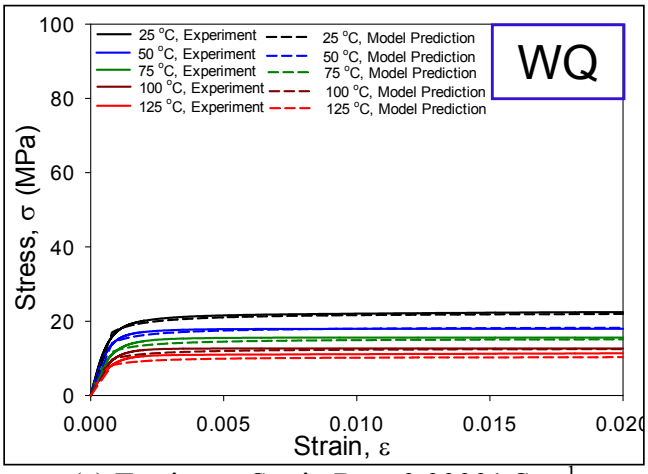

(c) Testing at Strain Rate 0.00001 Sec^{-1}

Figure 4.11 Correlation of the Anand Model Predictions with Experimental Stress-Strain Data [SAC305, Water Quenched, 20 Days Aging]

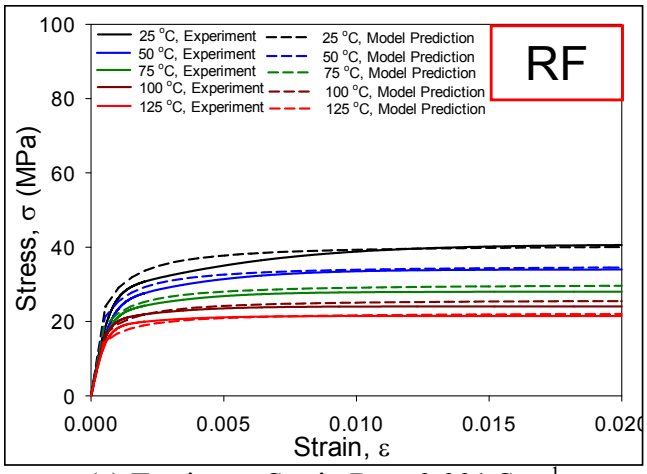

(a) Testing at Strain Rate 0.001 Sec^{-1}

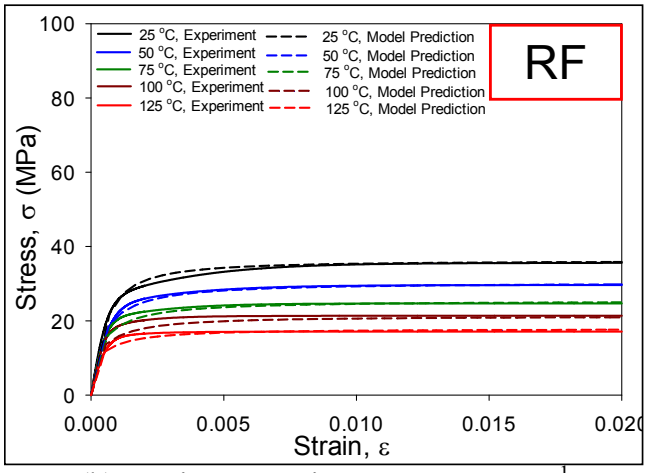

(b) Testing at Strain Rate 0.0001 Sec^{-1}

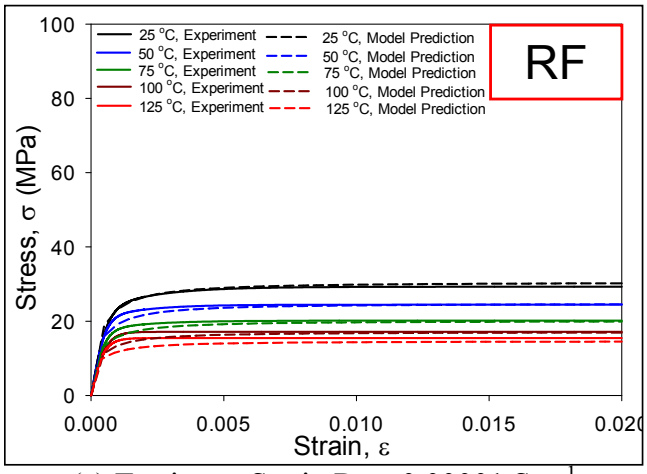

(c) Testing at Strain Rate 0.00001 Sec^{-1}

Figure 4.12 Correlation of the Anand Model Predictions with Experimental Stress-Strain Data [SAC305, Reflowed, No Aging]

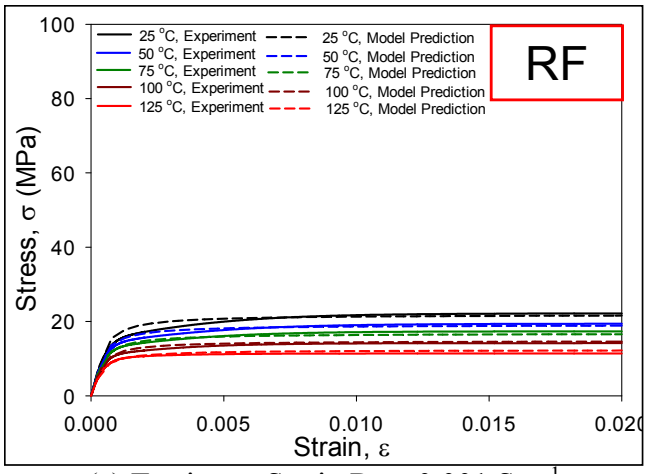

(a) Testing at Strain Rate 0.001 Sec^{-1}

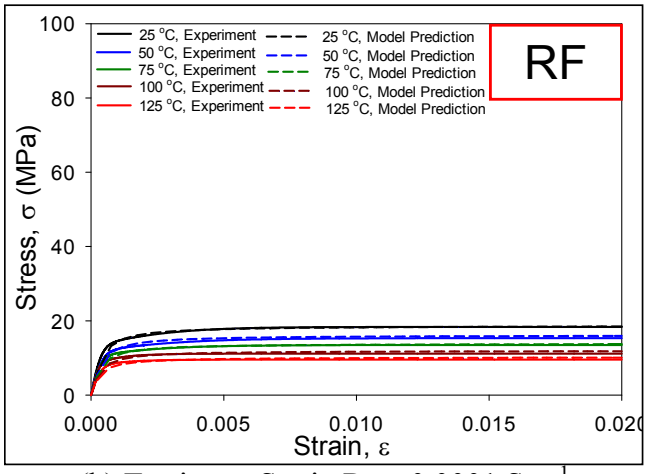

(b) Testing at Strain Rate 0.0001 Sec^{-1}

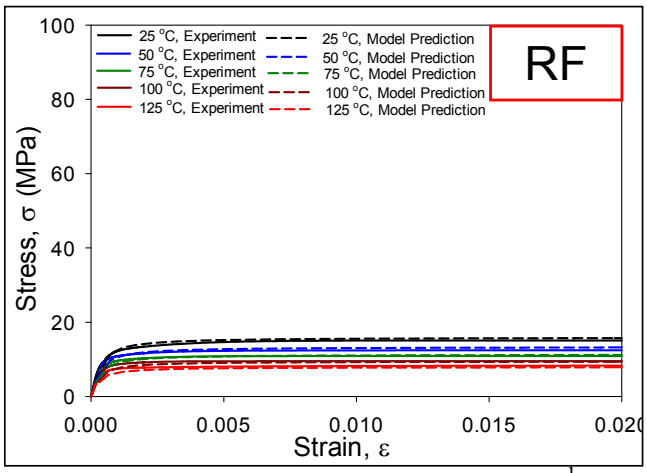

(c) Testing at Strain Rate 0.00001 Sec^{-1}

Figure 4.13 Correlation of the Anand Model Predictions with Experimental Stress-Strain Data [SAC305, Reflowed, 20 Days Aging]

4.7 Summary and Discussion

In this work, the Anand viscoplastic stress-strain relations for Pb-free solders have been adapted to include material parameters that evolve with the thermal history of the solder material. In particular, aging effects have been examined by performing uniaxial tensile tests on SAC305 samples that were aged for various durations (0-360 days) at temperature of 100 ^{o}C. For each set of aging conditions, several sets of constant strain rate and temperature tests were conducted on the aged solder samples. Testing conditions included strain rates of 0.001, 0.0001, and 0.00001 (1/sec), and temperatures of 25, 50, 75, 100, and 125 ^{o}C. Using the measured uniaxial test data, the Anand parameters were calculated for each set of aging conditions, and the effects of aging on the nine Anand model parameters were determined.

Mechanical tests have been performed using both water quenched (WQ) and reflowed (RF) SAC305 samples (two unique specimen microstructures). In the case of the water quenched samples, there is rapid microstructural transitioning during the brief time that occurs between placing molten solder into the glass tubes and immersing the tubes in water bath. On the other hand, the reflowed samples are first cooled by water quenching, and then sent through a reflow oven to re-melt the solder in the tubes and subject them to a desired temperature profile matching that used in PCB assembly.

From the experimental results, the differences between the extracted Anand model parameters of water quenched and reflowed samples were high for samples with no prior aging. As expected, the water quenched samples had much higher mechanical properties (stiffness and strength) than reflowed samples prior to aging. For both the water quenched and reflowed specimens, significant degradation of the mechanical

properties was observed with aging. The variations of the Anand model parameters with aging time have been characterized, and empirical relationships were established to model the observed changes. After long aging times, the water quenched and reflowed SAC305 materials were found to exhibit similar mechanical properties, and thus their Anand parameters converged and became nearly identical. These works has been published in the references [150-151].

CHAPTER 5

EFFECTS OF SILVER CONTENT ON THE ANAND CONSTITUTIVE MODEL FOR SAC LEAD FREE SOLDER

5.1 Introduction

As discussed in the Chapter 1, the electronic packaging industry has transitioned to Pb-free solders due to environmental concerns. Among the diversity of Pb-free solders, the Sn-Ag-Cu (SAC) alloys have become the most popular and are often considered to be the standard lead-free alloys. NEMI (National Electronics Manufacturing Initiative) recommended to replace Sn-Pb solders by eutectic Sn-Ag-Cu solder in reflow processing and eutectic Sn-Cu solder in wave soldering [152]. Depending on the percentage of silver (Ag), there are several types of SAC alloys available in the market. Solder joint fatigue life under thermal cycling has been shown to increase with increasing Ag content in the SAC solders joints, due to improved mechanical properties and increased fatigue resistance [153]. However, the drop performance of electronic assemblies with SAC Pb-free solder joints is often reduced when increasing the Ag content in the SAC solder [154]. Low silver content solders are increasingly used in electronic assembly for handheld electronic products to improve the drop performance of the solder joints and to lower costs. Hence, there are trade-offs based on the silver content, and no one SAC alloy is typically suitable for all applications.

In the Chapter 4 the effects of aging and solidification profile effect on the material properties and Anand model were explored. In this chapter, basically the effects

of silver content on the material properties and Anand model have been investigated. There are several publications listing values of Anand parameters for particular solder alloys. For example, Anand parameters for alloys such as Sn-3.5Ag, SAC105, SAC305, and SAC387 have been documented [78, 130, 133,135, 155-156]. However, there has been no systematic study by a single group on how the Anand parameters for SAC alloys vary with the percentage of Ag in the alloy. As discussed above, the silver content of a SAC alloy has been shown to be critical in optimizing thermal cycling and drop reliability of lead free electronics.

In this work, it was performed an investigation on the Anand constitutive model and its application to SAC solders of various Ag contents (i.e. SACN05, with N = 1, 2, 3, 4). For each alloy, both water quenched (WQ) and reflowed (RF) solidification profiles were utilized to establish two unique specimen microstructures, and the same reflow profile was used for all four of the SAC alloys so that the results could be compared and the effects of Ag content could be studied systematically.

The nine Anand parameters were determined for each unique solder alloy and microstructure from a set of stress-strain tests performed at several strain rates and temperatures. Testing conditions included strain rates of 0.001, 0.0001, and 0.00001 (sec^{-1}), and temperatures of 25, 50, 75, 100, and 125 ^{o}C. The Anand parameters were calculated from each set of stress-strain data using an established procedure that is described in detail in the paper. Using the calculated results for the various SAC alloys and microstructures, a set of empirical models have been established to describe the effects of SAC alloy Ag content on the Anand model parameters. After deriving the Anand parameters for each alloy, the stress-strain curves have been calculated for various

conditions, and excellent agreement was found between the predicted results and experimental stress-strain curves.

5.2 Test Matrix

The solder alloy test matrix is shown in Table 5.1. The SAC solder alloys investigated in this work include 98.5Sn1.0Ag0.5Cu (SAC105), 97.5Sn2.0Ag0.5Cu (SAC205), 96.5Sn3.0Ag0.5Cu (SAC305), and 95.5Sn4.0Ag0.5Cu (SAC405). Stress-strain tests on the SACN05 (N = 1, 2, 3, 4) lead free solder samples were performed for samples prepared by both water quenched and reflow cooling profiles. For each SACN05 alloy and microstructure (cooling profile), stress-strain experiments were performed at five temperatures (T = 25, 50, 75, 100, and 125 ^{o}C), and three strain rates ($\dot{\varepsilon}$ = .001, .0001, and .00001 sec^{-1}) as indicated in Table 5.2. Using the measured stress-strain data and calculation procedure presented above, the nine Anand model parameters have been determined for the SACN05 alloys in Table 5.1.

	SACN05			
	SAC105	SAC205	SAC305	SAC405
RF	√	√	√	√
WQ	√	√	√	√

Table 5.1 SAC Solder Test Matrix

Temp. (C)	Reflow (RF)			Water Quenched (WQ)		
	10^{-3}/s	10^{-4}/s	10^{-5}/s	10^{-3}/s	10^{-4}/s	10^{-5}/s
25	√	√	√	√	√	√
50	√	√	√	√	√	√
75	√	√	√	√	√	√
100	√	√	√	√	√	√
125	√	√	√	√	√	√

Table 5.2 Text Matrix for a Particular SACN05 Alloy

5.3 Effects of Silver Content on the Mechanical Properties

The recorded stress-strain curves for the four SACN05 alloys and a strain rate of 0.001 sec^{-1} are shown in Figures 5.1 and 5.2 for the water quenched and reflowed cooling profiles, respectively. Each curve in these plots is an "average" stress-strain curve representing the fit to the 10 recorded stress-strain curves for a given SAC alloy, strain rate, and temperature. The five colored curves in each graph are the stress-strain results for temperatures of T = 25 (black), 50 (blue), 75 (green), 100 (brown), and 125 ^{o}C (red). As expected, the data for the various SAC alloys all demonstrate a steady decline in the effective elastic modulus, yield stress (YS), and ultimate tensile strength (UTS) with temperature. For example, Figure 5.3 illustrates the variation of mechanical properties (E, YS, UTS) with temperature for the water quenched SACN05 alloys and a strain rate of 0.001 sec^{-1}. The observed degradations have an approximately linear variation with temperature. In addition, the material properties increase dramatically with the percentage of Ag present in the SAC alloy.

Analogous results were found for the material properties of the reflowed alloys at the strain rate of 0.001 sec^{-1}. For example, a comparison of the UTS values for the four SACN05 alloys in bar graph form are shown in Figure 5.4 for the water quenched and reflowed microstructures. From these plots, it is clear that the largest percentage changes in strength occur between SAC105 and SAC205. For example, the UTS (WQ) values at T = 25 C for SAC105, SAC205, SAC305, and SAC405 are 47.2 MPa, 65.0 MPa, 74.1 MPa, and 81.7 MPa, respectively. In this case, the strength of SAC205 is 38% higher than that for SAC105, while SAC305 and SAC405 show additional increases of 14% and 10.2%, respectively. The Ag content affects the size and density of the Ag_3Sn

intermetallic compound (IMC) precipitates. Increasing the Ag content of the solder causes it to exhibit higher strength and fatigue resistance because of precipitate strengthening [157].

The corresponding experimental stress-strain curves for the four SACN05 alloys at the other two strain rates of 0.0001 sec^{-1} and 0.00001 sec^{-1} are shown in Figures 5.5-5.6 (water quenched) and Figures 5.7-5.8 (reflowed). Analogous trends were observed for the material property variations with temperature and alloy composition (silver content).

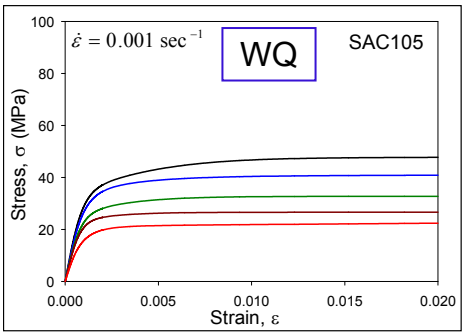

(a) SAC105 [No Aging, Water Quenched]

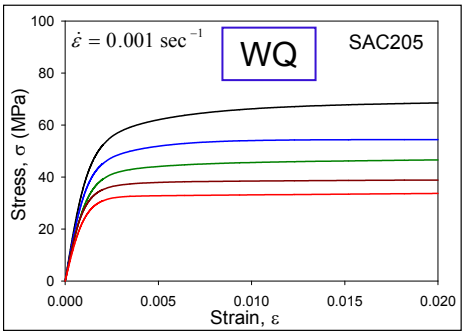

(b) SAC205 [No Aging, Water Quenched]

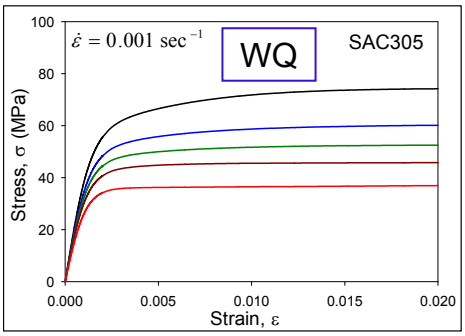

(c) SAC305 [No Aging, Water Quenched]

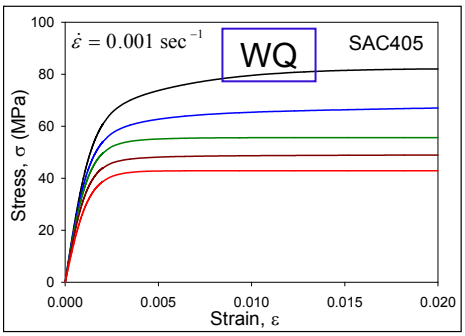

(d) SAC405 [No Aging, Water Quenched]

Figure 5.1 Stress-Strain Curves of SAC Alloys for Strain Rate of $\dot{\varepsilon} = 0.001\ \text{sec}^{-1}$ [No Aging, Water Quenched]

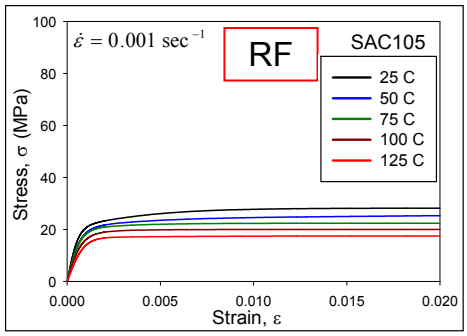

(a) SAC105 [No Aging, Reflowed]

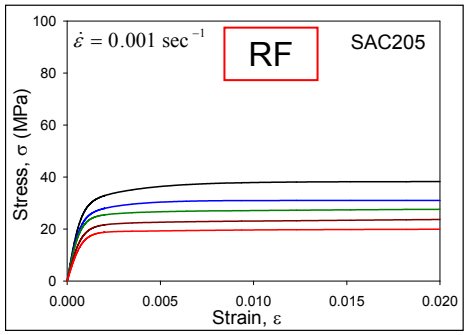

(b) SAC205 [No Aging, Reflowed]

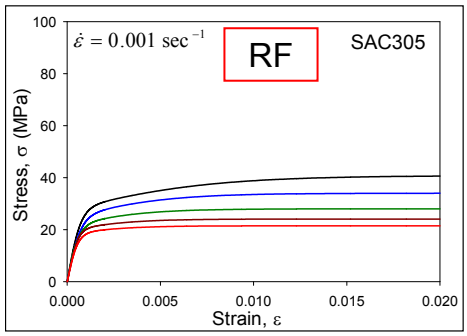

(c) SAC305 [No Aging, Reflowed]

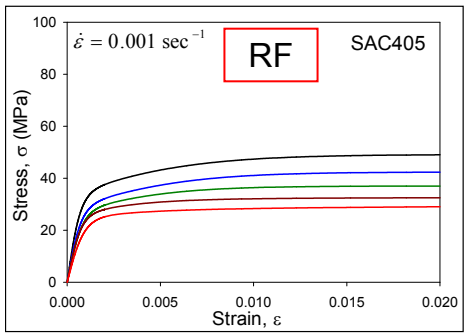

(d) SAC405 [No Aging, Reflowed]

Figure 5.2 Stress-Strain Curves of SAC Alloys for Strain Rate of $\dot{\varepsilon} = 0.001\ \text{sec}^{-1}$ [No Aging, Reflowed]

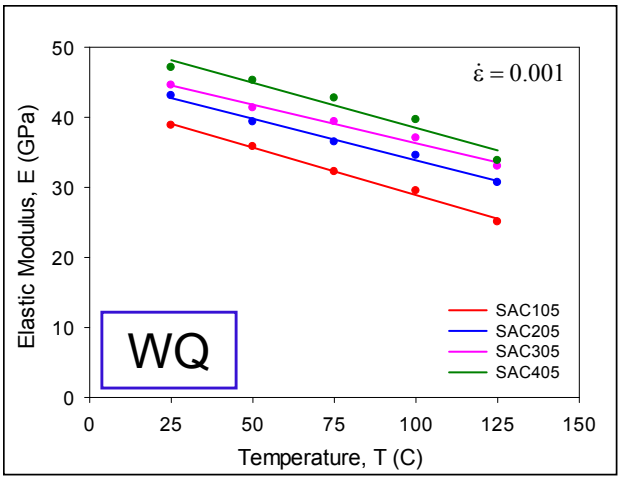

(a) Elastic Modulus

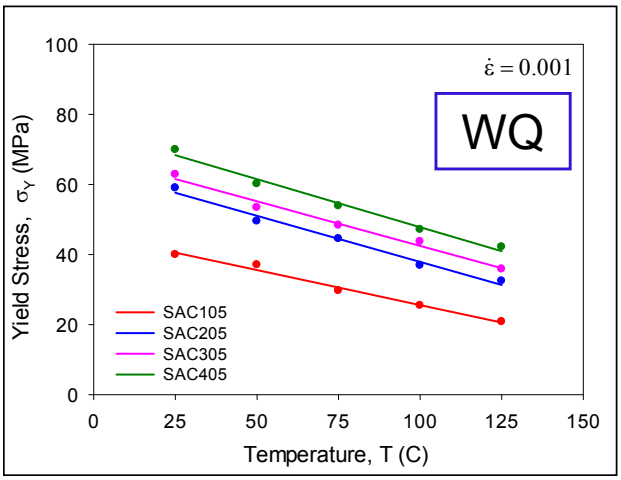

(b) Yield Strength

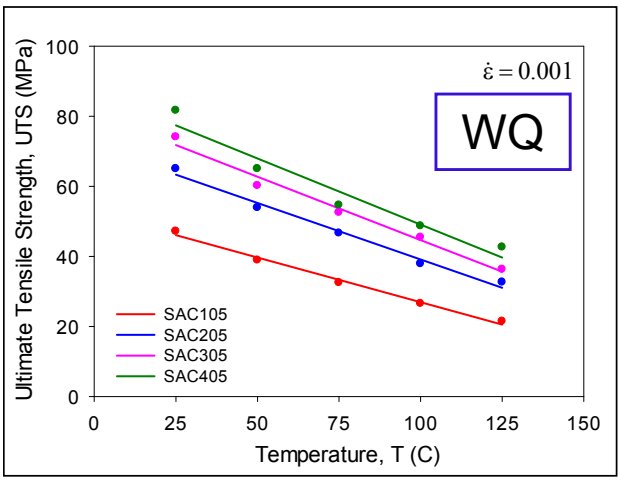

(c) Ultimate Strength

Figure 5.3 Variation of Mechanical Properties with Temperature [Water Quenched]

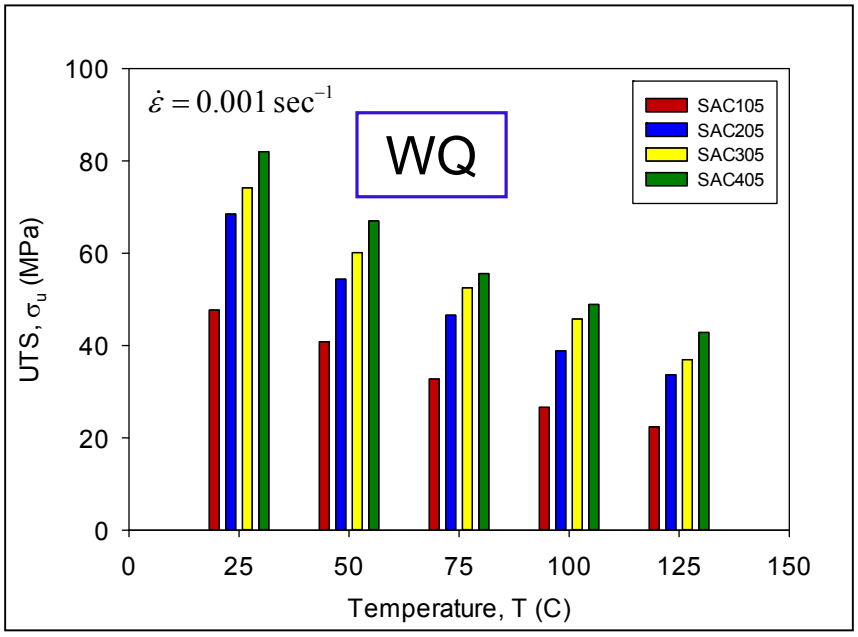

(a) Water Quenched (WQ)

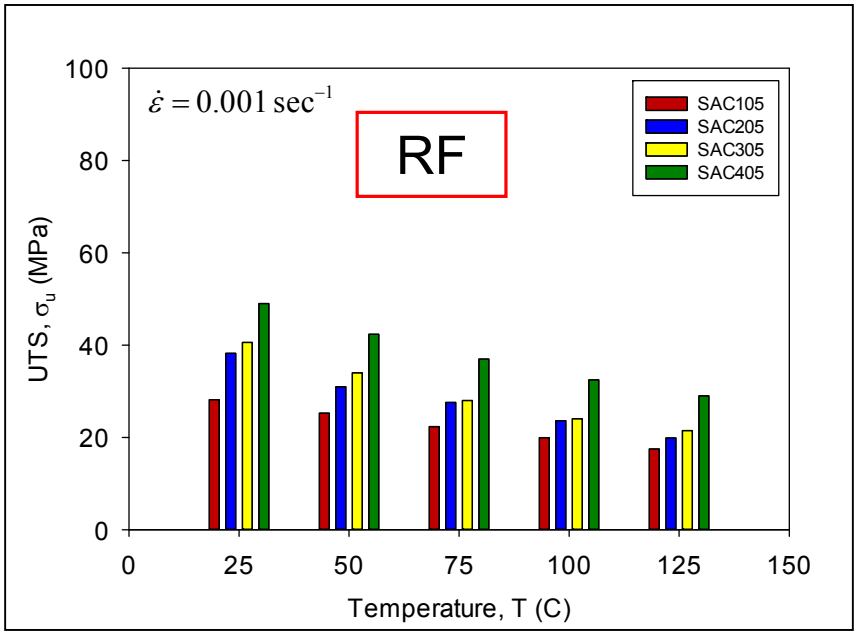

(b) Reflowed (RF)

Figure 5.4 Ultimate Strength Variation for SACN05 Alloys [No Aging]

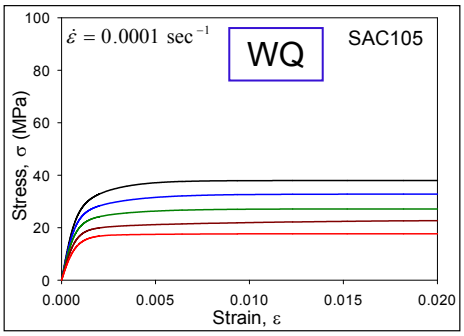

(a) SAC105 [No Aging, Water Quenched]

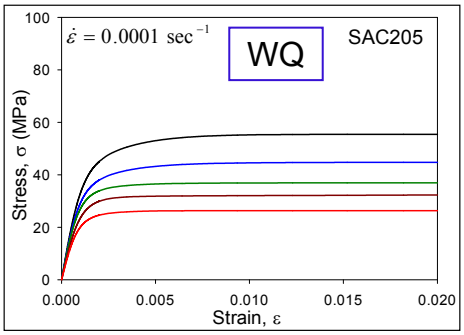

(b) SAC205 [No Aging, Water Quenched]

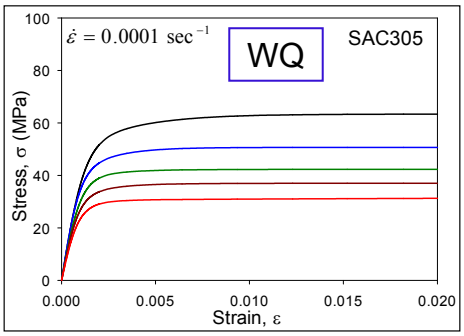

(c) SAC305 [No Aging, Water Quenched]

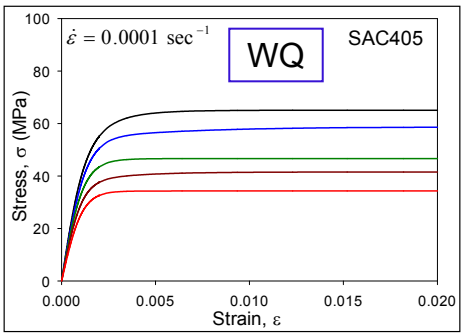

(d) SAC405 [No Aging, Water Quenched]

Figure 5.5 Stress-Strain Curves of SAC Alloys for Strain Rate of $\dot{\varepsilon}$ = 0.0001 sec^{-1} [No Aging, Water Quenched]

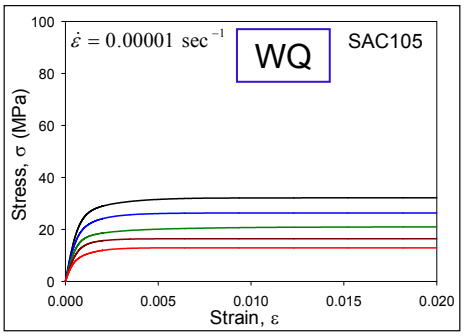

(a) SAC105 [No Aging, Water Quenched]

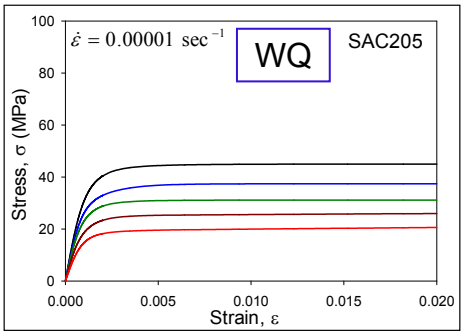

(b) SAC205 [No Aging, Water Quenched]

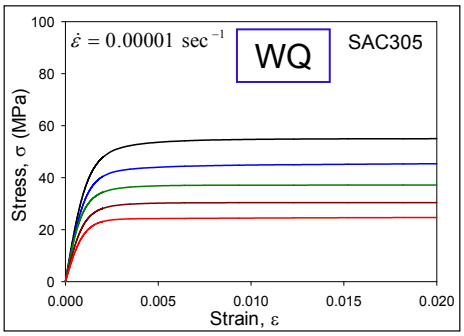

(c) SAC305 [No Aging, Water Quenched]

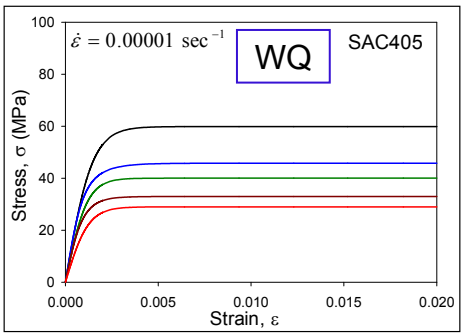

(d) SAC405 [No Aging, Water Quenched]

Figure 5.6 Stress-Strain Curves of SAC Alloys for Strain Rate of $\dot{\varepsilon} = 0.00001\ \text{sec}^{-1}$ [No Aging, Water Quenched]

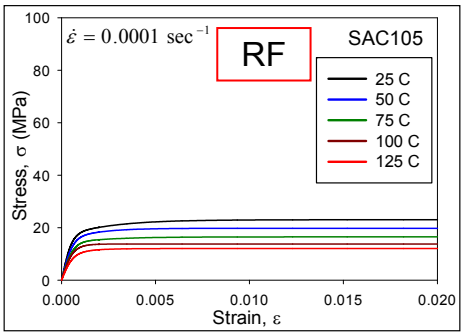

(a) SAC105 [No Aging, Reflowed]

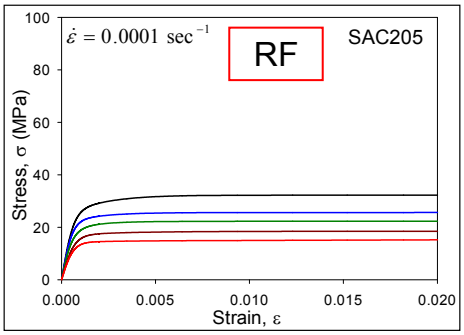

(b) SAC205 [No Aging, Reflowed]

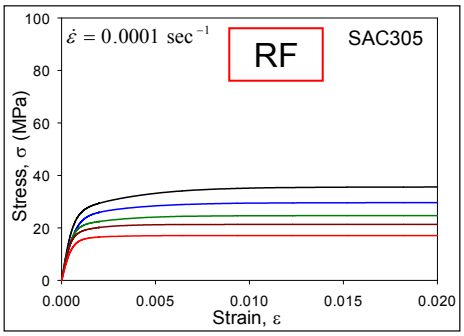

(c) SAC305 [No Aging, Reflowed]

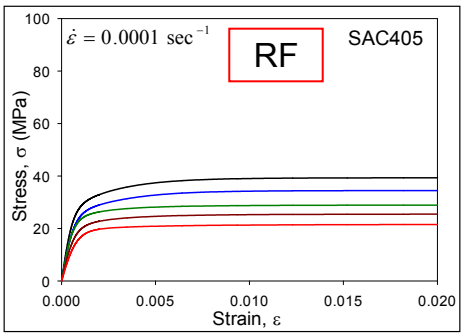

(d) SAC405 [No Aging, Reflowed]

Figure 5.7 Stress-Strain Curves of SAC Alloys for Strain Rate of $\dot{\varepsilon}$ = 0.0001 sec^{-1} [No Aging, Reflowed]

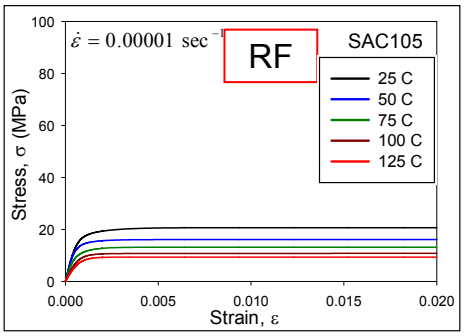

(a) SAC105 [No Aging, Reflowed]

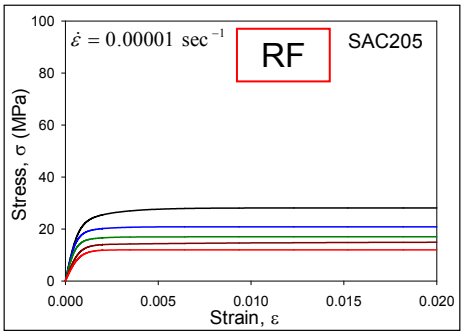

(b) SAC205 [No Aging, Reflowed]

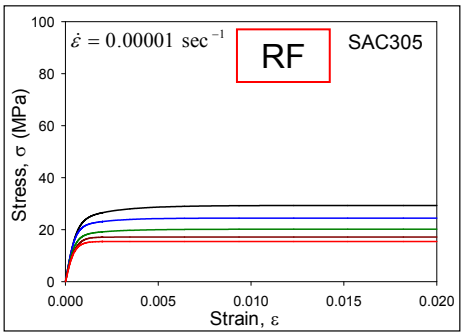

(c) SAC305 [No Aging, Reflowed]

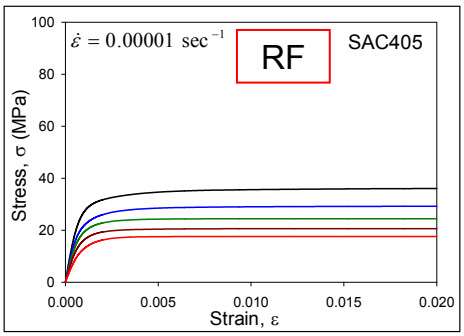

(d) SAC405 [No Aging, Reflowed]

Figure 5.8 Stress-Strain Curves of SAC Alloys for Strain Rate of $\dot{\varepsilon} = 0.00001\ \text{sec}^{-1}$ [No Aging, Reflowed]

5.4 Effects of Silver Content on the Anand Material Parameters

The Anand model parameters for each SACN05 (SAC105, SAC205, SAC305 and SAC405) lead free solder material have been determined from the strain rate and temperature dependent stress-strain data shown in Figures 5.1-5.2 and 5.5-5.8. These calculations have been performed for both the water quenched and reflowed solder solidification profiles. Saturation stress (UTS) values at the various strain rates and temperatures were first extracted from the stress-strain data for each SAC alloy and solidification profile. In addition, stress vs. plastic strain data for each SAC alloy and cooling profile were found at several strain rates and temperatures. From these extracted results, the nine Anand parameters for each alloy and cooling profile were found using the nonlinear regression analysis procedure discussed in section 3.5. The calculated Anand parameters for SAC105, SAC205, SAC305, and SAC405 are tabulated in Table 5.3 and Table 5.4 for water quenched and reflowed samples, respectively.

Anand Parameters	Units	SAC105	SAC205	SAC305	SAC405
s_o	MPa	16.7	27.9	32.2	34.35
Q/R	1/K	8846	9080	9320	9560
A	sec^{-1}	5500	3200	2800	2650
ξ	-	4	4	4	4
m	-	0.25	0.28	0.29	0.3
h_o	MPa	142,000	174,000	186,000	192,000
$\hat{s}$	MPa	38.15	43.00	44.67	45.51
n	-	0.0100	0.0115	0.0120	0.0123
a	-	1.85	1.75	1.72	1.70

Table 5.3 Anand Model Parameters for SACN05 [No Aging, Water Quenched]

Anand Parameters	Units	SAC105	SAC205	SAC305	SAC405
s_o	MPa	7.5	16.5	21.0	23.65
Q/R	1/K	8850	9090	9320	9580
A	sec^{-1}	6900	4300	3501	3175
ξ	-	4	4	4	4
m	-	0.215	0.238	0.250	0.263
h_o	MPa	137500	169000	180000	183,000
$\hat{s}$	MPa	25.1	29	30.2	31.3
n	-	0.0062	0.0087	0.0100	0.011
a	-	1.96	1.84	1.78	1.77

Table 5.4 Anand Model Parameters for SACN05 [No Aging, Reflowed]

5.5 Effects of Severe Aging on the Mechanical and Anand Material Parameters

Chapter 4 investigated the effects of isothermal aging on the uniaxial stress-strain behavior of SAC305 lead free solder were explored in detail. Specimens subjected to 9 different sets of aging conditions prior to testing: 0, 1, 5, 20, 60, 120, 180, 270 and 360 days of aging at 100 ^oC. For each aging time and SAC305 alloy microstructure (WQ and RF), stress-strain data were measured at five temperatures (T = 25, 50, 75, 100, and 125 ^oC), and three strain rates ($\dot{\varepsilon}$=.001, .0001, and .00001 sec^{-1}) as indicated in the text matrix of Table 5.2. The measured data demonstrated that the majority of the aging effects occurred in the first 0 to 20 days of aging. For longer aging times, much slower changes in the response and mechanical properties occurred.

To investigate the range of aging effects for the other SACN05 alloys, it has been performed tensile testing on reflowed specimens subjected to 180 Days of aging at 100 ^oC. After this level of aging, any further changes in the mechanical response and properties will be rather small. Reflowed samples were chosen since they have coarser initial microstructure and lower mechanical properties than the WQ samples. Thus, the

results for these tests can be regarded as approaching the highest level of mechanical behavior degradation possible for a "severely aged" lead free solder material.

The stress-strain curves for SAC105, SAC205, and SAC305 for 180 days prior aging condition have been presented in the Figures 5.9-5.11. As expected, aging causes large degradations in the material properties (elastic modulus, yield stress, and UTS) of SAC solders (SACN05). The changes in UTS (maximum/saturation stress) with aging are especially evident from each of the 3 plots in Figures 5.12-5.14. It can also be seen that the UTS drops to about 50% due to this 180 days of aging at 100 ^{o}C.

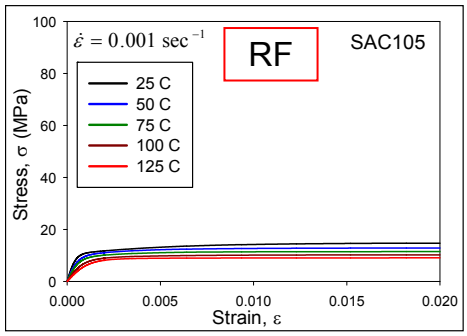

(a) SAC105 [180 Days Aging, Reflowed]

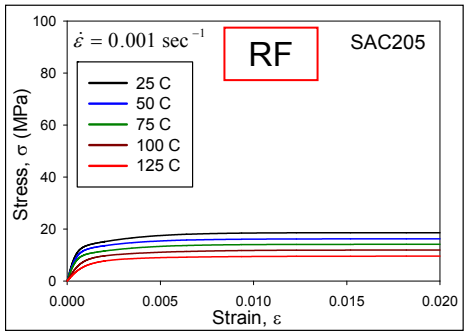

(b) SAC205 [180 Days Aging, Reflowed]

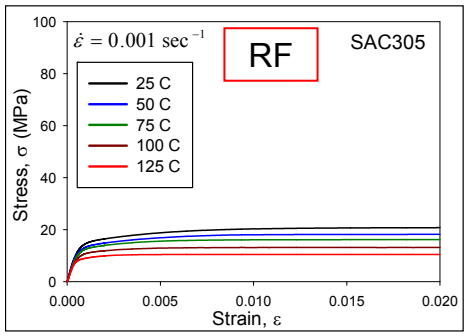

(c) SAC305 [180 Days Aging, Reflowed]

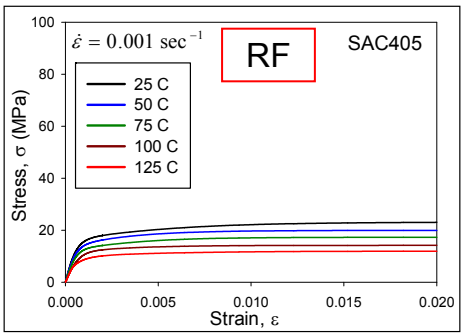

(d) SAC405 [180 Days Aging, Reflowed]

Figure 5.9 Stress-Strain Curves of SAC Alloys for Strain Rate of $\dot{\varepsilon} = 0.001\ \text{sec}^{-1}$ [180 Days Aging, Reflowed]

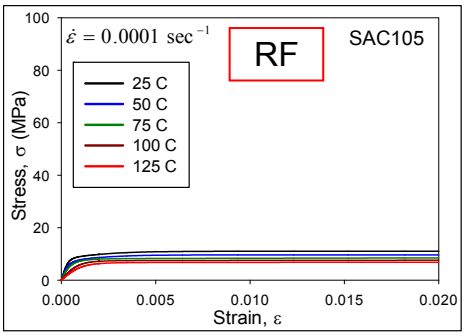

(a) SAC105 [180 Days Aging, Reflowed]

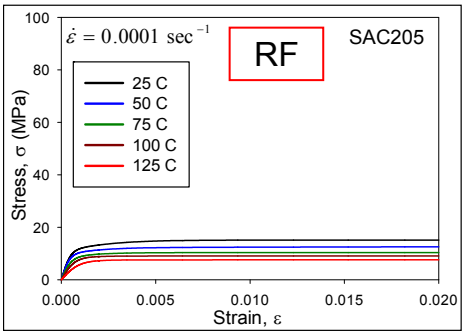

(b) SAC205 [180 Days Aging, Reflowed]

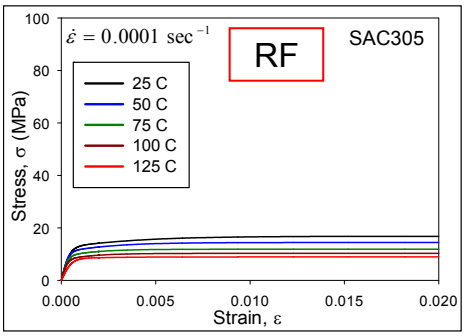

(c) SAC305 [180 Days Aging, Reflowed]

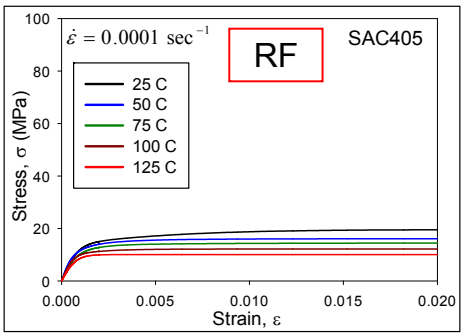

(d) SAC405 [180 Days Aging, Reflowed]

Figure 5.10 Stress-Strain Curves of SAC Alloys for Strain Rate of $\dot{\varepsilon}$ = 0.0001 sec^{-1} [180 Days Aging, Reflowed]

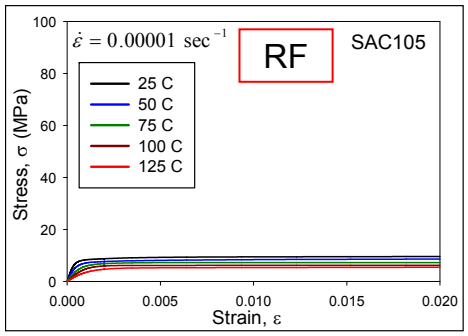

(a) SAC105 [180 Days Aging, Reflowed]

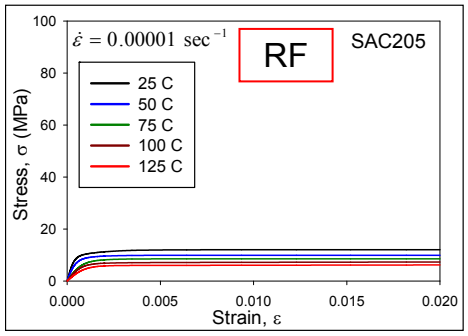

(b) SAC205 [180 Days Aging, Reflowed]

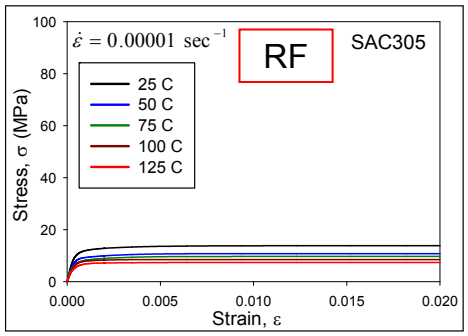

(c) SAC305 [180 Days Aging, Reflowed]

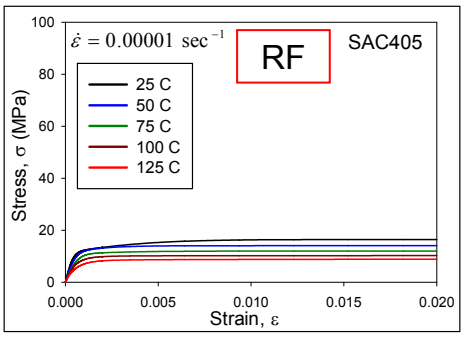

(d) SAC405 [180 Days Aging, Reflowed]

Figure 5.11 Stress-Strain Curves of SAC Alloys for Strain Rate of $\dot{\varepsilon} = 0.00001\ \text{sec}^{-1}$ [180 Days Aging, Reflowed]

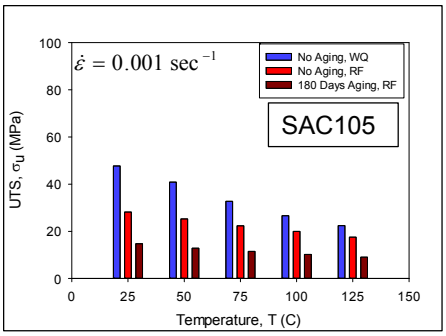

(a) SAC105

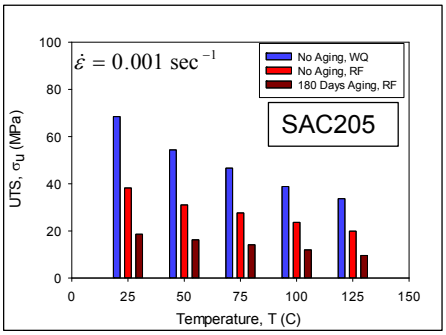

(b) SAC205

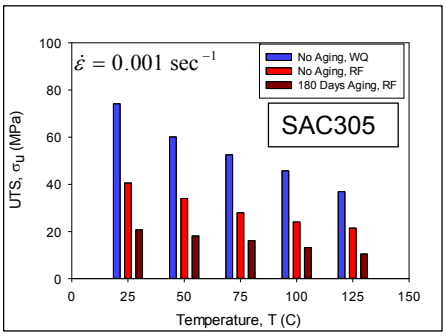

(c) SAC305

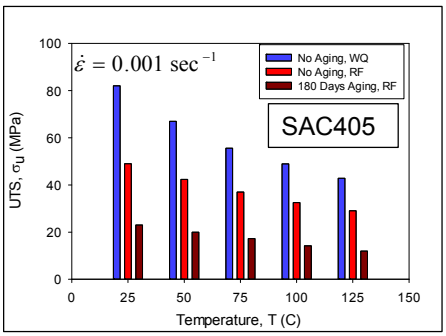

(d) SAC405

Figure 5.12 Effects of Severe Aging on the Strength of SACN05 Testing at Strain Rate of 0.001 sec^{-1}

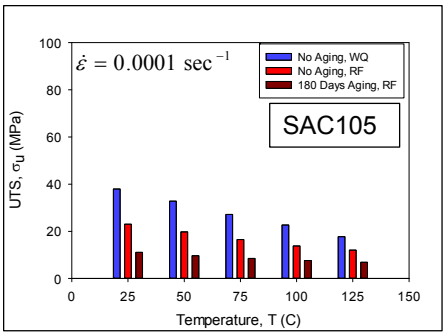

(a) SAC105

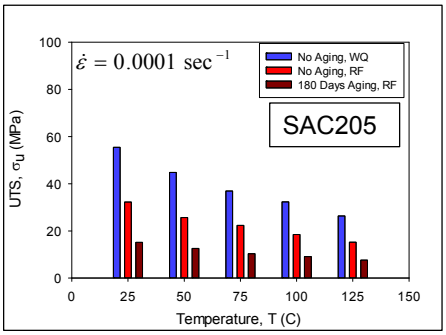

(b) SAC205

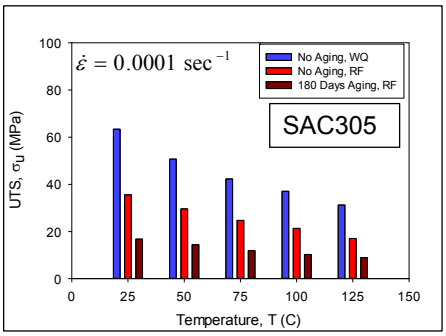

(c) SAC305

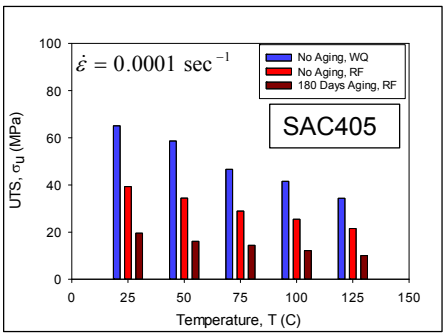

(d) SAC405

Figure 5.13 Effects of Severe Aging on the Strength of SACN05 Testing at Strain Rate of 0.0001 sec^{-1}

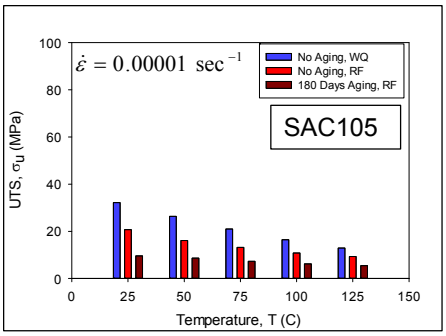

(a) SAC105

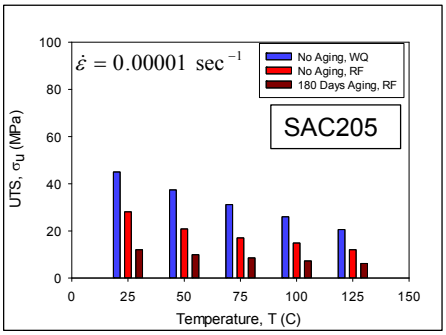

(b) SAC205

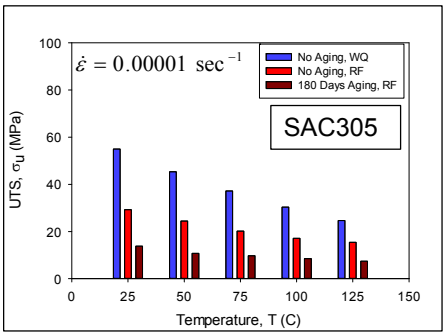

(c) SAC305

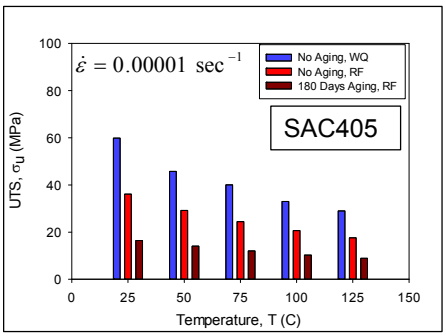

(d) SAC405

Figure 5.14 Effects of Severe Aging on the Strength of SACN05 Testing at Strain Rate of 0.00001 sec^{-1}

5.6 Effects of Silver Content and Severe Aging on Anand Material Parameters

The Anand model parameters for each SACN05 (SAC105, SAC205, SAC305 and SAC405) lead free solder material have been determined from the strain rate and temperature dependent stress-strain data shown in Figures 5.1-5.2 and 5.5-5.11. These calculations have been performed for both the water quenched and reflowed solder solidification profiles, as well as the reflowed profile with severe aging. These material configurations represent the extreme limits of microstructure possible in SAC materials. Saturation stress (UTS) values at the various strain rates and temperatures were first extracted from the stress-strain data for each SAC alloy, solidification profile, and aging condition. In addition, stress vs. plastic strain data for each SAC alloy were found at several strain rates and temperatures. From these extracted results, the nine Anand parameters for each alloy and cooling profile were found using the nonlinear regression analysis procedure discussed above. The calculated Anand parameters for SAC105, SAC205, SAC305, and SAC405 alloys with various microstructures are tabulated in Table 5.3 and 5.4. To visualize the effects of solidification profile and severe aging on the material behavior of the various SACN05 alloys, the Anand parameters have been plotted as a function of silver content (%) for each of the three microstructures (WQ, RF, RF+Aging) as shown in Figure 5.15. Empirical models have been used to fit the data points at integer values of the silver content, and provide estimates for the Anand parameters for other alloys with non-integer silver content percentages.

The results in Figure 5.15 illustrate the range of values possible for Anand parameters for the SACN05 alloys. The blue curves represent the water quenched limit, where the materials have extremely fine microstructures and high mechanical properties.

The brown curves represent the severely aged limit, where the materials have extremely coarsened microstructures and highly degraded mechanical properties. While further degradations are certainly possible with even further aging, the limiting values found for a severely aged SAC alloy can be used by designers as a conservative set of constitutive parameters representing the lower end of the material properties for that alloy.

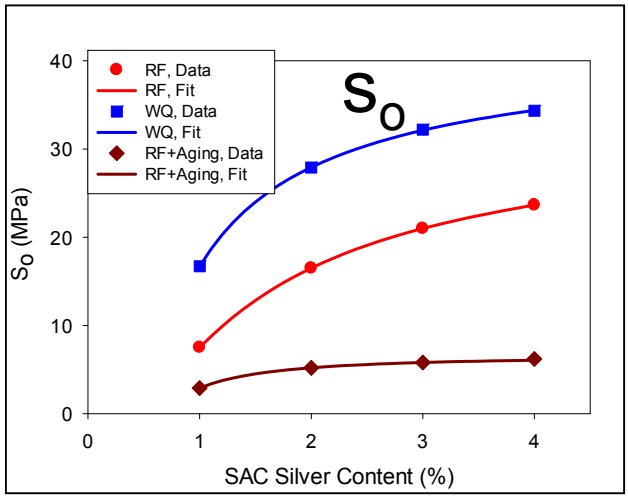

(a)

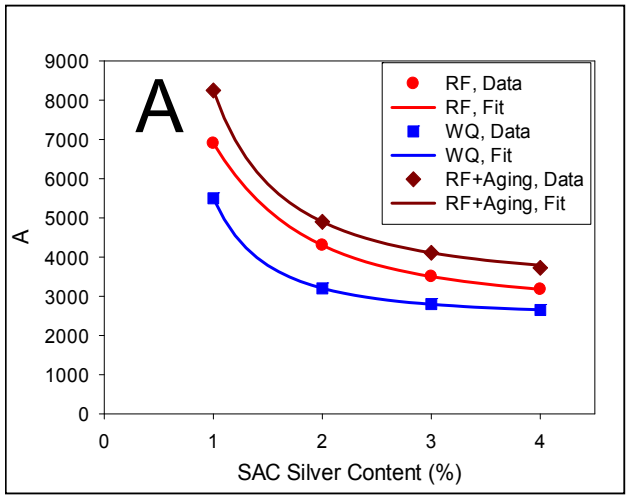

(b)

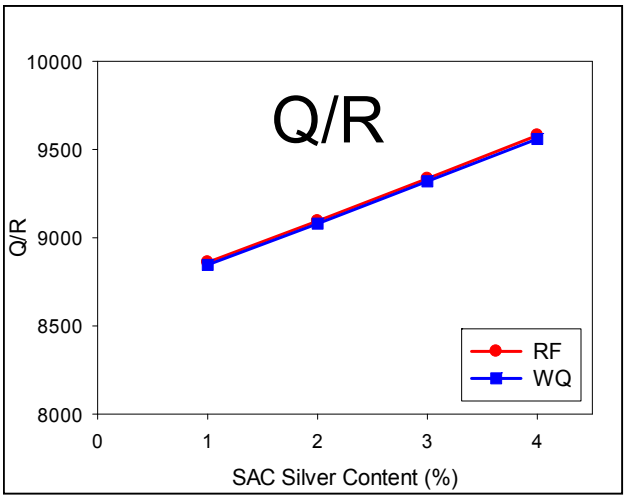
Q/R
10000
9500
9000
8500
8000
Q/R
0
1
2
3
4
SAC Silver Content (%)
RF
WQ

(c)

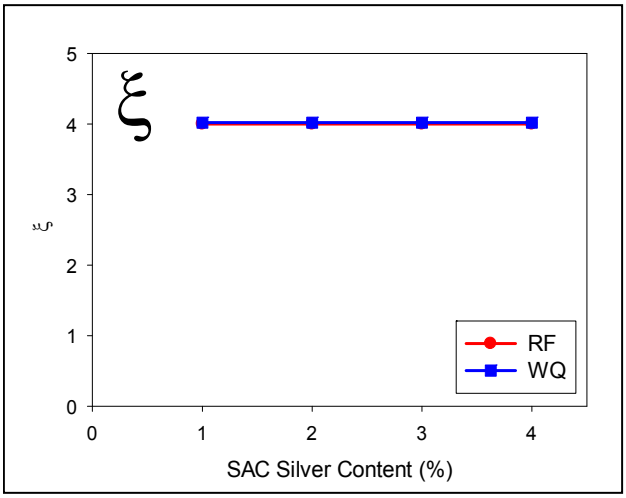
ξ
5
4
3
2
1
0
ξ
0
1
2
3
4
SAC Silver Content (%)
RF
WQ

(d)

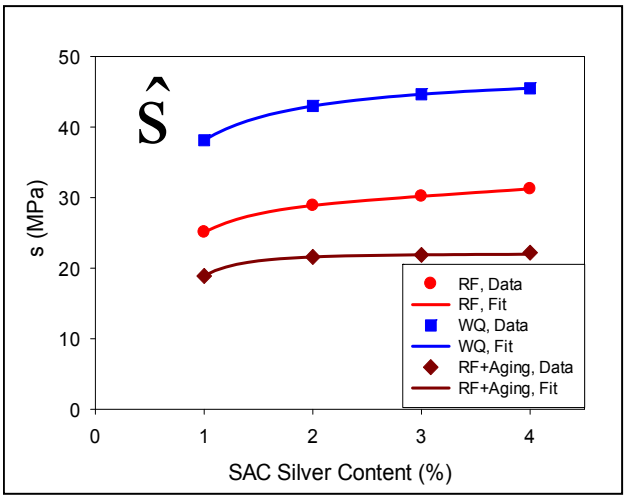
Ŝ
50
40
30
20
10
0
s (MPa)
0
1
2
3
4
SAC Silver Content (%)
RF, Data
RF, Fit
WQ, Data
WQ, Fit
RF+Aging, Data
RF+Aging, Fit

(e)

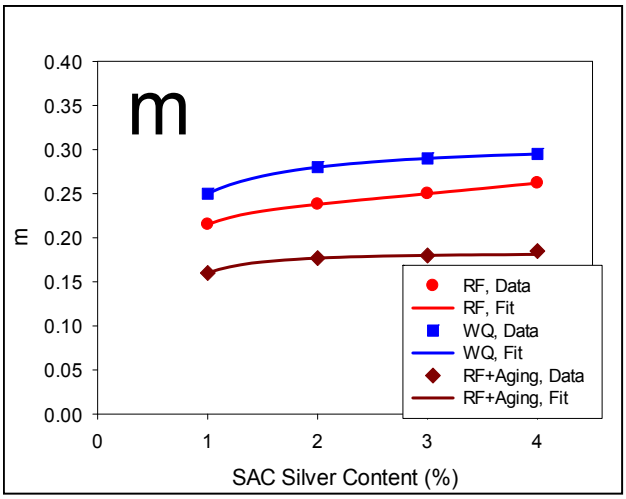
m
m
0.40
0.35
0.30
0.25
0.20
0.15
0.10
0.05
0.00
0
1
2
3
4
SAC Silver Content (%)
RF, Data
RF, Fit
WQ, Data
WQ, Fit
RF+Aging, Data
RF+Aging, Fit

(f)

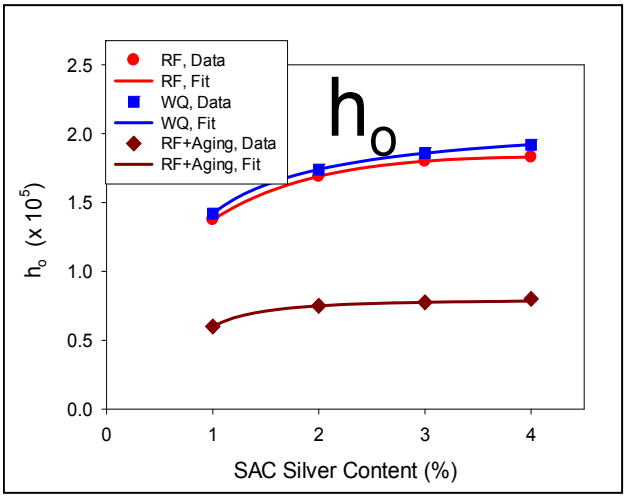
h_o
h_o (x 10^5)
2.5
2.0
1.5
1.0
0.5
0.0
0
1
2
3
4
SAC Silver Content (%)
RF, Data
RF, Fit
WQ, Data
WQ, Fit
RF+Aging, Data
RF+Aging, Fit

(g)

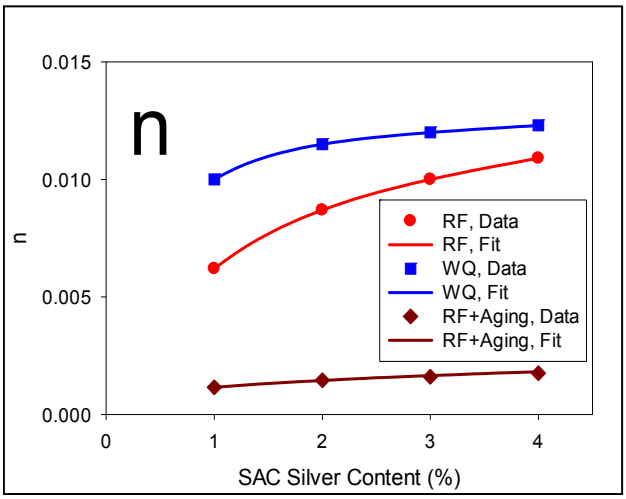
n
n
0.015
0.010
0.005
0.000
0
1
2
3
4
SAC Silver Content (%)
RF, Data
RF, Fit
WQ, Data
WQ, Fit
RF+Aging, Data
RF+Aging, Fit

(h)

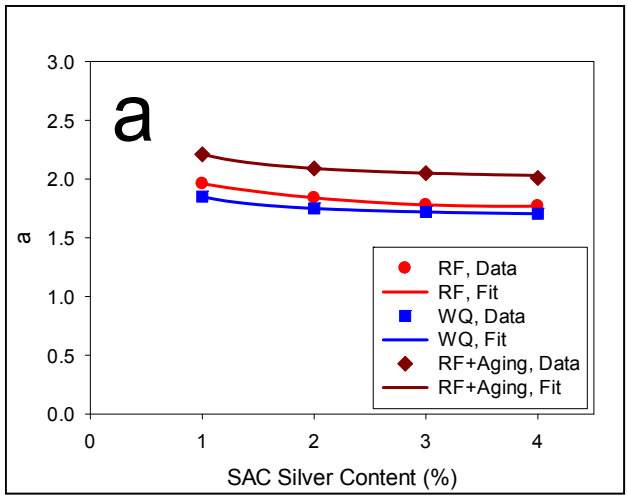

(i)

Figure 5.15 Variations of the Anand Model Parameters with Silver Content

5.7 Calculated and Experimental Stress-Strain Curves

For different SACN05 alloys, it was calculated the stress (σ) vs. plastic strain (ε_p) data of each aging condition by using Eq. (3.13) and the Anand model parameters shown in the Figures 5.15. These results can then be converted to stress (σ) vs. total strain curve (ε) by adding the elastic strain to the plastic strain:

$$\varepsilon = \varepsilon_e + \varepsilon_p \qquad \varepsilon_e = \frac{\sigma}{E} \tag{5.1}$$

where E is the initial elastic modulus of the SAC alloy at the selected strain rate and temperature.

After calculating all the stress-strain curves, here it has been shown some example to demonstrate the correlation between the calculated and experimental curves.

In Figure 5.16-5.22 illustrates the correlations between the model predictions and the experimental stress-strain curves for the water quenched and reflowed SAC105, SAC205, SAC305, and SAC405 alloy for no aging condition. In the case of water

quenched, and reflowed the Anand model constants in Table 5.3, and Table 5.4, respectively were utilized. The experimental curves were those shown earlier in Figure 5.1-5.2, and 5.5-5.8. Good correlations are obtained, with the Anand model able to represent the stress-strain curves accurately over a wide range of temperatures and strain rates. In all cases, the Anand model predictions match the experimental stress-strain curves well for all strain rates and temperatures. Therefore, the updated Anand model parameters can be used to model both aging induced degradation behavior, microstructural and silver content effects on the stress-strain curves.

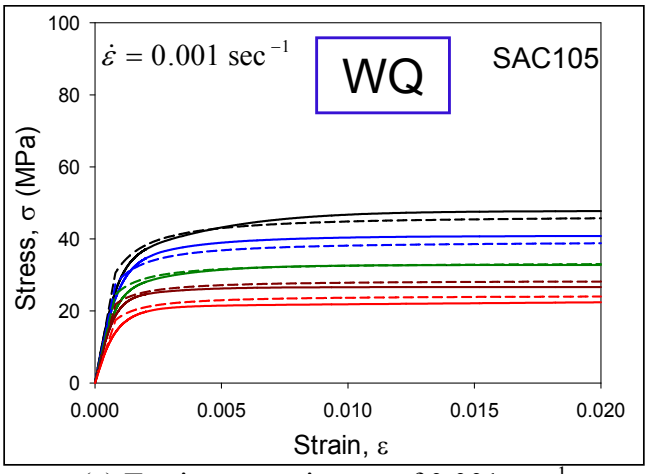

(a) Testing at strain rate of 0.001 sec^{-1}

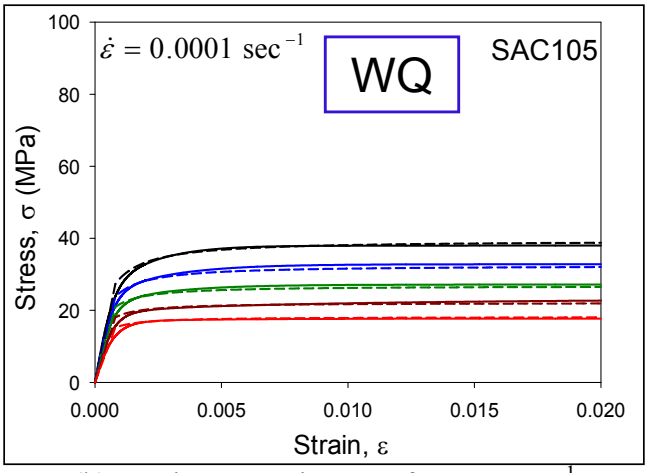

(b) Testing at strain rate of 0.0001 sec^{-1}

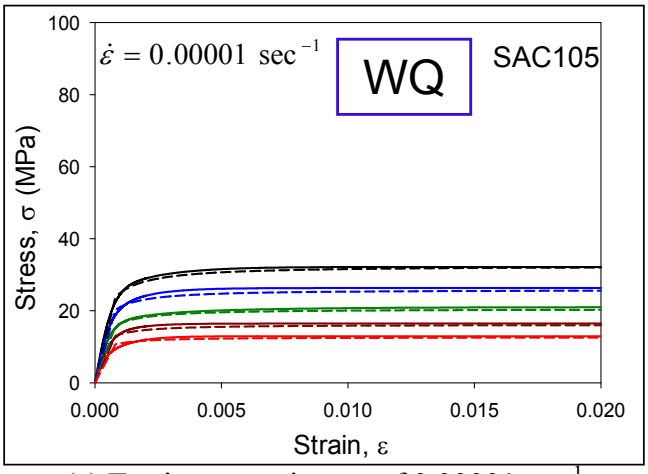

(c) Testing at strain rate of 0.00001 sec^{-1}

Figure 5.16 Correlation of the Calculated and Experimental Stress-Strain Data [SAC105, Water Quenched]

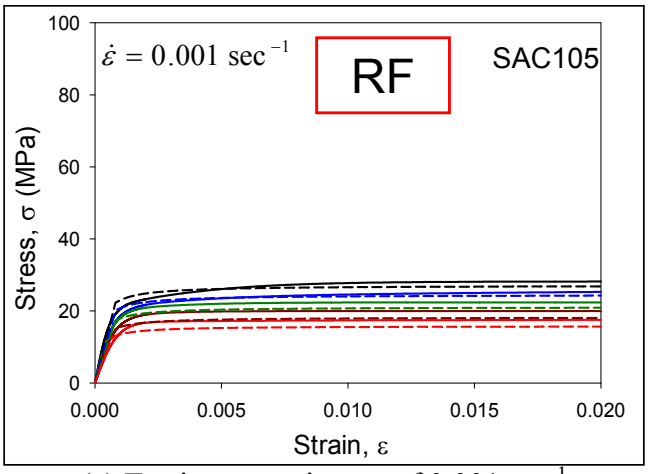

(a) Testing at strain rate of 0.001 sec^{-1}

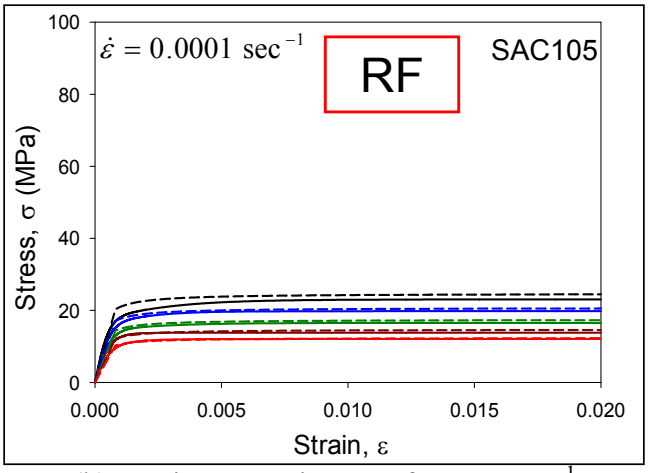

(b) Testing at strain rate of 0.0001 sec^{-1}

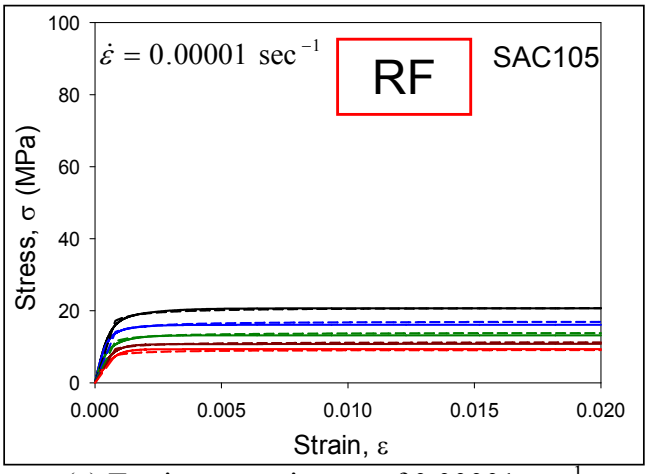

(c) Testing at strain rate of 0.00001 sec^{-1}

Figure 5.17 Correlation of the Calculated and Experimental Stress-Strain Data [SAC105, Reflowed]

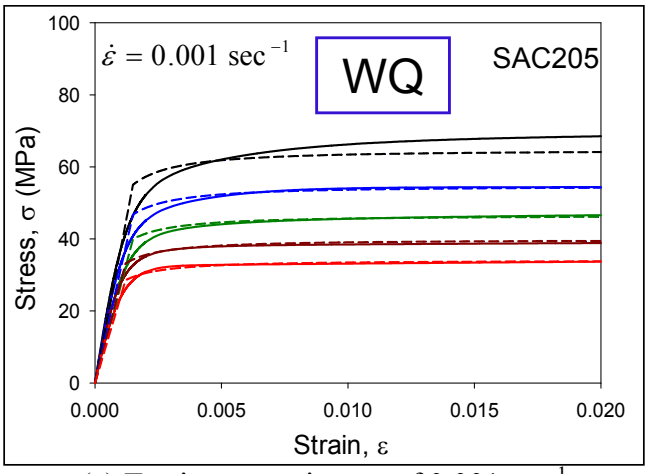

(a) Testing at strain rate of 0.001 sec^{-1}

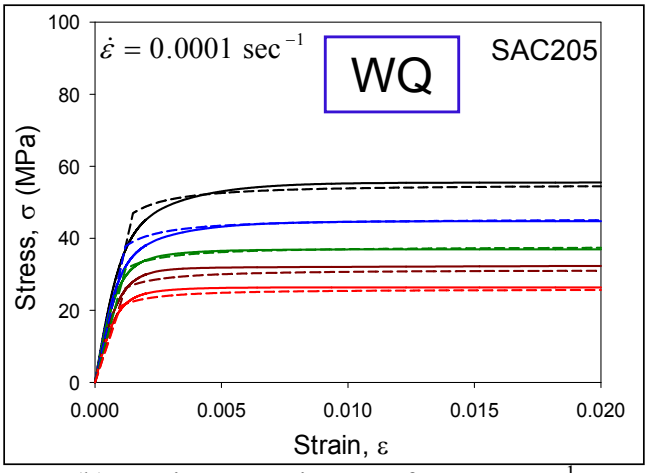

(b) Testing at strain rate of 0.0001 sec^{-1}

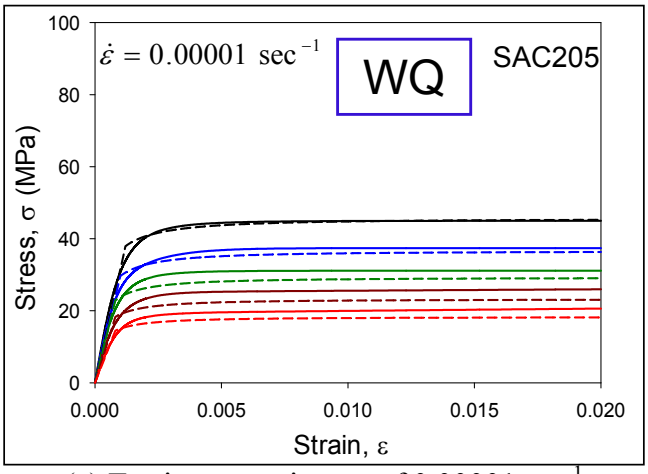

(c) Testing at strain rate of 0.00001 sec^{-1}

Figure 5.18 Correlation of the Calculated and Experimental Stress-Strain Data [SAC205, Water Quenched]

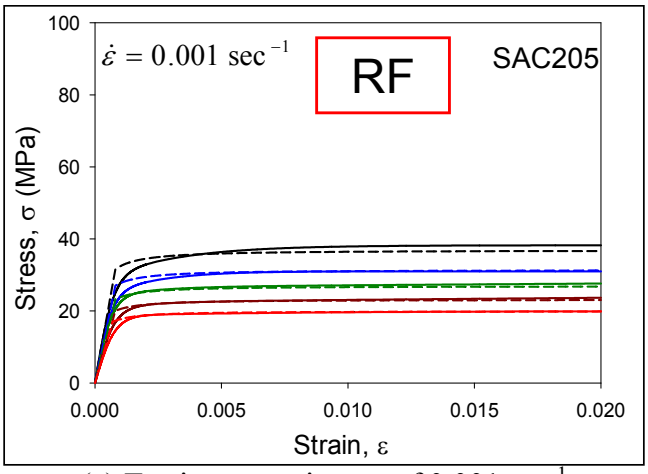

(a) Testing at strain rate of 0.001 sec^{-1}

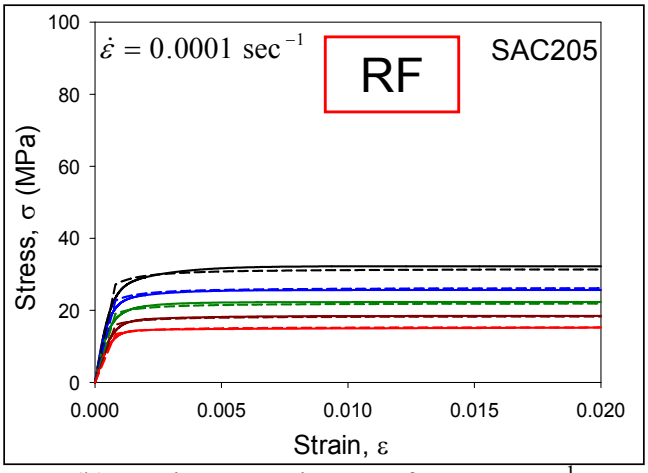

(b) Testing at strain rate of 0.0001 sec^{-1}

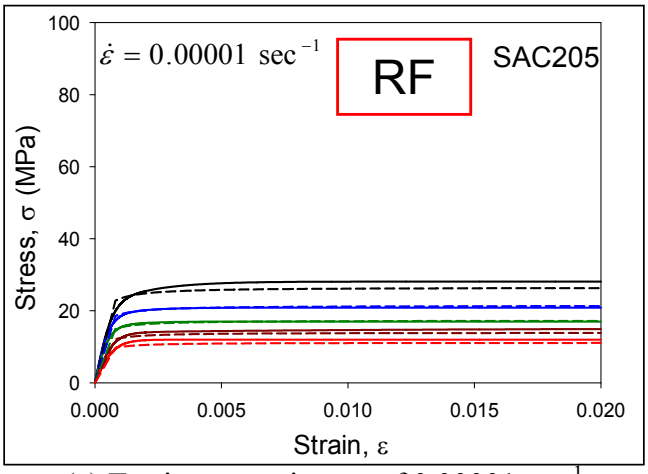

(c) Testing at strain rate of 0.00001 sec^{-1}

Figure 5.19 Correlation of the Calculated and Experimental Stress-Strain Data [SAC205, Reflowed]

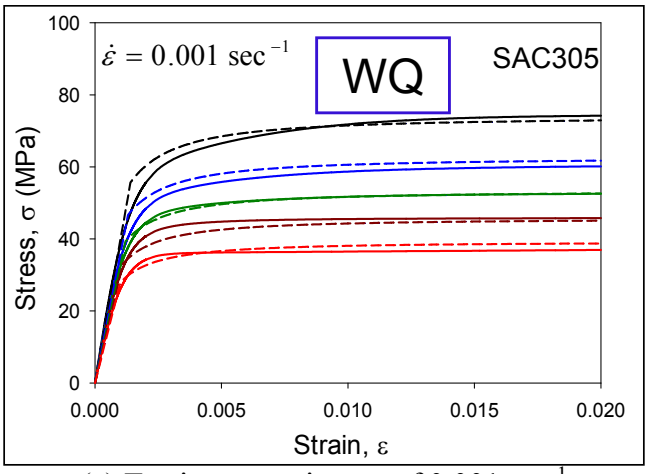

(a) Testing at strain rate of 0.001 sec^{-1}

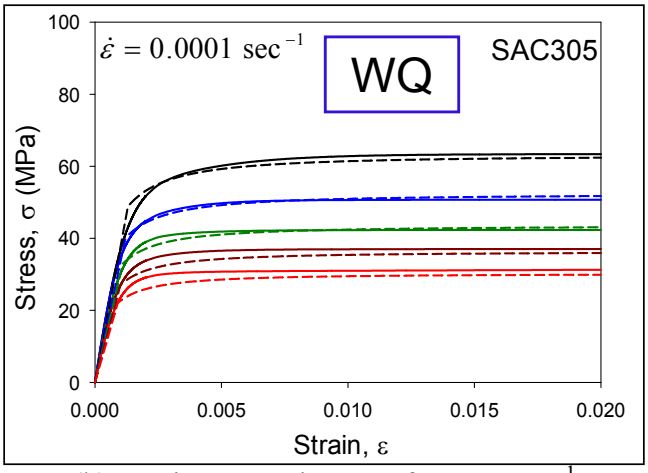

(b) Testing at strain rate of 0.0001 sec^{-1}

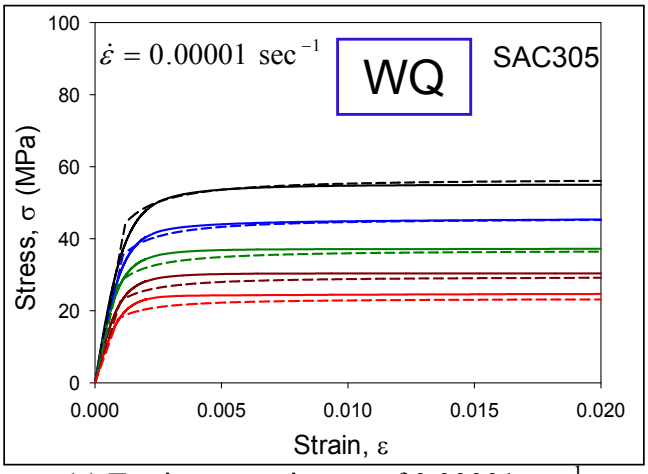

(c) Testing at strain rate of 0.00001 sec^{-1}

Figure 5.20 Correlation of the Calculated and Experimental Stress-Strain Data [SAC305, Water Quenched]

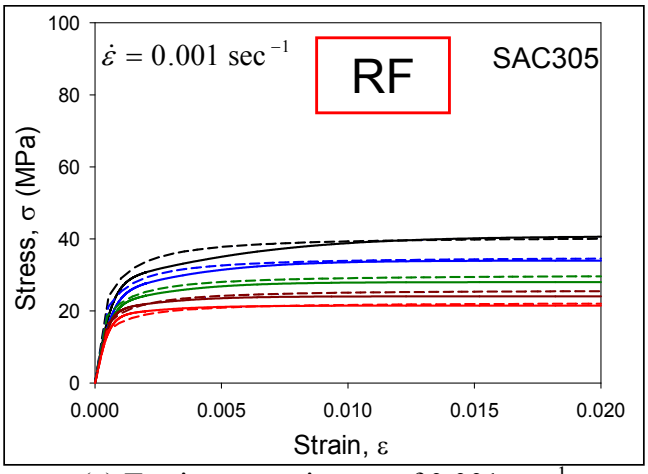

(a) Testing at strain rate of 0.001 sec^{-1}

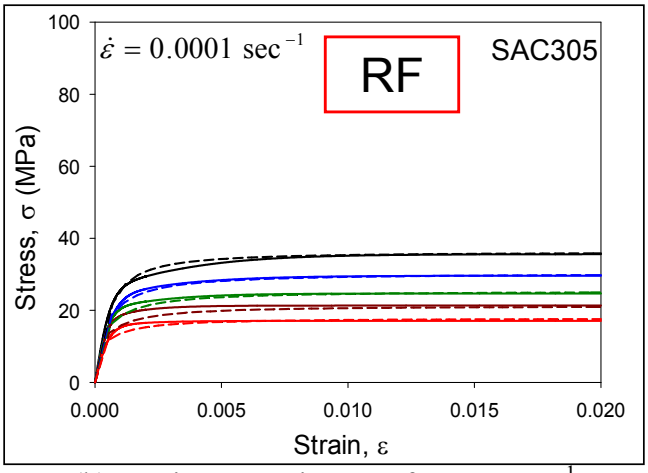

(b) Testing at strain rate of 0.0001 sec^{-1}

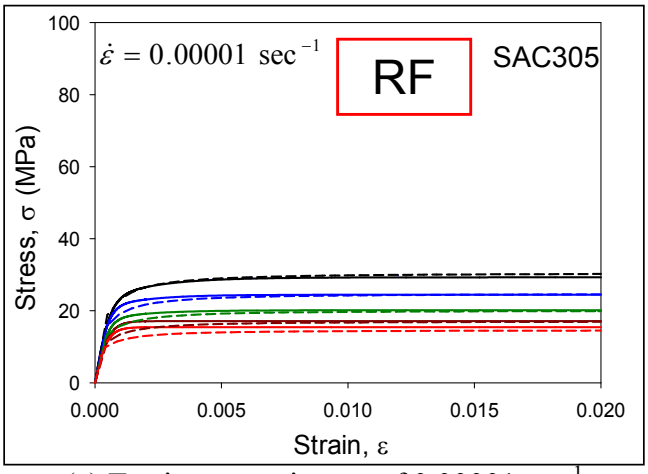

(c) Testing at strain rate of 0.00001 sec^{-1}

Figure 5.21 Correlation of the Calculated and Experimental Stress-Strain Data [SAC305, Reflowed]

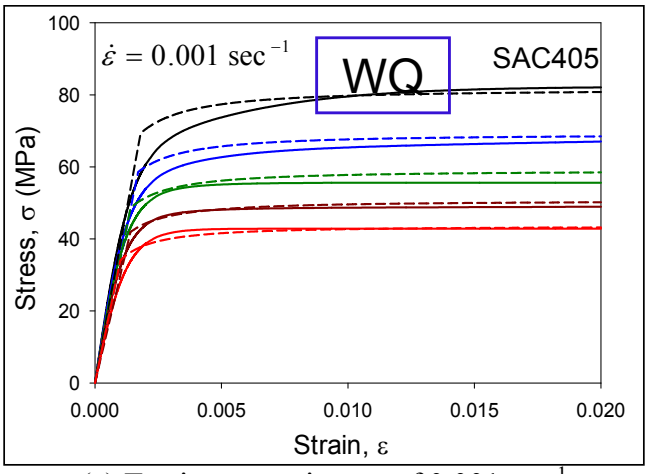

(a) Testing at strain rate of 0.001 sec^{-1}

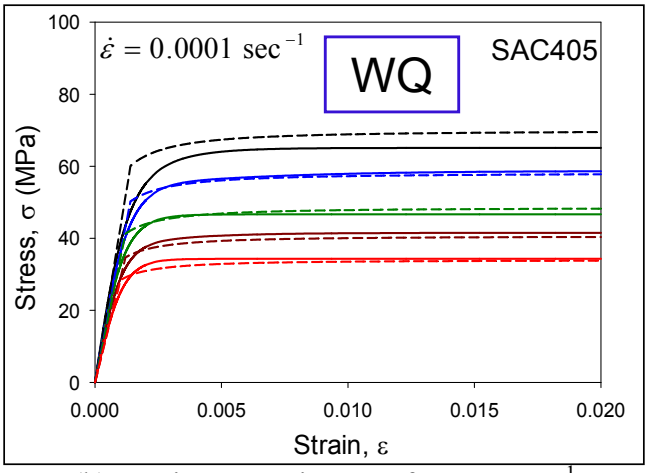

(b) Testing at strain rate of 0.0001 sec^{-1}

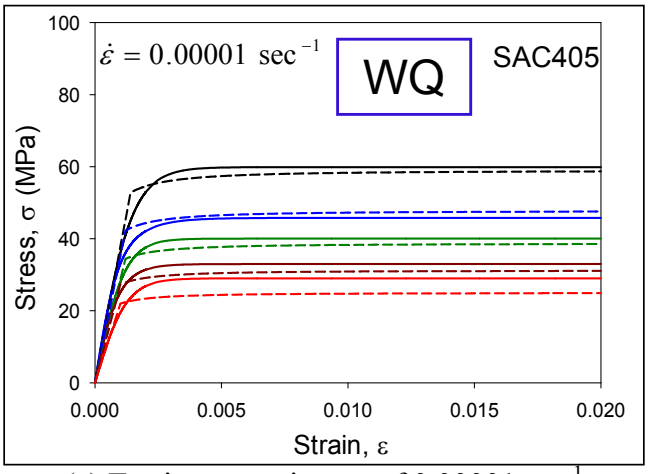

(c) Testing at strain rate of 0.00001 sec^{-1}

Figure 5.22 Correlation of the Calculated and Experimental Stress-Strain Data [SAC405, Water Quenched]

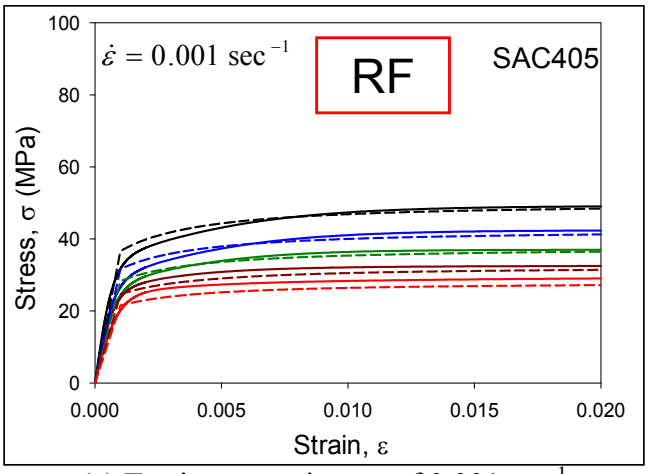

(a) Testing at strain rate of 0.001 sec^{-1}

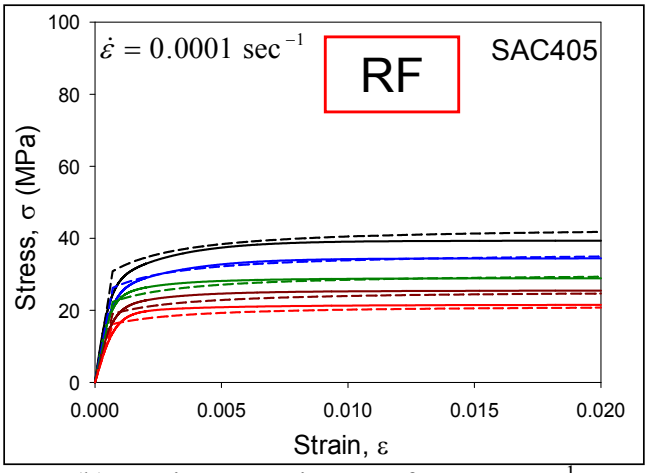

(b) Testing at strain rate of 0.0001 sec^{-1}

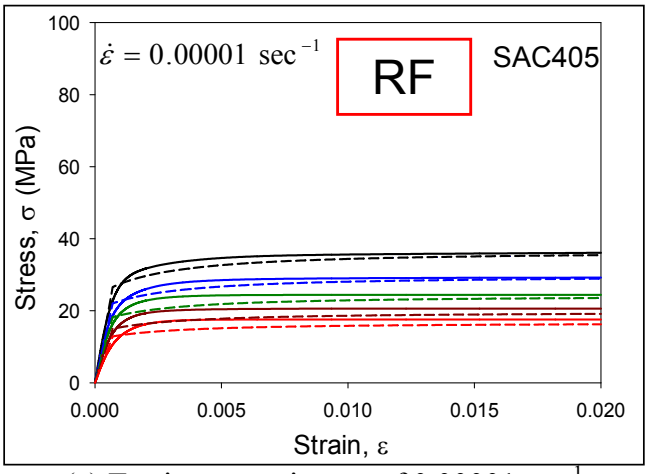

(c) Testing at strain rate of 0.00001 sec^{-1}

Figure 5.23 Correlation of the Calculated and Experimental Stress-Strain Data [SAC405, Reflowed]

5.8 Summary and Discussion

In this study it has been explored the combined the effects of silver content, solidification profile, and aging on the Anand viscoplastic constitutive model of lead free solders. To investigate these effects it has been performed the uniaxial tests on SACN05 (N = 1, 2, 3, 4) alloys. For each alloy, both water quenched (WQ) and reflowed (RF) solidification profiles were utilized to establish two unique specimen microstructures, and the same reflow profile was used for all four of the SAC alloys so that the results could be compared and the effects of Ag content could be studied systematically. In addition, it has been performed tensile testing on reflowed specimens subjected to 180 days of aging at 100 ^{o}C. After this level of aging, any further changes in the mechanical response and properties will be rather small. Thus, the results for these tests can be regarded as approaching the highest level of mechanical behavior degradation possible for a "severely aged" lead free solder material.

The nine Anand parameters were determined for each unique solder alloy and microstructure from a set of stress strain tests performed at several strain rates and temperatures. Testing conditions included strain rates of 0.001, 0.0001, and 0.00001 (sec^{-1}), and temperatures of 25, 50, 75, 100, and 125 ^{o}C. As expected, the mechanical properties (modulus and strength) increase with the percentage of Ag content, and these changes strongly affect the Anand parameters. The sensitivity of the mechanical properties and Anand parameters to silver content is higher at lower silver percentages (1-2%). Also, the observed mechanical properties of water quenched samples were better (higher in magnitude) than the corresponding mechanical properties of the reflowed samples. Although the differences in elastic modulus between the water quenched and

reflowed samples are relatively small, significant differences are present for the yield and ultimate tensile stresses of all four SAC alloys.

The changes in the Anand model parameters after severe aging (180 days at 100 ^{o}C) were significant. The measured experimental results have been used to illustrate the range of values possible for Anand parameters for the SACN05 alloys. The upper extreme was the water quenched limit, where the materials have extremely fine microstructures and high mechanical properties. The lower extreme was the severely aged limit, where the materials have extremely coarsened microstructures and highly degraded mechanical properties. While further degradations are certainly possible with even further aging, the limiting values found for a severely aged SAC alloy can be used by designers as a conservative set of constitutive parameters representing the lower end of the material properties for that alloy.

After deriving the Anand parameters for each alloy and microstructure, the stress-strain curves have been calculated for various conditions, and excellent agreement was found between the predicted results and experimental stress-strain curves. These works has been published in the references [158-159].

CHAPTER 6

THERMAL CYCLING RELIABILITY OF AGED PBGA ASSEMBLIES

6.1 Introduction

The goal of this chapter was to research on the influence of aging on lead free solder material behavior to explore the effects of prior aging on solder joint (board level) reliability in actual assemblies. The overall objective was to develop new reliability prediction procedures that incorporate aging effects, and then to validate the new approaches through correlation with thermal cycling accelerated life testing experimental data for pre-aged assemblies. Traditional finite element based predictions for solder joint reliability during thermal cycling accelerated life testing are based on solder constitutive equations (e.g. Anand viscoplastic model [105-106]) and failure models (e.g. Darveaux energy dissipation per cycle model [132]) that do not evolve with material aging. Thus, there will be significant errors in the calculations with lead free SAC alloys that illustrate dramatic aging phenomena.

In this work it has been developed a framework for correcting this limitation and including aging effects in the reliability modeling. The approach involves the use of: (1) a revised set off Anand viscoplastic stress-strain relations for solder that included material parameters that evolve with the thermal history of the solder material, and (2) a revised solder joint failure criterion that included aging effects. In the Chapter 4, the effects of aging on the nine Anand model parameters were determined experimentally for SAC305 lead free solder as a function of aging temperature and aging time. The revised Anand constitutive equations for solder with aging effects were then incorporated into

standard finite element codes. The developed aging-aware failure criterion was based on the Morrow-Darveaux (dissipated energy based, DeltaW) approach, with both the fatigue criterion for crack initiation and the crack growth law incorporating material constants that depend on the prior aging of the solder material. Fatigue data were measured for SAC solder using uniaxial and shear test specimens that were aged for various durations and temperatures prior to cycling.

This chapter reports on the efforts to model the effects of aging on the board level reliability of a family of assembled BGA components subjected to isothermal aging followed by thermal cycling accelerated life testing. The model predictions were correlated with solder joint reliability test data for the same components. The experimental test vehicle incorporated several sizes (5, 10, 15, 19 mm) of BGA daisy chain components with 0.4 and 0.8 mm solder joint pitches (SAC305). PCB test boards with 3 different surface finishes (ImAg, ENIG and ENEPIG) were utilized. Before thermal cycling began, the assembled test boards were divided up into test groups that were subjected to several sets of aging conditions (preconditioning) including 0, 180, and 360 days aging at T = 125 ^{o}C. After aging, the assemblies were subjected to thermal cycling (-40 to +125 ^{o}C) until failure occurred. The failure data for each test group were fit with the two parameter Weibull model, and the failure plots have demonstrated that the thermal cycling reliabilities of pre-aged assemblies were significantly less than those of analogous non-aged assemblies.

Finite element modeling using the modified Anand model for solder was performed for the four different components sizes to predict the stress-strain histories of both non-aged PBGA assemblies and aged assemblies that had been subjected to constant

temperature exposures for various times before being subjected to thermal cycling. The plastic work (DeltaW) per cycle results from the finite element calculations were then combined with the aging aware fatigue and crack growth models to estimate the reliability (cycles to failure) for the aged and non-aged assemblies. Finally, correlations were performed between the predictions of the new reliability modeling procedure that includes aging and the set of measured solder joint reliability data that includes multiple component sizes, board surface finishes, and aging times.

6.2 Experimental Weibull Failure Data

Thermal cycling experiments were performed on non-aged and aged lead free PBGA assemblies to explore the effects of prior isothermal aging on solder joint (board level) reliability. The test vehicle (see Figure 6.1) included four sizes of BGA components including 19 x 19 mm, 15 x 15 mm, 10 x 10 mm and 5 x 5 mm packages with SAC305 and SAC105 solder joints. Table 6.1 lists the component specifications. The test boards had dimensions of 100 x 67 x 1.5 mm, with a variety of surface finishes including Im-Ag, ENIG, and ENEPIG.

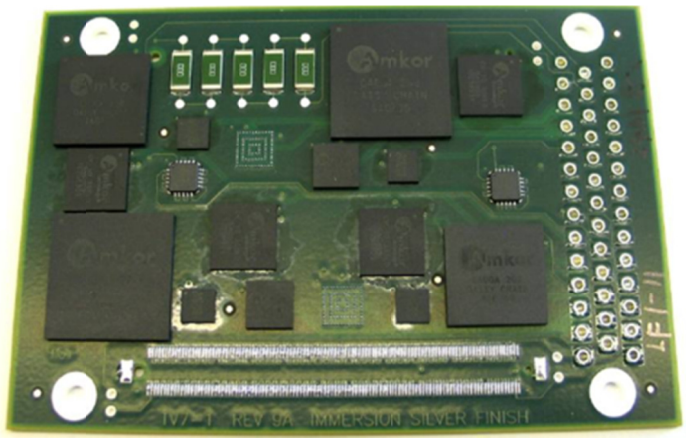

Figure 6.1 Assembled BGA Test Board

Body Size (mm)	Die Size (mm)	Ball Count	Pitch (mm)	Ball Alignment
19 x 19	12.0 x 12.0	288	0.8	Perimeter
15 x 15	12.7 x 12.7	208	0.8	Perimeter
10 x 10	5.0 x 5.0	360	0.4	Perimeter
5 x 5	3.2 x 3.2	97	0.4	Full Array

Table 6.1 BGA Component Specifications

The PBGA daisy chain test assemblies were subjected to up to 2 years of aging at four different temperatures (25, 55, 85, and 125 ^{o}C), followed by thermal cycling from -40 to 125 C or -40 to 85 C to failure. The daisy chain networks were monitored during cycling using a high-accuracy digital multimeter coupled to a high-performance switching system controlled by LabView software. In this work, failure was defined to occur when a daisy chain resistance reached >300 ohm for five sequential resistance measurements. Details of the testing procedure and selected results have been published previously in references [80, 160-161] for ImAg surface finish. Additional results for ENIG and ENEPIG surface finishes are in press [162].

For all lead free solder alloys and component sizes, the thermal cycling reliabilities of the BGA component solder joints were severely reduced by prior aging. For example, a typical Weibull failure rate plot is shown in Figure 6.2 for non-aged and aged 19 mm BGA components. In this case, the solder joint alloy was SAC305, the board surface finish was ImAg, the aging temperature was T = 125 ^{o}C, the aging times were 180 days and 360 days, and the thermal cycling range was from -40 to 125 ^{o}C. Using the 63.2% Weibull characteristic life (η) as the failure metric, the reliability (number of cycles to failure) for the non-aged components was N_f = 4719 cycles, while the reliabilities of the aged components were N_f = 2990 cycles for 180 days of prior

aging, and N_f = 2216 cycles for 360 days of prior aging. This represents reliability degradations of 37% (180 days aging) and 53% (360 days aging).

Similar results have been obtained for the various component sizes, lead free alloys, aging conditions, board finishes, and thermal cycling ranges. In this work, it has been concentrated on modeling only a subset of the experimental thermal cycling test matrix because of the more limited scope of the material characterization experiments (see next section). In particular, it was considered the BGA components with SAC305 solder joints, the aging temperature of T = 125 ^{o}C, and the thermal cycling temperature range of -40 to 125 ^{o}C. Table 6.2 contains the tabulated experimental failure data for these conditions.

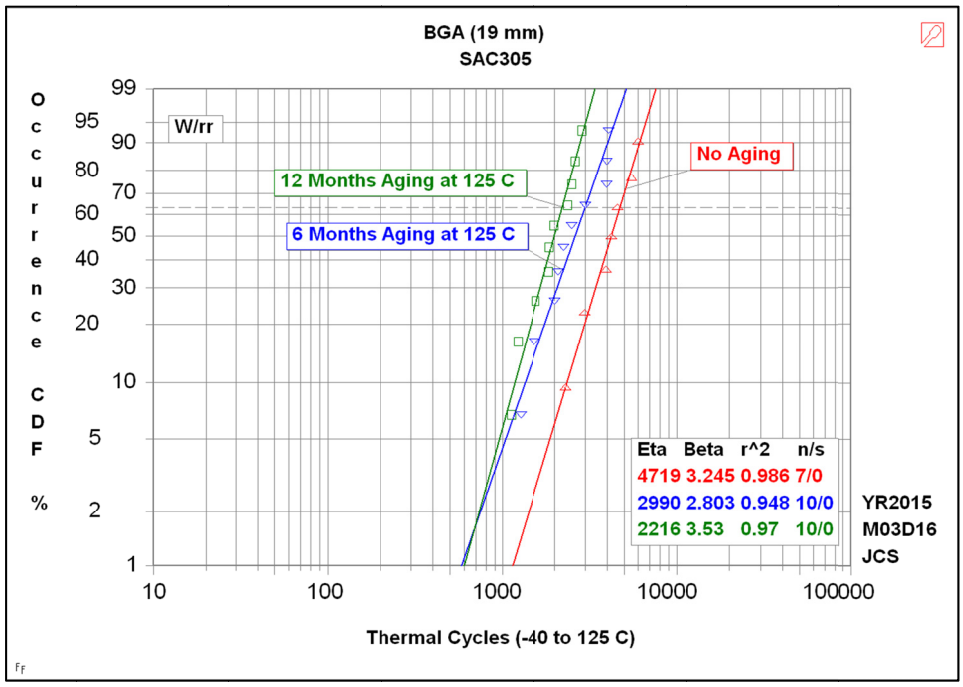

Figure 6.2 Typical Thermal Cycling Weibull Failure Plot

Aging Time (T = 125 °C)	Board Finish	N_f (Testing) [143-145]			
		19 mm	15 mm	10 mm	5 mm
None (0)	ImAg	4722	3743	3329	5171
	ENIG	-	3875	3974	-
	ENEPIG	-	3595	4661	-
180 days	ImAg	2989	2082	1740	3210
	ENIG	-	3049	2894	-
	ENEPIG	-	2253	2635	-
360 days	ImAg	2216	1884	1551	3012
	ENIG	-	2663	2671	-
	ENEPIG	-	2018	2536	-

Table 6.2 Experimental Thermal Cycling Reliability Data

6.3 Finite Element Reliability Models

Three-dimensional finite element analysis (FEA) has been used to calculate the stress/strain histories in the BGA component solder joints during thermal cycling accelerated life testing. Models were developed for the 15 mm, 10 mm, and 5 mm components with SAC305 interconnects. The 19 mm PBGA component was previously modeling by the authors in reference [78]. The effects of prior aging have been included by using a modified Anand constitutive model that includes aging effects, while temperature dependent stress-strain behaviors were included for the remaining packaging materials. Simulation for thermal cycling between -40 to 125 °C was performed for the cases of no prior aging, and 6 and 360 days of aging at T = 125 °C. For each case, the plastic energy dissipation per cycle in the critical solder ball was calculated. These values were then combined with an aging aware fatigue criterion to make life predictions for the components with different aging conditions. The energy based criteria proposed by Darveaux [132] have been used for predicting crack initiation and crack growth rate in the aged solder joints using the energy dissipation values calculated from the finite

element analysis. Correct prediction of the solder joint response is significantly dependent on the details of structural model including the mesh density, accuracy of material models used in the simulation, and adequacy of the prescribed loading and boundary conditions. Details of the utilized modeling procedure are now discussed.

6.3.1 BGA Component Constructions

Figure 6.3 illustrates the BGA component geometries before SMT assembly. There were 208, 360, and 97 solder balls in the 15 mm, 10 mm, and 5 mm components, respectively. The 15 mm and 10 mm packages were symmetric about horizontal and vertical center lines as shown by the red dashed lines. Thus, quarter symmetry FEA models could be developed. The 5 mm package was designed with 3 missing solder balls near the package center, and was symmetric about a diagonal as indicated by the red dashed line, so that a diagonal symmetry half model could be developed. The die outlines are represented by black boxes in Figure 6.3, and solder balls outside of the die shadow were indicated with pink coloring on the package cross-sections. In the 15 mm package, only half of the outside row solder joints were outside of the die shadow, while the entire outside row of balls was outside of the die shadow in the 5 mm components. For the 10 mm packages, no solder balls were under the die.

6.3.2 Solder Ball Shape, Layer Thickness, and Meshing

To determine the actual dimensions of the SAC305 solder joints, and other thin layers in the packages, several assembled PBGA components were cross-sectioned. For example, Figure 6.4 shows an optical microscopy image of the region near a solder ball in one of the assembled 15 mm packages. A measurement microscope was used to extract dimensions from the cross-sections for use in the finite element mesh design. In particular, the thicknesses of the three soldermask (SM) layers, mold compound, die attachment layer, BT substrate, and copper pad layers were observed in each package as tabulated in Table 6.3. The shapes of a typical solder joints were also determined. Finally, the dimensions of the copper vias present in the PCB under the pads of the fine pitch components (10 mm and 5 mm BGAs) were measured.

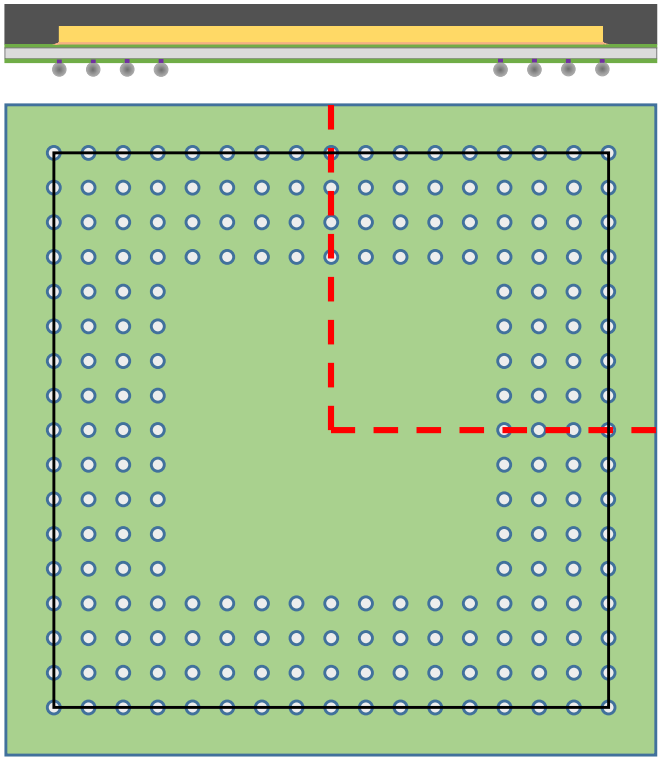

(a) 15 mm BGA

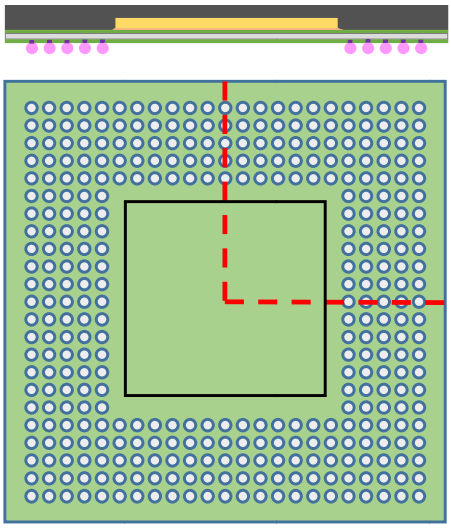

(b) 10 mm BGA

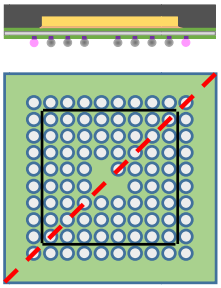

(c) 5 mm BGA

Figure 6.3 BGA Component Constructions

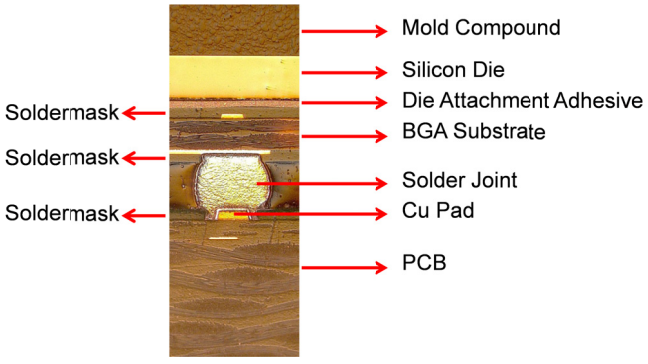

Figure 6.4 Optical Microscopy Cross-Section of 15 mm BGA

Dimension	15mm BGA	10 mm BGA	5 mm BGA
Die Edge Length	12.7	5.0	3.2
Die Thickness	0.280	0.165	0.165
Mold Thickness	0.73	0.45	0.44
Die Attach Thickness	0.05	0.02	0.02
Soldermask Thickness	0.06	0.05	0.05
BT Substrate Thickness	0.20	0.10	0.07
Copper Pad Thickness	0.025	0.025	0.025

Table 6.3 Package Dimensions (mm) from Microscopy

The PBGA packages were meshed in ANSYS using Solid185 elements, which support viscoplasticity, hyperelasticity, stress stiffening, creep, large deformation and large strain capabilities. The meshes for the 15 mm, 10 mm, and 5 mm components contained are shown in Figures 6.5, 6.6, and 6.7, respectively. They contained 1,134,708, 1,005,120, and 764,420 elements, respectively. Brick elements were used exclusively in the meshes (no tetrahedrons), and aspect ratios were kept small. A close-up of the mesh of the 15 mm BGA near the solder balls with details of the various material layers is shown in Figure 6.8.

6.3.3 Material Behavior Models

The Anand viscoplastic material model [105-106] was employed to accurately model the behavior of the SAC305 joints in the various FEA models. Aging was included by using different values of the 9 Anand model parameters for the various prior aging conditions (reflecting the different initial microstructures prior to thermal cycling). Determination of the aging dependence of the Anand parameters has been discussed in detail in the Chapter 4. The parameters used in this work for no aging, and 6 and 360 days of prior aging at 125 ^{o}C are tabulated in Table 6.4.

The remaining packaging materials (silicon, copper, soldermask, die attachment adhesive, mold compound, BT substrate, and PCB) were assumed to be linear elastic materials. The directional behaviors of the BT substrate and PCB were included by using orthotropic material constants including temperature dependence. The material constants were measured using stress-strain and CTE (TMA) testing [78], and are tabulated in Table 6.5. All materials were assumed to be homogenous. Process variations and intermetallic growth were not included.

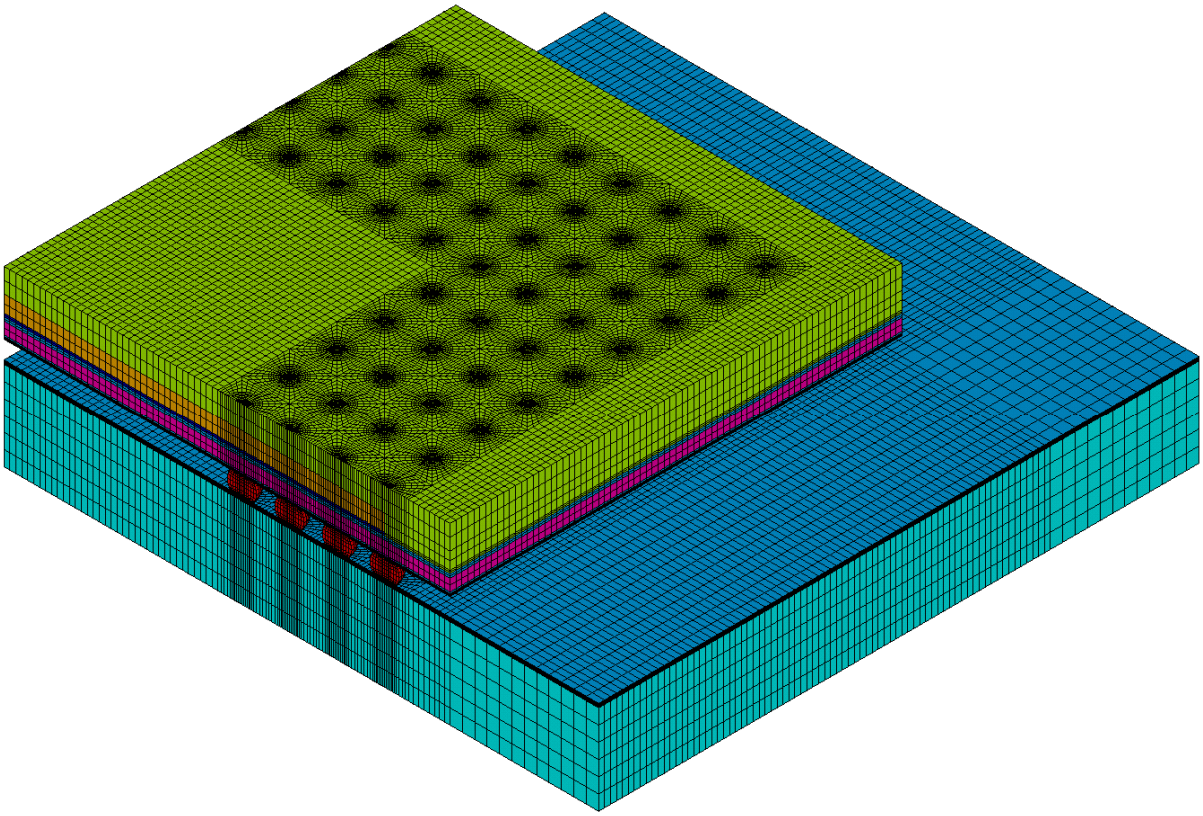

(a) Quarter model

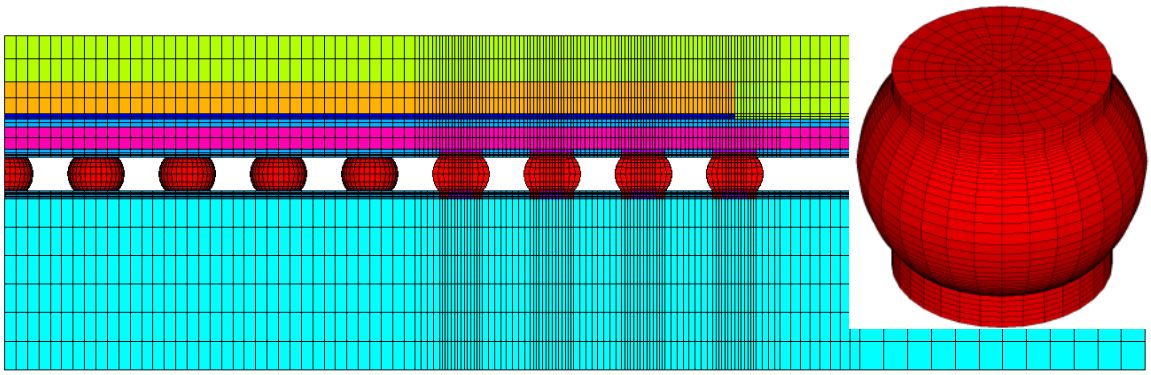

(b) Front View

Figure 6.5 Finite Element Mesh (15 mm BGA)

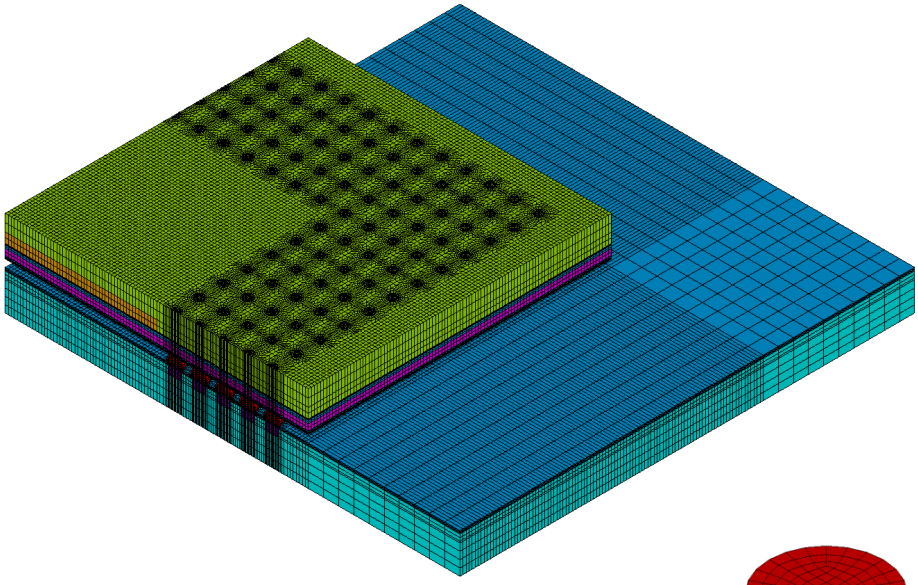

(a) Quarter Model

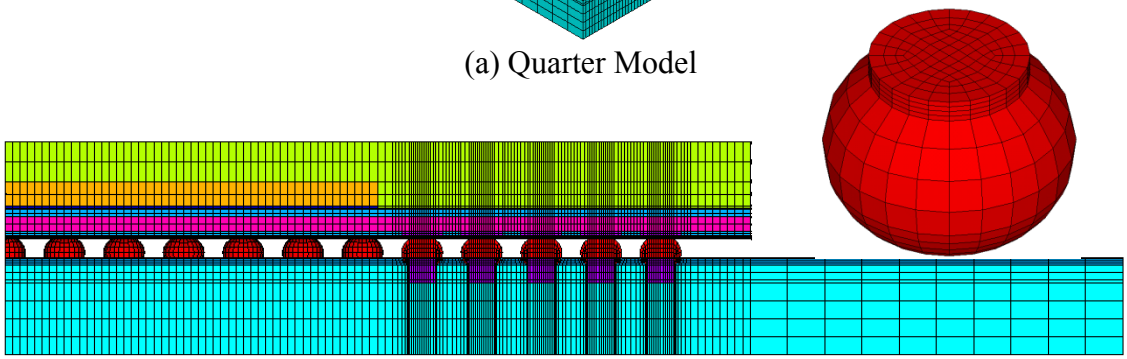

(b) Front View

Figure 6.6 Finite Element Mesh (10 mm BGA)

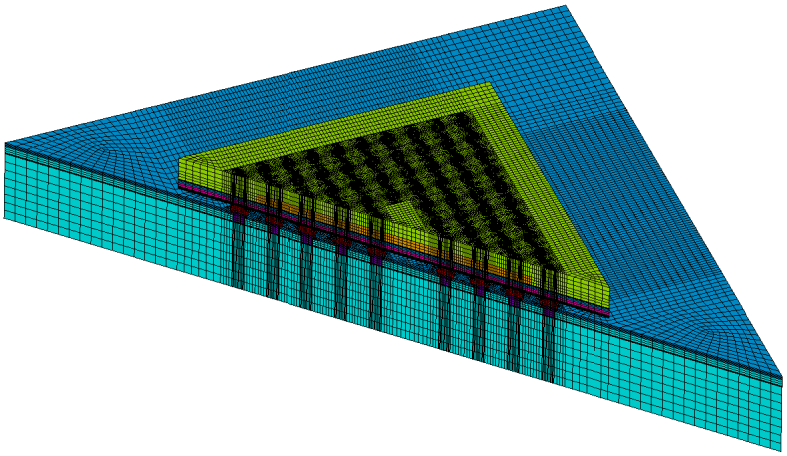

(a) Half Model

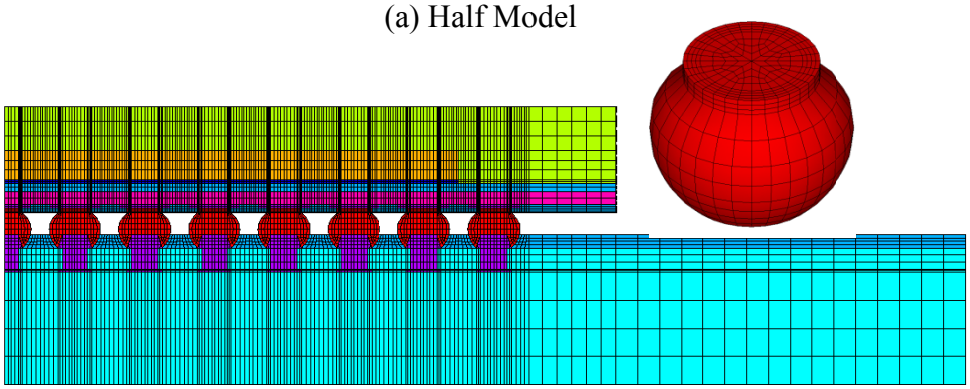

(b) Front View

Figure 6.7 Finite Element Mesh (10 mm BGA)

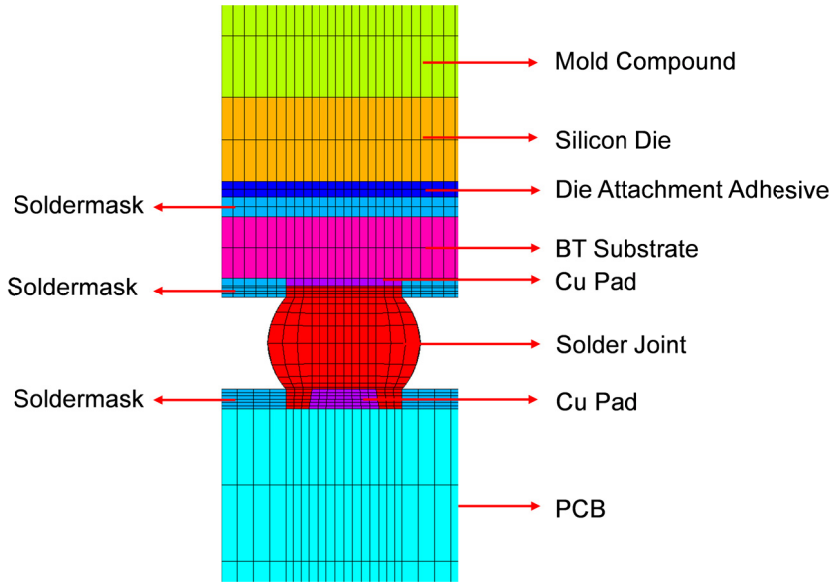

Figure 6.8 Mesh Near Solder Joints (15 mm BGA)

Constant Number	Anand Constant	Units	SAC305 No Aging	SAC305 6 Months Aging	SAC305 12 Months Aging
1	s_o	MPa	21.0	5.10	4.84
2	Q/R	1/K	9320	9320	9320
3	A	sec^{-1}	3501	4137	4240
4	ξ	Dimensionless	4	4	4
5	m	Dimensionless	0.25	0.1764	0.1758
6	h_o	MPa	180000	76296	72417
7	$\hat{S}$	MPa	30.2	21.487	21.024
8	n	Dimensionless	0.0100	0.000587	0.000626
9	a	Dimensionless	1.78	2.0601	2.0652

Table 6.4 Aging Dependent Anand Parameters

Material	Elastic Modulus (GPa)	Shear Modulus (GPa)	Poisson's Ratio	CTE [1/°C]
Copper Pad	129.0		0.34	16.3×10^{-6}
Silicon Die	163.0		0.28	2.5×10^{-6}
Die Attachment	6.77		0.35	83.6×10^{-6}
Soldermask	3.10		0.30	30×10^{-6}
Mold Compound	23.52		0.25	10×10^{-6}
PCB	19.30 (xy, -40 C)	8.71 (xy, -40 C)	0.11 (xy)	14.5×10^{-6} (xy)
	13.20 (xy, 125 C)	5.95 (xy, 125 C)		
	8.48 (z, -40 C)	3.80 (xz, yz; -40 C)	0.39 (xz, yz)	67.2×10^{-6} (z)
	5.84 (z, 125 C)	2.60 (xz, yz; 125 C)		
BT Substrate	17.89 (xy)	8.06 (xy)	0.11 (xy)	12.4×10^{-6} (xy)
	7.85 (z)	2.82 (xz, yz)	0.39 (xz, yz)	57.0×10^{-6} (z)

Table 6.5 Table of Material Properties

6.3.4 Loads and Boundary Condition

The loading applied to the models consisted of a time dependent temperature distribution that matched the thermal cycling from -40 to 125 °C experienced by the assemblies in the life testing experiments. Figure 6.9 shows the applied temperature

history consisting of 1.5 hour (90 minute) temperature cycles, which featured ramp and dwell times of 30 minutes and 15 minutes, respectively to match the experimental in-chamber profile. Each ramp step was divided into 6 load steps, while each dwell step was divided into 2 load steps. Within each load step, the temperature changes were linear in time. The package assembly was assumed to be in a stress-free state at 25 ^{o}C (room temperature), with no initial residual stresses/deformations induced in the manufacturing process. After the cooldown from 25 ^{o}C to -40 ^{o}C, three thermal cycles were simulated. In all of the models, it was found that the cycle to cycle variation of the solder stress/strain behavior became stable by the third cycle. The values during the third cycle were extracted to evaluate the dissipated plastic work per cycle (ΔW) that was used to predict fatigue life.

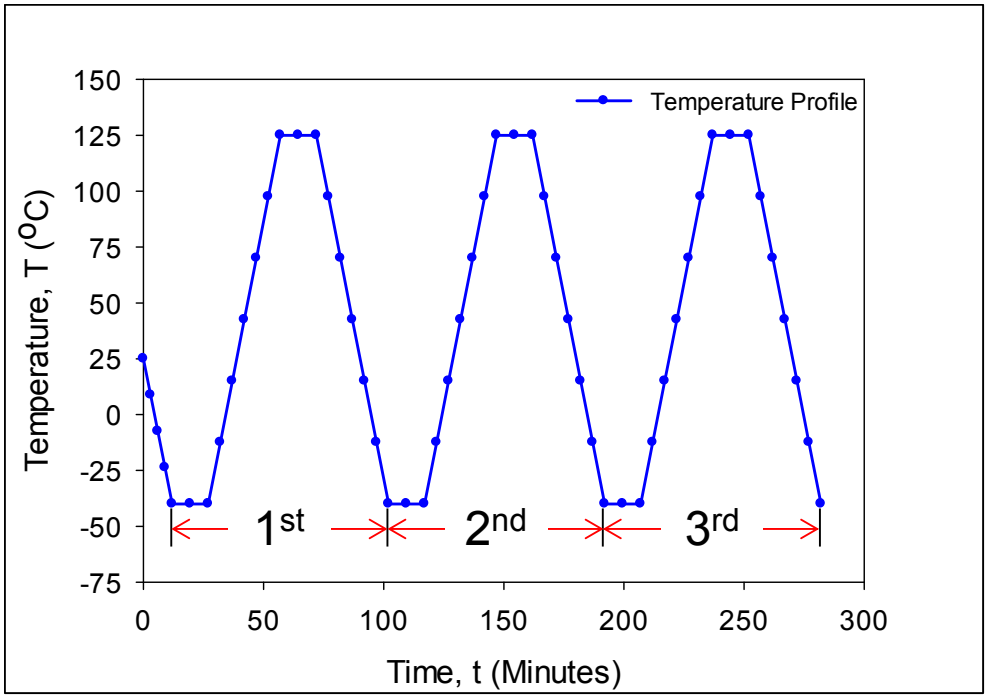

Figure 6.9 Temperature Profile of Thermo-Cycling

The quarter model for the 15 mm and 10 mm BGA components were appropriately constrained along the axes of symmetry, so that for a node in a symmetry plane, the displacement component perpendicular to the symmetry plane was required to be zero. In addition, all three displacements were set to zero for the center node at the bottom surface of the PCB to prevent any rigid body motions. The half model for the 5 mm BGA was similarly constrained along its diagonal line of symmetry. Perfect bonding was assumed at all interfaces between different materials. Iterative solution procedures have been used due to the nonlinear material and kinematic (large deformation) characteristics of the model.

6.4 EFEA Results and Discussion

6.4.1 Effects of Aging on Accumulated Plastic Work

A body accumulates plastic work (W_{pl}) when external loads imposed on the body induce inelastic strain in the body. Thermal cycling of BGA packages induces plastic work in the solder joints due to coefficient of thermal expansion (CTE) mismatches between the different materials comprising the assembly. Figures 6.10(a), (b) and (c) show the predicted contours of accumulated plastic work (W_{pl}) in the solder joints of the 15 mm, 10 mm, and 5 mm BGA components, respectively, after completion of three complete thermal cycles for the non-aged assemblies. The critical joints with the highest values were found to be at the package outside corners, and are enlarged. This finding agreed well with the experimental measurements, where first failures were found in the corner joints of the all the BGA packages. In addition, typical crack propagation paths in

failed joints from the experimental test boards are included. These crack locations agreed well with the predicted regions of highest plastic work.

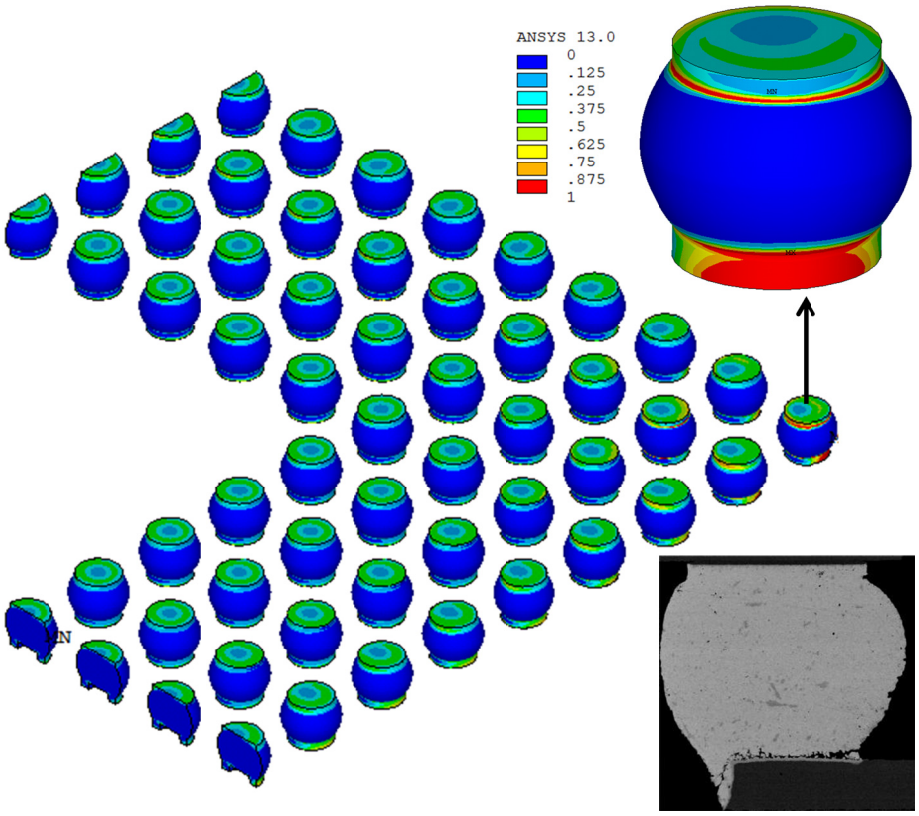

(a) 15 mm BGA

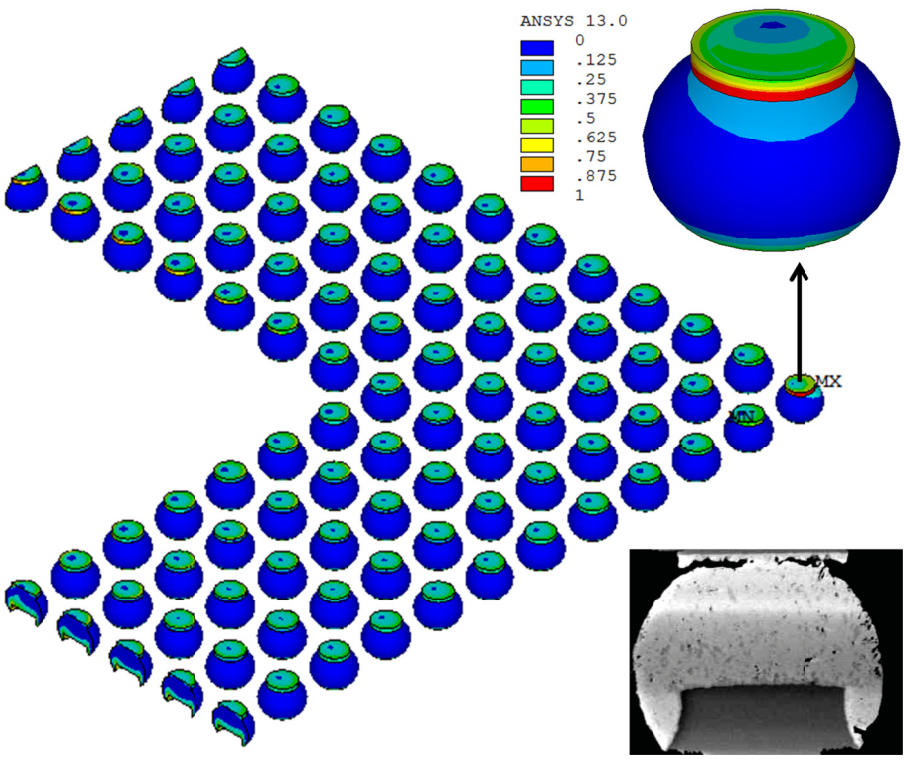

(b) 10 mm BGA

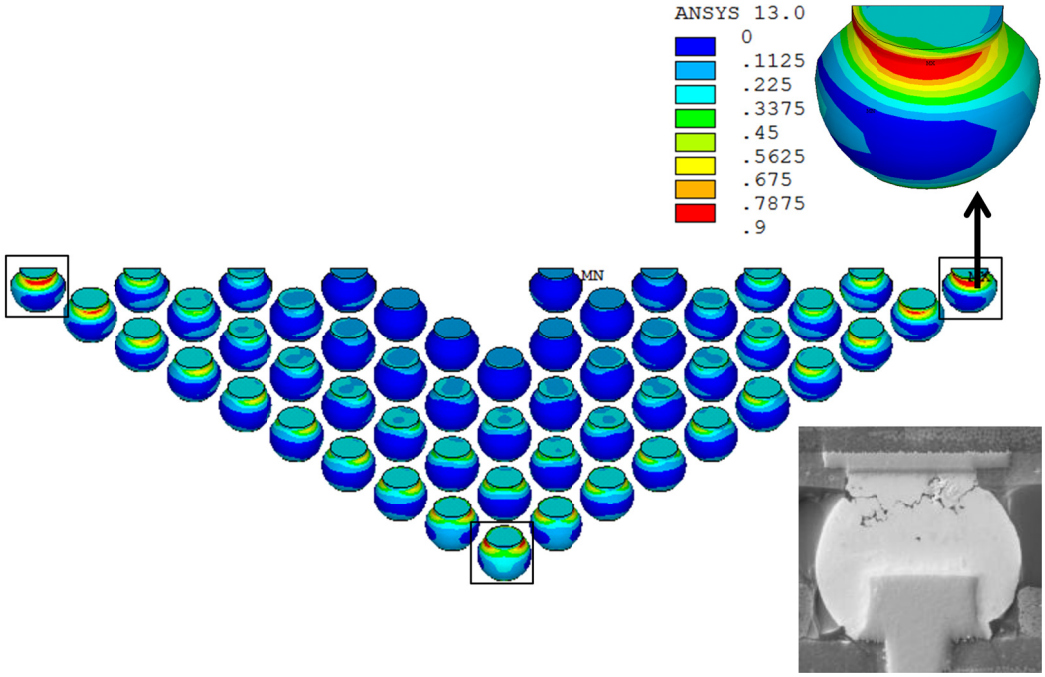

(c) 5 mm BGA

Figure 6.10 Contours of Accumulated Plastic Work (MPa)

For the finer pitch solder interconnections (0.4 mm) in the 10 mm and 5 mm BGA components, the cracks initiated at one of the top corners of the solder joint at the alloy/package interface where the maximum accumulated plastic work occurred, and then propagated along the top of the solder joints. For the aged assemblies, the cracks tended to stay less close to the IMC layer at the BGA pad interface, and angled more into the bulk solder during thermal cycling (e.g., Figure 6.10 (c)). The finite element modeling results in Figure 6.10 (b) and (c) confirmed these locations at the top of the joints, but below the BGA pad interface. The precise crack path will often be related to the degree of brittleness and the thickness of the intermetallic layers at the top of the joints. In addition, local recrystallization can occur in the high plastic strain regions, and these regions can interact with the brittle intermetallic layers in a complicated manner. There is also heightened grain structure movement along this interfacial region, which encourages cracks to nucleate in and propagate through the recrystallized solder [163]. For the 15 mm BGA (0.8 mm pitch), the region of highest plastic work accumulation and crack propagation was at the bottom of the solder joints (board side). Copper vias below the PCB pads were required for routing purposes in the test board for the two fine pitch components. Such vias did not exist below the pads for the 15 mm BGA, suggesting that those joints were relatively more compliant on the package side.

To minimize the mesh dependency of the calculated plastic work values in the joints, it is conventional to calculate volume averaged values across a set of N elements along the crack path using the relationship:

$$\left(W_{pl}\right)_{Averaged} = \frac{\sum_{i=1}^{N}(W_{pl})_i V_i}{\sum_{i=1}^{N} V_i} \tag{6.1}$$

where $(W_{pl})_i$ and V_i are the elemental values of the accumulated plastic work and Volume. Figures 6.11-6.13 show the contour plots of critical solder joints for 15 mm, 10 mm, and 5 mm packages due to different prior aging conditions. Plots of the variations of volume averaged plastic work values in the critical solder joints in the 15 mm, 10 mm, and 5 mm components with time during thermal cycling are shown in Figure 6.14 for the various aging conditions. In each plot, the red curves represent the non-aged case, while the tan and green curves represent the results for 180 days and 360 days prior aging, respectively. As expected, the lowest rate of plastic work accumulation occurs in the non-aged assemblies for each component size. For the assemblies with prior aging, the mechanical properties of the solder material were degraded (through the use of different Anand material parameters), leading to higher rates of plastic work accumulation compared to the non-aged configuration. The results for the 180 days and 360 days aging cases are relatively close together, supporting prior observations that aging causes large changes during the first 20 days of aging, and smaller steady degradations after that point.

The plastic work dissipated per cycle (ΔW) was calculated for each of the first 3 cycles at the critical solder joints using values extracted from the curves in Figure 6.14. Similar calculations were performed at the other joints in the package. For example, Figure 6.15 illustrate the plastic work per cycle (ΔW) of each solder joint in the 15 mm, and 10 mm BGA with no prior aging (quarter model). Form the Figure 15(a), it is clear

from this graph that the value of ΔW = 0.223 MPa at the corner (critical) joint was considerably higher relative to the other joints in the package.

The calculated values of ΔW for the critical solder joints are tabulated in Table 6.6 for the four components and 3 aging conditions. For the most extreme aging conditions (360 days aging at 125 ^{o}C), a 46% increase occurred in the plastic work per cycle (ΔW) in the 15 mm BGA critical solder joints relative to that for the non-aged assembly. As expected, longer aging times prior to cycling resulted in additional plastic work dissipation (and thus more damage accumulation) in the solder joints. Additional FEA runs were performed for other prior aging times using the aging dependent Anand parameters in reference [133]. For example, Figure 6.17 illustrates the variation of (ΔW) with prior aging time for the 15 mm, and 10 mm BGA. As discussed previously, there are rapid degradations (increases in ΔW) for the first 30 to 50 days of prior aging, followed by further changes at a slower rate.

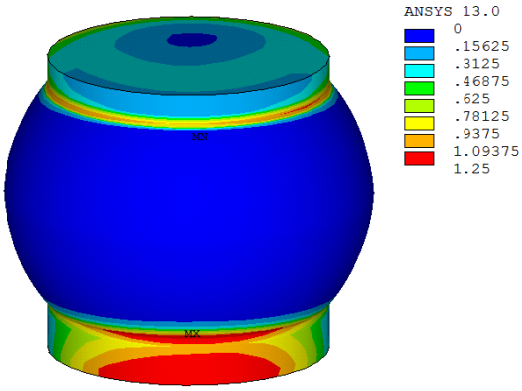

(a) No Prior Aging

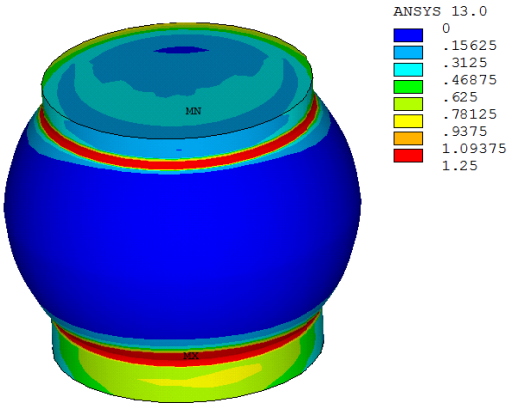

(b) 180 Days of Prior Aging

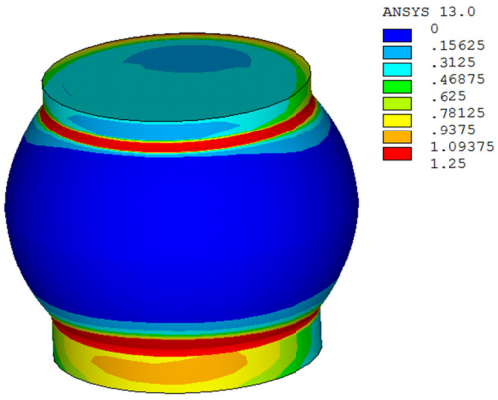

(c) 360 Days of Prior Aging

Figure 6.11 Accumulation of Plastic Work of 15 mm BGA for Different Prior Aging

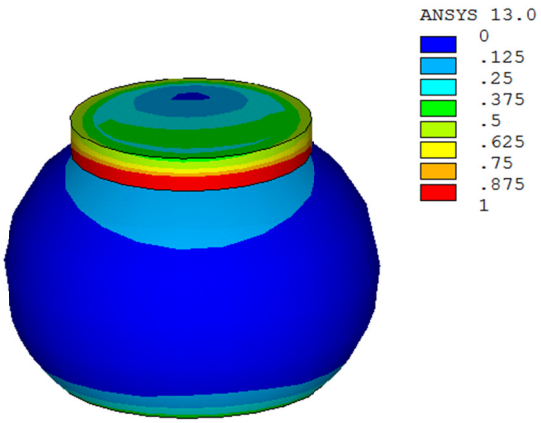

(a) No Prior Aging

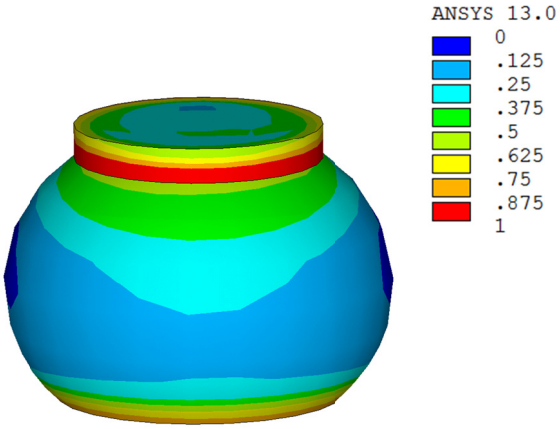

(b) 180 Days of Prior Aging

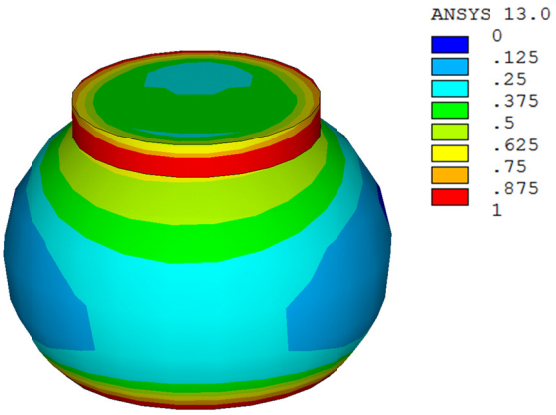

(c) 360 Days of Prior Aging

Figure 6.12 Accumulation of Plastic Work of 10 mm BGA for Different Prior Aging

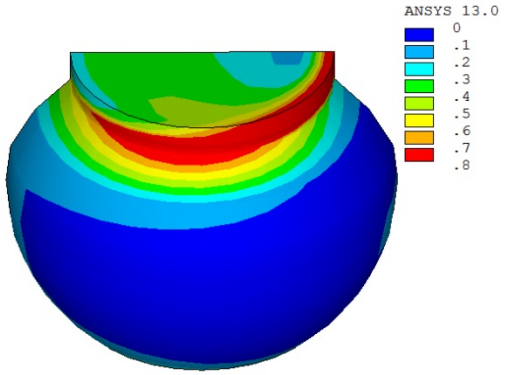

(a) No Prior Aging

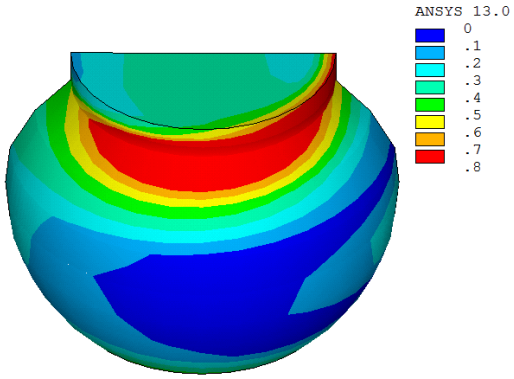

(b) 180 Days of Prior Aging

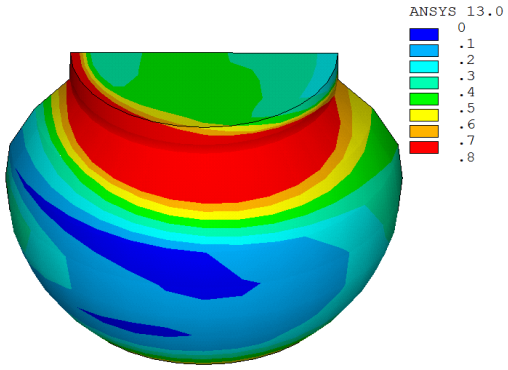

(c) 360 Days of Prior Aging

Figure 6.13 Accumulation of Plastic Work of 5 mm BGA for Different Prior Aging

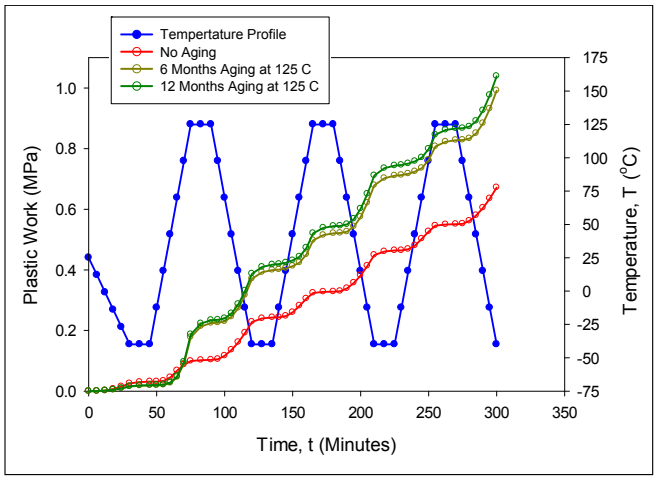

(a) 15 mm PBGA Assemby

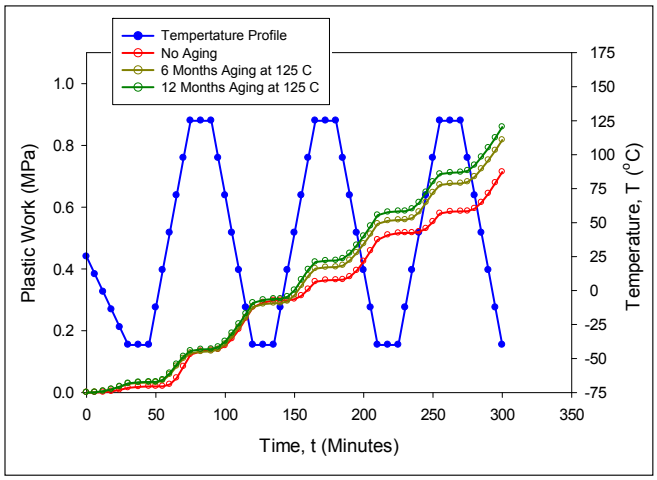

(b) 10 mm PBGA Assemby

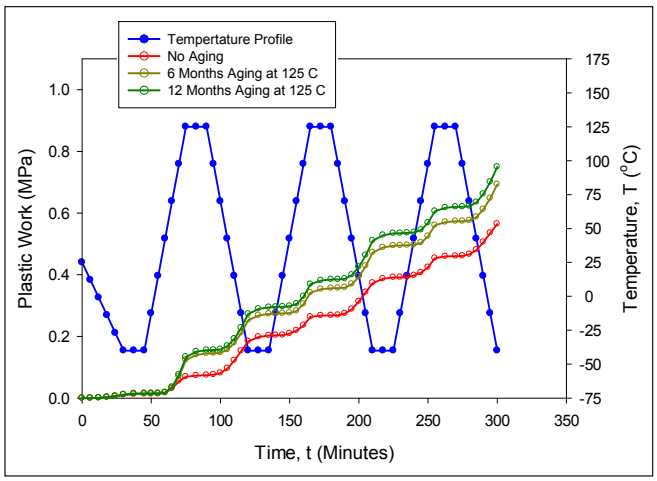

(c) 5 mm PBGA Assemby

Figure 6.14 Volume Averaged Accumulated Plastic Work vs. Time

Aging Time	ΔW (MPa)			
	19 mm	15 mm	10 mm	5 mm
No Aging	0.229	0.223	0.219	0.191
180 days	0.326	0.312	0.271	0.220
360 days	0.344	0.322	0.286	0.230

Table 6.6 Plastic Work per Cycle (ΔW) for Different BGA Components and Prior Aging Conditions

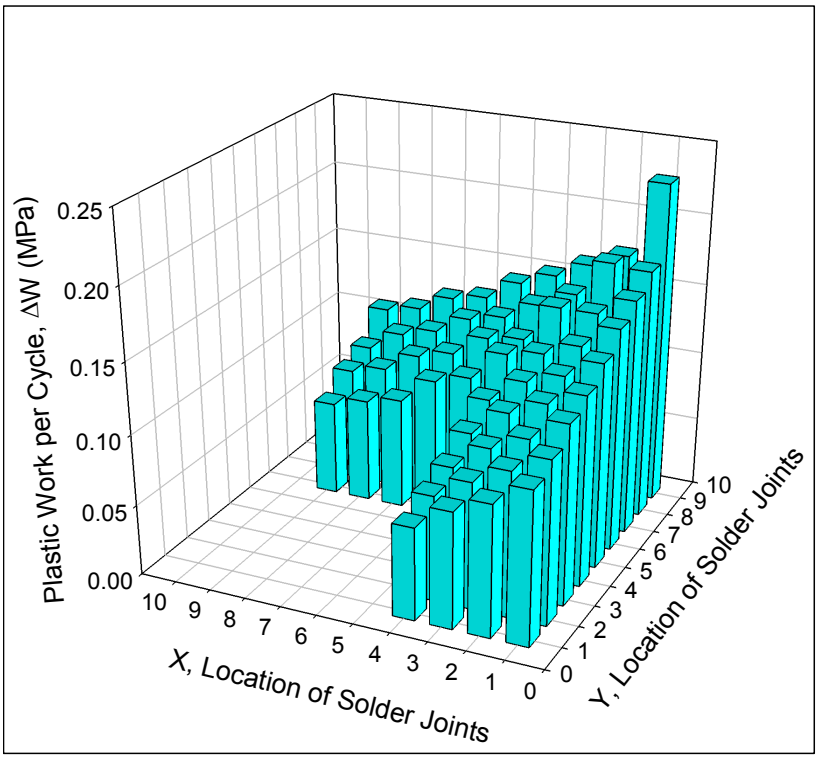

(a) 15 mm Package

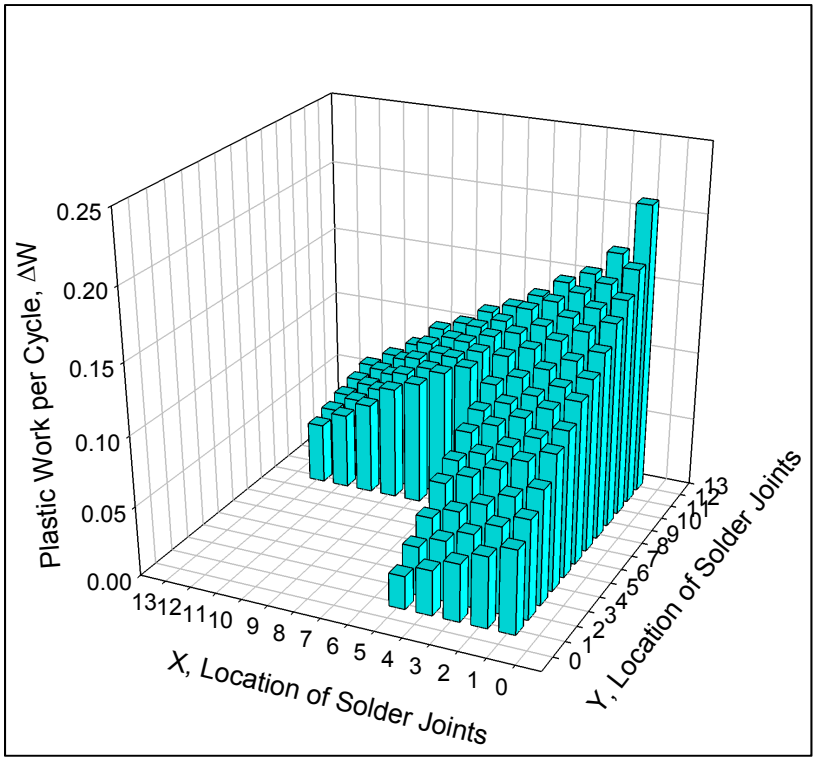

(b) 10 mm Package

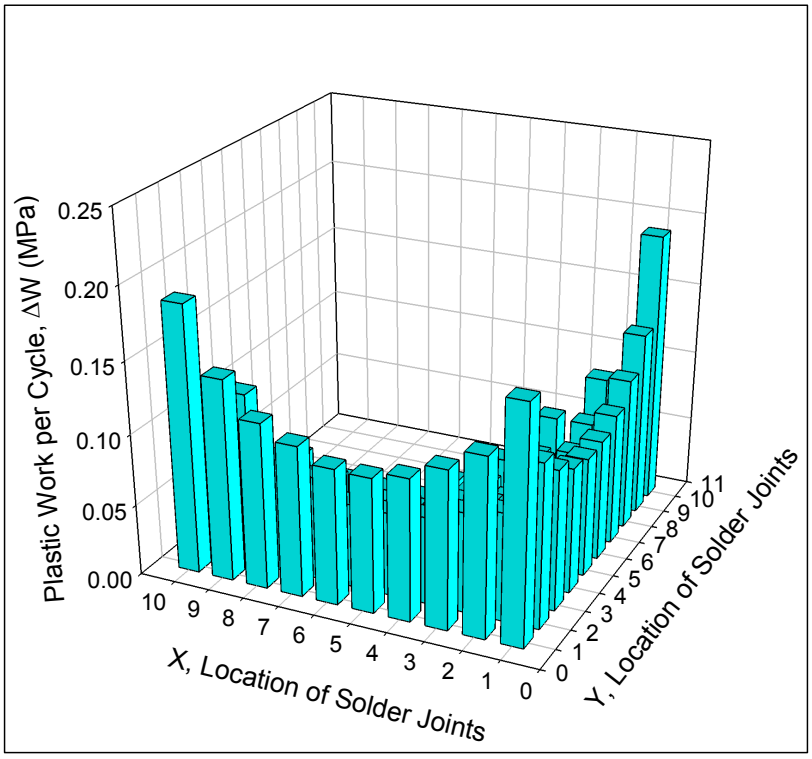

(c) 5 mm Package

Figure 6.15 Plastic Work per Cycle (ΔW) for Different Solder Joints

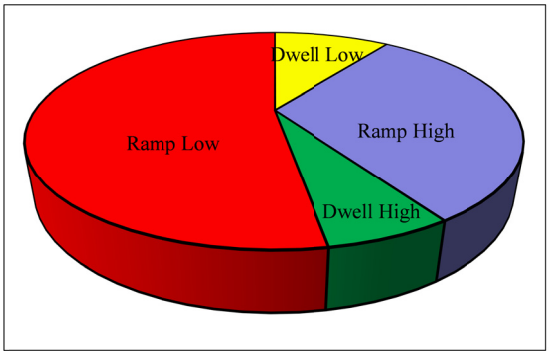

Figure 6.16 Accumulation of Plastic Work in Different Stages of Thermal Cycle

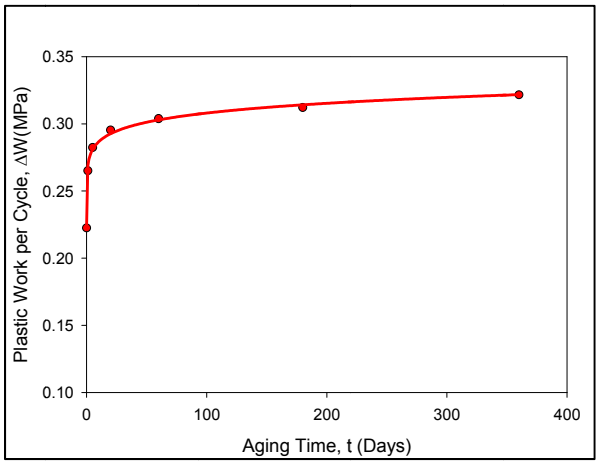

(a) 15 mm Package

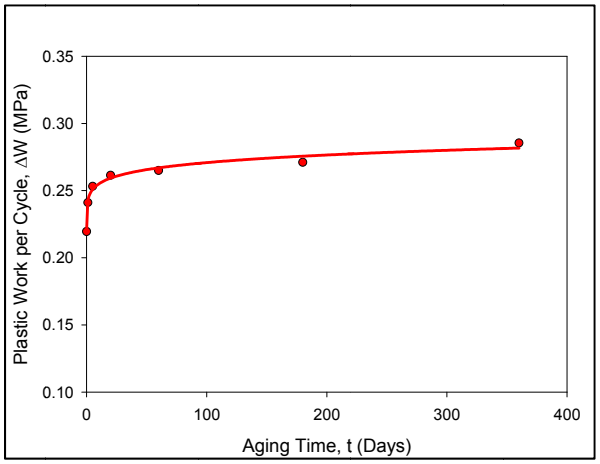

(b) 10 mm Package

Figure 6.17 Variation of Plastic Work per Cycle (ΔW) with Prior Aging Time

6.4.2 Effects of Aging on Stress

The thermally induced stresses in the solder joints are due to mismatches among the CTEs of the various bonded materials that constitute the electronic packaging assembly. Figures 6.18 shows variations of equivalent (von Mises) stress for two different prior aging conditions of the 15 mm PBGA assemblies. As seen in Figure 6.18, the cyclic stresses in the solder joints follow the similar trends, but have large differences in magnitude. After the first thermal cycle, the solder joints reach a stabilized cyclic pattern where the highest stress is experienced at the beginning of the low temperature dwell and the lowest stress at the end of the high temperature dwell. For the no prior aging condition, the induced stress is the highest with a maximum value of 45.6 MPa. Whereas for 180 days of prior aging at 125 C, the maximum values of the predicted von Mises stress drop to 21.52 MPa. It should be noted that these variations in the stress levels result from the differences in the aged solder joint material properties. Aging leads to reductions in the stiffness and increases in the creep rate of the solder material, which results in a reduction of the stress in the solder joints. Similar results trend has been found for the 10 mm and 5 mm packages.

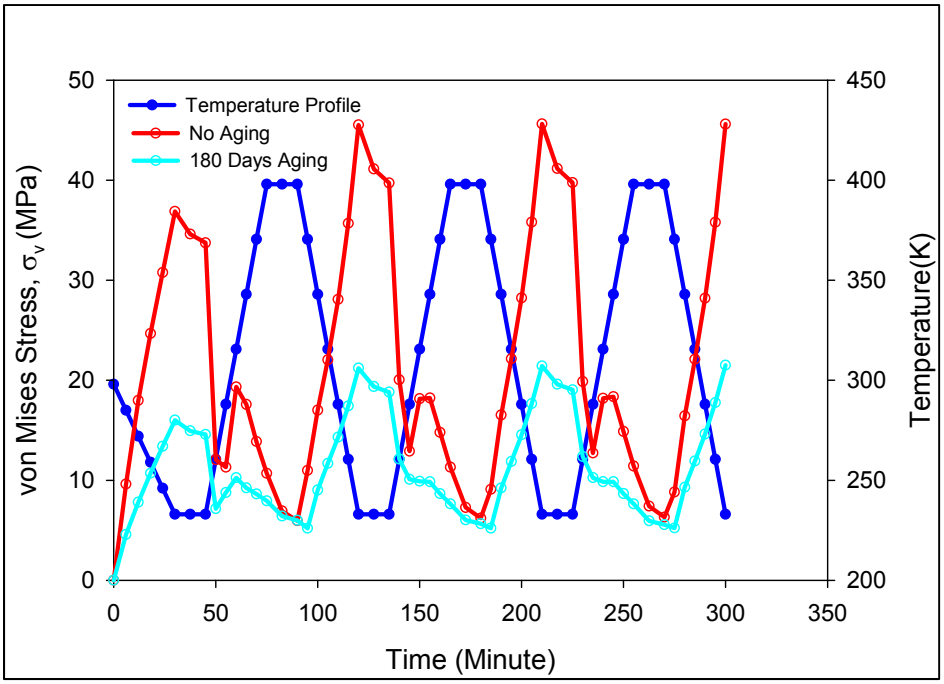

Figure 6.18 von Mises Stress (MPa) of Critical Solder Joints

Figure 6.19(a) shows the von-Mises stress-strain hysteresis curve in the solder joint of the 15 mm package. The hysteresis curve becomes stable after the second cycle. In the Figures 6.19 (b) and (c) the separated (slightly adjusted) hysteresis curves for one complete cycle of no prior aging and 180 days prior aging condition are plotted. It is evident that there is a significant difference in the stress-strain range of the hysteresis curves due to isothermal prior aging. It could be noted that, the area enclosed by the curve related to the magnitude of the plastic work per cycle (ΔW). In the case of hysteresis curve for no prior aging condition, the stress range is higher than 180 days of prior aging whereas strain range is vice versa. Overall, the enclosed area of 180 days prior aging curve is bigger than no prior aging curve. However, the overall nature of these two curves is same. For example, the sign of von-Mises stress is assigned to be positive for decreasing temperature and negative for increasing temperature (Figure 6.16

(b). In -40 C temperature dwell period, the plastic strain rate is increased while stress relaxation occurs in the solder joints. While the temperature is increased from -40 C to 125 C, the stress is significantly relaxed.

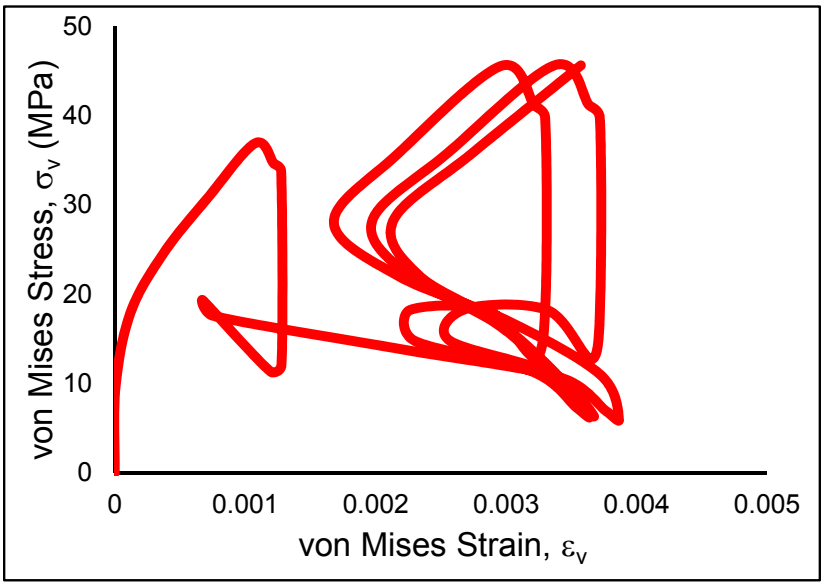

(a) von Mises Stress vs von Mises Strain up to Third Cycle

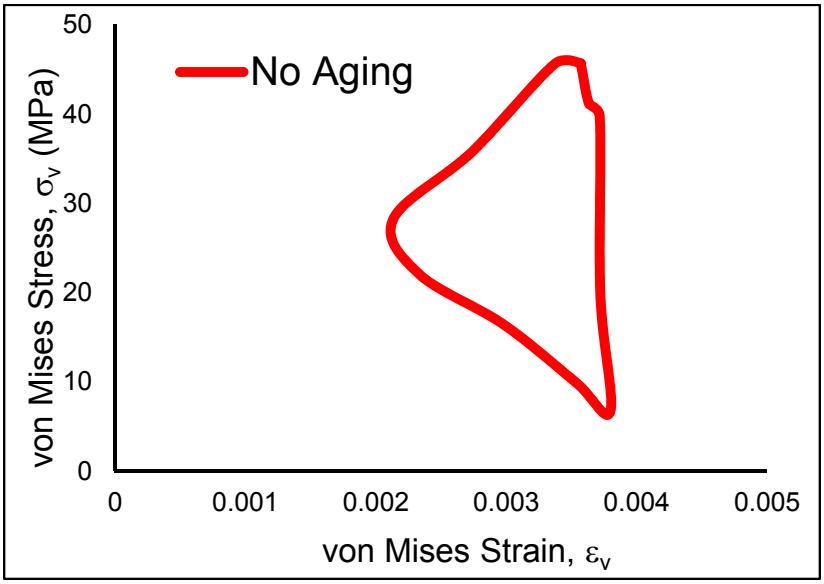

(b) One Complete Cycle, No Prior Aging

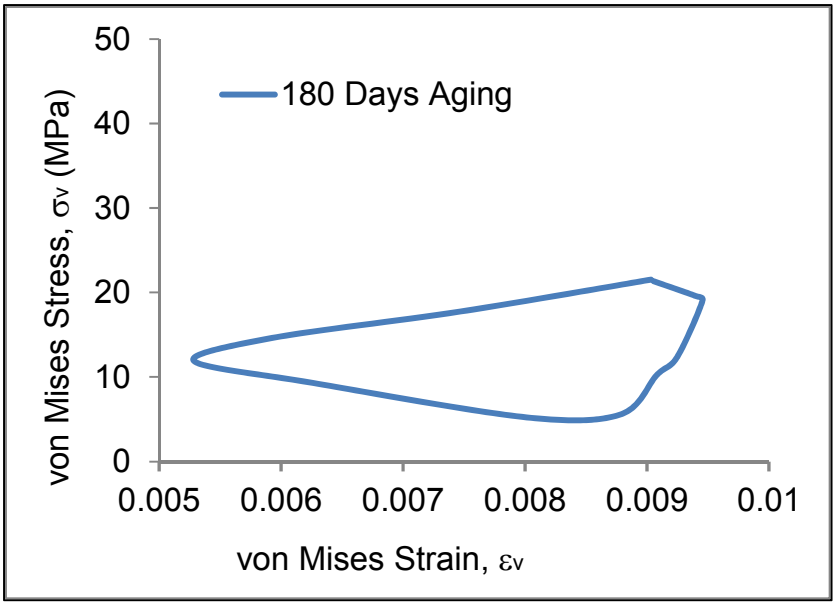

(c) One Complete Cycle, 180 Days of Prior Aging

Figure 6.19 von Mises Stress vs von Mises Strain Plot for Critical Solder Joints

6.4.3 Effects of Aging on Reliability Model and Fatigue Life

Darveaux [132] has developed a life prediction methodology for solder joints based on the energy dissipation (ΔW) occurring during thermal cycling. The procedure uses a pair of power law type relations for estimating crack initiation and crack growth rate in solder joints:

$$N_i = K_1 (\Delta W)^{K_2} \tag{6.2}$$

$$\frac{da}{dN} = K_3 (\Delta W)^{K_4} \tag{6.3}$$

where N_i is the number of thermal cycles to crack initiation, da/dN is the crack growth rate (assumed constant) occurring after crack initiation, ΔW is the energy dissipation per cycle in the solder sample (e.g. critical solder ball), and K_1, K_2, K_3, and K_4 are material

constants. Once the crack location and path are known in the solder joint, the number of cycles to failure can be estimated using:

$$N_f = N_i + \frac{a_c}{\left[\frac{da}{dN}\right]} \tag{6.4}$$

where N_f is the number of cycles to failure, a_c is the length of the fully developed crack at failure/fracture, and N_i and da/dN are calculated from ΔW using Eqs. (6.2-6.3).

Values of K_1 and K_2 for SAC305 solder have been determined using uniaxial (mechanical) fatigue testing for samples aged for different durations at T = 125 ^{o}C [78], and values are tabulated in Figure 20 below. Calculation of parameters K_3 and K_4 in Eq. (6.3) requires crack propagation data from assemblies with a similar component form factor (BGA), solder alloy (SAC305), and board surface finish. When such information is not available (usually the case), it is possible to estimate the values for these parameters using the Weibull failure data in Figure 4 and the assumption of a constant crack propagation rate. Rearranging Eq. (6.4) yields

$$\frac{da}{dN} = \frac{a_c}{\left[N_f - N_i\right]} \tag{6.5}$$

This expression can be used to approximate the crack growth rates for various aging conditions by using the following: $N_f = \eta$ = Weibull Characteristic Lifetimes from Figure 4; a_c = 0.60 mm, 0.38 mm, 0.20 mm, and 0.185 mm are the crack lengths for the known crack paths in 19 mm, 15 mm, 10 mm, and 5 mm BGA assemblies; and N_i are the cycles to crack initiation calculated using Eq. (6.2) with the K_1 and K_2 values from Table 6.7 and ΔW from the finite element calculations in Table 6.6. With this approach, the

crack growth rates were estimated for the various BGA components, surface finishes, and aging conditions. These values were then fit with the crack propagation model in Eq. (6.3) to yield the values of parameters K_3 and K_4 tabulated in Table 6.7.

Aging Time	Board Finish	K_1 [78]	K_2 [78]	K_3	K_4
No Aging	ImAg	37.97	-2.8	0.027	3.08
	ENIG			0.038	3.41
	ENEPIG			0.033	3.05
180 days	ImAg	1.413	-3.13	0.0055	2.97
	ENIG			0.006	3.34
	ENEPIG			0.0055	2.94
360 days	ImAg	1.413	-3.16	0.0055	2.92
	ENIG			0.0056	3.315
	ENEPIG			0.005	2.92

Notes: Units of K_1 and K_3 are (Cycles/MPa^{K2}) and (mm/Cycle-MPa^{K4})

Table 6.7 Failure Model Material Constants

Combination of Eqs. (6.2), (6.3), and (6.4) leads to an expression for the predicted reliability of the components in terms of the ΔW calculated in the critical solder joints from finite element analysis:

$$N_f(\text{FEA}) = K_1(\Delta W)^{K_2} + \frac{a_c}{K_3(\Delta W)^{K_4}} \tag{6.6}$$

This expression was evaluated for the various package sizes, surface finishes, and aging conditions using the material constants in Table 6.7, and the plastic work values in Table 6.6. A summary of the results is presented in Table 6.8 along with their correlations to the thermal cycling data. In most cases, very good agreement was obtained.

Aging Time	Board Finish	N_f (Experimental) [143-145]				N_f (FEA)				% Difference			
		19 mm	15 mm	10 mm	5 mm	19 mm	15 mm	10 mm	5 mm	19 mm	15 mm	10 mm	5 mm
0 Day	ImAg	4722	3743	3329	5171	4431	3993	3455	5013	6	6	3	3
	ENIG	-	3875	3974	-	4754	4233	3592	5266	-	9	9	-
	ENEPIG	-	3595	4661	-	3979	3679	3282	4766	-	2	29	-
180 days	ImAg	2989	2082	1740	3210	3081	2247	1841	3159	3	7	5	1
	ENIG	-	3049	2894	-	4255	3146	2695	4969	-	3	6	-
	ENEPIG	-	2253	2635	-	2980	2171	1774	3026	-	3	32	-
360 days	ImAg	2216	1884	1551	3012	2510	1948	1488	2602	13	3	4	13
	ENIG	-	2663	2671	-	3739	2967	2352	4454	-	11	11	-
	ENEPIG	-	2018	2536	-	2757	2138	1629	2847	-	5	35	-

Table 6.8 Correlation of Finite Element Predictions and Experimental Data

Comparisons between the predicted and measured thermal cycling lifetimes for the 15 mm BGA components are shown graphically in Figure 6.20 or the various aging times and surface finishes. In general, the highest reliabilities were obtained with the ENIG surface finish. The ImAg surface finish yielded the lowest lifetimes for all components and aging conditions. Ha, et al. [145] reported that use of ImAg finish led to greater average IMC thicknesses during thermal aging relative to ENIG/ENEPIG finishes. This is likely due to the lack of a Ni diffusion barrier, and could lead to increased crack growth rates during thermal cycling.

An example prediction of the continuous reliability degradation with increasing prior aging time is shown in Figure 6.21 for the 15 mm BGA assembly. The three square data points in this plot are the experimental (thermal cycling) characteristic life values from Table 6.2. The continuous curve was generated by performing several other finite element analyses with prior aging times other than 6 and 360 days. From Figure 6.21, it is evident that the characteristics life changes rapidly during the first 30 days of aging, with slower degradations for longer aging times. This agrees with the results in Figure 6.17.

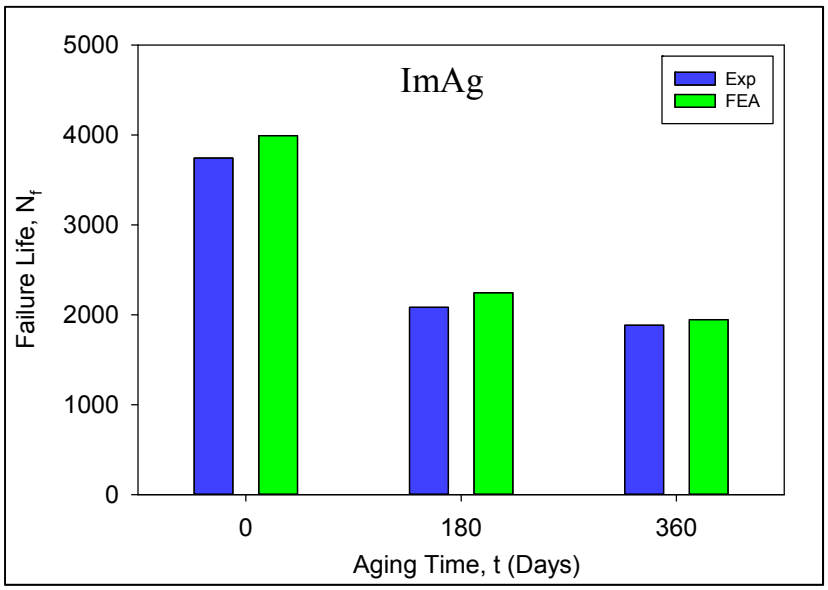
ImAg
Exp
FEA
Failure Life, N_f
5000
4000
3000
2000
1000
0
0
180
360
Aging Time, t (Days)

(a) ImAg

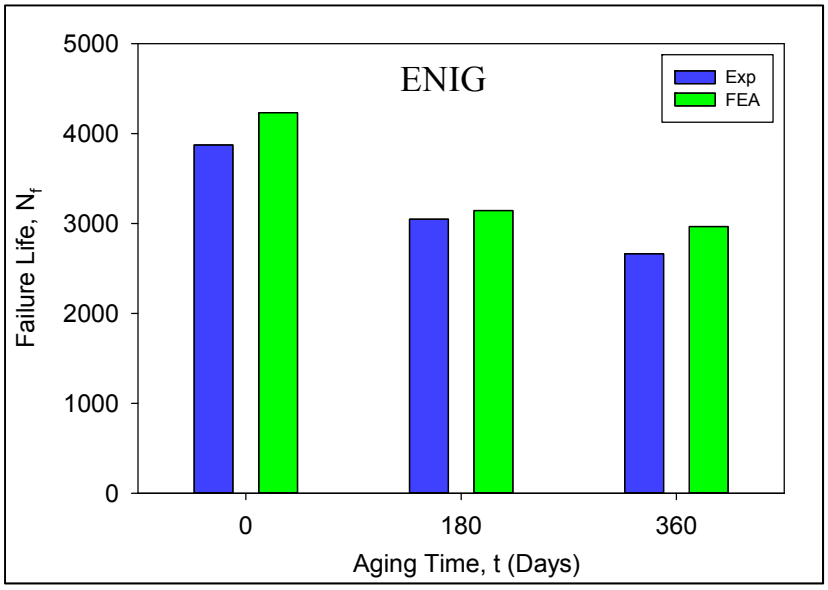
ENIG
Exp
FEA
Failure Life, N_f
5000
4000
3000
2000
1000
0
0
180
360
Aging Time, t (Days)

(b) ENIG

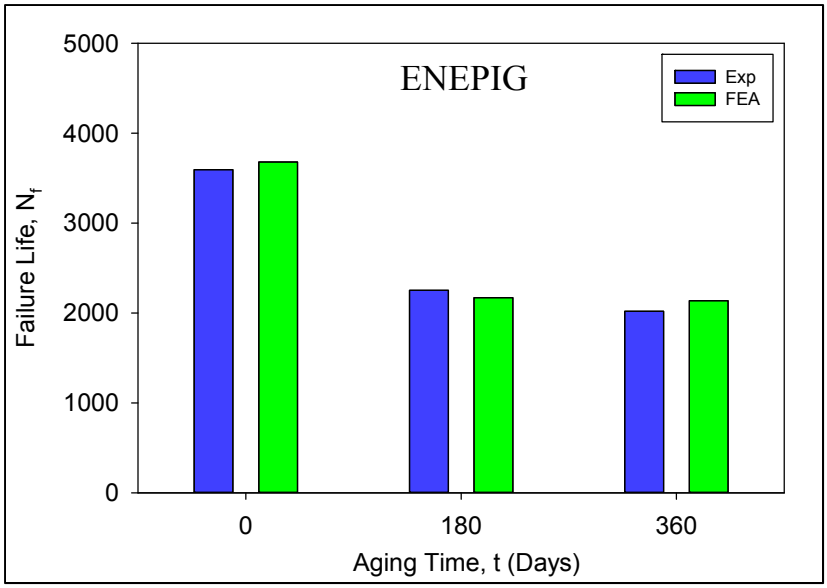

(c) ENEPIG

Figure 6.20 Comparisons of Thermal Cycling Reliability

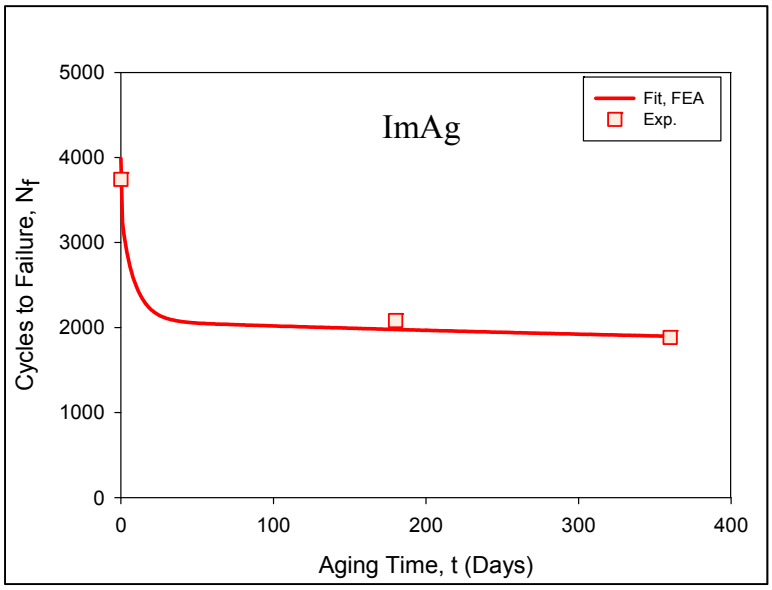

Figure 6.21 Variation of Thermal Cycling Reliability with Prior Aging Time (15 mm BGA, ImAg Finish)

6.5 Summary and Conclusions

In the current work, it has been extended the previous research on the effects of aging on lead free solder material behavior to explore the effects of prior aging on solder joint (board level) reliability in actual assemblies. The overall objective was to develop new reliability prediction procedures that incorporate aging effects, and then to validate the new approaches through correlation with thermal cycling accelerated life testing experimental data for pre-aged assemblies.

The developed reliability modeling procedure has been applied to a family of assembled PBGA components. In the simulations, the packages were subjected to isothermal aging followed by thermal cycling accelerated life testing. The model predictions were correlated with solder joint reliability test data for the same components. The experimental test vehicle incorporated several sizes (5, 10, 15, 19 mm) of BGA daisy chain components with 0.4 and 0.8 mm solder joint pitches (SAC305). PCB test boards with 3 different surface finishes (ImAg, ENIG and ENEPIG) were utilized. Before thermal cycling began, the assembled test boards were divided up into test groups that were subjected to several sets of aging conditions (preconditioning) including 0, 180 days, and 360 days aging at T = 125 ^{o}C. After aging, the assemblies were subjected to thermal cycling (-40 to +125 ^{o}C) until failure occurred. The failure data for each test group were fit with the two parameter Weibull model, and the failure plots have demonstrated that the thermal cycling reliabilities of pre-aged assemblies were significantly less than those of analogous non-aged assemblies with degradations of up to 53% for one year of prior aging.

Finite element modeling using a modified Anand model for SAC305 solder was performed for the four different components sizes to predict the stress-strain histories of both non-aged PBGA assemblies and aged assemblies that had been subjected to constant temperature exposures for various times before being subjected to thermal cycling. The plastic work (ΔW) per cycle results from the finite element calculations were then combined with aging aware fatigue and crack growth models to estimate the reliability (cycles to failure) for the aged and non-aged assemblies. As expected, the predictions showed significant degradations in the solder joint life for assemblies that had been pre-aged before accelerated life testing. The coefficients in the aging aware crack growth model were selected to reflect the board surface finish and SAC solder combination. With this approach, good correlation was obtained between the new reliability modeling procedure that includes aging and the entire set of measured solder joint reliability data that includes multiple component sizes, prior aging conditions, and board surface finishes. These works has been published in the references [121, 164].

CHAPTER 7

SUMMARY

7.1 Literature Review

Aging effects are acknowledged to be responsible for the large discrepancies existing in the mechanical property databases for solder materials. A vast body of studies has already demonstrated that isothermal aging is the root cause for the ever-changing microstructure of lead free solders. Most of the lead free solders, especially the Sn-Ag-Cu solder family, experience dramatic loss in strength (both tensile and shear), stiffness and creep resistance as aging progresses. This effect was found to be exacerbated for elevated temperature exposure. Large discrepancies in measured solder mechanical properties from one study to another have been found and widely acknowledged due to the differences in the microstructures of the tested samples. This problem is exacerbated by the aging issue, as it is evident that the microstructure and material behavior of the samples change rapidly even at room temperature. For elevated temperature aging, this effect has been found to cause more dramatic change in the microstructure, material behavior and the reliability of lead free solder. Thus, the effects of aging on solder behavior must be better understood so that more accurate viscoplastic constitutive equations can be developed for SAC solders. Modifications to the Anand model will be necessary to incorporate aging effects. Without incorporating aging effect in the finite element code of Anand model, it is doubtful that finite element reliability predictions can ever reach their full potential.

The effects of cooling profile and testing conditions on mechanical properties of solder alloys were also discussed through reviewing previous work. In general, fast

cooling rates (i.e. water quenching) during solidification yield finer/smaller phases in the microstructure, which in turn strengthens the solder material. However, quickly cooled samples may also exhibit more brittle behavior when subject to deformation, indicating a loss in strain-to-failure. Testing conditions such as strain rate, stress level, and testing temperature are also known to be key factors affecting the mechanical properties of solders. In general, higher strain rates during tensile tests cause strain hardening, and thus increase the strength and stiffness of the material. In creep testing, the response is highly accelerated by small increases in the applied stress loading. Softening effects in material properties have been reported for both tensile and creep tests performed under elevated temperatures.

7.2 Specimen Preparation and Experimental

A unique specimen preparation procedure was developed in this study to fabricate micro-scale uniaxial tensile specimens. All solder specimens were formed in glass tubes with rectangular cross-section by using a vacuum suction system. Two cooling profiles were adapted in this study, including water quenching and controlled reflow oven cooling. Typical uniaxial samples with nominal dimensions of $80 \times 3 \times 0.5$ mm were utilized.

Uniaxial tensile tests were performed by using a multifunctional microtester. Tensile stress-strain tests were performed for different lead-free SAC alloys for a wide range of temperatures, strain rates, and aging conditions. In this study, the experimental data were modeled by empirical constitutive laws so that the corresponding mechanical properties of solder materials could be extracted. A four parameter hyperbolic tangent model was used to fit the experimental data.

7.3 Effect of Aging on the Material Properties and Constitutive Model

The effects of aging on the nine Anand model parameters have been examined by performing stress-strain tests on water quenched and reflowed SAC305 samples that were aged for various durations (0-360 days) at a temperature of 100 C. For each aging time, stress-strain data were measured at three strain rates (.001, .0001, and .00001 1/sec) and five temperatures (25, 50, 75, 100, and 125 C). Under each testing condition, a set of 10 tests were conducted for stress-strain testing. The material properties (such as effective modulus, yield stress, ultimate strength,) under each testing condition were determined from the model fitting curves. Then variations of the material properties (elastic modulus, yield stress, ultimate strength, etc.) were observed as a function of aging time. Using the measured uniaxial test data, the Anand parameters were calculated for each set of aging conditions, and the effects of aging on the nine Anand model parameters were determined.

The theoretical equations for the uniaxial stress-strain response of solder at constant strain rate have been established from the Anand viscoplastic model, and a nonlinear regression based procedure has been developed for extracting the Anand model constants from the experimental stress-strain data. Using the developed procedure and solder stress-strain data, the Anand model material parameters have been determined for the various aging conditions. Mathematical expressions were then developed to model the evolution of each Anand model parameter with aging time. As expected, the material properties and Anand model parameters evolved (degraded) dramatically during first few 20 days of aging, and then the degradation becomes linear for longer aging times. Mechanical tests have been performed using both water quenched (WQ) and reflowed

(RF) SAC305 samples (two unique specimen microstructures). In general, it was found that neither the adoption of a different solidification cooling profile or the use of other testing conditions were able to reduce aging effects. From the experimental results, the differences between the extracted Anand model parameters of water quenched and reflowed samples were high for samples with no prior aging. As expected, the water quenched samples had much higher mechanical properties (stiffness and strength) than reflowed samples prior to aging. For both the water quenched and reflowed specimens, significant degradation of the material properties was observed with aging. The variations of the Anand model parameters with aging time have been characterized, and empirical relationships were established to model the observed changes. After long aging times, the water quenched and reflowed SAC305 materials were found to exhibit similar mechanical properties, and thus their Anand parameters converged and became nearly identical.

7.4 Effect of Solidification Profile on the Material Properties and Constitutive Model

The effects of solidification cooling profile and testing conditions on the material properties of SAC alloys have been examined by performing a series of tensile tests on SACN05 alloys. The specimens were prepared with two different types of cooling profile, namely, water quenching profile and reflow profile. In the case of the water quenched samples, there is rapid microstructural transitioning during the brief time that occurs between placing molten solder into the glass tubes and immersing the tubes in water bath. On the other hand, the reflowed samples are first cooled by water quenching,

and then sent through a reflow oven to re-melt the solder in the tubes and subject them to a desired temperature profile matching that used in PCB assembly.

It has been demonstrated that the higher cooling rate (water quenching) resulted in enhanced material properties for each SACN05 solder materials under the same testing condition. The water quenched samples have higher stiffness, better tensile and yield strength, than the analogous reflowed specimens. Although it is impossible to "water quench" real electronic packages, the water quenched data is still meaningful because it approaches the optimal case of extremely fine microstructure, and can serve as a guideline for design purposes. The effects of testing conditions (such as strain rate and testing temperature effect) were also presented in this chapter. The testing results in this study agreed with prior studies in the literature. The elastic modulus, yield stress and UTS of SAC solders are highly strain rate and testing temperature dependent. Higher strain rates led to enhanced tensile performance for both SAC solder materials. The elastic modulus, yield stress and UTS increase with increasing strain rate, but decrease with increasing temperature.

7.5 Effect of Silver Content on the Material Properties and Constitutive Model

An investigation on the Anand constitutive model and its application to SAC solders of various Ag contents (i.e. SACN05, with N = 1, 2, 3, 4). For each alloy, both water quenched (WQ) and reflowed (RF) solidification profiles were utilized to establish two unique specimen microstructures, and the same reflow profile was used for all four of the SAC alloys so that the results could be compared and the effects of Ag content could be studied systematically. As expected, the mechanical properties (modulus and strength) increase with the percentage of Ag content, and these changes strongly affect

the Anand parameters. The sensitivity of the mechanical properties and Anand parameters to silver content is higher at lower silver percentages (1-2%). The nine Anand parameters were determined for each unique solder alloy and microstructure from a set of stress-strain tests performed at several strain rates and temperatures. The Anand parameters were calculated from each set of stress-strain data using an established procedure that is described in detail in the paper. Using the calculated results for the various SAC alloys and microstructures, a set of empirical models have been established to describe the effects of SAC alloy Ag content on the Anand model parameters. After deriving the Anand parameters for each alloy, the stress-strain curves have been calculated for various conditions, and excellent agreement was found between the predicted results and experimental stress-strain curves.

7.6 Effects of Aging on the Reliability Model Parameters

A new aging aware failure criteria has been developed based on fatigue data for lead free solder uniaxial specimens that were aged at elevated temperature for various durations prior to mechanical cycling. Using measured SAC305 fatigue data for different aging conditions, the evolution of reliability model parameters K_1 and K_2 with aging were determined. Empirical models for these parameters were developed, and similar to the findings for mechanical/constitutive behavior, the values of these two parameters were affected significantly with aging.

The other two reliability model parameters, K_3 and K_4 were determined from the crack growth experimental data for the test vehicle incorporated several sizes (5, 10, 15, 19 mm) of BGA daisy chain components with 0.4 and 0.8 mm solder joint pitches

(SAC305). Failure data were available for these packages at different aging temperatures for no aging, 180 days, and 360 days aging prior to thermal cycling. The evolution of parameters K_3 and K_4 with aging were determined from these experimental data, and the results showed that aging has significant effects on the model parameters.

Traditional finite element based predictions for solder joint reliability during thermal cycling accelerated life testing are based on solder constitutive equations and failure models that do not evolve with material aging. Due to the strong influence of aging on the thermal cycling reliability of lead free solder assemblies, it is critical that aging effects be included in any reliability prediction methodology. The reliability model parameters K_1, K_2 , K_3 and K_4 that were determined that have been used to estimate the life of SAC solder balls in PBGA components that were subjected to thermal cycling between -40 to 125 ^{o}C with various aging conditions prior to thermal cycling.

7.7 Thermal Cycling Reliability Prediction for Lead Free Solder Joint in PBGA Assemblies with Aging Effects

It was demonstrated in Chapters 4, and 5 that isothermal aging leads to large reductions (up to 50%) in several key material properties for lead free solders including stiffness (modulus), yield stress, ultimate strength, and strain to failure. Traditional finite element based predictions for solder joint reliability during thermal cycling accelerated life testing are based on solder constitutive equations (e.g. Anand viscoplastic model) and failure models (e.g. energy dissipation per cycle models) that do not evolve with material aging. Thus, there will be significant errors in the calculations with lead free SAC alloys that illustrate dramatic aging phenomena. In this study, a new reliability prediction procedure was developed that utilizes constitutive relations and failure criteria that

incorporate aging effects, and then the new approach was validated through correlation with thermal cycling accelerated life testing experimental data.

The developed Anand constitutive equations for solder with aging effects were implemented into the finite element code ANSYS and then the finite element simulations have been performed to model the solder joint deformations of two different PBGA components attached to FR-4 printed circuit boards that were subjected to thermal cycling. Calculations were made for non-aged PBGA assemblies, as well as for assemblies that had been aged under various conditions before being subjected to thermal cycling.

In this study, a three-dimensional finite element analysis of a family of assembled PBGA components with SAC305 interconnects discussed in Chapter 6 was performed to calculate the stress/strain histories in the solder joints during thermal cycling accelerated life testing. Simulation of thermal cycling between -40 to 125 C was performed, and several sets of aging conditions (aging temperature and time) prior to thermal cycling were considered. For each case, the plastic energy dissipation per cycle in the critical solder ball was calculated. These values were then combined with the aging aware fatigue criterion to perform life predictions for the components with various aging conditions. The energy based criteria proposed by Darveaux [132] was used for predicting crack initiation and crack growth in the aged solder joints using the energy dissipation values calculated from the finite element analysis. Good correlation was found between the predicted results and experimental findings for the reliability of the component.

REFERENCES

[1] Vianco, P. T., "Development of Alternatives to Lead-Bearing Solders," *Proceedings of the Technical Program on Surface Mount International*, San Jose, CA, 1993.

[2] Hwang, J. S., *Implementing Lead-Free Electronics*, McGraw-Hill, New York, 2005.

[3] Zhang, Q., Dasgupta, A., and Haswell, P., "Creep and High-Temperature Isothermal Fatigue of Pb-Free Solders," *Proceedings of InterPACK 2003*, pp. 955-960, 2003.

[4] NCMS, *Lead-Free Solder Project Final Report*, National Center for Manufacturing Sciences, Michigan,1997.

[5] Lee, N. C., "Getting Ready for Lead-free Solders," *Soldering & Surface Mount Technology*, Vol. 9, pp. 65-69, 1997.

[6] Kim, K. S., Huh, S. H., and Suganuma, K., "Effects of Intermetallic Compounds on Properties of Sn–Ag–Cu Lead-Free Soldered Joints," *Journal of Alloys and Compounds*, Vol. 352, pp. 226-236, 2003.

[7] Yoon, J.-W., Kim, S.-W., and Jung, S.-B., "IMC Morphology, Interfacial Reaction and Joint Reliability of Pb-Free Sn–Ag–Cu Solder on Electrolytic Ni BGA Substrate," *Journal of Alloys and Compounds*, Vol. 392, pp. 247-252, 2005.

[8] Yu, D. Q. and Wang, L., "The Growth and Roughness Evolution of Intermetallic Compounds of Sn–Ag–Cu/Cu Interface During Soldering Reaction," *Journal of Alloys and Compounds*, Vol. 458, pp. 542-547, 2008.

[9] Wu, C. M. L., Yu, D. Q., Law, C. M. T., and Wang, L., "Properties of Lead-Free Solder Alloys with Rare Earth Element Additions," *Materials Science and Engineering: R: Reports*, Vol. 44, pp. 1-44, 2004.

[10] Wang, C. H., and Chen, S. W., "Sn–0.7 wt.% Cu/Ni Interfacial Reactions at 250 °C," Acta Materialia, Vol. 54, pp. 247-253, 2006.

[11] Li, D., Liu, C., and Conway, P. P., "Characteristics of Intermetallics and Micromechanical Properties During Thermal Aging of Sn–Ag–Cu Flip-Chip Solder Interconnects," *Materials Science and Engineering: A*, Vol. 391, pp. 95-103, 2005.

[12] Chan, Y. C., and Yang, D., "Failure Mechanisms of Solder Interconnects Under Current Stressing in Advanced Electronic Packages," *Progress in Materials Science*, Vol. 55, pp. 428-475, 2010.

[13] Abtew, M., and Selvaduray, G., "Lead-Free Solders in Microelectronics," *Materials Science and Engineering: R: Reports*, Vol. 27, pp. 95-141, 2000.

[14] Furusawa, A., Suetsugu, K., Yamaguchi, A., and Taketomo, H., "Thermoset Pb Free Solder Using Heat-Resistant Sn Ag Paste," *National Technical Report Osaka*, Vol. 43, pp. 46-53, 1997.

[15] McCormack, M., and Jin, S., "Improved Mechanical Properties in New, Pb-Free Solder Alloys," *Journal of Electronic Materials*, Vol. 23, pp. 715-720, 1994.

[16] Liul, P. L., and Shang, J. K., "Interfacial Embrittlement by Bismuth Segregation in Copper/Tin-Bismuth Pb-Free Solder Interconnect," *Journal of Materials Research*, Vol. 16, pp. 1651-1659, 2001.

[17] Habassis, H., Rutte, J. W. r, and Winegard, W. C., "Phase Relationships In Bi–In–Sn Alloy System," *Materials Science and Technology*, Vol. 2, pp. 985-988, 1986.

[18] Glazer, J., "Metallurgy of Low Temperature Pb-Free Solders For Electronic Assembly," *International Materials Reviews*, Vol. 40, pp. 65-93, 1995.

[19] McCormack, M., S. Jin, Kammlott, G. W., and Chen, H. S., "New Pb Free Solder Alloy With Superior Mechanical Properties," *Applied Physics Letters*, Vol. 63, pp. 15-17, 1993.

[20] Nogita, K., "Stabilization of Cu6Sn5 by Ni in Sn-0.7Cu-0.05Ni Lead-Free Solder Alloys," *Intermetallics*, Vol. 18(1), pp. 145-149, 2010.

[21] Che, F. X., Luan, J. E., and Baraton, X., "Effect of Silver Content and Nickel Dopant on Mechanical Properties of Sn-Ag-Based Solders," *Proceedings of the 58th Electronic Components and Technology Conference*, pp. 485-490, 2008.

[22] Guo, F., Lee, J., Choi, S., Lucas, J. P., Bieler, T. R., and Subramanian, K. N., "Processing And Aging Characteristics of Eutectic Sn-3.5 Ag Solder Reinforced With Mechanically Incorporated Ni Particles," *Journal of Electronic Materials*, Vol. 30, pp. 1073-1082, 2001.

[23] Chen, Z. G., Shi, Y. W., Xia, Z. D., and Yan, Y. F., "Study on the Microstructure of a Novel Lead-Free Solder Alloy SnAgCu-RE and its Soldered Joints," *Journal of Electronic Materials*, Vol. 31, pp. 1122-1128, 2002.

[24] Law, C. M. T., and Wu, C. M. L., "Microstructure Evolution and Shear Strength of Sn-3.5Ag-RE Lead-free BGA Solder Balls," *Proceedings of the Sixth High Density Microsystem Design and Packaging and Component Failure Analysis Conference*, pp. 60-65, 2004.

[25] Lee, N.-C., "Lead-Free Soldering-where the World is Going," *Advancing Microelectronics*, Vol. 26, pp. 29-35, 1999.

[26] Gao, F., Mukherjee, S., Cui, Q., and Gu, Z., "Synthesis, Characterization, and Thermal Properties of Nanoscale Lead-Free Solders on Multisegmented Metal Nanowires," *The Journal of Physical Chemistry C,* Vol. 113, pp. 9546-9552, 2009.

[27] Pirondi, A., "Mechanical Failure in Microelectronic Packaging," *Convegno IGF XIII Cassino*, Vol. IGF 13, 1997.

[28] Hertzberg, R. W., Vinci, R. P., and Hertzberg, J. L., *Deformation and Fracture Mechanics of Engineering Materials*, 4th edition, John Wiley & Sons Inc, 1996.

[29] Wiese, S., Schubert, A., Walter, H., Dukek, R., Feustel, F., Meusel, E., and Michel, B., "Constitutive Behavior of Lead-free Solders vs. Lead-containing Solders - Experiments on Bulk Specimens and Flip-Chip Joints," *Proceeding of the 51st Electronic Components and Technology Conference*, pp. 890-902, 2001.

[30] McCabe, R. J., and Fine, M. E., "Athermal And Thermally Activated Plastic Flow in Low Melting Temperature Solders At Small Stresses," *Scripta Materialia*, vol. 39, pp. 189-195, 1998.

[31] Lau, J. H., "Solder Joint Reliability of Flip Chip and Plastic Ball Grid Array Assemblies Under Thermal, Mechanical, And Vibrational Conditions," *IEEE Transactions on Components, Packaging, and Manufacturing Technology, Part B: Advanced Packaging*, vol. 19, pp. 728-735, 1996.

[32] Ralls, K. M., Courtney, T. H., and Wulff, J., *Introduction to Materials Science and Engineering*, Wiley, 1976.

[33] Cadek, J., *Creep in metallic materials*, Elsevier Science Publisher, 1988.

[34] Garofalo, F., and Butrymowicz, D. B., "Fundamentals of creep and creep-rupture in metals," *Physics Today*, Vol. 19, p. 100, 1966.

[35] Evans, R. W. and Wilshire, B., "*Creep of Metals and Alloys*," The Institute of Metals, 1985.

[36] Ashby, M. F., "A First Report on Deformation-Mechanism Maps," *Acta Metallurgica*, Vol. 20, pp. 887-897, 1972.

[37] Weertman, J., "Steady-State Creep through Dislocation Climb," *Journal of Applied Physics*, Vol. 28, pp. 362-365, 1957.

[38] Coble, R. L., "A Model for Boundary Diffusion Controlled Creep in Polycrystalline Materials," *Journal of Applied Physics*, Vol. 34, pp. 1679-1682, 1963.

[39] Herring, C., "Diffusional Viscosity of a Polycrystalline Solid," *Journal of Applied Physics*, Vol. 21, pp. 437-445, 1950.

[40] E606-92, Standard Practice for Strain-Controlled Fatigue Testing, *Annual Book of ASTM Standards*, Vol. 3, 2004.

[41] Mustafa, M., Roberts, J. C., Suhling, J. C., Lall, P., "The Effects of Aging of the Cyclic Stress-Strain and Fatigue Behaviors of Lead Free Solders," *Proceedings of InterPACK 2013*, pp. 1-12, 2013.

[42] Coffin, L. F., "A Study of the Effects of Cyclic Thermal Stresses on Ductile Metal," *ASME Transactions*, Vol. 76, 1954.

[43] Ma, H., and Suhling, J. C., "A Review of Mechanical Properties of Lead-Free Solders for Electronic Packaging," *Journal of Materials Science*, vol. 44, pp. 1141-1158, 2009.

[44] Ma, H., Suhling, J. C., Zhang, Y., Lall, P., and Bozack, M. J., "The Influence of Elevated Temperature Aging on Reliability of Lead Free Solder Joints," *Proceedings of the 57th Electronic Components and Technology Conference*, pp. 653-668, 2007.

[45] Ma, H., Suhling, J. C., Lall, P., and Bozack, M. J., "Reliability of the Aging Lead Free Solder Joint," *Proceedings of the 56th Electronic Components and Technology Conference*, pp. 849-864, 2006.

[46] Zhang, Y., Cai, Z., Suhling, J. C., Lall, P., and Bozack, M. J., "The Effects of Aging Temperature on SAC Solder Joint Material Behavior and Reliability," *Proceedings of the 58th Electronic Components and Technology Conference*, pp. 99-112, 2008.

[47] Medvedev, A. S., "Aging of Tin-Lead Solders and Joints Soldered by Them," *Metallovedenie Obrabotka Metallov*, Vol. 7, pp. 16-23, 1956.

[48] Lampe, B. T., "Room Temperature Aging Properties of Some Solder Alloys," *Welding Journal*, Vol. 55, pp. 330-340, 1976.

[49] Yoon, J.-W., Lee, C.-B., and Jung, S.-B., "Growth of An Intermetallic Compound Layer With Sn-3.5 Ag-5Bi On Cu And Ni-P/Cu During Aging Treatment," *Journal of Electronic Materials*, Vol. 32, pp. 1195-1202, 2003.

[50] Choi, S., Bieler, T. R., Lucas, J. P., and Subramanian, K. N., "Characterization of The Growth of Intermetallic Interfacial Layers of Sn-Ag and Sn-Pb Eutectic Solders

and Their Composite Solders on Cu Substrate during Isothermal Long-Term Aging," *Journal of Electronic Materials*, Vol. 28, pp. 1209-1215, 1999.

[51] Xu, L., Pang, J. H. L., Prakash, K. H., and Low, T. H., "Isothermal And Thermal Cycling Aging on IMC Growth Rate in Lead-Free and Lead-Based Solder Interface," *IEEE Transactions on Components and Packaging Technologies*, Vol. 28, pp. 408-414, 2005.

[52] Anderson, I. E., Walleser, J. W., Harringa, J. L., Laabs, F., and Kracher, A., "Nucleation Control and Thermal Aging Resistance of Near-Eutectic Sn-Ag-Cu-X Solder Joints by Alloy Design," *Journal of Electronic Materials*, Vol. 38, pp. 2770-2779, 2009.

[53] T. C. Hsuan and K. L. Lin, "Effects of Aging Treatment of Mechanical Properties and Microstructure of Sn-8.5Zn-0.5Ag-0.01Al-0.1Ga Solder," *Materials Science and Engineering*, A, Vol. 456, pp. 202-209, 2007.

[54] Chuang, C. M., Lui, T.-S., and Chen, L.-H., "Effect of Aluminum Addition on Tensile Properties of Naturally Aged Sn-9Zn Eutectic Solder," *Journal of Materials Science*, Vol. 37, pp. 191-195, 2002.

[55] Pang, J. H. L., Low, T. H., Xiong, B. S., Luhua, X., and Neo, C. C., "Thermal cycling aging effects on Sn–Ag–Cu solder joint microstructure, IMC and strength," *Thin Solid Films*, Vol. 462-463, pp. 370-375, 2004.

[56] Darveaux, R., "Shear Deformation of Lead Free Solder Joints," *Proceedings of the 55th Electronic Components and Technology Conference*, pp. 882-893, 2005.

[57] Wiese, S. and Wolter, K. J., "Creep of Thermally Aged SnAgCu-Solder Joints," *Microelectronics Reliability*, Vol. 47, pp. 223-232, 2007.

[58] Dutta, I., Pan, D., Marks, R. A., and Jadhav, S. G., "Effect of Thermo-Mechanically Induced Microstructural Coarsening on the Evolution of Creep Response of SnAg-Based Microelectronic Solders," *Materials Science and Engineering A*, Vol. 410-411, pp. 48-52, 2005.

[59] Z Cai., Zhang, Y., Suhling, J. C., Lall P., Johnson, R. W., and Bozack, M. J., "Reduction of Lead Free Solder Aging Effects Using Doped SAC Alloys," *Proceedings of the 60th Electronic Components and Technology Conference*, pp.1493-1511, 2010.

[60] Darveaux, R. and Banerji, K., "Fatigue Analysis of Flip Chip Assemblies Using Thermal Stress Simulations and A Coffin-Manson Relation," *Proceedings of the 41st Electronic Components and Technology Conference*, pp. 797–805, 1991.

[61] Zhang, Y., "The Effects of Aging on the Mechanical Behavior of Lead Free and Mixed Formulation Solder Alloys," *Ph.D. Dissertation, Auburn University*, 2010.

[62] Ding, Y., Wang, C., Tian, Y., and Li, M., "Influence of Aging Treatment on Deformation Behavior of 96.5Sn3.5Ag Lead Free Solder Alloy During In Situ Tensile Tests," *Journal of Alloys and Compounds*, Vol. 428, pp. 274–285, 2007.

[63] Xiao, Q., Bailey, H. J., and Armstrong, W. D., "Aging Effects on Microstructure and Tensile Property of Sn3. 9Ag0. 6Cu Solder Alloy," *Journal of Electronic Packaging*, Vol. 126, p. 208, 2004.

[64] Zhang, Y., Cai, Z., Suhling, J. C., Lall, P., and Bozack, M. J., "The Effects of SAC Alloy Composition on Aging Resistance and Reliability," *Proceedings of the 59th Electronic Components and Technology Conference*, pp. 370-389, 2009.

[65] Kim, K.-S., Yu, C.-H., and Yang, J.-M., "Aging Treatment Characteristics of Solder Bump Joint for High Reliability Optical Module," *Thin solid films*, Vol. 462, pp. 402-407, 2004.

[66] Anderson, I. E., and Harringa, J. L., "Elevated Temperature Aging of Solder Joints Based on Sn-Ag-Cu: Effects on Joint Microstructure and Shear Strength," *Journal of Electronic Materials*, Vol. 33, pp. 1485-1496, 2004.

[67] Mysore, K., Chan, D., Bhate, D., Subbarayan, G., Dutta, I., Gupta, Zhao, V., J., and Edwards, D., "Aging-Informed Behavior of Sn3.8Ag0.7Cu Solder Alloys," *Proceedings of ITHERM 2008*, pp. 870-875, 2008.

[68] Chavali, S., Singh, Y., Kumar, P., Subbarayan, G., Dutta, I., and Edwards, D. R., "Aging Aware Constitutive Models for SnAgCu Solder Alloys," *Proceedings of the 61st Electronic Components and Technology Conference*, pp.701-705, 2011.

[69] Bansal, A., Lee, T. K., Liu, K.C., and Xue, J., "Effects of Isothermal Aging and In-Situ Current Stress on The Reliability of Lead-Free Solder Joints," *Proceedings of the 60th Electronic Components and Technology Conference*, pp. 1529-1535, 2010.

[70] Mustafa, M., Cai, Z., Suhling, J. C., and Lall, P., "The Effects of Aging on The cyclic Stress-Strain Behavior and Hysteresis Loop Evolution of Lead Free Solders," *Proceedings of the 61th Electronic Components and Technology Conference*, pp. 927-939, 2011.

[71] Fix, A. R., Nüchter, W., and Wilde, J., "Microstructural Changes of Lead-Free Solder Joints During Long-Term Aging, Thermal Cycling and Vibration Fatigue," *Soldering and Surface Mount Technology*, Vol. 20, pp. 13-21, 2008.

[72] Chen, W. M., McCloskey, P., and O'Mathuna, S. C., "Isothermal Aging Effects on the Microstructure and Solder Bump Shear Strength of Eutectic Sn37Pb and Sn3. 5Ag Solders," *Microelectronics Reliability*, Vol. 46, pp. 896-904, 2006.

[73] Allen, S. L., Notis, M. R., Chromik, R. R., and Vinci, R. P., "Microstructural Evolution in Lead-Free Solder Slloys: Part I. Cast Sn–Ag–Cu eutectic," *Journal of Materials Research*, Vol. 19, pp. 1417-1424, 2004.

[74] Miyazawa, Y. and Ariga, T., "Influences of Aging Treatment on Microstructure and Hardness of Sn-(Ag, Bi, Zn) Eutectic Solder Alloys," *Materials Transactions of the Japan Institute of Metals*, Vol. 42(5), pp. 776-782, 2001.

[75] Gagliano, R., "Shear Testing of Solder Joints: The Effect of Various Parameters on the Maximum Shear Stress of Eutectic Tin-Lead Solder," Advanced Materials for the 21st Century: *Proceedings of the 1999 Julia R. Weertman Symposium*, pp. 107-116, 1999.

[76] Lee, S. W. R., Tsui, Y.-K., Hunag, X., and Yan, E. C. C., "Effects of Room Temperature Storage Time on the Shear Strength of PBGA Solder Balls," *Proceedings of the 2002 ASME International Mechanical Engineering Congress and Exposition*, pp. 1-4, 2002.

[77] Hasnine, M., Mustafa, M., Suhling, J. C., Porok, M., Bozack, M., Lall, P. , "Characterization of Aging Effects in Lead Free Solder Joints using Nanoindentation," *Proceedings of the 63rd Electronic Components and Technology Conference*, pp. 166-178, 2013.

[78] Motalab, M., Mustafa, M., Suhling, J. C., Zhang, J., Evans, J. L., Bozack, M. J., Lall, P., "Correlation of Reliability Models Including Aging Effects with Thermal Cycling Reliability Data," *Proceedings of the 63rd Electronic Components and Technology Conference*, pp. 986-1004, 2013.

[79] Zhang, T., Evans, J., Mitchell, C., Li, Z. Z., Crandall, E., Ridenour, J., and Xie, F., "Reliability of Lead-Free BGA with SnPb Solder Paste for Harsh Environments," *Proceedings SMTA/CAVE Symposium on AIMS Harsh Environment Electronics*, 2009.

[80] Zhang, J., Thirugnanasambandam, S., Evans, J. L., Bozack, M. J., Zhang, Y., Suhling, J. C., "Correlation of Aging Effects on the Creep rate and Reliability in Lead Free Solder Joints," *SMTA Journal*, Vol. 25(3), pp. 19-28, 2012.

[81] Lee, T. K., and Ma, H., "Aging Impact on the Accelerated Thermal Cycling Performance of Lead-Free BGA Solder Joints in Various Stress Conditions," *Proceedings of the 62nd Electronic Components and Technology Conference*, pp. 477-482, 2012.

[82] Yin, L., Meilunas, M., Arfaei, B., Wentlent, L., and Borgesen, P., "Effect of Microstructure Evolution on Pb-Free Solder Joint Reliability in Thermomechanical Fatigue," *Proceedings of the 62nd Electronic Components and Technology Conference*, pp. 493-499, 2012.

[83] Mustafa, M., Roberts, J. C., Suhling, J. C., and Lall, P., "The Effects of Aging on the Fatigue Life of Lead Free Solders," *Proceedings of the 64th Electronic Components and Technology Conference*, pp. 666-683, Orlando, FL, May 27-30, 2014.

[84] Hasnine, M, Suhling, J. C., Prorok, B. C., Bozack, M. J., and Lall, P., "Exploration of Aging Induced Evolution of Solder Joints Using Nanoindentation and Microdiffraction," *Proceedings of the 64th Electronic Components and Technology Conference*, pp. 379-394, Orlando, FL, May 27-30, 2014.

[85] Lall, P., Shantaram, S., Suhling, J., and Locker, D., "Effect of Aging on the High Strain Rate Mechanical Properties of SAC105 and SAC305 Lead free Alloys," *Proceedings of the 63rd IEEE Electronic Components and Technology Conference*, pp. 1277-1293, Las Vegas, NV, May 28-31, 2013.

[86] Yoon, J. W., Kim, S. W., and Jung, S. B., "Interfacial Reaction and Mechanical Properties of Eutectic Sn–0.7Cu/Ni BGA Solder Joints During Isothermal Long-term Aging," *Journal of Alloys and Compounds*, Vol. 391, pp. 82–89, 2005.

[87] Kim, K.S., Yu, C. H., Kim N. H., Kim N. K., Chang H. J., and Chang E. G., "Isothermal Aging Characteristics of Sn–Pb Micro Solder Bumps," *Microelectronics Reliability*, Vol. 43, pp. 757–763, 2003.

[88] Kim, D. G., Kim, J. W., and Jung S. B., "Effect of Aging Conditions on Interfacial Reaction and Mechanical Joint Strength between Sn–3.0Ag–0.5Cu Solder and Ni–P UBM," *Materials Science and Engineering B*, Vol. 121, pp. 204–210, 2005.

[89] Dompierre, B., Aubina, V., Charkaluk, E., Maia Filho, W. C., and Brizoux, M., "Influence of Thermal Aging on Cyclic Mechanical Properties of SnAgCu Alloys for Microelectronic Assemblies," *Procedia Engineering 2*, pp. 1477-1486, 2010.

[90] Coyle, R. J., Solan, P. P., Serafino, A. J., and Gahr, S. A., "The Influence of Room Temperature Aging on Ball Shear Strength and Microstructure of Area Array Solder Balls," *Proceedings of the 50th Electronic Components and Technology Conference*, pp. 160-169, 2000.

[91] Lee, T. K., Ma, H., Liu, K. C., and Xue, J., "Impact of Isothermal Aging on Long-Term Reliability of Fine-Pitch Ball Grid Array Packages with Sn-Ag-Cu Solder Interconnects: Surface Finish Effects," *Journal of Electronic Materials*, Vol. 39, pp. 2564-2573, 2010.

[92] Chilton, A. C., Whitmore, M. A., and Hampshire, W. B., "Fatigue Failure in a Model SMD Joint," *Soldering and Surface Mount Technology*, Vol.1, pp. 21-24, 1989.

[93] Li, M., Lee, K. Y., Olsen, D. R., Chen, W. T., Tan, B. T. C., and Mhaisalkar, S., "Microstructure, Joint Strength and Failure Mechanisms of SnPb and Pb-Free Solders in BGA Packages," *IEEE Transactions on Electronics Packaging Manufacturing*, Vol. 25, pp. 185-192, 2002.

[94] Koo, J.-M., and Jung, S.-B., "Effect of Displacement Rate on Ball Shear Properties for Sn–37Pb and Sn–3.5 Ag BGA Solder Joints During Isothermal Aging," *Microelectronics Reliability*, Vol. 47, pp. 2169-2178, 2007.

[95] Oliver, J. R., Liu, J., and Lai, Z., "Effect of Thermal Aging on the Shear Strength of Lead-free Solder Joints," *Proceedings of the International Symposium on Advanced Packaging Materials: Processes, Properties and Interfaces*, pp. 152-157, 2000.

[96] Pang, J. H. L., Tan, K. H., Shi, X. Q., and Wang, Z. P., "Microstructure and Intermetallic Growth Effects on Shear and Fatigue Strength of Solder Joints Subjected to Thermal Cycling Aging," *Materials Science and Engineering: A*, Vol. 307, pp. 42-50, 2001.

[97] Lee, T. K., Zhou, B., and Bieler, T. R., "Impact of Isothermal Aging and Sn Grain Orientation on the Long-Term Reliability of Wafer-Level Chip-Scale Package Sn–Ag–Cu Solder Interconnects," *IEEE Transactions on Components, Packaging and Manufacturing Technology*, Vol. 2, Issue 3, pp. 496-501, 2012.

[98] Smetana, J., Coyle, R., Read, P., Popowich, R., Fleming, D., and Sack, T., "Variations in Thermal Cycling Response of Pb-free Solder Due to Isothermal Preconditioning," *Proceedings of SMTAI 2011*, pp. 641-654, 2011.

[99] Hu, X., Li, Y., Liu, Y., and Min, Z., "Microstructure and Shear Strength of Sn37Pb/Cu Solder Joints Subjected to Isothermal Aging," *Microelectronics Reliability*, Vol. 54, pp. 1575-1582, 2014.

[100] Wang, J., and Nishikawa, H., "Impact Strength of Sn–3.0Ag–0.5Cu Solder Bumps during Isothermal Aging," *Microelectronics Reliability*, Vol. 54, pp. 1583-1591, 2014.

[101] Choi, H., Lee, T. K., Kim, Y., Kwon, H., Tseng, C. F., Duh, J. G., and Choe, H., "Improved Strength of Boron-Doped Sn-1.0Ag-0.5Cu Solder Joints Under Aging Conditions," *Intermetallics*, Vol. 20, pp. 115-159, 2012.

[102] Zhang, Q. K., Zhang, Z. F., "Fracture Mechanism and Strength-Influencing Factors of Cu/Sn–4Ag Solder Joints Aged for Different Times," *Journal of Alloys and Compounds*, Vol. 485, pp. 853–861, 2009.

[103] Lin, F., Bi. W., Ju, G., Wang, W., and Wei, X., "Evolution of Ag3Sn at Sn–3.0Ag–0.3Cu–0.05Cr/Cu Joint Interfaces During Thermal Aging," *Journal of Alloys and Compounds*, Vol. 509, pp.6666–6672, 2011.

[104] Zou, H. F., and Zhang, Z. F., "Effects of Aging Time, Strain Rate and Solder Thickness on Interfacial Fracture Behaviors of Sn–3Cu/Cu Single Crystal Joints," *Microelectronic Engineering*, Vol. 87, pp. 601–609, 2010.

[105] Peng, W., Monlevade, E., and Marques, M. E., "Effect of Thermal Aging on the Interfacial Structure of SnAgCu Solder Joints on Cu," *Microelectronics Reliability*, Vol. 47, pp. 2161–2168, 2007.

[106] Wiese, S., Roellig, M., and Wolter, K. J., "Creep of Eutectic SnAgCu in Thermally Treated Solder Joints," *Proceedings of the 55th Electronic Components and Technology Conference*, pp. 1272-1281, 2005.

[107] Jones, W. K., Liu, Y., Zampino, M. A., Gonzalez, G., and Shah, M., "Design and Reliability of Solders and Solder Interconnections," *TMS Proceedings*, 1997.

[108] Jones, W. K., Liu, Y. Q., Zampino, M. A., and Gonzalez, G. L., "The at-Temperature Mechanical Properties of Lead-Tin Based Alloys," *Microelectronic Interconnections and Assembly*, pp. 53-58, 1998.

[109] Shi, X. Q., Zhou, W., Pang, H. L. J., Wang, Z. P., and Wang, Y. P., "Effect of Temperature and Strain Rate on Mechanical Properties of 63Sn/37Pb Solder Alloy," *Journal of Electronic Packaging*, Vol. 121, pp. 179-185, 1999.

[110] Nose, H., Sakane, M., Tsukada, Y., and Nishimur, H., "Temperature and Strain Rate Effects on Tensile Strength and Inelastic Constitutive Relationship of Sn-Pb Solders," *Journal of Electronic Packaging*, Vol. 125, pp. 59-66, 2003.

[111] Plumbridge, W. J., and Gagg, C. R., "Effects of Strain Rate and Temperature on the Stress–Strain Response of Solder Alloys" *Journal of Materials Science: Materials in Electronics*, vol. 10, pp. 461-468, 1999.

[112] Lang, F., Tanaka, H., Munegat, O., Taguchi, T., and Narita, T., "The Effect of Strain Rate and Temperature on the Tensile Properties of Sn3.5 Ag Solder," *Materials Characterization*, Vol. 54, pp. 223-229, 2005.

[113] Dai, L. H. and Lee, S.-W. R., "Characterization of Strain Rate-Dependent Behavior of 63Sn-37Pb Solder Alloy," *Proceedings of InterPACK 2001*, pp. 307-313, 2001.

[114] Pang, J. H. L., Xiong, B. S., and Che, F. X., "Modeling Stress Strain Curves for Lead-Free 95.5Sn-3.8Ag-0.7Cu Solder," *Proceedings of the 5th EuroSimE Conference*, pp. 449-453, 2004.

[115] Harper, J. G., Shepard, L. A., and Dorn, J. E., "Creep of Aluminum Under Extremely Small Stresses," *Acta Metallurgica*, Vol. 6, pp. 509-518, 1958.

[116] Yang, H., Deane, P., Magill, P., and Murty, K. L., "Creep Deformation of 96.5Sn-3.5Ag Solder Joints in a Flip-Chip Package," *Proceedings of the 46th Electronic Components and Technology Conference*, pp. 1136-1142, 1996.

[117] Shi, X. Q., Wang, Z. P., Yang, Q. J., and Pang, H. L. J., "Creep Behavior and Deformation Mechanism Map of Sn-Pb Eutectic Solder Alloy," *Journal of Engineering Materials and Technology*, Vol. 125, pp. 81-88, 2003.

[118] Clech, J.-P., "An Obstacle-Controlled Creep Model for Sn-Pb and Sn-based Lead-Free Solders," *Proceedings of the SMTA International Conference*, 2004.

[119] Anand, L., "Constitutive Equations for Hot-Working of Metals," *International Journal of Plasticity*, Vol. 1, pp. 213-231, 1985.

[120] Brown, S. B., Kim, K. H., and Anand, L., "An Internal Variable Constitutive Model for Hot Working of Metals," *International Journal of Plasticity*, Vol. 5, pp. 95-130, 1989.

[121] Basit, M., Motalab, M., Suhling, J. C., Hai, Z., Evans, J. L., Bozack, M. J., Lall, P., "Thermal Cycling Reliability of Aged PBGA Assemblies - Comparison of Weibull Failure Data and Finite Element Model Predictions," *Proceedings of the 63rd Electronic Components and Technology Conference*, 2015.

[122] Che, F. X., Pang, H. L. J., Zhu, W. H., Sun, W., and Sun, A. Y. S., "Modeling Constitutive Model Effect on Reliability of Lead-Free Solder Joints," *Electronic Packaging Technology*, pp. 1-6, 2006.

[123] Pei, M., and Qu, J., "Constitutive Modeling of Lead-Free Solders," *Advanced Packaging Materials: Processes, Properties and Interfaces*, pp. 45-49, 2005.

[124] Yan, X., and Li, G., "Study of Thermal Fatigue Lifetime of Fan-in Package on Package (FiPoP) by Finite Element Analysis," *International Conference on Electronic Packaging Technology & High Density Packaging*, pp.1176-1180, 2009.

[125] Mysore, K., Subbarayan, G., Gupta, V., and Zhang, R., "Constitutive and Aging Behavior of Sn3. 0Ag0. 5Cu Solder Alloy," *IEEE Transactions on Electronics Packaging Manufacturing*, vol. 32, pp. 221-232, 2009.

[126] Wang, Q., Zhang, Y., Liang, L., "Anand Parameter Test for Pb-Free Material SnAgCu and Life Prediction for a CSP," *8th International Conference on Electronic Packaging Technology*, pp. 1-9, Shanghai, China, August 14-17, 2007.

[127] Varia, B., Fan, X., and Han, Q., "Effects of Design, Structure and Material on Thermal Mechanical Reliability of Large Array Wafer Level Packages," *International Conference on Electronic Packaging Technology & High Density Packaging*, pp. 1059-69, Beijing, China, August 10-13, 2009.

[128] Bai, N., Chen, X., and Ga, H., "Simulation of Uniaxial Tensile Properties for Lead-Free Solders with Modified Anand Model," *Materials and Design*, Vol. 30, pp. 122-128, 2009.

[129] Chen, X., Chen, G., and Sakane, M., "Modified Anand Constitutive Model for Lead-Free Solder Sn-3.5 Ag," *Proceedings of ITHERM 2004*, pp. 447-452, 2004.

[130] Amagai, M., Watanabe, Omiya, M., M., Kishimoto, K., and Shibuya, T., "Mechanical Characterization of Sn–Ag-Based Lead-free Solders," *Microelectronics Reliability*, vol. 42, pp. 951-966, 2002.

[131] Kim, Y., Noguchi, H., and Amagai, M., "Vibration Fatigue Reliability of BGA-IC Package with Pb-Free Solder and Pb–Sn Solder," *Microelectronics Reliability*, Vol. 46, pp. 459-466, 2006.

[132] Wilde, J., Becke, K., Thoben, M., Blum, W., Jupitz, T., Wang, G., and Cheng, Z. N., "Rate Dependent Constitutive Relations Based on Anand Model for 92.5 Pb5Sn2. 5Ag Solder," *IEEE Transactions on Advanced Packaging*, Vol. 23, pp. 408-414, 2000.

[133] Wang, G. Z., Cheng, Z. N., Becker, K., and Wilde, J., "Applying Anand Model to Represent the Viscoplastic Deformation Behavior of Solder Alloys," *Journal of Electronic Packaging*, Vol. 123, pp. 247-253, 2001.

[134] Rodgers, B., Flood, B., Punch, J., and Waldron, F., "Determination of the Anand Viscoplasticity Model Constants for SnAgCu," *Proceedings of InterPACK 2005*, pp. 17-22, 2005.

[135] Bhate, D., Chan, D., Subbarayan, G., Chiu, T. C., Gupta, V., and Edwards, D. R., "Constitutive Behavior of Sn3. 8Ag0. 7Cu and Sn1. 0Ag0. 5Cu Alloys at Creep and Low Strain Rate Regimes," *IEEE Transactions on Components and Packaging Technologies*, Vol. 31, pp. 622-633, 2008.

[136] Syed, A., "Updated Life Prediction Models for Solder Joints with Removal of Modeling Assumptions and Effect of Constitutive Equations," *Proceedings of the 7th EuroSimE Conference*, pp. 1-9, 2006.

[137] Schubert, A., Dudek, R., Auerswald, E., Gollbardt, A., Michel B., and Reichl, H., "Fatigue Life Models for SnAgCu and SnPb Solder Joints Evaluated by Experiments and Simulation," *Proceedings of the 53rd Electronic Components and Technology Conference*, pp. 603-610, 2003.

[138] Zhang, Q., Dasgupta, A., and Haswell, P., "Viscoplastic Constitutive Properties and Energy-Partitioning Model of Lead-Free Sn3. 9Ag0. 6Cu Solder Alloy," *Proceedings of the 53rd IEEE Electronic Components and Technology Conference*, pp. 1862-1868, 2003.

[139] Zahn, B., "Solder Joint Fatigue Life Model Methodology for 63Sn37Pb and 95.5 Sn4Ag0.5Cu Materials," *Proceedings of the 53rd IEEE Electronic Components and Technology Conference*, pp. 83-94, 2003.

[140] Lee, W. W., Nguyen, L. T., and Selvaduray, G. S., "Solder Joint Fatigue Models: Review and Applicability to Chip Scale Packages," *Microelectronics Reliability*, Vol. 40, pp. 231-244, 2000.

[141] Ridout, S. and Bailey, C., "Review of Methods to Predict Solder Joint Reliability Under Thermo-Mechanical Cycling," *Fatigue & Fracture of Engineering Materials and Structures*, Vol. 30, pp. 400-412, 2007.

[142] Basaran, C. and Tang, H., "A Damage Mechanics Based Fatigue Life Prediction Model for Solder Joints," *Journal of Electronic Packaging*, Vol. 125, pp. 120-125, 2003.

[143] Gustafsson, G., Guven, I., Kradinov, V., and Madenci, E., "Finite Element Modeling of BGA Packages for Life Prediction," *Proceedings of the 50th IEEE Electronic Components and Technology Conference*, pp. 1059-1063, 2000.

[144] Pang, J. H. L., Tan, T.-I., and Sitaraman, S. K., "Thermo-Mechanical Analysis of Solder Joint Fatigue and Creep in a Flip Chip on Board Package Subjected to Temperature Cycling Loading," *Proceedings of the 48th IEEE Electronic Components and Technology Conference*, pp. 878-883, 1998.

[145] Shnawah, D. A., Sabri, M. F. M., and Badruddin, I. A., "A Review on Thermal Cycling and Drop Impact Reliability of SAC Solder Joint in Portable Electronic Products," *Microelectronics Reliability*, Vol. 52, pp. 90-99, 2012.

[146] Liu, H., Zhang, J., Chen, S., Du, M., Feng, N., and Wang, Q., "Board Level Thermal Cycle Reliability of BGA for a New Type of Pad Structure with OSP Surface Finish," 2007, *Proceedings of 2007 ICEPT Conference*, pp.1-3, 2007

[147] Yu, S. Y., Kwon, Y.-M., Kim, J., Jeong, T., Choi, S., and Paik, K.-W., "Studies on the Thermal Cycling Reliability of BGA System-in-Package (SiP) with an Embedded Die," *IEEE Transactions on Components, Packaging and Manufacturing Technology*, vol. 2, pp. 625-633, 2012.

[148] Vasudevan ,V., and Fan, X., "An Acceleration Model for Lead-Free (SAC) Solder Joint Reliability Under Thermal Cycling," *Proceedings of the 58th IEEE Electronic Components and Technology Conference*, pp. 139-145, 2008.

[149] Darveaux, R., "Effect of Simulation Methodology on Solder Joint Crack Growth Correlation," *Proceedings of the 50th IEEE Electronic Components and Technology Conference*, pp. 1048-1058, 2000.

[150] Basit, M., Motalab, M., Suhling, J. C., Lall, P., "The Effects of Aging on the Anand Viscoplastic Constitutive Model for SAC305 Solder," *Proceedings of ITHERM 2014*, pp. 112-126, 2014.

[151] Motalab, M., Basit, M., Suhling, J. C., Lall, P., "A Revised Anand Constitutive Model for Lead Free Solder that Includes Aging Effects," *Proceedings of InterPACK 2013*, pp. V001T05A009-29, 2013.

[152] Zeng, K., and Tu, K. N., "Six Cases of Reliability Study of Pb-Free Solder Joints in Electronic Packaging Technology," *Materials Science and Engineering R*, Vol 38(2), pp. 55-105, 2002.

[153] Terashima, S., Kariya, Y., Hosoi, T., and Tanaka, M., J., "Effect of Silver Content on Thermal Fatigue Life of Sn-Xag-0.5Cu Flip-Chip Interconnects," *Journal of Electronic Materials*, Vol. 32(12), pp. 1527-1533, 2003.

[154] Amagai, M., Toyoda, Y., and Tajima, T., "High Solder Joint Reliability with Lead Free Solders," *Proceedings of Electronic Components and Technology Conference*, pp. 317-322, 2003.

[155] Motalab, M., Cai, Z., Suhling, J. C., Zhang, J., Evans, J. L., Bozack, M. J., Lall, P., "Improved Predictions of Lead Free Solder Joint Reliability that Include Aging Effects," *Proceedings of the 62nd IEEE Electronic Components and Technology Conference*, pp. 513-531, San Diego, CA, May 30 - June 1, 2012.

[156] Herkommer, D., Punch, J. and Reid, M., "A Reliability Model for SAC Solder Covering Isothermal Mechanical Cycling and Thermal Cycling Conditions," *Microelectronics Reliability*, Vol. 50, pp. 116-126, 2010.

[157] Li, D., Liu, C., and Conway, P. P., "Microstructure and Shear Strength Evolution of Sn-Ag-Cu Solder Bumps During Aging at Different Temperatures," *Journal of Electronic Materials*, Vol. (35), pp. 388-398, 2006.

[158] Basit, M., Motalab, Roberts, J. C., M., Suhling, J. C., Lall, P., "The Effects of Silver Content and Solidification Profile on the Anand Constitutive Model for SAC Lead Free Solders," *Proceedings of ITHERM 2014*, pp. 488-502, 2014.

[159] Basit, M., Motalab, M.,Suhling, J. C., Lall, P., "Viscoplatic Constitutive Model for Lead-Free Solder Including Effects of Silver Content, Solidification Profile, and Severe Aging," *Proceedings of InterPACK 2015*, 2015.

[160] Zhang, J., Hai, Z., Thirugnanasambandam, S., Evans, J. L., Bozack, M. J., Zhang, Y., Suhling, J. C., "Thermal Aging Effects on Thermal Cycling Reliability of Lead-Free Fine Pitch Packages," *IEEE Transactions on Components, Packaging, and Manufacturing Technology*, Vol. 3(8), pp. 1348-1357, 2013.

[161] Hai, Z., Zhang, J., Shen, C., Snipes, E. K., Suhling, J. C., Bozack, M. J., Evans, J. L., "Reliability Degradation of SAC105 and SAC305 BGA Packages Under Long-Term, High Temperature Aging," *SMTA Journal*, Vol. 27(2), pp. 11-18, 2014.

[162] Hai, Z., Zhang, J., Shen, C., Evans, J. L., Bozack, M. J., Basit, M., Suhling, J. C., "Reliability Comparison of Aged SAC Fine-Pitch Ball Grid Array Packages vs. Surface Finishes," *Accepted for Publication in the IEEE Transactions on Components, Packaging, and Manufacturing Technology*, 2014.

[163] Xu, L., Pang, J. H. L., "Interfacial IMC and Kirkendall Void on SAC Solder Joints Subjected to Thermal Cycling," *Proceedings of the Electronic Packaging and Technology Conference*, pp. 863-867, 2005.

[164] Basit, M., Motalab, M.,Suhling, J. C., Evans, J. L., Lall, P., "FEA BAsed Reliability Predictions for PBGA Packages Subjected to Isothermal Aging Prior to Thermal Cycling," *Proceedings of InterPACK 2015*, 2015.

APPENDIX

APPENDIX

A.1 Correlation of Predicted Stress-Strain Curves with Experimental Measurements for Different Aging Times

The correlations between the model predictions and the experimental stress-strain curves for no aging and 20 days of aging were shown in Chapter 4. For the prediction of stress-strain curves of the water quenched and reflowed SAC305 alloys the Anand parameters of Table 4.3 and Table 4.4 were utilized. Here the correlations of other aging conditions are shown. The experimental curves were those shown earlier in Chapter 4. Good correlations were obtained, with the Anand model was able to represent the stress-strain curves accurately over a wide range of temperatures and strain rates, aging condition, and cooling profile prepare to specimen.

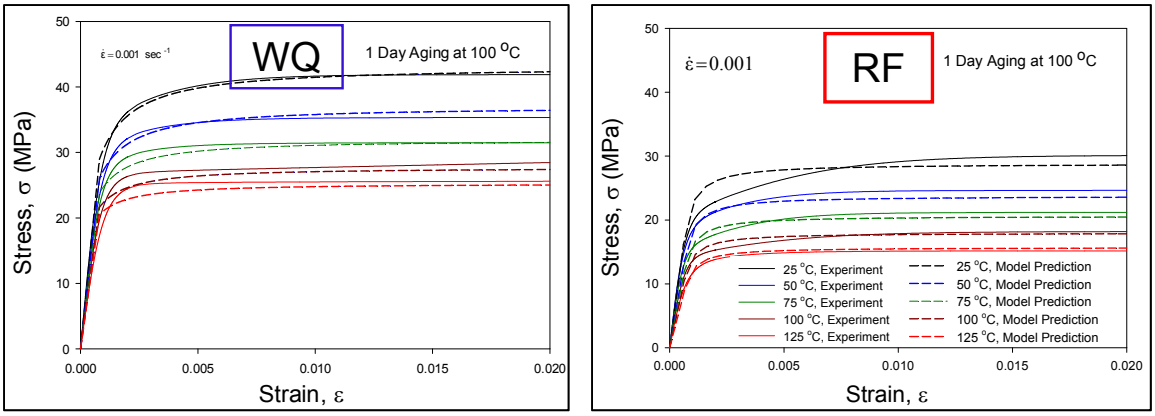

(a) $\dot{\varepsilon} = 0.001$

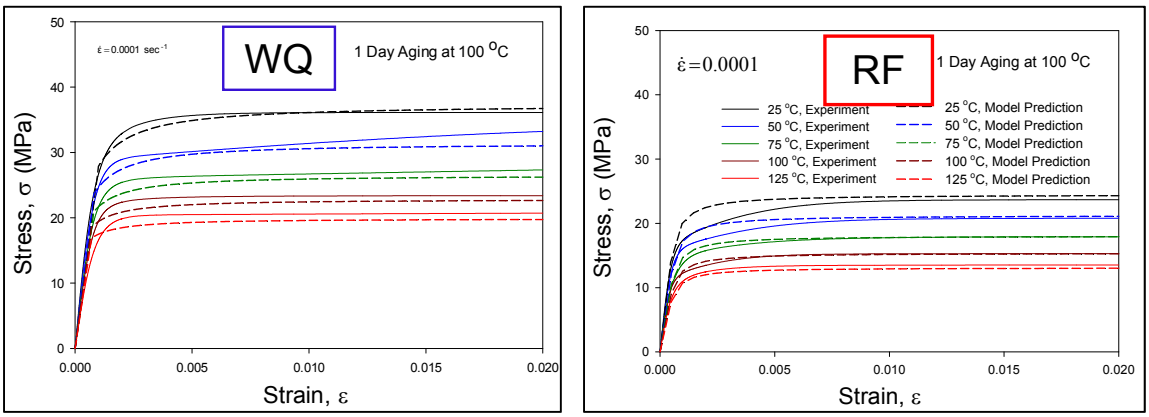

(b) $\dot{\varepsilon} = 0.0001$

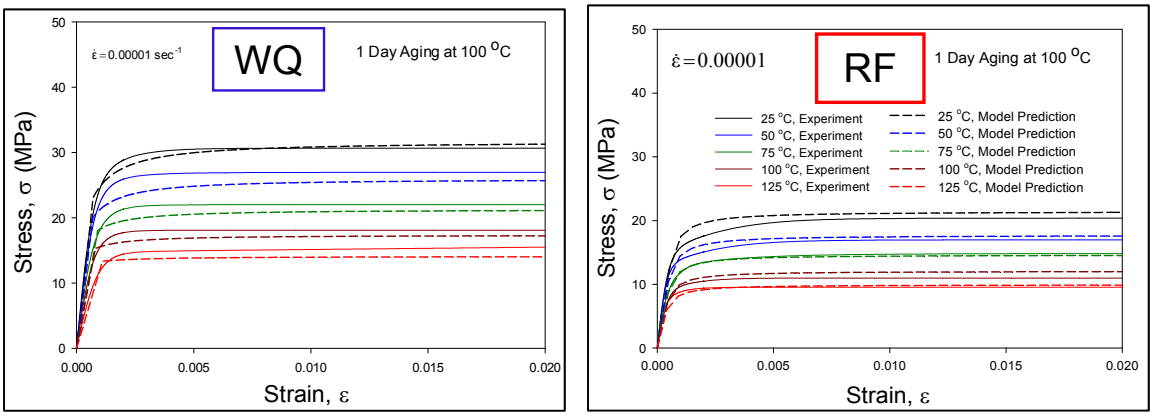

(c) $\dot{\varepsilon} = 0.00001$

Figure A.1 Correlation of the Anand Model Predictions with Experimental Stress-Strain Data for 1 Day Aging

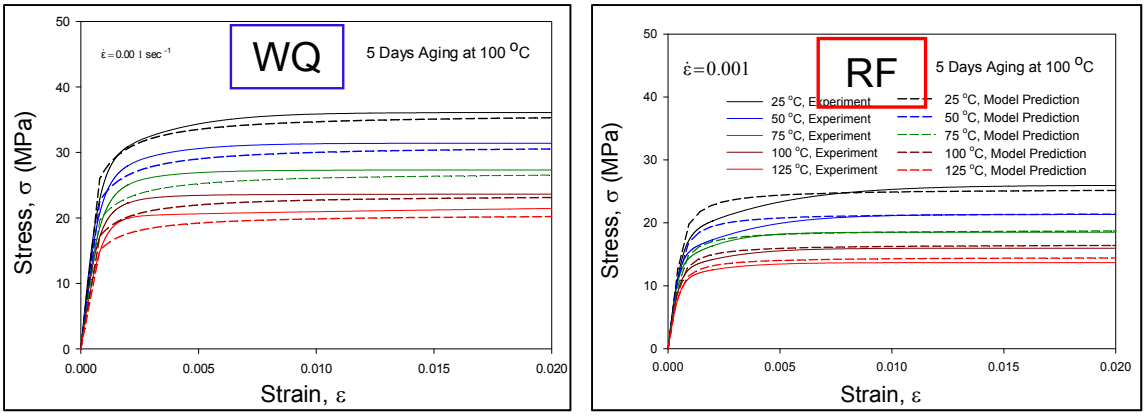

(a) $\dot{\varepsilon} = 0.001$

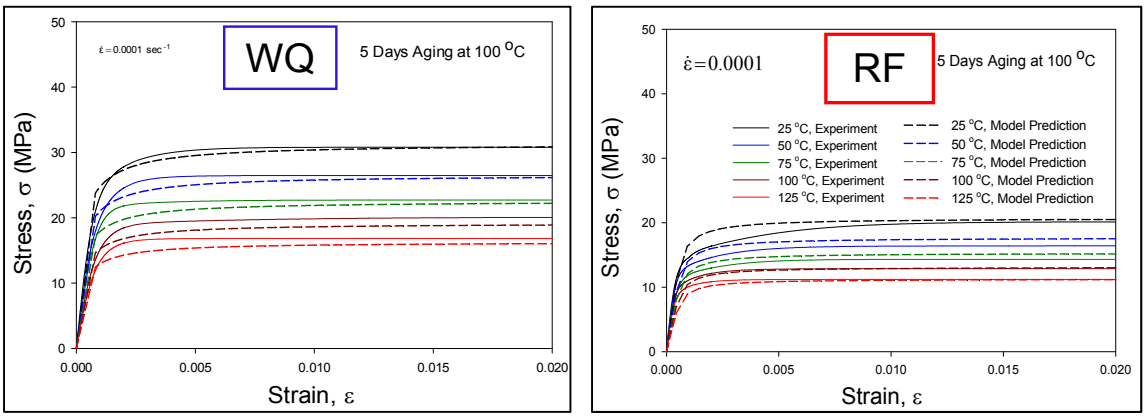

(b) $\dot{\varepsilon} = 0.0001$

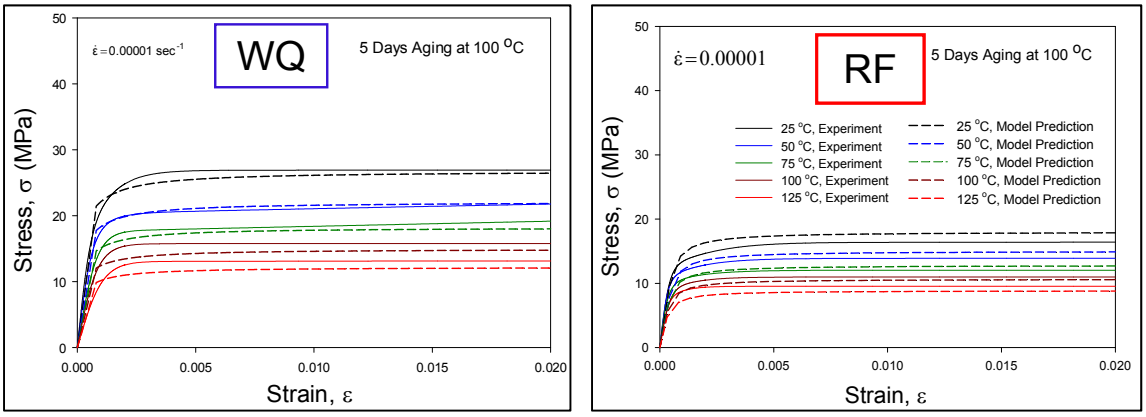

(c) $\dot{\varepsilon} = 0.00001$

Figure A.2 Correlation of the Anand Model Predictions with Experimental Stress-Strain Data for 5 Days Aging

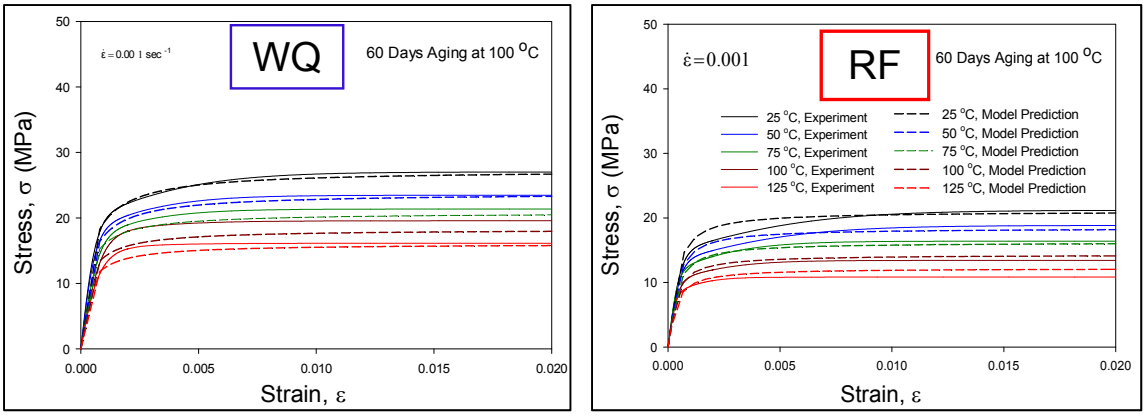

(a) $\dot{\varepsilon} = 0.001$

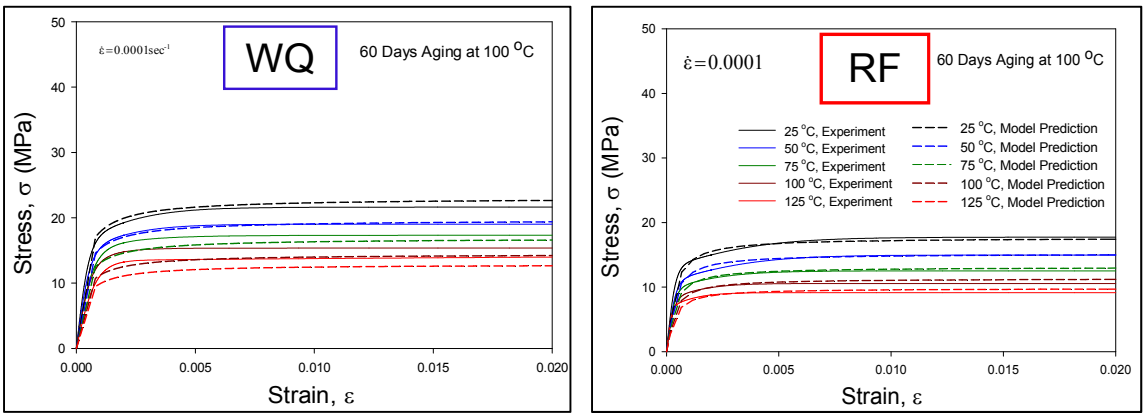

(b) $\dot{\varepsilon} = 0.0001$

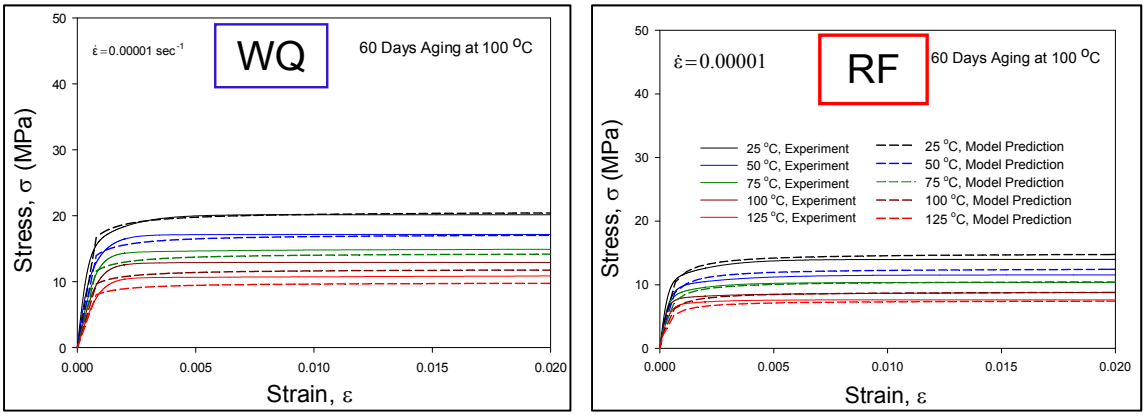

(c) $\dot{\varepsilon} = 0.00001$

Figure A.3 Correlation of the Anand Model Predictions with Experimental Stress-Strain Data for 60 Days Aging

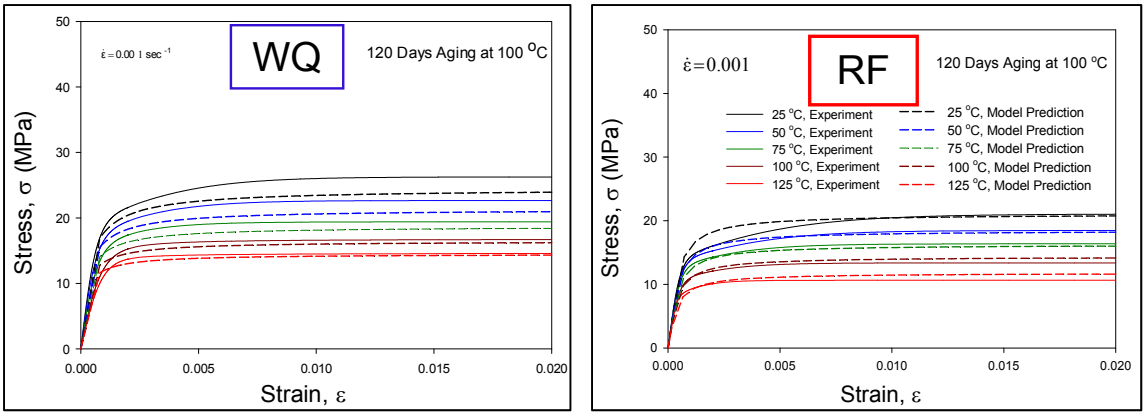

(a) $\dot{\varepsilon} = 0.001$

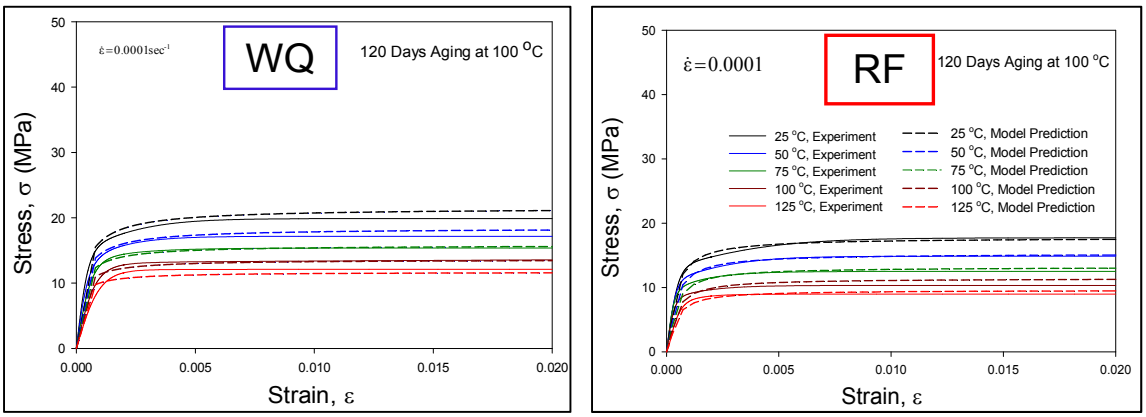

(b) $\dot{\varepsilon} = 0.0001$

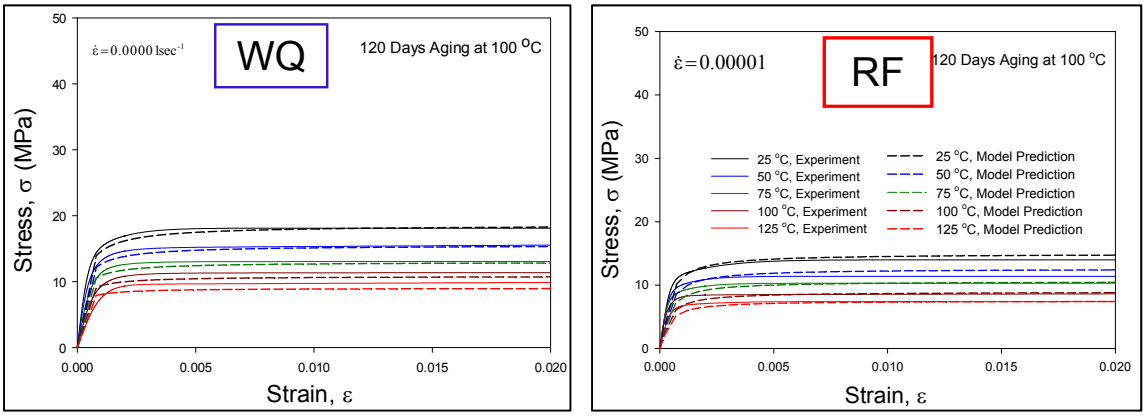

(c) $\dot{\varepsilon} = 0.00001$

Figure A.4 Correlation of the Anand Model Predictions with Experimental Stress-Strain Data for 120 Days Aging

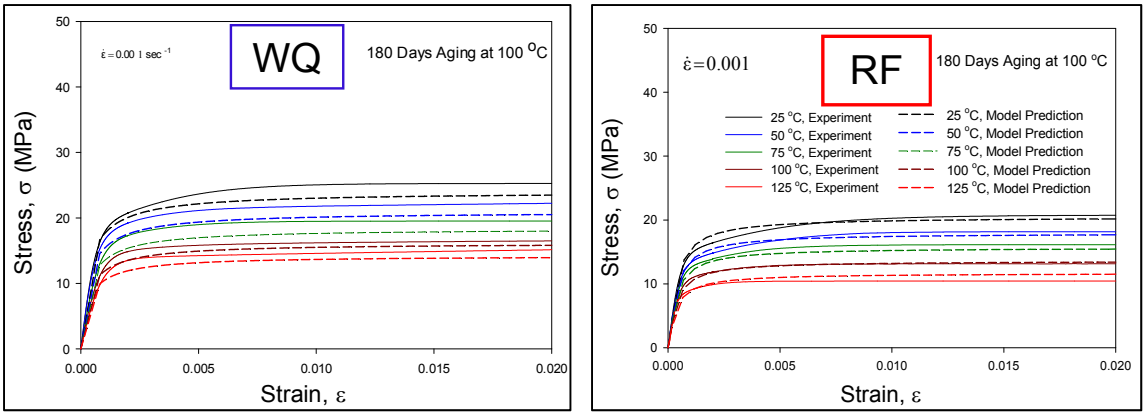

(a) $\dot{\varepsilon} = 0.001$

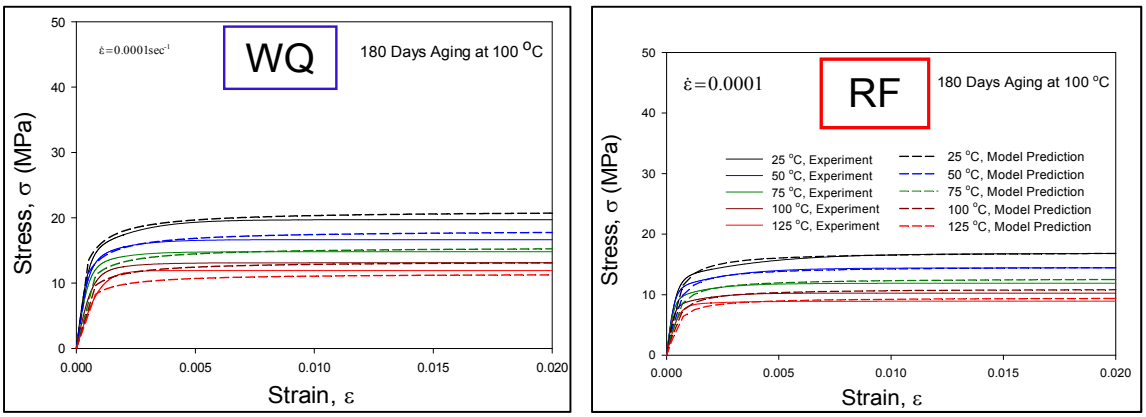

(b) $\dot{\varepsilon} = 0.0001$

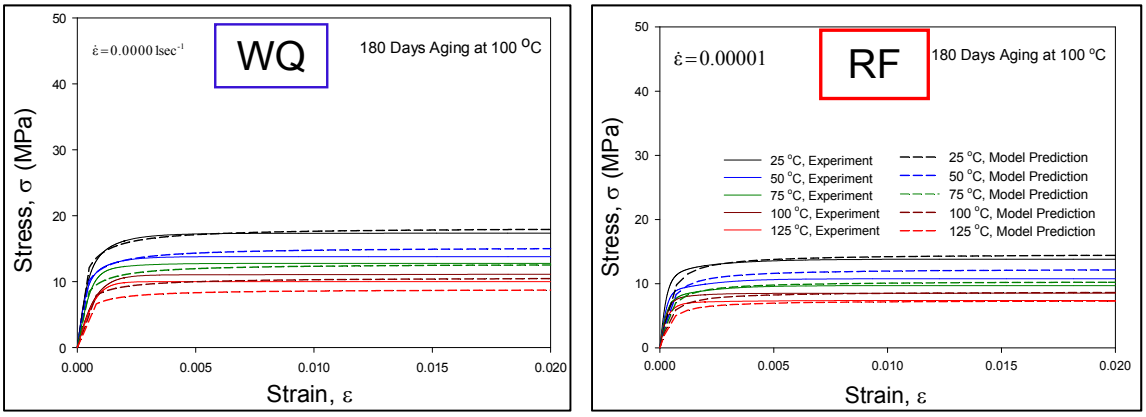

(c) $\dot{\varepsilon} = 0.00001$

Figure A.5 Correlation of the Anand Model Predictions with Experimental Stress-Strain Data for 180 Days Aging

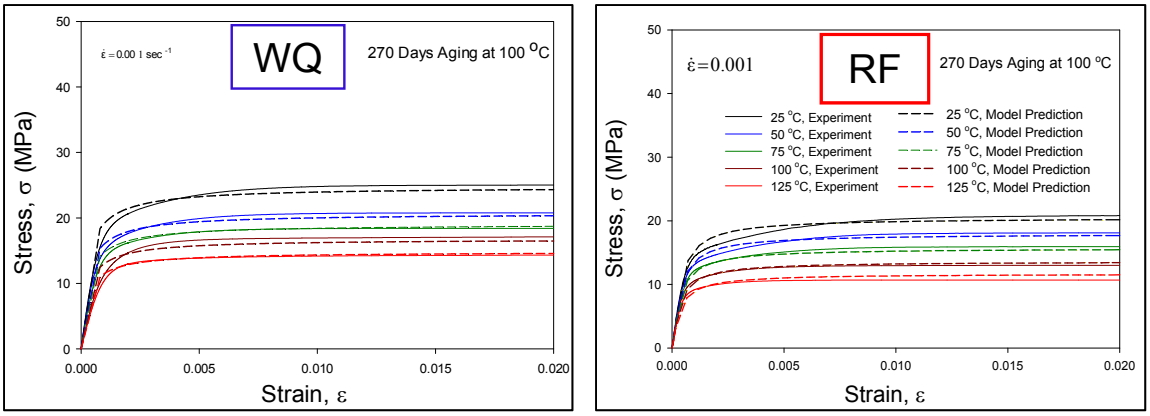

(a) $\dot{\varepsilon} = 0.001$

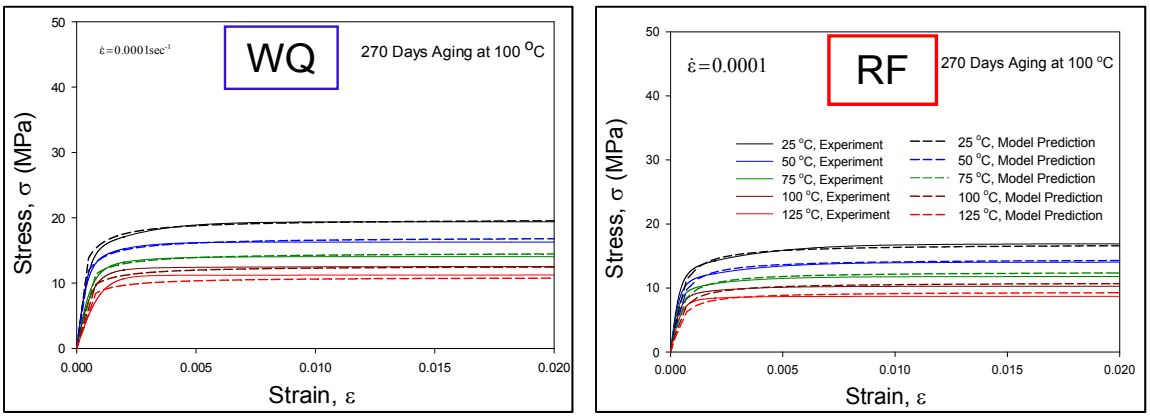

(b) $\dot{\varepsilon} = 0.0001$

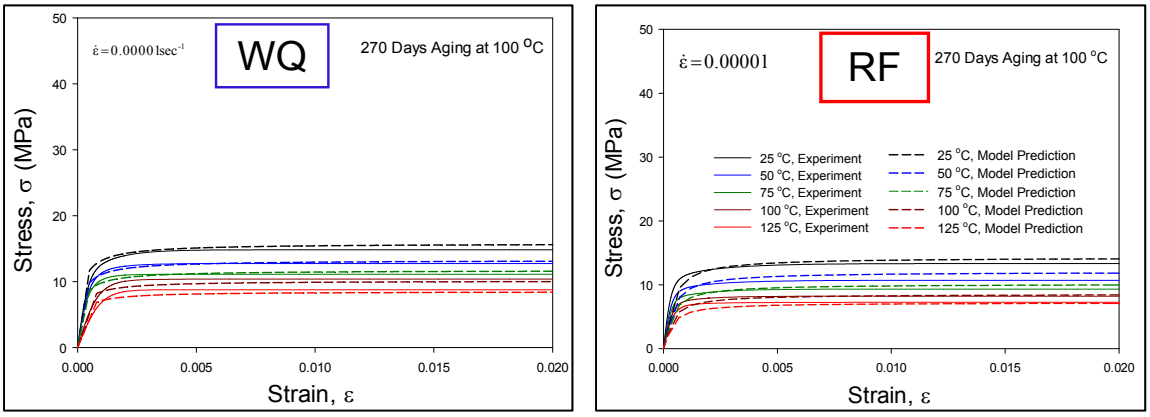

(c) $\dot{\varepsilon} = 0.00001$

Figure A.6 Correlation of the Anand Model Predictions with Experimental Stress-Strain Data for 270 Days Aging

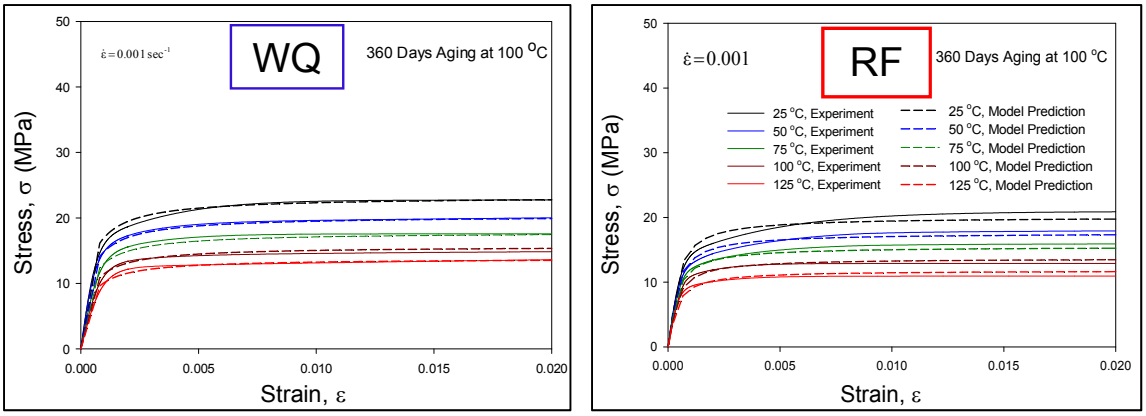

(a) $\dot{\varepsilon} = 0.001$

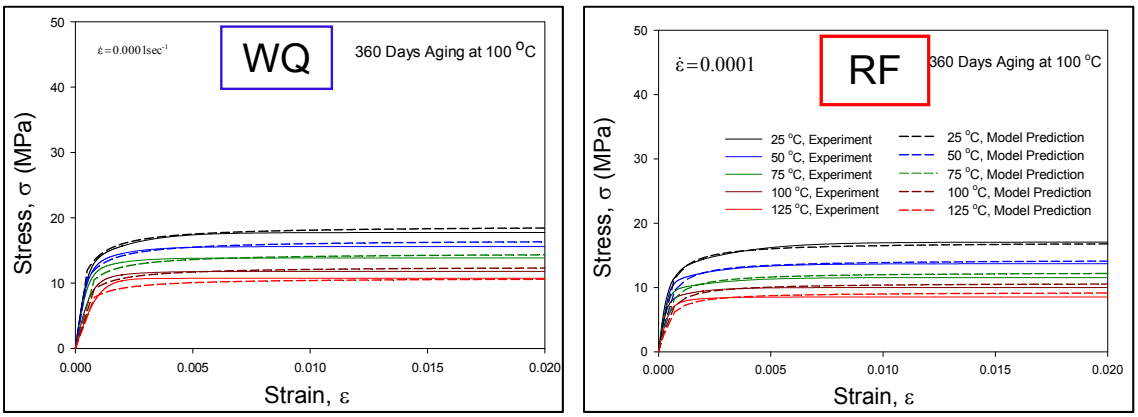

(b) $\dot{\varepsilon} = 0.0001$

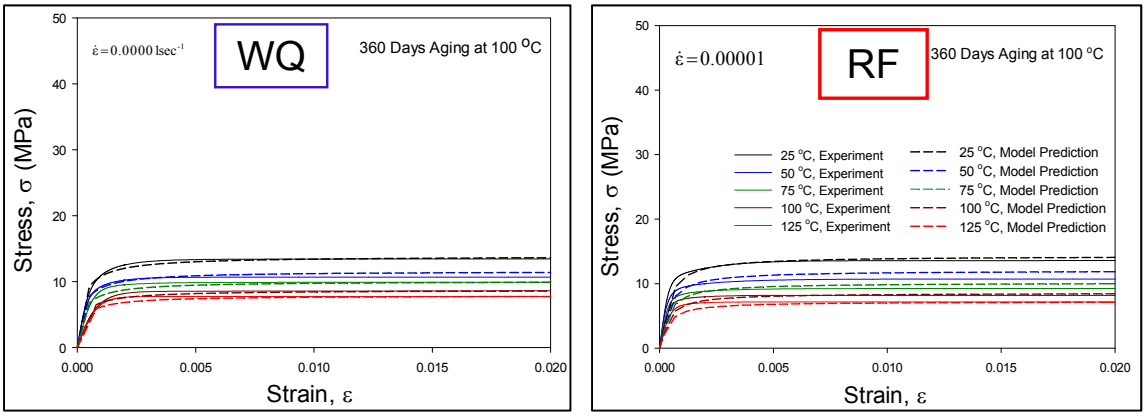

(c) $\dot{\varepsilon} = 0.00001$

Figure A.7 Correlation of the Anand Model Predictions with Experimental Stress-Strain Data for 360 Days Aging

A.2 Effects of Aging on the SACN05 alloys

The effects of Aging on SAC305 have been discussed on Chapter 4. Investigation of the effects of aging on the mechanical properties and constitutive model was determined by conducting experiments. However, there are 150 tensile tests (10 tests at 5 temperatures and 3 strain rates) need for each aging time. Thus, 150 x 9 = 1350 tests were performed to complete Table 4.3 for SAC305 alloy. Extending this procedure to other SACN05 alloys would necessitate performing a similar set of stress-strain experiments. Obviously, this would be an extremely time consuming exercise. This procedure was shortened in this work, and an extrapolation technique was developed to estimate the variation of the Anand parameters at other SAC105, SAC205, and SAC405 alloys. The estimation procedure is based on making the engineering assumption that the Anand parameters of SAC105, SAC205, and SAC405 vary with aging time in a similar manner of SAC305.

Empirical models were first used to fit the evolution of the Anand parameters with aging time for SAC305. The same functional forms were then assumed to be valid at other SAC105, SAC205, and SAC405 alloys. Only no aging condition testing data were used to determine the constants in the empirical models and scale them (extrapolate) to the other aging time. Such no aging condition data of SAC105, SAC205, and SAC405 are available in chapter 5. Figure A.8 shows the extrapolation results of ultimate strength variation with aging time for SAC105, SAC205, SAC305 and SAC405 alloys at room temperature. Similar other testing temperature results are shown in Figures A.9-A.12. Again, the variation of ultimate strength of SAC305 with aging time was determined

experimentally. The evaluation of Anand parameters with aging time are presented in Figure A.13.

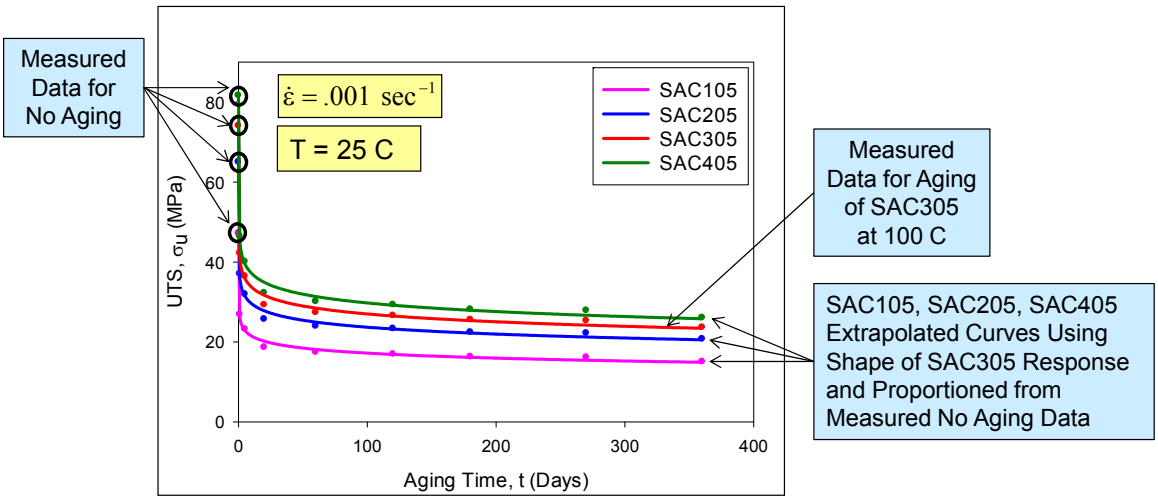

Figure A.8 Variation of UTS for SACN05 with Aging Time at 25 C

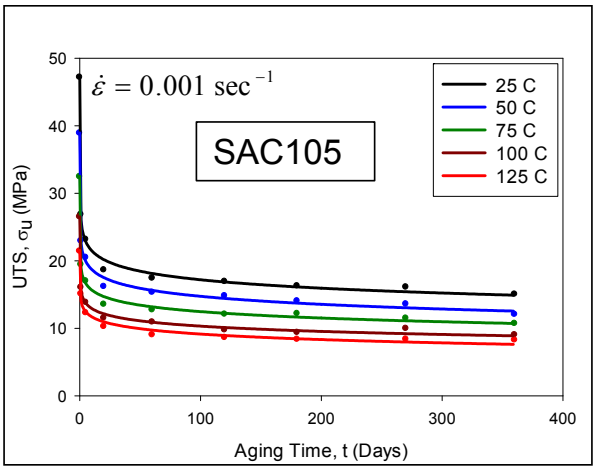

(a) $\dot{\varepsilon} = 0.001$

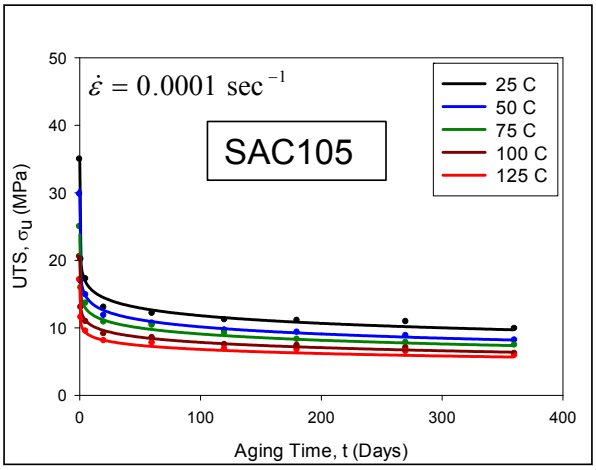

(b) $\dot{\varepsilon} = 0.0001$

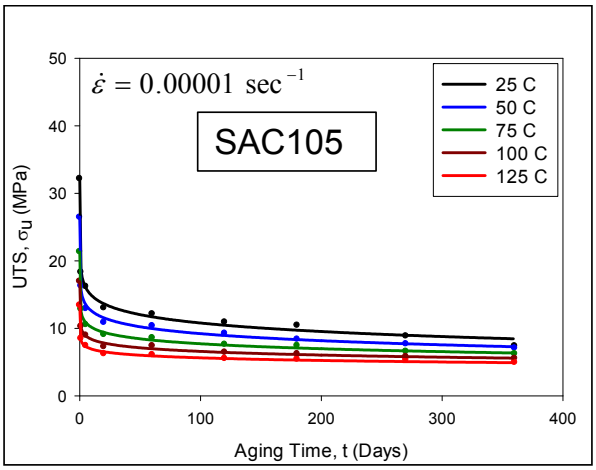

(c) $\dot{\varepsilon} = 0.00001$

Figure A.9 Variation of UTS of SAC105 with Aging Time [Extrapolation]

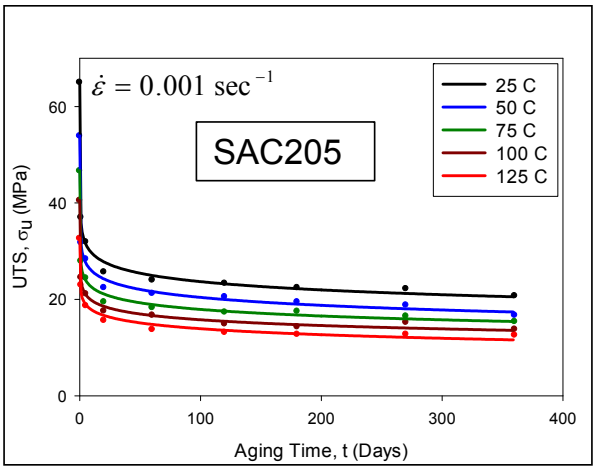

(a) $\dot{\varepsilon} = 0.001$

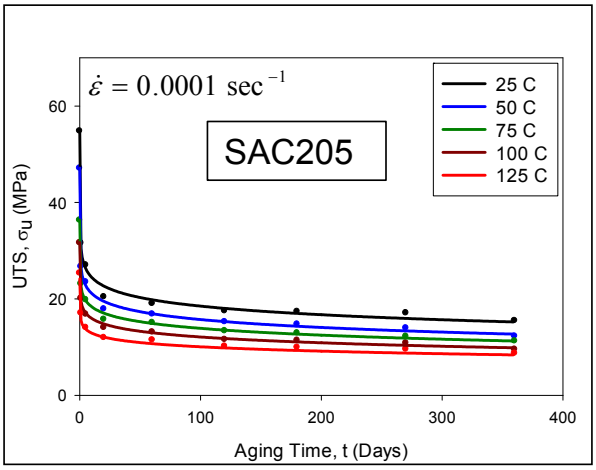

(b) $\dot{\varepsilon} = 0.0001$

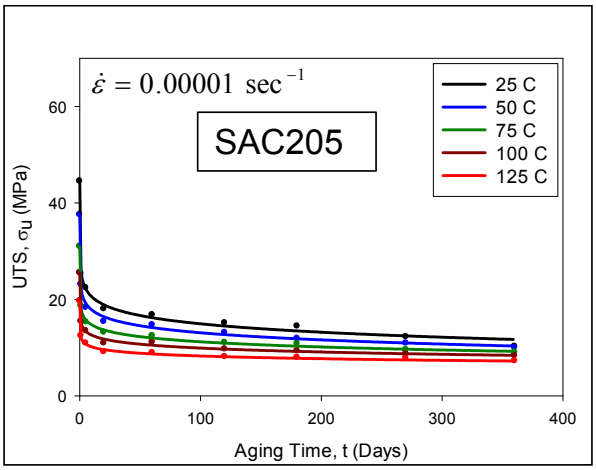

(c) $\dot{\varepsilon} = 0.00001$

Figure A.10 Variation of UTS of SAC205 with Aging Time [Extrapolation]

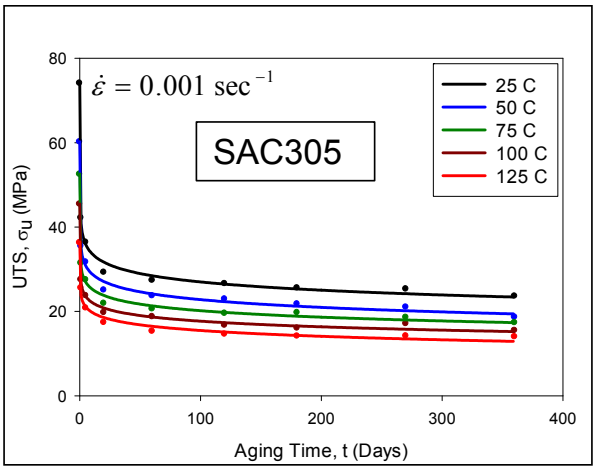

(a) $\dot{\varepsilon} = 0.001$

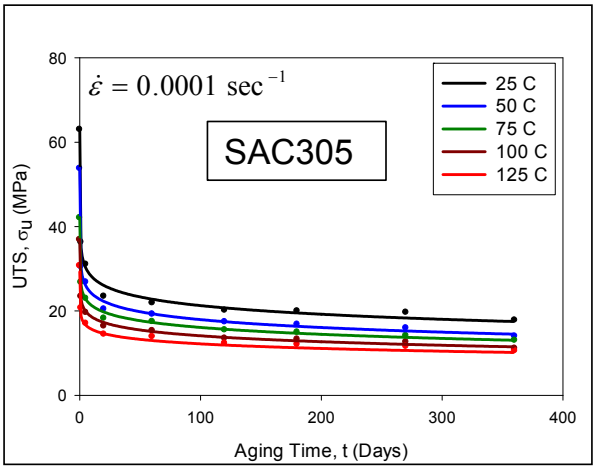

(b) $\dot{\varepsilon} = 0.0001$

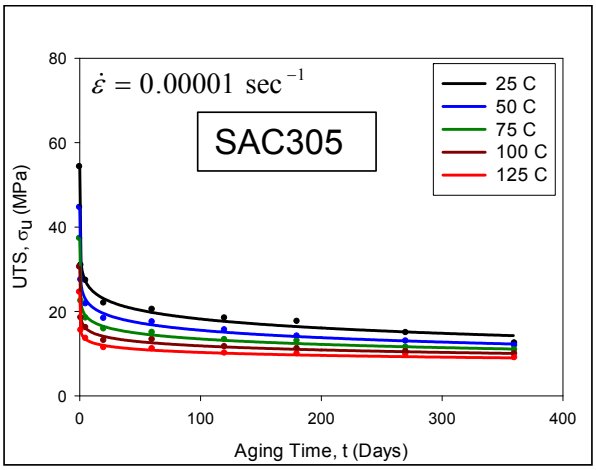

(c) $\dot{\varepsilon} = 0.00001$

Figure A.11 Variation of UTS of SAC305 with Aging Time [Experimental]

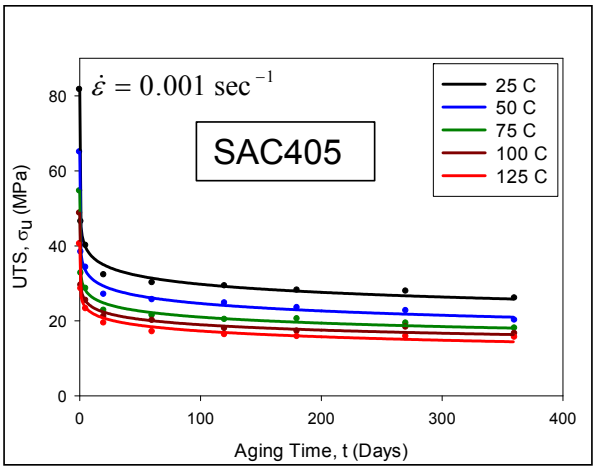

(a) $\dot{\varepsilon} = 0.001$

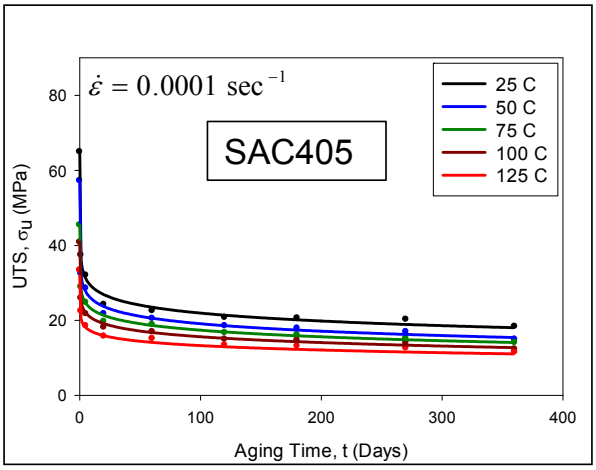

(b) $\dot{\varepsilon} = 0.0001$

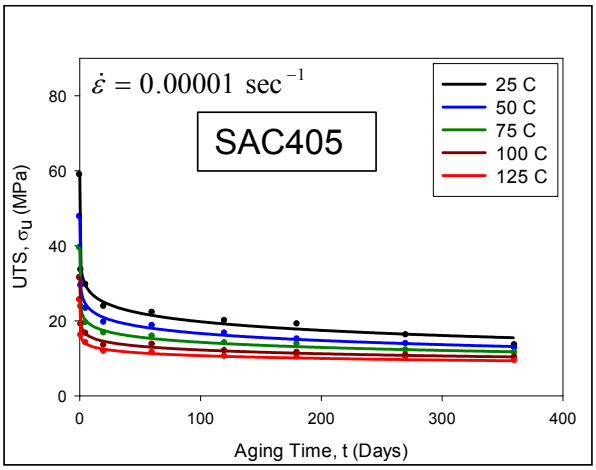

(c) $\dot{\varepsilon} = 0.00001$

Figure A.12 Variation of UTS of SAC405 with Aging Time [Extrapolation]

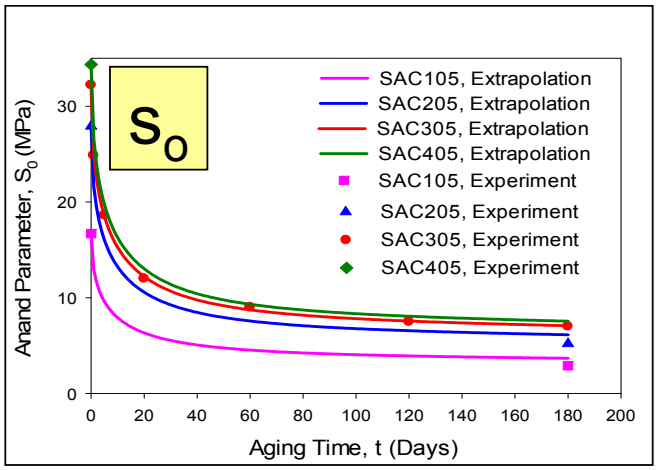
So
SAC105, Extrapolation
SAC205, Extrapolation
SAC305, Extrapolation
SAC405, Extrapolation
SAC105, Experiment
SAC205, Experiment
SAC305, Experiment
SAC405, Experiment
Anand Parameter, S0 (MPa)
Aging Time, t (Days)
0
10
20
30
0
20
40
60
80
100
120
140
160
180
200

(a)

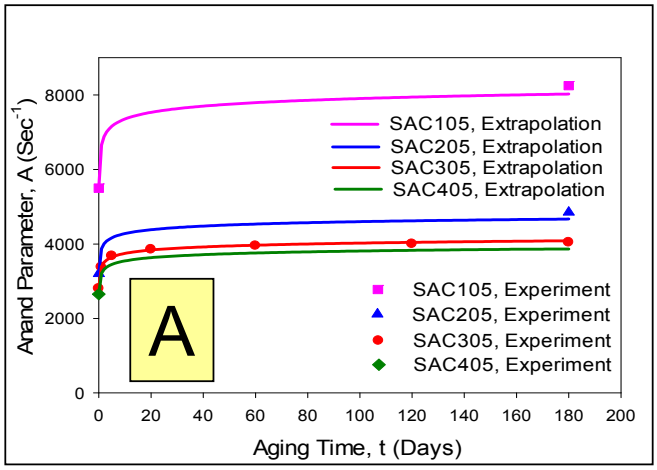
A
SAC105, Extrapolation
SAC205, Extrapolation
SAC305, Extrapolation
SAC405, Extrapolation
SAC105, Experiment
SAC205, Experiment
SAC305, Experiment
SAC405, Experiment
Anand Parameter, A (Sec-1)
Aging Time, t (Days)
0
2000
4000
6000
8000
0
20
40
60
80
100
120
140
160
180
200

(b)

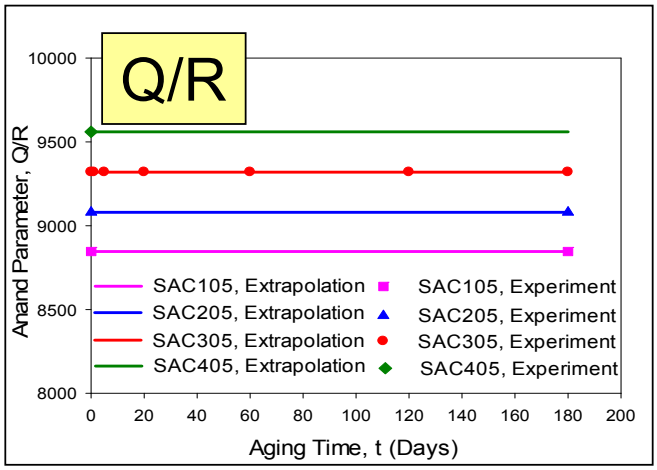
Q/R
SAC105, Extrapolation
SAC205, Extrapolation
SAC305, Extrapolation
SAC405, Extrapolation
SAC105, Experiment
SAC205, Experiment
SAC305, Experiment
SAC405, Experiment
Anand Parameter, Q/R
Aging Time, t (Days)
8000
8500
9000
9500
10000
0
20
40
60
80
100
120
140
160
180
200

(c)

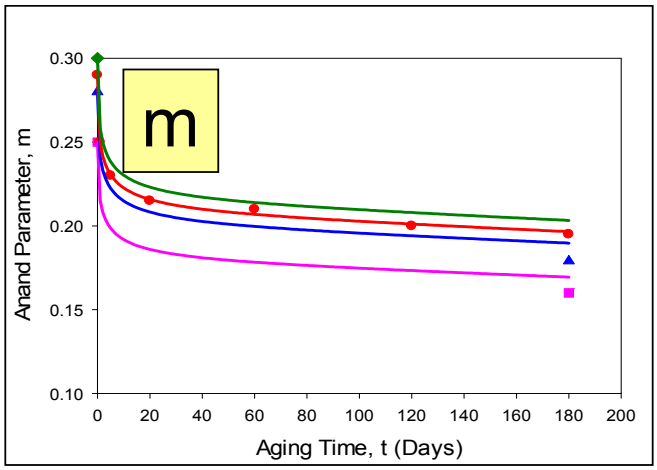
m
Anand Parameter, m
0.30
0.25
0.20
0.15
0.10
0
20
40
60
80
100
120
140
160
180
200
Aging Time, t (Days)

(d)

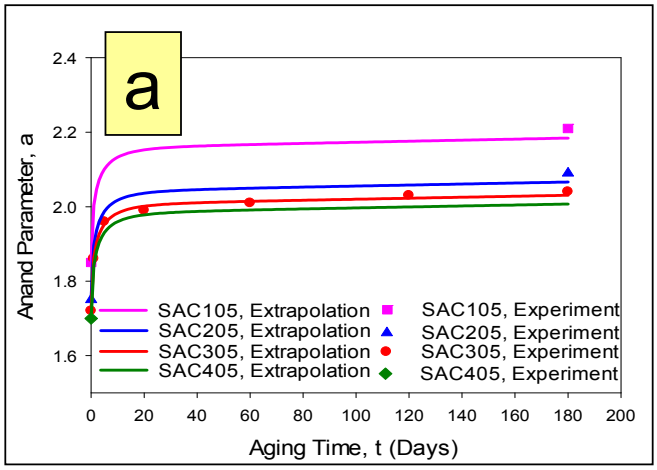
a
Anand Parameter, a
2.4
2.2
2.0
1.8
1.6
SAC105, Extrapolation
SAC205, Extrapolation
SAC305, Extrapolation
SAC405, Extrapolation
SAC105, Experiment
SAC205, Experiment
SAC305, Experiment
SAC405, Experiment
0
20
40
60
80
100
120
140
160
180
200
Aging Time, t (Days)

(e)

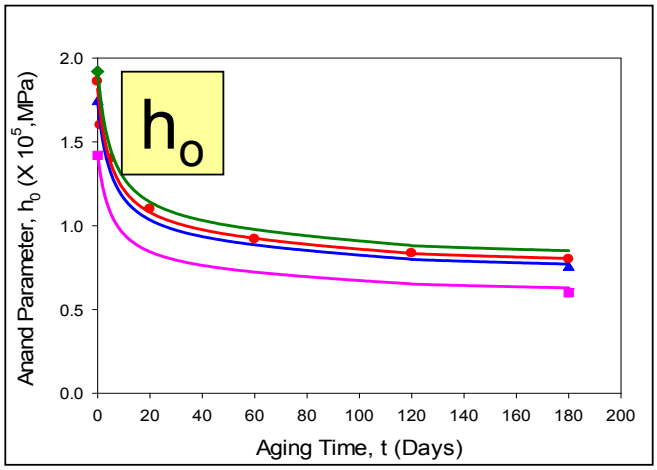
ho
Anand Parameter, h0 (X 10^5,MPa)
2.0
1.5
1.0
0.5
0.0
0
20
40
60
80
100
120
140
160
180
200
Aging Time, t (Days)

(f)

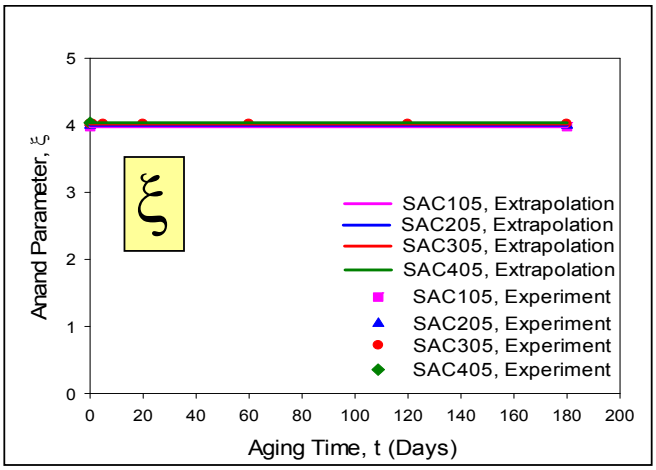

(g)

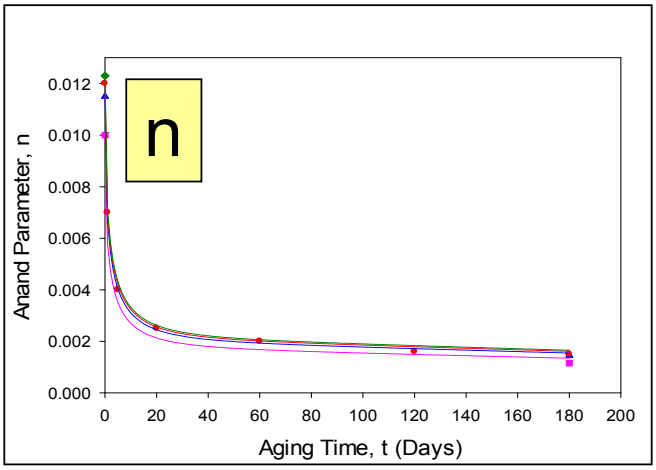

(h)

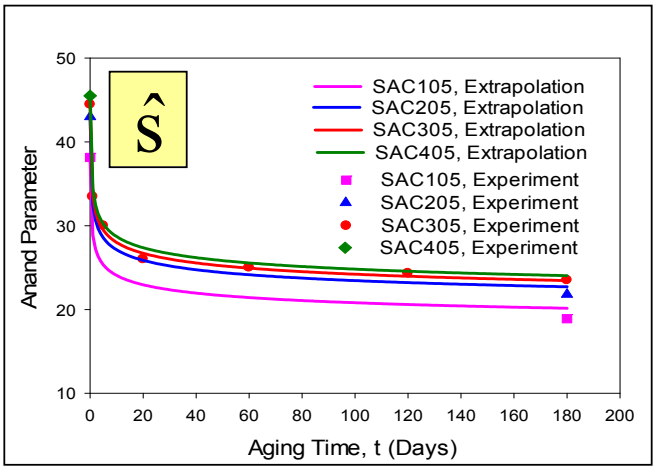

(i)

Figure A.13 Variation of Anand Parameters of SACN05 with Aging Time

A.3 Optical Microscopy of Different Packages

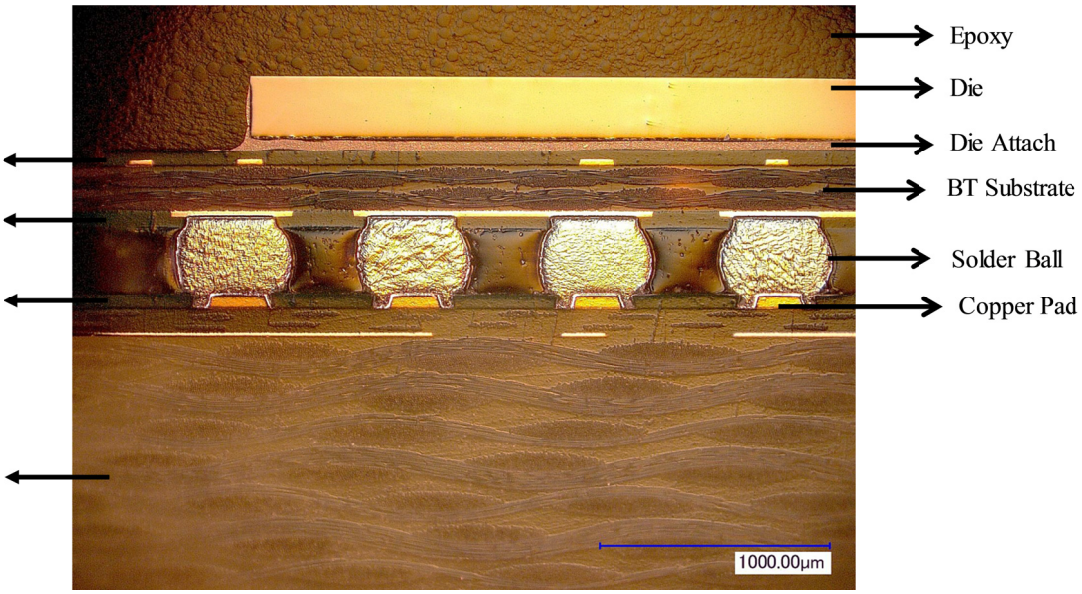

Figure A.14 Cross-Section of 15 mm Package [Middle Cut]

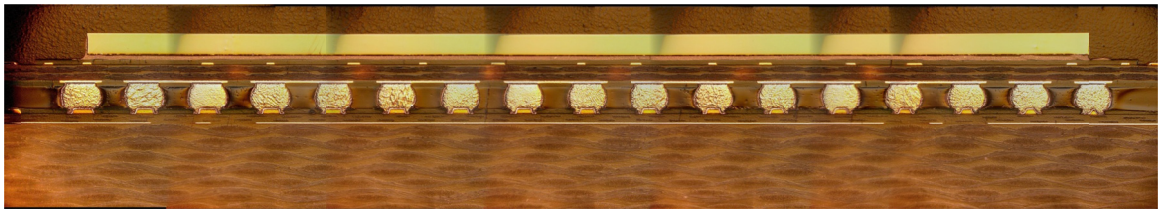

Figure A.15 Cross-Section of 15 mm Package [SIde Cut]

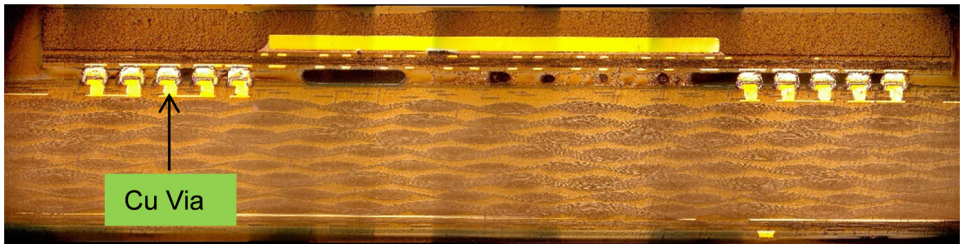

Figure A.16 Cross-Section of 10 mm Package [Middle Cut]

Figure A.17 Cross-Section of 10 mm Package [Side Cut]

A.4 Optical Microscopy of Different Packages

Figure A. 18 illustrate the critical region (green colour) in the solder ball used to calculate plastic work. For 15 mm package it is the outer ring elements of the shoulder (bottom) of the solder ball. For 10 mm package critical region was considered as the outer ring elements of the shoulder (top) of the solder ball shown in Figure A. 18 (b). The combined of outer ring elements of the shoulder (top) and neck of the solder ball was considered critical region of the 5 mm package.

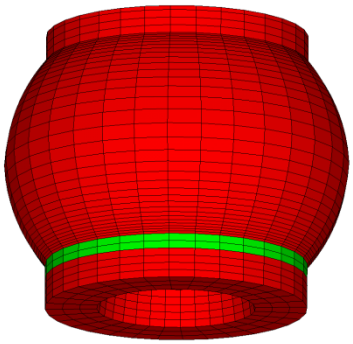

(a) 15 mm Package

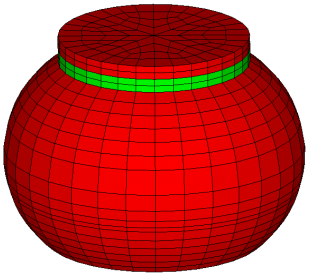

(b) 10 mm Package

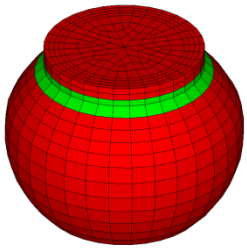

(b) 5 mm Package

Figure A.18 Critical Region of Solder Joints for Different BGA Packages